

CHARACTERIZATION AND OPTIMIZATION OF RADIOGRAPHY BY  
SELECTIVE DETECTION BACKSCATTER X-RAY IMAGING MODALITY

By

BENJAMIN TEICHMAN ADDICOTT

A THESIS PRESENTED TO THE GRADUATE SCHOOL  
OF THE UNIVERSITY OF FLORIDA IN PARTIAL FULFILLMENT  
OF THE REQUIREMENTS FOR THE DEGREE OF  
MASTER OF ENGINEERING

UNIVERSITY OF FLORIDA

2006

Copyright 2006

by

Benjamin Teichman Addicott

The Dude

## ACKNOWLEDGMENTS

I would like to thank my friends and family, especially my parents and brothers, my Aunt Deborah, Dr. Alan Jacobs, Dr. Samim Anghaie, Dr. Alireza Haghightat, Dr. Edward Dugan, The Balta-Cooks', The Dude (and family), and my research group. I would also like to thank NANT, Lockheed-Martin Space Systems Co. and NASA and the University of Florida Department of Nuclear and Radiological Engineering for support and funding of this project.

## TABLE OF CONTENTS

	<u>page</u>
ACKNOWLEDGMENTS .....	iv
LIST OF TABLES .....	viii
LIST OF FIGURES .....	ix
ABSTRACT .....	xix
CHAPTER	
1 INTRODUCTION .....	1
New Foam Imaging Backscatter Modality .....	1
Motivation .....	1
Spray On Foam Insulation .....	2
Purpose of Investigation .....	3
Radiography by Selective Detection .....	4
2 BACKGROUND .....	5
Premise .....	5
New Backscatter Radiography System .....	7
System Description and Configuration .....	7
3 THEORY .....	10
Photons .....	10
General Physics of Photons .....	10
Photon Interactions .....	11
Photoelectric effect .....	13
Compton scattering .....	14
Rayleigh scattering .....	16
Photon Production and Energy Distribution Spectrum .....	17
Attenuation .....	19
Detection Modalities .....	20
Detector Components .....	20
Scintillator .....	20
Photo multiplier .....	21

Preamplifier .....	21
Modes of Operation .....	21
Pulse mode .....	21
Integrating mode .....	22
NaI .....	22
Plastic Scintillator.....	23
Detector Comparison.....	23
Compton Backscatter Radiography .....	25
Radiography by Selective Detection .....	26
Monte Carlo Methods (MCNP5).....	27
SABRINA Supplemental Track Plotter.....	28
4 RADIOGRAPHY BY SELECTIVE DETECTION .....	29
RSD.....	29
Photon Transport Model.....	48
Introduction and Concept .....	48
Support /Evidence and Characteristics .....	51
Image contrast (bright vs. dark images).....	53
Collimation trends (optimization) .....	64
Image pixel shifts and shadows.....	73
Signal intensity .....	75
Applications and Limitations.....	76
5 BACKSCATTER FIELD DISTRIBUTION AND DETECTOR PLACEMENT .....	77
Backscattered X-ray Signal Profile .....	77
Detector Placement Considerations.....	80
6 RSD OPTIMIZATION AND IMAGING CHARACTERISTICS .....	84
Optimization Principles .....	84
SOFI Foam .....	85
Voids in foam .....	89
High density absorber and scattering type flaws.....	94
Shadows .....	97
Aluminum.....	101
Plastic .....	112
Concrete and Gypsum .....	114
Reactor Insulation.....	118
Space Shuttle Thermal Protection Shield (TPS) Insulation Tiles .....	121
7 SPECTROSCOPY .....	123
Flaw Type and Orientation .....	124
Flaw Material.....	124
Flaw Depth .....	130
Target Material .....	134

Detector Material.....	140
Detector and Collimation Configuration .....	142
Detector to sample spacing.....	142
Collimation extension.....	144
Monte Carlo Verification.....	149
Applications.....	149
8 CONCLUSIONS .....	151
Applications.....	151
Recommendations for Further Developments.....	152
Detector Configuration.....	152
Detector Materials and Operation Modes.....	153
MCNP5 Simulations to be Considered.....	154
Optimizing Geometrical Variables.....	155
APPENDIX	
A SELECTED SABRINA GENERATED PHOTON TRACK PLOTS.....	156
B ONE SCATTER SIMPLIFIED PHOTON TRANSPORT MODEL.....	182
C COLLIMATION DEPENDENT CONTRAST TREND ANALYSIS.....	187
D IMAGED SAMPLE DESCRIPTIONS .....	193
E SPECTROSCOPIC TRENDS .....	195
F PHOTON CROSS-SECTION DATA.....	209
LIST OF REFERENCES.....	219
BIOGRAPHICAL SKETCH .....	222

## LIST OF TABLES

<u>Table</u>	<u>page</u>
4.1 Relative contrasts as calculated and observed experimentally .....	64
7.1 Percent contrast for various flaw types in aluminum.....	129

## LIST OF FIGURES

<u>Figure</u>	<u>page</u>
1.1 Mean free path of various peak energy photon beams in SOFI and in aluminum.....	3
2.1 Simple schematic of landmine detection system .....	6
2.2 Tiled sample landmine scans. VS-1.6 antipersonnel mine, 2.5 cm depth-of-burial, 15 mm resolution.....	6
2.3 Schematic of detector components. Gray arrow represents photon beam direction. Center of detector is 9 cm from photon beam center. ....	8
2.4 System signal flow chart for image acquisition.....	9
2.5 Yxlon x-ray tube head and four NaI collimated detectors .....	9
3.1 Oscillating electric (E) and magnetic (M) fields about a propagating photon.....	10
3.2 Dominant interaction type as a function of energy and material Z number .....	13
3.3 Photoelectric cross-section for aluminum. Log / Log scale.....	14
3.4 Compton interaction between photon and stationary electron.....	15
3.5 Relative Klein-Nieshena Compton collision cross-section as a function of energy and scattering angle.....	16
3.6 Typical bremsstrahlung x-ray energy spectrum .....	18
3.7 Bremsstrahlung spectrum with characteristic x-rays.....	18
3.8 Scatter components of Compton backscatter radiography signal.....	26
3.9 Scatter component contributions to collimated RSD backscatter imaging signal. ....	27
4.1 First collision components in SOFI reaching the detector with collimator extension.....	32
4.2 Multiple collision components in SOFI reaching the detector with collimator extension.....	32

4.3 First collision components in aluminum.....	33
4.4 Multiple collision components in aluminum..	34
4.5 First collision components.....	35
4.6 Second collisions components.....	35
4.7 Third collisions components.....	36
4.8 Fourth collisions components.....	36
4.9 Higher order (fifth and greater) collisions components.....	37
4.10 Scatter component contribution to detector current tally for geometry of Figures 4.5 to 4.9 .....	38
4.11 Relative contrast by scatter order.....	39
4.12 Directional distribution of tally components by scatter order.....	40
4.13 Percent signal, relative contrast and total contrast contribution by scatter components for 1 cm collimator extension.....	41
4.14 Percent signal, relative contrast and total contrast contribution by scatter components for 1.32 cm collimator extension .....	42
4.15 Percent signal, relative contrast and total contrast contribution by scatter components for 1.5 cm collimator extension .....	42
4.16 Percent signal, relative contrast and total contrast contribution by scatter components for 2.32 cm collimator extension .....	43
4.17 Schematic of CRP. Photons at and below CRP can pass under collimator and enter detector.....	45
4.16 Severely under-collimated. first scatters. 5.08 cm radius NaI 1.14 cm from SOFI. Dark line indicates CRP above which no first scatters can enter the detector. ....	46
4.19 First Scatters. NaI 6.14 cm from SOFI 5 cm collimator extension.....	47
4.20 First Scatters. NaI 11.14 cm from SOFI 10 cm collimator extension.....	47
4.21 First Scatters. NaI 14.15cm from SOFI 14cm collimator extension.....	48
4.22 One scatter photon transport model. Double lines indicate upper and lower bounds from important scatters.....	49

4.23	SABRINA generated photon track plot. Aluminum plate with shallow scattering type flaw.....	52
4.24	SABRINA generated photon track plot. Aluminum plate with shallow scattering type flaw.....	53
4.25	Difference is important photon exiting paths caused by a focusing collimator extension.....	54
4.26	VShL: Void shallow long.....	56
4.27	VShI: Void shallow incident.....	57
4.28	VShE: Void shallow exit.....	57
4.29	VDL: Void deep long.....	58
4.30	VDI: Void deep incident.....	58
4.31	VDE: Void deep exit.....	59
4.32	ScShL: Scatterer shallow long.....	59
4.33	ScShI: Scatter shallow incident.....	60
4.34	ScShE: Scatter shallow exit.....	60
4.35	ScDL: Scatter deep long.....	61
4.36	ScDI: Scatter deep incident.....	61
4.37	ScDE: Scatterer deep exit.....	62
4.38	MCNP data plots of contrast vs. collimation length.....	65
4.39	Experimental data points of contrast vs. collimation length.....	65
4.40	Analytically derived contrast trend as CRP is moved from sample surface to flaw top.....	67
4.41	Analytically derived contrast trend as CRP moves below flaw bottom.....	68
4.42	Contrast vs collimator extension trend. MCNP5 simulations and 1st scatter model.....	69
4.43	Contrast vs collimation extension. MCNP5 simulation data and 1st scatter model approximation.....	70

4.44 Contrast vs collimation extension. MCNP5 simulation data and 1st scatter model approximation.....	70
4.45 Geometrical considerations for shadow pixel shifting relative to detector position.....	74
4.46 Bright shadow cast by void in Al seen by detector in lower right hand corner.....	75
4.47 Bright shadow cast by void in Al seen by detector in lower left hand corner.....	75
5.1 Klien-Nishiena differential scattering cross-section for 55 keV photon .....	78
5.2 Backscattered photon flux across a plane parallel to SOFI sample surface .....	79
5.3 Percent difference in signal due to void flaw in SOFI as a function of scatter field component. ....	80
5.4 RSD focusing. Each collimation configuration A, B, C selects for photons originating at and below each specific depth A, B, C, respectively.....	82
6.1 Two important paths of a backscattered photon .....	86
6.2 MCNP5 simulated geometry. Four, two inch thick layers of SOFI on aluminum substrate.....	88
6.3 Detector contribution by cell as a function of collimation. 60 keV incident spectrum. ....	88
6.4 Detector contribution by cell as a function of collimation. 75 keV incident spectrum .....	89
6.5 Void-type flaw in SOFI. CRP is optimally set to be just above flaw.....	91
6.6 Images of foam calibration panel with varying degrees of collimation. Collimation increases clockwise from lower left.....	93
6.7 Void-type flaw in SOFI. Thin arrow demonstrates the path difference induced by the lack of scatter at the void site.....	94
6.8 Two mechanisms (1-lack of scatter, 2- increased attenuation) for generating low intensity signal from an absorber-type flaw in SOFI.....	95
6.9 Scan of depth staggered aluminum inserts in SOFI. Bright inserts are above CRP and dark inserts are below CRP. ....	97
6.10 Mechanism for shadow image generation. Dashed line represents true flaw position, solid arrow indicated shadow image detection position.....	98
6.11 SOFI panel with contoured aluminum substrate. B&W .....	99

6.12 SOFI ramp panel with contoured aluminum substrate. ....	100
6.13 Bolt of flange panel under SOFI. ....	101
6.14 Clockwise from upper left, detectors 1,2,3,4. ....	103
6.15 Photon exit paths across a void channel. ....	104
6.16 Shadow shifting with detector position. ....	105
6.17 Bright shadow images of aluminum flaw plate. 5 cylindrical void flaws at various depths are imaged as bright with severe over-collimation. ....	106
6.18 Schematic of flaw shadow and detector orientation relationship ....	107
6.19 Correlated (processed) image of sample aluminum plate. ....	108
6.20 Uncollimated image of aluminum flaw plate. ....	109
6.21 Collimation set to discriminate just above shallowest flaw. Flaw depth increases from lower right, counterclockwise to center. ....	110
6.22 Over-collimated image of aluminum sample plate. ....	111
6.23 Over-collimated image of small channel aluminum plate. ....	112
6.24 Under-collimated image of small channel aluminum plate. ....	112
6.25 Plastic flawed plate #1, uncollimated on left, collimated on right. ....	113
6.26 Correlated image of LANL block. ....	115
6.27 LANL block color image. ....	115
6.28 Clock radio, glass tube, wire, and acrylic rod inside cinder block. ....	116
6.29 Various objects behind 1 inch of gypsum. ....	117
6.30 Miniature stereo, glass, fiber optic cable, copper wire, behind 1 inch of gypsum (drywall). ....	117
6.31 Reactor insulation panel image showing steel nameplate and shadow also corrugated interior foil structure evident. ....	118
6.32 Steel reactor insulation panel with boric acid residue. ....	119
6.33 Color image of insulation panel, boric acid on far side clearly evident. ....	119

6.34	Reactor insulation panel correlation image. Plastic bag with boric acid on far side of panel. Interior structure of foil also apparent. ....	120
6.35	Side view of reactor insulation panel, showing several layers of corrugated foil. .	120
6.36	Internal structure of corrugated foil inside reactor insulation panel. ....	120
6.37	Space shuttle insulation tile. Density variation in surface adhesive evident. Dark spots are glue conglomerations between ceramic tile and laminate covering.....	121
6.38	Space shuttle insulation tile, under-collimated. Bright smears are glue below CRP, dark circles on left are drilled holes.....	122
7.1	MCNP5 generated backscatter spectra of various flaw materials in Al, high collimation.....	126
7.2	MCNP5 generated backscatter spectra of various flaw materials in Al, low collimation.....	127
7.3	Unresolved experimental spectral trends. Experimentally acquired data for the spectral shift observed for void type flaw at various depths. ....	132
7.5	Unresolved simulated spectral trends. MCNP5 simulations for spectral shifts observed from void flaws at various indicated depths. ....	133
7.6	Resolved simulated spectral trends. MCNP5 simulations for spectral shifts observed from void flaws at various indicated depths. ....	134
7.7	Normalized (first moment) experimental data 75 keV backscatter spectra from a plastic target. ....	136
7.8	Normalized (first moment) experimental data 75 keV backscatter spectra from an aluminum target.....	136
7.9	Normalized (first moment) experimental data 75 keV backscatter spectra from a steel target. ....	137
7.10	Normalized (first moment) experimental data 75 keV backscatter spectra. No collimator extension, 6 cm from NaI to Sample surfaces. ....	137
7.11	Normalized (first moment) experimental data 75 keV backscatter spectra. ....	138
7.12	Photoelectric cross-sections for lead.....	139
7.13	Photoelectric cross-sections for aluminum. ....	140
7.15	Normalized experimental spectral shifts for various detector to sample distances over aluminum.....	143

7.16 Collimator extension and CRP.....	146
7.17 Normalized experimental spectral shifts as a function of collimation extension. ...	148
A1 Photons having four or less collisions (void flow).....	156
A2 Photons having one collision (void flow) .....	157
A3 All photons entering detector (history filtered for clarity-void flow).....	157
A4 All photons entering detector. Scatter sites marked with black X (plastic flow).....	158
A5 All collision components, history filtered (plastic flow).....	158
A6 No flaw first through fourth collision components.....	159
A7 Plastic flaw first through fourth collision components .....	159
A8 No flaw all collision components, zoomed in view.....	160
A9 Plastic flaw all collision components zoomed in view .....	160
A10 Plastic flaw first collision components .....	161
A11 Plastic flaw first collision component.....	162
A12 Plastic flaw first collision scatter points. ....	162
A13 Plastic flaw, all scatter components (note many scatters off the NaI surface and down back into Al).....	162
A14 First and second scatter points.....	163
A15 Multiple scatter sites .....	163
A16 First, second, third scatter points. ....	164
A17 First, second, third, fourth scatter points.....	164
A18 All scatter points. ....	165
A19 Void flaw first collision components.....	165
A20 Void flaw all collision components. ....	166
A21 First collision components .....	166
A22 Second collision components.....	167
A23 Third collision components.....	167

A24 Fourth collision components.....	168
A25 All collisions.....	168
A26 First collision.....	169
A27 All collisions.....	169
A28 No flaw.....	170
A29 SSL.....	170
A30 SSL zoomed in view of tracks across flaw and aluminum.....	171
A31 SSL. Flaw is above CRP.....	171
A32 SSL.....	172
A33 ADL flaw is below CRP.....	172
A24 ADL zoomed in view.....	173
A35 VDL. Flaw is below CRP.....	173
A36 VDL zoomed in view.....	174
A37 VSL. Flaw is above CRP.....	174
A38 VDL, flaw shown opaque.....	175
A39 VDL.....	175
A40 VDL, flaw is transparent.....	176
A41 VSL zoomed in view.....	176
A42 VDE. Aluminum and flaw are both set to invisible to emphasize simple photon tracks.....	177
A43 ASL. Photon on far right are reflecting off NaI, going up into it.....	177
A44 ASL zoomed in view.....	178
A45 ADL.....	178
A46 VDL.....	179
A47 VDL.....	179
A48 VSL.....	180

A49	SSL.....	180
A50	SDI zoomed in view of flaw and photon tracks. Aluminum is set to transparent.	181
B.1	Typical photon path across a flaw.....	182
B.2	Parameters used to determine optimal collimation length for focusing to a specified depth.....	186
C.1	Signal intensity as a function of depth and across a void type flaw.....	187
C.2	Contrast versus collimator extension for collimator from zero to critical (optimal) extension. This optimal corresponds to collimating to top of flaw.....	189
C.3	Contrast versus collimator extension for collimator from critical (optimal) extension to flaw bottom.....	190
C.4	Contrast versus collimator extension for collimator extension corresponding to flaw bottom to maximum extension.....	191
C.5	Contrast versus collimator extension.....	192
E1	Spectroscopic trend for flaw depth by incident energy spectra.....	195
E2	Trends for flaw depth. Flaws depth increases from A to E.....	196
E3	Scatter component break down for spectra.....	197
E4	Spectral break down by scatter component.....	197
E5	Spectral break down by scatter component. MCNP5 current tally.....	198
E6	Current tally spectra for various flaw depths and collimation configurations.....	198
E7	Collision component signal contribution for various flaw depths in aluminum.....	199
E8	Collision component contributions for various flaw depths with uncollimated detector in aluminum.....	199
E9	Collision component contributions to 0.6cm void flaw in aluminum with various collimations configurations.....	200
E10	Spectroscopic trend with flaw depth. Flaw depth increases from A to E.....	200
E11	Experimental spectroscopic trend with detector height.....	201
E12	MCNP5 current tally spectroscopic trend with detector height.....	201

E13 Scatter component contribution for various detector and collimator configurations.....	202
E14 Spectral breakdown by collision component.....	202
E15 Spectral breakdown by scatter component.....	203
E16 Spectral breakdown by scatter component.....	203
E17 Spectral breakdown by scatter component.....	204
E18 Experimental trend with flaw depth.....	204
E19 Experimental trend with flaw depth.....	205
E20 MCNP5 trend with collimation extension.....	205
E21 Experimental trend with collimation extension.....	206
E22 Scatter component contribution trends with varying collimation.....	206
E23 Scatter component contribution by collimation.....	207
E24 Experimental spectral trend with flaw depth.....	207

Abstract of Thesis Presented to the Graduate School  
of the University of Florida in Partial Fulfillment of the  
Requirements for the Degree of Master of Engineering

CHARACTERIZATION AND OPTIMIZATION OF RADIOGRAPHY BY SELECTIVE  
DETECTION BACKSCATTER X-RAY IMAGING MODALITY

By

Benjamin Addicott

May 2006

Chair: Edward Dugan

Cochair: Alan Jacobs

Major Department: Nuclear and Radiological Engineering

Backscatter x-ray imaging techniques have been developed at the University of Florida for applications ranging from the detection of buried landmines to the non-destructive-examination (NDE) of various industrial materials such as aluminum and carbon-carbon composites. Recently, a new backscatter x-ray imaging system with geometries and components different than that employed in previous systems has been developed under contract with Lockheed Martin.

The primary purpose of this new system is the NDE of the foam thermal insulation material used by NASA on the space shuttle external fuel tank. The imaging modality has also been applied to evaluate other objects such as samples made from aluminum, plastics, steel, concrete, gypsum and titanium as well as to reactor vessel head steel insulation panels. Detailed subsurface images were acquired on each of these various materials indicating the wide range of applicability of this imaging modality.

This investigation aims at describing the physics and phenomena associated with this new imaging modality. The photon transport and interaction processes leading to an acquired image are explored. Both Monte Carlo simulations and analytical calculations are used, in conjunction with experimental results, to develop an analytical model detailing the mechanics of the photon transport process governing the imaging modality.

Trends in detector response and spectroscopic profiles due to variations in parameters such as detector collimation length, detector to target-object spacing, flaw type (i.e., void, scattering or absorbing type flaws) and orientation and media type is cataloged and explained in terms of this model. System variations such as detector type and detector mode of operation are also investigated.

Consideration of these trends as well as the simple analytical model developed is then applied, in conjunction with experiments and previously collected data, to identify key parameters in detection efficiency and apply them towards system optimization and an overall assessment of the applicability and limitation of the imaging modality.

## CHAPTER 1 INTRODUCTION

This research endeavor details the design and optimization of a unique Compton backscatter type non-destructive x-ray imaging modality developed over the past several years at the University of Florida.<sup>1-4</sup> The origin of the system dates back to systems initially designed for the detection of buried landmines.<sup>5-8</sup> Success of this imaging modality at acquiring definitive images of subsurface landmines had led to its application in the NDE (non-destructive examination) of various industrial materials. Currently, a new state-of-the-art system has been developed at the University of Florida designed specifically for the NDE of the foam thermal insulation on the space shuttle external tank<sup>9</sup>, but applicable, with modification, to a wide range of industrial type materials.

### **New Foam Imaging Backscatter Modality**

#### **Motivation**

The new system is essentially a derivative of the original landmine oriented system. The present system, funded largely by a contract from Lockheed Martin,<sup>10</sup> is designed for and applied primarily to the imaging of the special foam like material used for thermal insulation of the space shuttle fuel tanks. This foam insulation, or spray-on-foam insulation (SOFI),<sup>11, 12</sup> because of its extremely low density, represents a unique imaging challenge.

The integrity of the insulating SOFI barrier must be ensured before shuttle launch is permitted. Imaging this material and optimizing the system for detecting certain classes

of flaws in this material has consequently become a priority and much of the optimization methods and investigations have been conducted towards this end.

### **Spray On Foam Insulation**

The SOFI material used by Lockheed Martin and NASA roughly comprises a mixture of carbon, nitrogen, chlorine, fluorine, oxygen, and hydrogen. The exact chemical composition was deemed proprietary and therefore had to be estimated<sup>13</sup> from the composition of similar industrial foam insulation materials. The density of the material is given as  $0.03\text{ g/cm}^3$ , about two orders of magnitude lower than that of previously imaged materials such as aluminum ( $2.7\text{ g/cm}^3$ ), plastics and composites ( $\sim 1\text{ g/cm}^3$ ).

Due to the extremely low density of the foam, a photon, on average, will have significantly fewer interactions, or travel a greater distance in the medium, before it scatters and returns to the detector. The mean free path in this material (SOFI), roughly inversely proportional to the density, is orders of magnitude larger than that of any previously investigated materials. It is therefore reasonable to expect the physical processes resulting in the imaging of this material to be somewhat different than those for other higher density materials, such as aluminum or landmines. Figure 1.1 displays the average mean free paths obtained from MCNP5<sup>14</sup> Monte Carlo calculations of several incident photon spectra in both aluminum and SOFI.

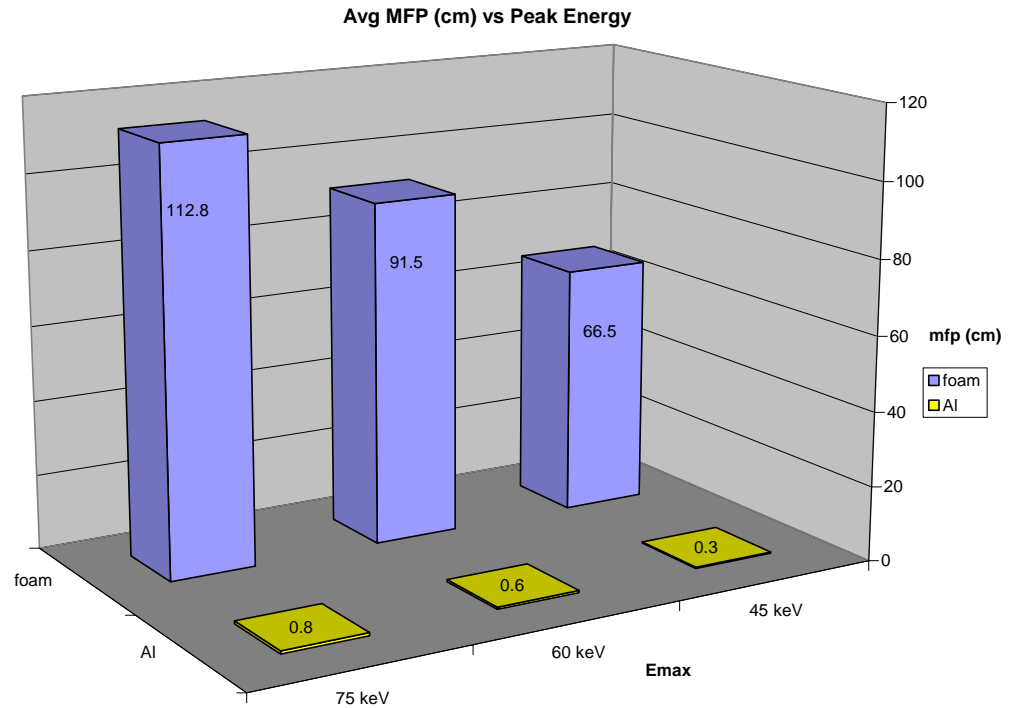


Figure 1.1 Mean free path of various peak energy photon beams in SOFI and in aluminum

### Purpose of Investigation

This discussion aims at describing the physics and phenomena which govern the new imaging modality. Detector response and spectral features of this imaging modality and the parameters which affect them will be investigated and their mechanisms detailed. Also covered will be the methods employed to investigate these phenomena and how they are applied to the optimization of the present system as well as suggested modifications for further development of future generation backscatter type imaging modalities.

Careful observations and experimentation, complemented by MCNP5 Monte Carlo simulations have afforded a comprehensive understanding of the photon interactions and detector responses indicated by particular images. This knowledge has allowed simple

algorithms to be established to optimize image quality and increase system efficiency. Methods have also been developed to systematically and accurately focus the detector collimators to target a specific depth in material as well as to distinguish between types of flaws in various materials and, in some situations, to describe flaw depth and three-dimensional orientations.

### **Radiography by Selective Detection**

Detector response and image acquisition observed throughout this investigation are described by a concept referred to as Radiography by Selective Detection (RSD). The theory of RSD is that by preferentially selecting specific components of a scattered photon field, information relating to specific locations and properties of an imaged sample can be extracted. That is, sensitizing the detector towards selected photons within a specific volume will result in larger relative signal fluctuations caused by flaws and features within that volume.

In this imaging modality, collimators are used in conjunction with the detectors to discriminate against certain components of the reflected scatter field. This effectively enhances the relative contribution and, thus, the contrast resulting from more important and often deeper regions of a sample where a flaw or region of interest lies. In this study, a simplified analytical model of the RSD imaging modality is developed and supported. Detector responses and imaging characteristics of the system are then described in terms of this proposed model.

## CHAPTER 2 BACKGROUND

### **Premise**

Backscatter radiography methods were developed at the University of Florida<sup>15</sup> as a means to effectively detect and positively identify buried landmines. The method was developed in response to problems arising from other land mine detection systems available at the time.<sup>16-18</sup> Most significant among these problems was that of false positive identification of buried landmines. Previous methods identified landmines only as subsurface irregularities making it difficult and often impossible to distinguish between true landmines and landmine sized objects (e.g. rocks, debris, etc.).<sup>19</sup>

In the system designed at the University of Florida, positive landmine identification via realistic image acquisition was accomplished by placing some of the detectors behind a series of collimators.<sup>20</sup> The collimators were positioned so that the majority of the shallow first scattered photons would be prevented, geometrically, from reaching the detectors. This essentially provided the detectors with a less cluttered view of the subsurface features of the landmines and other buried objects. The landmine detection system configuration and a demonstration of its imaging capabilities is presented below in Figures 2.1<sup>21</sup> and 2.2.<sup>22</sup>

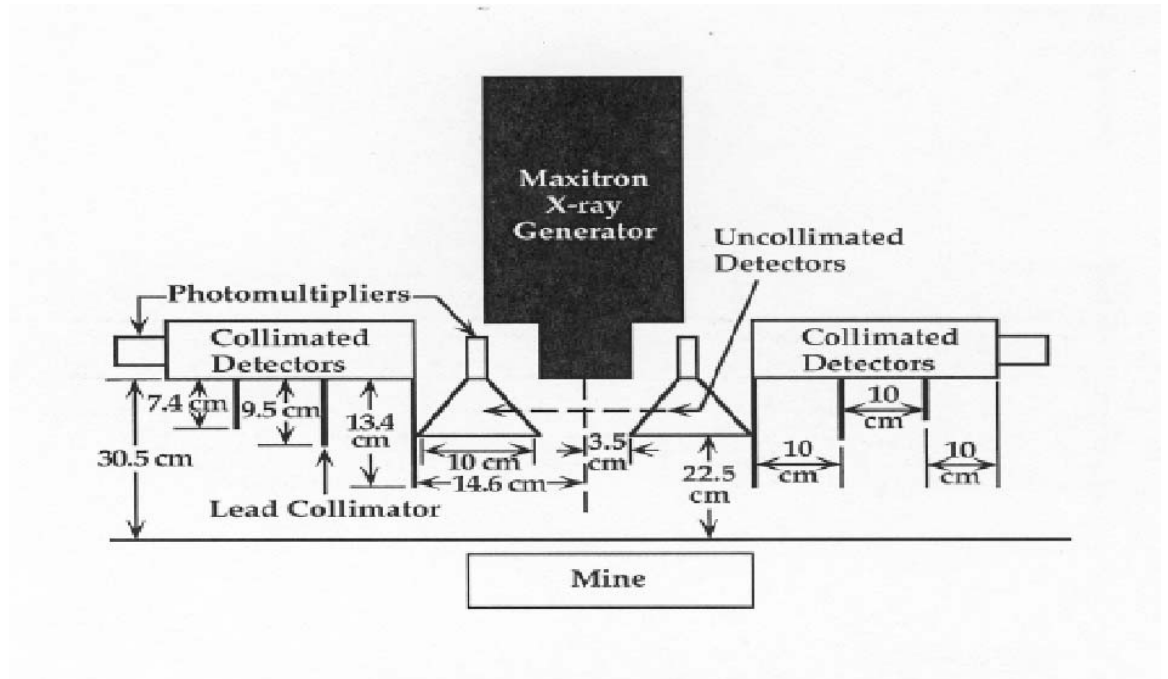


Figure 2.1 Simple schematic of landmine detection system

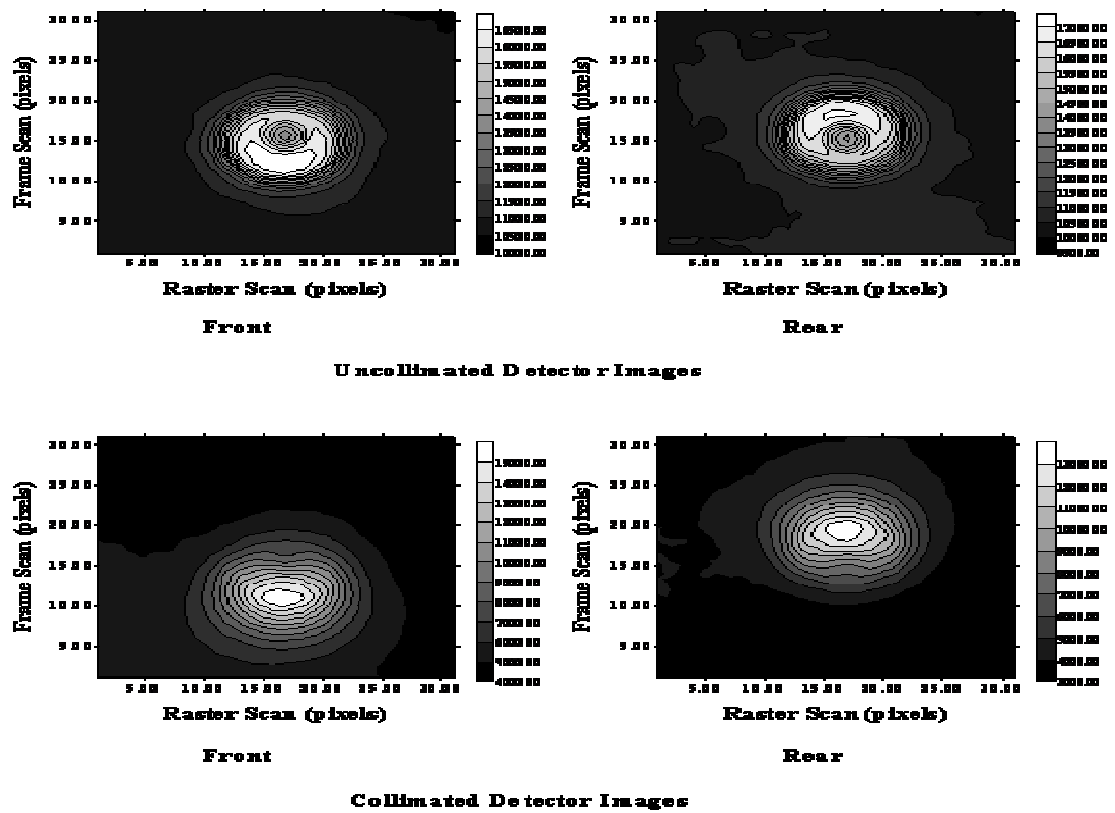


Figure 2.2 Tiled sample landmine scans. VS-1.6 antipersonnel mine, 2.5 cm depth-of-burial, 15 mm resolution

Previous research endeavors centered upon understanding this process and optimizing this system initially for landmine detection and, later, for other industrial non-destructive examination applications have been carried out over the past several year.<sup>21-</sup><sup>28</sup> Analysis and evaluation of these along with the inevitable progress of technology have led to a gradual and steady advancement of this imaging method and the understanding of the mechanisms which govern it.

### **New Backscatter Radiography System**

Recently, the backscatter x-ray system has been acutely modified and redesigned to meet the specific needs of imaging SOFI and other drastically different materials than the original system was designed for. The new system features different detector and collimator configurations, different photon beam energies as well as new electronic components and detector geometries. These differences, combined with the fresh perspective afforded by optimizing and testing a new system configuration on a new and unique material (i.e., SOFI), have led to new imaging approaches and concepts as well as a comprehensive analytical model which accurately describes the photon transport process and resultant detector responses.

### **System Description and Configuration**

The system used in this series of investigations consists of four sodium iodide [NaI (Tl)] scintillation detectors and an Yxlon MCG41 x-ray generator<sup>29</sup> mounted onto a scanning table with X – Y scan motion capabilities. The detectors are positioned at the corners of an eighteen by eighteen centimeter square, centered on the x-ray beam. Each detector comprises a two inch diameter by two inch thick NaI scintillation crystal mounted onto a photomultiplier tube (PMT) and a fast preamplifier specifically designed to handle high count rates. The customized, ultra-low-noise, high count rate preamps

have a maximum noise level of about 5 mV for a 1 volt pulse output, while operating in close proximity to a strong electro-magnetic field (x-ray generator tube). The preamp pulses have a typical rise time of 100 nano-seconds and fall time of about 1000 nano-seconds, yielding a total pulse width of about 1.1 micro-second. This specific pulse width (1.1 micro-seconds) allows sufficient light and charge collection time from the NaI and PMT (about five time constants), while allowing the detectors to measure backscatter fields up to 700,000 counts per second, without experiencing statistically significant pulse pile-up. A schematic of the RSD detector components and their configurations is presented below in Figure 2.3, followed by a flow chart of the entire image acquisition process from detection to display in Figure 2.4. Figure 2.5 is a picture of the x-ray generator tube head and collimated detectors.

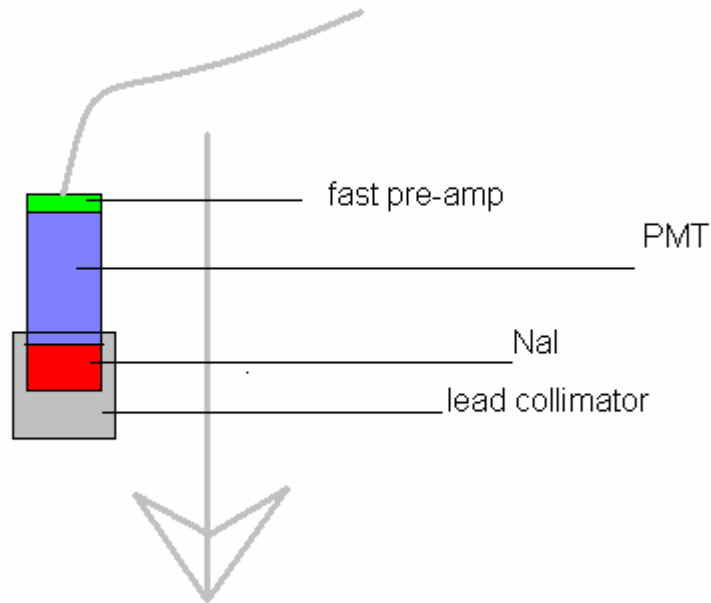


Figure 2.3 Schematic of detector components. Gray arrow represents photon beam direction. Center of detector is 9 cm from photon beam center.

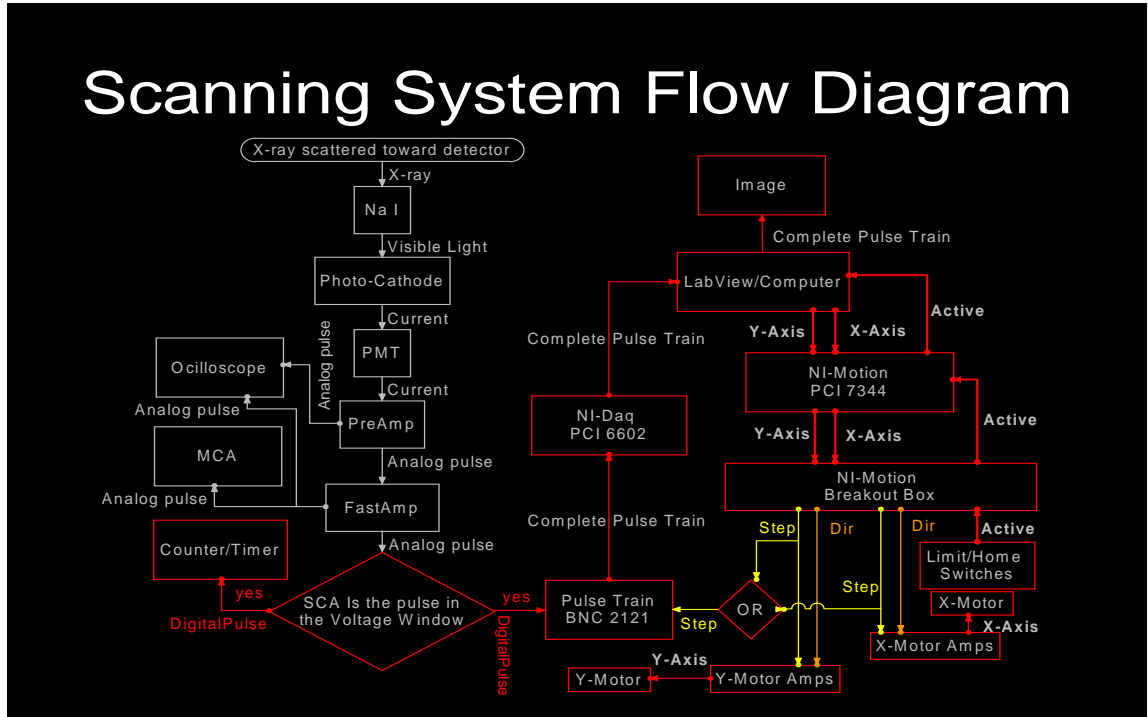


Figure 2.4 System signal flow chart for image acquisition



Figure 2.5 Yxlon x-ray tube head and four NaI collimated detectors

## CHAPTER 3 THEORY

### Photons

#### General Physics of Photons

Photons are a form of electromagnetic radiation. Like all forms of electromagnetic radiation, photons travel in waves and are accompanied by oscillating electric and magnetic fields. These fields are perpendicular to each other as well as to the direction of photon propagation and rotate about the axis of travel. A qualitative representation of propagation of electromagnetic waves and their associated electric and magnetic fields is presented in Figure 3.1.

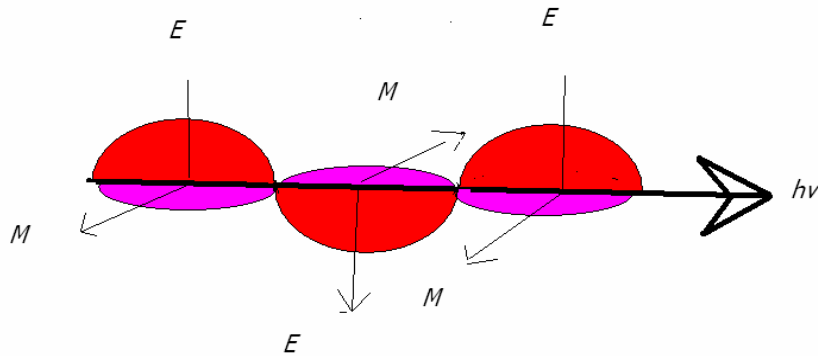


Figure 3.1: Oscillating electric (E) and magnetic (M) fields about a propagating photon.

Although photons are necessarily accompanied by an electric field, they have no net electric charge and, to a first approximation, are not influenced by the electric charges and fields of neighboring particles or waves.<sup>30</sup>

### **Photon Interactions**

Although photons, like all electromagnetic radiation, are most completely described by their quantum mechanical wave functions and probabilities, for our purposes, considering the energies (45-100 keV) and the processes that we are interested in (Compton scattering and photoelectric absorption), they can be well represented by discrete particles with energies dictated by a classical and definite wavelength.

Photon interactions, then, may be accurately and relatively completely described by five major interaction types. These are, photoelectric effect, Compton Scattering, pair production, Rayleigh (coherent) scattering, and photonuclear interactions. Each of these interaction types is described by a quantum mechanical or empirical microscopic cross-section detailing its probability of occurrence for a photon in a particular phase space. These cross-sections, modified by certain atom and energy dependent incoherent scattering functions and form factors, give the probability of each particular type of interaction per atom in a sample. The sum total of these, or the total cross-section, represents the total interaction probability per atom for a photon in a particular phase space. Multiplying these microscopic cross-sections by atom density produces the macroscopic cross-sections which represent the probability per unit path length of interaction of a particular type. Typically, microscopic cross-sections are given in units of  $\sigma \equiv cm^2 / atom$  or in barns ( $10^{-24} cm^2 / atom$ ) per atom, depending upon whether they

have been appropriately modified. Macroscopic cross-sections are typically given in units of  $\Sigma \equiv \sigma * \rho / M$  or  $(cm^2 / g)(g / cm^3) * (atoms / g) = cm^{-1}$ .

Once these cross-sections have been defined, another parameter, the mean free path (mpf) can then be introduced. This is a typical attenuation length or free flight travel length given as  $1 / \Sigma = cm$ . This is the length that the uncollided portion of a beam of photons will be attenuated by a factor of  $e^{-1}$  (2.718). The MFP can also be interpreted as the distance in a material that a photon of certain energy would have a probability  $e^{-1}$  of traveling through without interaction.<sup>31</sup>

Each of these photon cross-sections is a function of at least the energy of the photon and  $Z$  of the material. For the typical materials (low  $Z < 15$ ) and photon energies,  $< \sim 100$  keV, the dominant interaction types are Compton scattering and photoelectric effect. For lower energies,  $< 30$  keV coherent scattering of photons can also become important. Figure 3.2,<sup>31</sup> below, plots the three important cross-section, i.e. photoelectric, Compton, and pair production, as a function of both energy and material  $Z$  number. Clearly, the first two interaction mechanisms, photoelectric and Compton scattering, are the dominate interaction mechanisms for the typical  $Z$  range and energy range [highlighted in the (red) circle] that we are concerned with. The rest of our treatment of photons in this discussion will be for finite wave/particles with definite energies and knowable pre and post collision velocities.

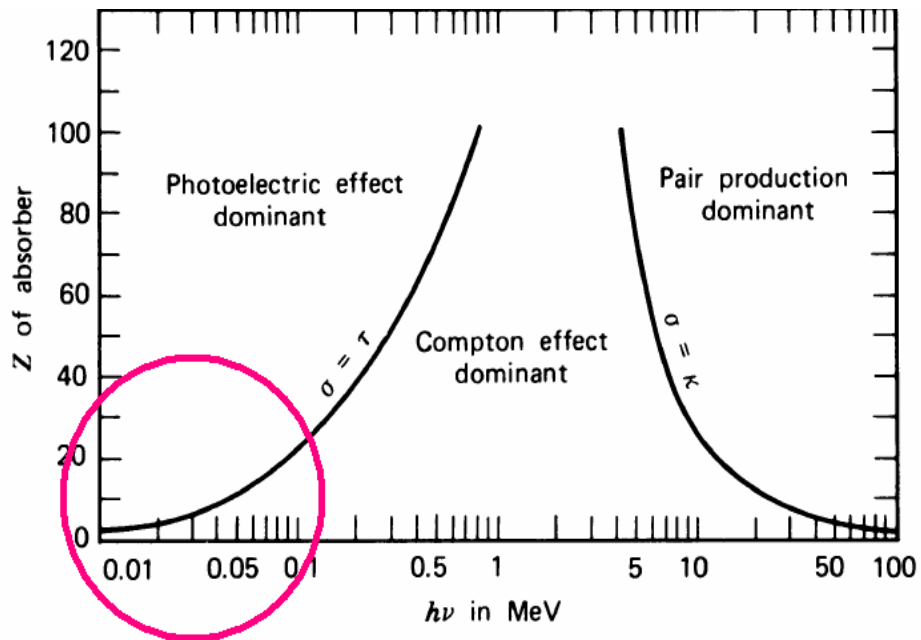


Figure 3.2 Dominant interaction type as a function of energy and material Z number

### Photoelectric effect

Photoelectric interaction is an interaction between a photon and a bound electron. In these interactions, a photon is completely absorbed by a bound atomic electron. This electron is then ejected from the atom. It is therefore necessary for the incident photon to carry at least the energy required to free the electron. This is effectively the electrons' binding energy. If the photon imparts less than the binding energy to the electron, the electron will merely be excited and consequently release a photon upon de-excitation rather than being ejected from the atom. A typical photoelectric cross-section, shown in Figure 3.3<sup>32</sup> for aluminum, is a strong function of energy. In fact it varies roughly as  $(1/E^3)^{.32}$ . This results in a very large absorption cross-section at low energies.

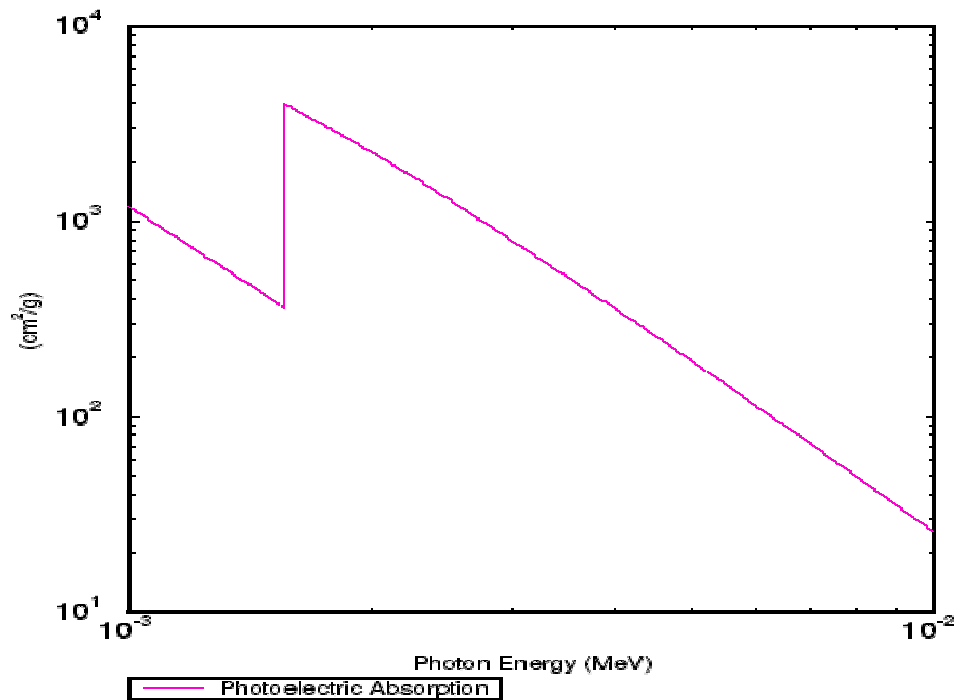


Figure 3.3: Photoelectric cross-section for aluminum.<sup>32</sup> Log / Log scale.

### Compton scattering

Compton scattering is best conceptualized as an elastic billiard ball type collision between a photon ‘particle’ and a free electron. In this process, a photon with known direction and energy collides with an assumed stationary (unbound) atomic electron. After the collision, both the photon and electron velocity vectors (energy and position vectors) can be accurately described via classically considered conservation laws of energy and momentum.

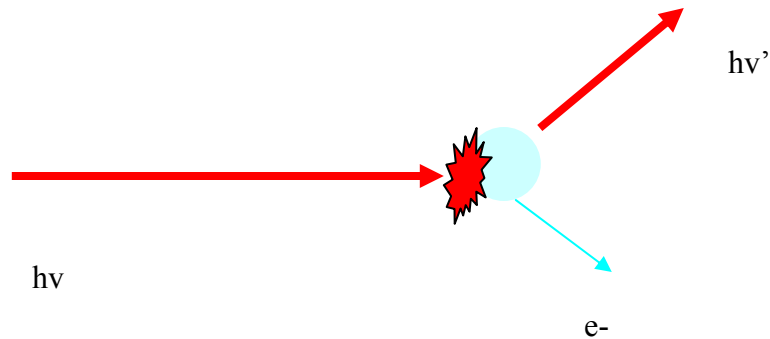


Figure 3.4: Compton interaction between photon (thick, red) and stationary electron (thin, blue)

It is, for the most part, these types of collision which concern us, as it is these collisions which predominately result in photons being backscattered from the target to the detector.

The Compton Scattering probability is described in terms of a differential cross-section which relates the probability in  $\text{cm}^2 / \text{steradian}$  per electron for a photon of a specific energy to scatter into a specific solid angle about a specified angle. This differential probability distribution is the Klein-Nieshena differential cross-section. The Klein-Nieshena cross-section uniquely relates initial energy, scattering angle and final

energy of a photon. This relationship is given as:  $\frac{d\sigma}{d\Omega} = \frac{v'}{v} \left( \frac{v'}{v} + \frac{v}{v'} - \sin^2 \theta \right)$  where,

$$\frac{v'}{v} = \frac{1}{1 + \alpha(1 - \cos \theta)}$$

is the ratio of scattered to initially photon energy and  $\alpha = \frac{h\nu}{m_o c^2}$ . Is

the reduced initial photon energy. As this relationship dictates, the scattering probabilities will be peaked (have local maximums) in the directly forward (0) and directly backward (180) directions. The scattering will also follow a forward peaking

trend as the energy is increased. The Klein-Nieshena relative scattering probabilities for several incident photon energies are plotted below in Figure 3.5 for 0 to 180 degrees scatters.

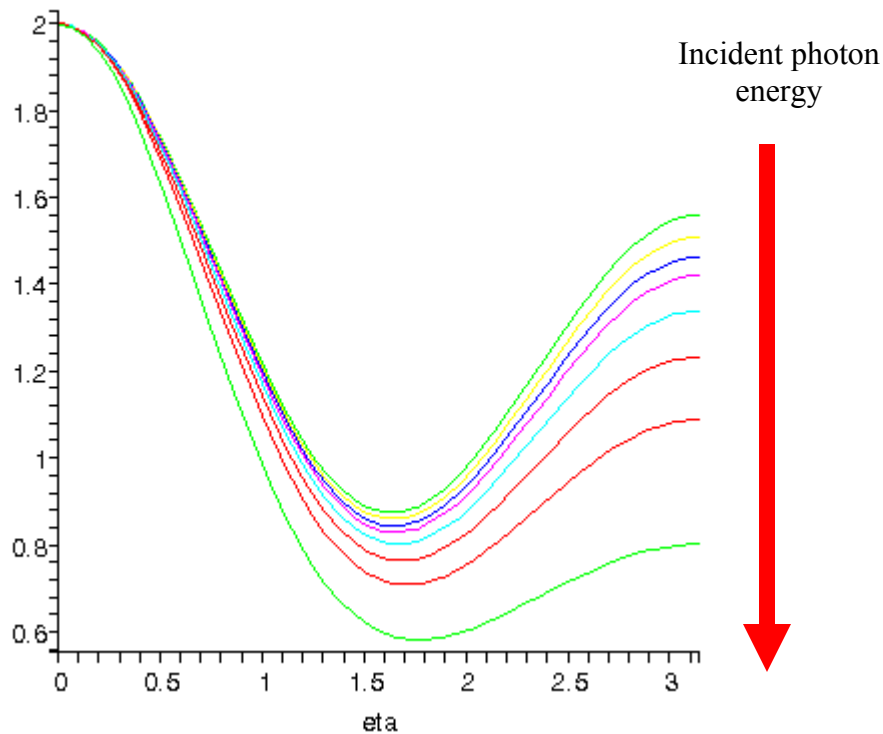


Figure 3.5: Relative Klein-Nieshena Compton collision cross-section as a function of energy and scattering angle, eta (in radians).

### Rayleigh scattering

Rayleigh scattering, pronounced mainly at low energies ( $h\nu < 30$  keV) and high  $Z$  materials, is the highly forward elastic scattering which occurs between an incident photon and a bound electron. The important difference between coherent (Rayleigh) and incoherent (Compton) scattering is that in Compton scattering, the collision is between a photon and an essentially unbound electron, whereas in coherent scattering the collision is between a photon and the target atom as a whole. This difference allows for the vast majority of the momentum and energy to be retained by the incident photon while the

target atom receives only the minimum amount of momentum to ensure conservation.

Due to the relatively huge mass of a target atom relative to a single electron (as in Compton scattering), the photon does not transfer much energy to the atom. This is very similar to bouncing a ball off of a wall. In this case, the wall, being fixed, does not absorb a significant amount of energy or momentum and the ball rebounds with essentially the same amount of energy as it had before the collision. Coherent scattering is highly forward peaked. Similar to incoherent (Compton) scattering this peaking is accentuated at higher energies.

### **Photon Production and Energy Distribution Spectrum**

Photons utilized in research are produced via an x-ray generator. X-ray generators operate on the principle that high energy electrons incident upon a tungsten target produce a spectrum of bremsstrahlung<sup>33</sup> photons. The initial production of these photons is more or less isotropic. The energy is distributed, initially, according to a typical bremsstrahlung spectrum as shown in Figure 3.6. The addition of aluminum or copper filters hardens the primary bremsstrahlung spectrum. Figure 3.7 shows target characteristic x-rays superimposed on the continuous bremsstrahlung spectrum. For a tungsten target, the generator voltage has to exceed at least 69.5 keV, the K-shell binding energy, for the characteristic x-rays to be generated. These are the type of spectra used in the investigations presented in Chapters Five through Seven.

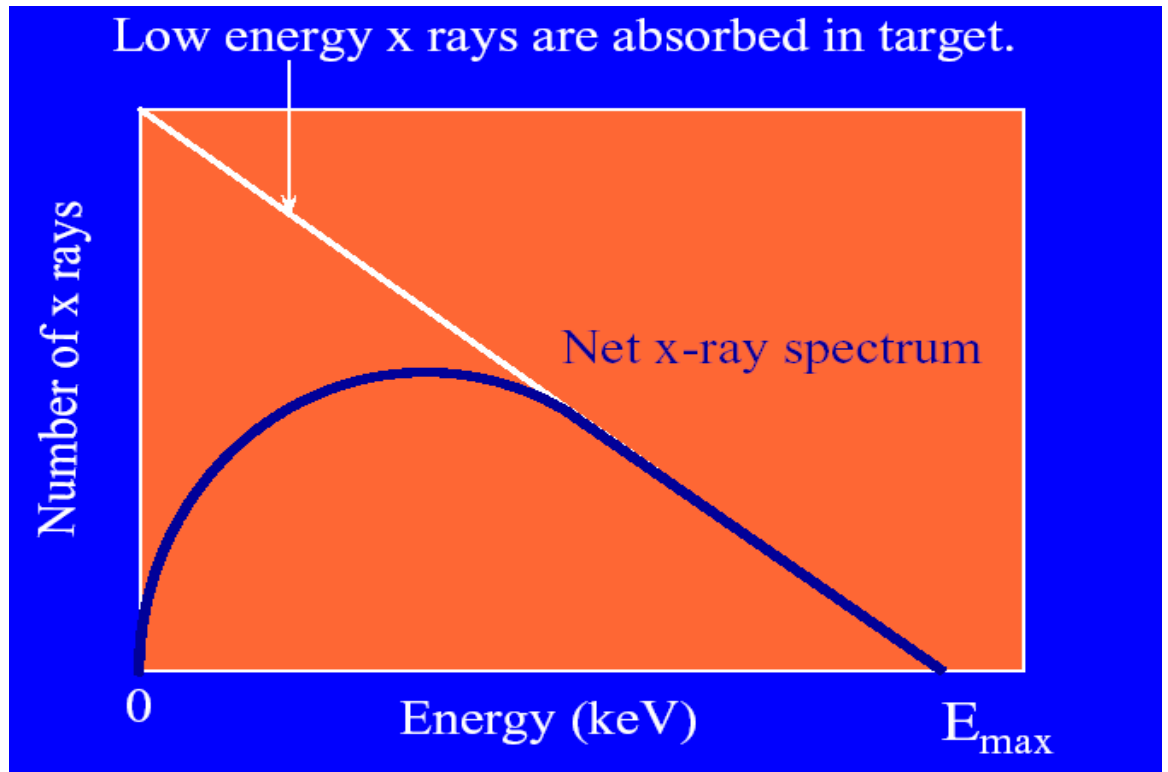


Figure 3.6 . Typical bremsstrahlung x-ray energy spectrum.<sup>33</sup>

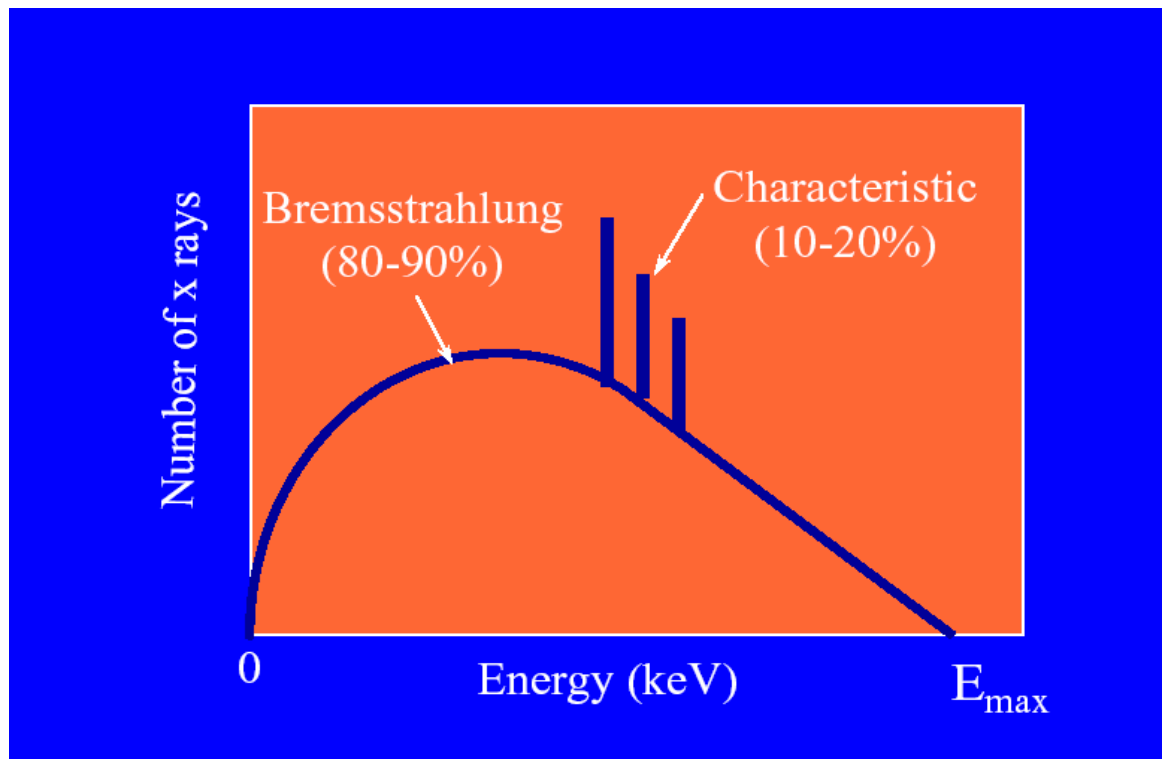


Figure 3.7. Bremsstrahlung spectrum with characteristic x-rays.<sup>33</sup>

Important parameters describing this spectrum are the most probable energy, the average energy, and the peak energy.

The spectral analysis completed as part of this investigation makes use of the scattering-to-absorption ratio. It is this ratio, which includes both coherent and incoherent scatters, that governs the spectral shifts and trends realized in our measurements and simulations. This can be visualized by considering a uniform spectrum of photons traveling through and being attenuated by a particular material. Since for lower energies the attenuation coefficients are higher, due to the photoelectric effect, it is logical to predict that the emergent beam spectra will be shifted towards higher energies. This is a result of the lower energy photons being preferentially absorbed. Other shifts in energy can likewise be explained.

For our particular situation where we are interested mainly in backscattered photons, an appropriate down shift in energy, due to energy lost in scattering can be observed. This downshift is theoretically dependent upon the initial photon energy, the scattering angle, and the number of scatters encountered before reaching the detector.

### **Attenuation**

Linear attenuation coefficients are described for monoenergetic uncollided photon beams as the sum of all interaction cross-sections multiplied by the appropriate atom density. This coefficient, given in terms of 1/cm is then multiplied by the photon path in cm and the exponential function of this product, given as  $e^{-N\sigma x}$  then represent the fractional uncollided photon intensity as a function of distance traveled in a medium.

This simple equation can easily be expanded into a series with appropriate coefficients and weighting parameters to provide a description of the uncollided photon intensity of a particular photon energy distribution.

## Detection Modalities

### Detector Components

#### Scintillator

Scintillation detectors function by turning radiation energy into visible light, which is subsequently collected and converted into an electrical signal. The process by which visible light is produced from incident radiation takes place in the scintillation material, the portion of the detector which interacts with the radiation, and the process is referred to as fluorescence. This process involves the absorption of some portion of the incident radiation's energy by an electron. The electron is then elevated from its normal energy state into an excited state. The excited state is necessarily less stable than the original ground state of the electron and thus de-excites back to this more stable ground state. With this de-excitation comes a photon of light of wavelength determined by the energy gap that the initial electron traversed in its excitation.<sup>34</sup>

In inorganic scintillation crystals, such as the sodium iodide (NaI) used in most of these investigations, electrons are excited from the valence band to a conducting band across an energy gap called the "forbidden band." In this energy gap, no sublevels are found so that there is no real probability of finding an electron between the valence and conduction bands. In pure inorganic crystals, the de-excitation of an electron to the valence band with the proper photon emission is not realistically efficient for practical detection requirements. To compensate for this, and to increase the probability of the resultant photon being in the useful visible range of the electromagnetic spectrum, small amounts of impurities, referred to as activators, are added to the crystal. These impurities

have an energy band within the forbidden band gap of the pure crystal. With the appropriate activator added, an electron-hole pair will migrate through the crystal until they reach an activator impurity site where they will quickly de-excite with the release of a useful photon of visible light. This light is then funneled into a photomultiplier tube where it is turned into a measurable electronic signal.<sup>34</sup>

### **Photo multiplier**

Photomultiplier tubes collect the visible scintillation photons and convert them into a measurable electric signal. The total process progresses in three distinct stages. Photons from the scintillation crystal impinge upon the photocathode region of the tube where they are converted to electrons. These electrons are then channeled down the electron multiplier where they are proportionately multiplied by several (typically 5-7) orders of magnitude. After this multiplication process, the electrons are then collected at the anode end of the tube where they have effectively become a now measurable electric signal proportionate to the incident scintillation photons and thus, to the original radiant energy deposition.<sup>34</sup>

### **Preamplifier**

The preamplifier serves as an intermediate signal amplification step between the detector and the analytical circuit used to process the detected signal. The circuit components and time constant of the preamplifier have important implications on the detector behavior as a whole.

## **Modes of Operation**

### **Pulse mode**

The detection of signal energy distribution (spectroscopy) or true count rates requires the detector to be used in pulse mode. In this mode, each incident quantum of

radiation produces a pulse. Each pulse in turn is individually collected by the detector and processed as a count. The voltage height of this pulse is proportional to the energy deposited. This is the most common mode of operation and for most of the experiments conducted in this investigations, pulse mode operation is used.<sup>34</sup>

### **Integrating mode**

In situations where the detected count rate is high so that pulse pile up occurs, current (or integral) mode of operation can be used to mitigate such detector saturation problems. In integral mode, the total charge generated over a set time is collected. This set time, known as the detector response time, is large compared to the time between individual events, and thus the association between charge created and individual interactions is lost. The benefit, however, is that the detector does not need a recovery time between individual pulses and thus is capable of handling much higher count rates.

One important property of integral mode of operation is that the current measured or detected is not exactly equivalent or necessarily strictly proportional to the true count rate. The reason for this is that it is the total charge deposited in the detector over a set time which is measured. This charge is dependent upon the number of particles interacting, the type of interaction, as well as the energy of the interacting particles. In other words one particle which deposits most of its energy will be detected the same as two particles each of which deposit half as much energy.<sup>34</sup>

### **NaI**

The NaI is the standard by which the other materials are measured. The system was originally designed with NaI detectors and most of the experiments and images acquired on the system have been with this detector type. The advantage of NaI is its fast response time and large photoelectric cross-section. This property allows NaI to be used

as thin crystals and still collect full energy deposition. Additionally, because most of the photons which impinge upon NaI deposit their full energy, it has good energy resolution and is appropriate for spectroscopic investigations. Disadvantages of NaI include that it is brittle and hygroscopic.

### **Plastic Scintillator**

The advantage of the plastic scintillation detectors is that they are more resilient, cheaper, not hygroscopic and can be produced in almost any desired shape. The plastic detectors are also capable of handling higher count rates. The mean free path (mfp) of a photon in plastic is on the order of 2 cm, much larger than that of NaI crystals (~mm). However, the relative photoelectric cross-section for plastic type scintillators is smaller than that of NaI (Appendix F). Consequently, many photons do not deposit their full energy within the plastic scintillation material. For this reason, energy resolution is poor in plastic type scintillators and they are of almost no use in spectroscopic analysis. Plastics are more conducive to integration mode operation at high count rates.

### **Detector Comparison**

Both the NaI and the plastic detectors may be operated in both pulse and integrating mode. The concept is that integral mode is not susceptible to pulse pileup problems encountered at high count rates. Since pulse mode counts each individual photon by collecting the appropriate charge deposited in the detector, pulse mode detectors are limited, in count rate, by an associated dead time which is the time required to collect and dissipate the charge of an individual photon. This dead time is ultimately limited by the charge collection time of the detector material itself which in NaI is about 0.23  $\mu$ s, indicating a maximum ideal (assuming cps could be limited only by this time constant ) count rate in pulse mode of about 800,000 cps (5 time constants<sup>35</sup>) before

significant pulse pile up and dead time effects result. In reality, however, the maximum count rate is governed by the time constant of the entire detector circuit, including the pre-amplifier. Current or integrating mode, however, collects the charge produced by multiple photons incident over a predetermined integration period. In integral mode, it is the total energy deposited over a period of time and not the energy deposited per interaction that is important. Because current mode operates on a voltage produced by the incident photons and the number of electron-hole pairs they generate, greater weight is given to a higher energy photon since they generally deposit more energy and thus create more electron-hole pairs in the detector material. This results in images which show biasing towards high energy photon detection. This effect is more pronounced in NaI than it is in the plastic scintillators. This is due to the fact that more energy is deposited in NaI than in the plastic material (per unit distance traveled by a photon). A photon impinging on a NaI crystal is likely to deposit all or most of its energy within that crystal resulting in a proportional amount of electron-hole pairs being produced. That same photon incident upon a plastic scintillation material (of comparable thickness) is less likely to deposit the majority of its energy in the detector. A lower energy photon, however, will deposit a larger portion of its energy since its MFP is smaller. The result of this phenomenon is that there is essentially a maximum energy deposition limit above which no single photon will usually deposit the rest of its energy. Consequently, unlike NaI, most photons, regardless of their energy deposit about the same amount of energy and therefore produce about the same number of electron-hole pairs in a relatively thin plastic scintillation material.

A problem with this feature of the integrating mode (primarily in the NaI) is that the change in signal strength resulting from photoelectric attenuation, which is dominant at low energies, is not observed as well. Often this differential photoelectric signal is a significant portion of the overall contrast and discounting it results in image degradation. Another problem with neglecting the low energy portion of the signal is that often the high energy portion of the incident spectrum does not interact as intimately with the medium and consequently contributes to noise rather than signal.

### **Compton Backscatter Radiography**

Compton Backscatter Imaging (CBI) Radiography is a non destructive imaging modality used to image objects when transmission type methods are not feasible. The important feature of CBI is that access to only one side of an object is required. For transmission type radiography a detector is placed on the opposite side of an object relative to the source and is sensitive to photons which traveled through the object; CBI techniques place the detector and source on the same side of the object and the detector is then sensitive to photons which interacted in the object and scattered backwards into the detector.

Many traditional Compton methods employ a large unobstructed detector which is sensitive to the entire distribution of backscattered photons (at least those scattering into the relevant solid angle subtended by the detector). Since the majority of backscattered photons will suffer a scatter near the surface (within half of a mean free path) of the substrate and then return to the detector, the signal and the image generated directly reflects electron density variation within this surface and shallow subsurface region of the sample. An example of this configuration is illustrated in Figure 3.5 below.

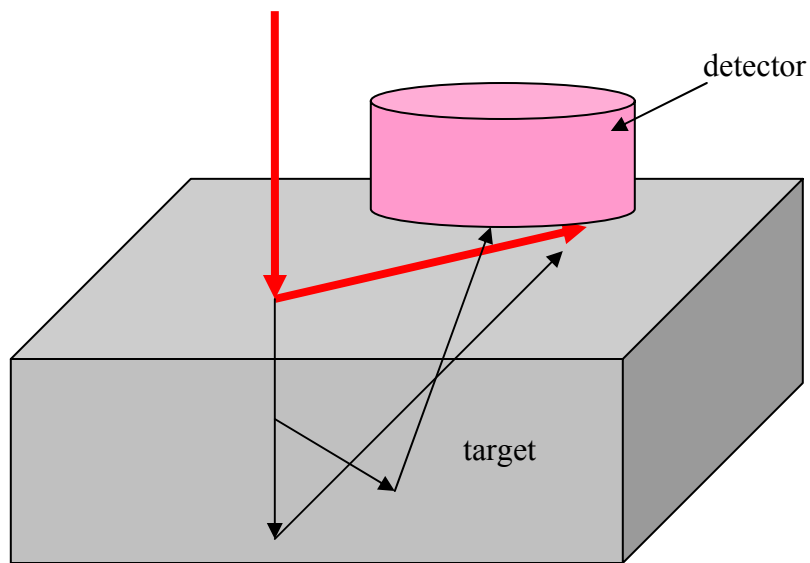


Figure 3.8 Scatter components of Compton backscatter radiography signal.

Here, the shallow first scattered component of the backscattered field, represented by the thick (red) arrow is the dominant signal contribution and clearly overwhelms the contribution of the deeper penetrating and/or multiple-collided photons which are usually considered as noise. This is intuitive if the exponential attenuation of photons is considered, necessitating that each additional distance traveled into the sample by the photon beam results in exponentially less photons available to scatter back into the detector. Additionally, the contributions of multiple-scattered photons are further reduced since these photons must both have and survive multiple collisions without being absorbed.

### **Radiography by Selective Detection**

Radiography by Selective Detection (RSD) techniques are similar to CBI methods in that they rely on Compton (mostly) backscattered photons to generate an image of the investigated object. The difference is that RSD techniques employ collimators and

calculated detector positioning to select for specific regions of a backscattered photon field. The effect of this is to enhance the sensitivity to the detector response function to variations of specific components of the backscatter field. A simple illustration of this principle is shown in Figure 3.9 below.

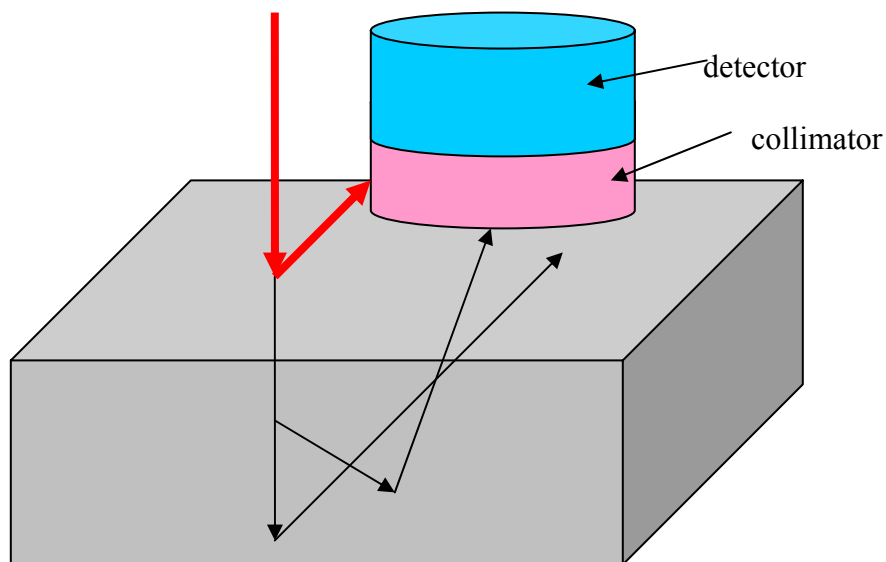


Figure 3.9. Scatter component contributions to collimated RSD backscatter imaging signal.

Here, the shallow first scattered field, represented by the thick (red) arrow is effectively discriminated against by the collimator (lower (pink) cylinder). The resultant image is thus generated largely from deeper penetrating photons. In RSD methods detector and collimator geometries and orientation are governing parameters in selecting the portion of the detected backscattered photon field, and hence the region of the sample, viewed by the detector.

### **Monte Carlo Methods (MCNP5)**

Throughout this investigation Monte Carlo methods, implemented via MCNP5, are used to simulate experimental setups and detector responses. Monte Carlo methods are a

means of solving a problem through statistical sampling of probabilities and are used when deterministic methods are not desirable. Effectively, Monte Carlo methods arrive at a particular solution by tracking particles and tallying individual events until enough information has been obtained to infer a reasonable answer. Each event is determined by sampling from a pool of random numbers distributed according to the appropriate interaction probabilities.

### **SABRINA Supplemental Track Plotter**

SABRINA<sup>36</sup> is an application code which, in conjunction with MCNP, graphically displays the simulated geometry and/or the photon tracks and interactions mechanics. It utilizes the MCNP geometry input deck and a special PTRAC card which causes MCNP to generate a file in which selected history data (location, interactions, and velocity components) of photons run in the MCNP simulation are recorded.

## CHAPTER 4 RADIOGRAPHY BY SELECTIVE DETECTION

### **RSD**

Radiography by Selective Detection (RSD) produces images via a signal differential due to a linear attenuation difference experienced by single and multiple scattered photons as they traverse various regions of a sample. The photons essentially travel in a simple reflection path between the source and the detector (much like optical photons), with an appropriate backwards scattering occurring in the target object. This approximation is roughened by photons which interact more than once in the sample before scattering into the detector. Photons having more than one scatter in the target material deviate, to varying degrees, from those having only one collision. For the examined configurations, analysis and experiments indicate that these multiple collided photons behave essentially as single scattered photons (for the purpose of providing contrast in imaging modalities) in that they transverse flaws directly, as the once scattered photons do, on the way from their last scatter to the detector. That is, the mechanism for generating flaw contrast is essentially the same for single and multiple scattered photons. The contrast, regardless of the number of scatters, is a function of the attenuation difference afforded by the flaw as the photons impinge upon it and exit, after scattering, towards the detector.

The effect of these multiple scattered photons, to a first approximation, is tantamount to a broadening of the initial impingent photon beam. Photons having more than one scatter lose some degree of their original incident directionality. Thus,

depending upon how many scatters the photons have suffered, their backscattered field distribution is skewed from the primary once scattered backscatter photon field. Additionally their final scattering points are necessarily displaced from the incident photon beam axis. The contrast observed by these photons, however, is generated by the same mechanism responsible for single scatter photon contrast. That is, the attenuation differential afforded by a flaw as a photon traverses it. For photons having many collisions (usually 4 or more) this attenuation differential can become negligible in comparison to the total photon path length in the target material and thus the contrast for these very high order photons is often much lower than for the primary and secondary scattered photons. This concept of effective beam spreading can be observed in Figures 4.1 and 4.2, below. Each of these figures is a SABRINA generated photon track plot from an MCNP5 simulation. The simulation models a one inch aluminum substrate below eight inches of SOFI foam. The detector is 2 inch diameter NaI and is located 9 cm, centerline-to-centerline, from the impinging beam (2mm in diameter) and 5.14 cm above the foam surface. The collimator is extended 4 cm past the NaI surface, or 1.14 cm from the SOFI surface. Figure 4.1 shows first collision components of the backscattered radiation field that reach the detector.

Intuitively, all these collisions occur along the axis of the impinging beam, shown by the black arrow. Figure 4.2 is the SABRINA generated plot of the same MCNP5 simulation displaying multiple (second order and higher) scattered photons. As demonstrated in the figure, except for a few outliers, the effect of multiple scattered photons can be approximated by an effective broadening of the impinging photon beam. That is, the result of total scatters from a narrow beam can be approximated well by

considering only single scatters from a broader, diverging beam. This concept is meant to augment the understanding of the contrast generating mechanism involved in the imaging modality rather than to be used as a quantitative model for system optimizations. The multiple scattered photons make up an effective source distribution within the target material which has a wider distribution than the effective source distribution of the once scattered photons. Thus, intuitively, the last scatter in the target material, before photon detection, of the multiple scattered photons does not occur along the impinging beam axis as the first scatter does. If the initial beam were diverging, however, then the first scatter site distribution for the diverging beam would be similar to the multiple scatter sites of the line source which is actually impinging. The dark arrows in Figure 4.2 demonstrate the concept of effective impinging beam widening which would account for the effect of multiple scatters. Many of the scatters occur within this area and upon their final scatter are directed towards the detector. These arrows are meant to indicate approximately the effective multiple scattered photon source distribution and are not a quantitative representation of an actual beam divergence. *(Note: the right half of the area within the arrows does not display scatters because the SABRINA plot was filtered to only include photons scattered into the detector shown.)*

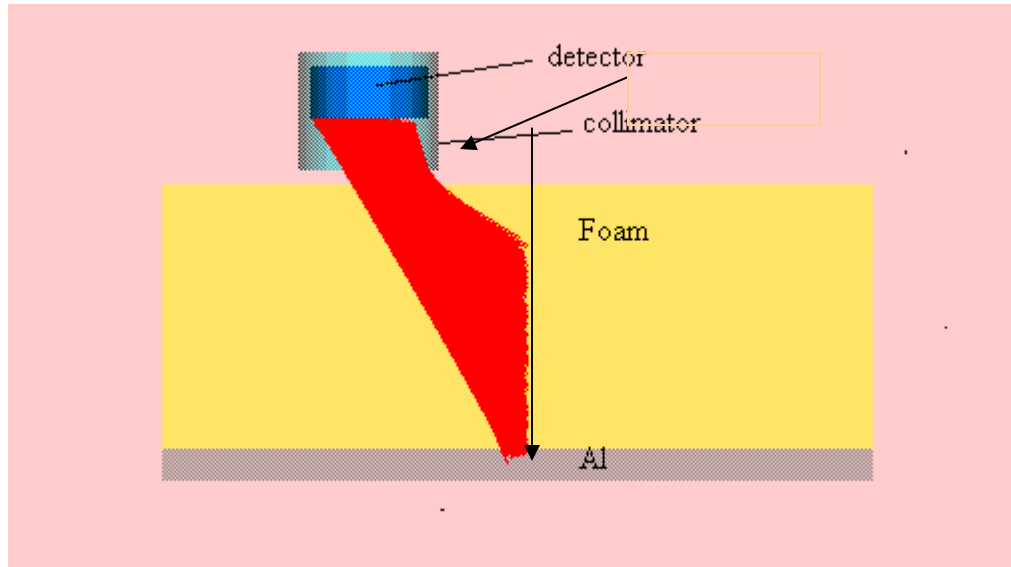


Figure 4.1 First collision components in SOFI reaching the detector with collimator extension.

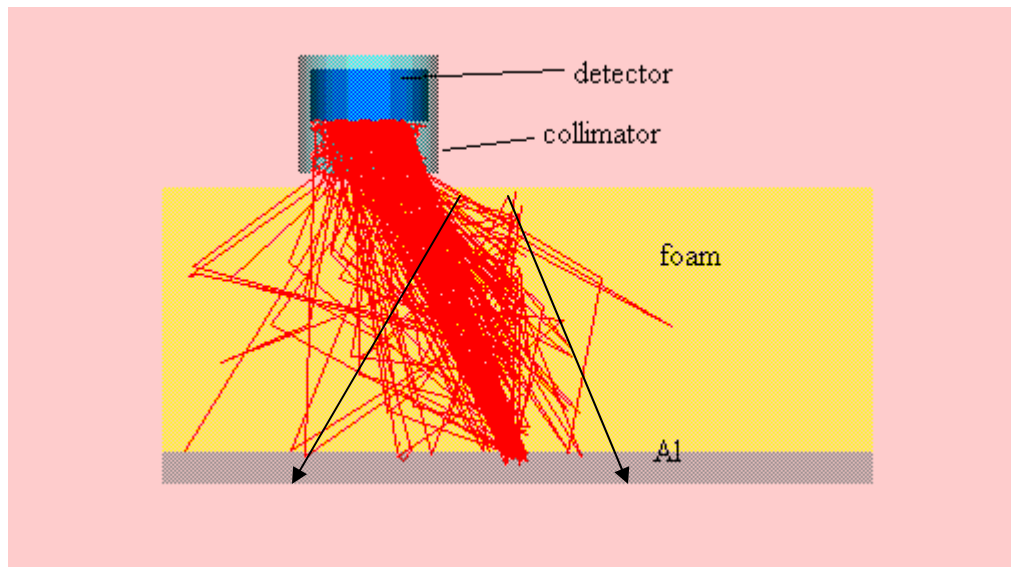


Figure 4.2 . Multiple collision components in SOFI reaching the detector with collimator extension. Diverging arrows demonstrate approximate area of multiple scattered source distribution.

The concept of effective beam broadening is further demonstrated, in aluminum targets, by the following figures, 4.3 and 4.4. Figures 4.3 and 4.4 are SABRINA plots of an aluminum target with a 75 keV impinging photon beam. The detectors are 5.08 cm

radius NaI positioned 9 cm from the photon beam and are 5 cm from the aluminum surface with a 4.4 cm collimator extension. Figures 4.3 and 4.4 show the first collision and multiple collision backscattered components which reach the NaI detectors, respectively. As again illustrated by the black arrows, the first collision components all originate along the impinging beam axis while the higher order components can be modeled as originating from a radial axis of a broader, diverging beam. The validity of this approximation is based upon the fact that, upon suffering a scattering collision, a photon is necessarily deflected at some angle away from the initial photon beam. In order for the photon to be detected, it must either scatter directly into the NaI, or suffer another event that scatters it into the detector. The photons which do not scatter directly into the NaI, as the figures illustrate, effectively make up a distributed source within the target itself. This effective distributed source of multiple scatters is very similar in effect to the primary scatters of an initially broader, diverging, beam having a spread approximated by the black arrows in Figure 4.4.

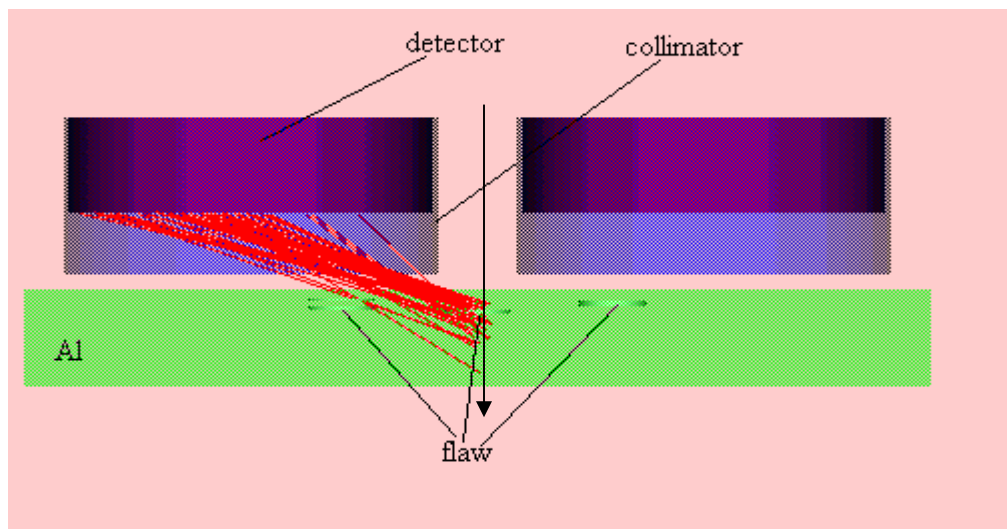


Figure 4.3 First collision components in aluminum

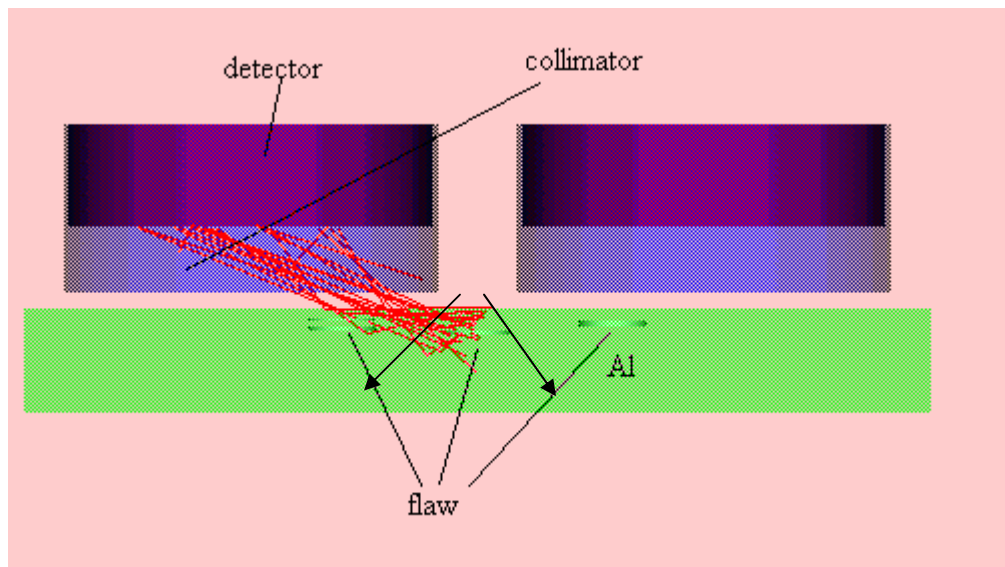


Figure 4.4 Multiple collision components in aluminum. Arrows indicate approximate multiple scattered photon source distribution.

The following set of figures, 4.5 – 4.9, show the effective beam spreading as a function of scatter components. These plots demonstrate that the dominant mechanism for image contrast generation regardless of the number of collisions is the attenuation difference provided by the flaw as the photons directly traverse it. The figures are again generated by the SABRINA application using MCNP5 simulation data. Each figure models a 10 x 10 x 1 inch aluminum plate with a void type flaw running along the axis from beam to detector. The flaw is 0.4 cm in height and 1 cm wide and 1 cm below the aluminum surface. The 2.54 cm radius detector is positioned at 9 cm from the beam center and 2.9 cm above the aluminum surface with a 1.5 cm lead collimator extension. This collimation is configured so that the CRP (critical reference plane, see Figure 4.17) is located just below the flaw channel bottom. In each figure the black arrows again roughly indicate the effective single scatter beam divergence that would approximate the multiple scattered photons. As each of these demonstrate the vast majority of photons directly and linearly traverse the flaws and consequently the resulting acquired image

contrast can be directly related to the difference in attenuation properties induced by the flaw. This is the same effect we would observe if the signal comprised all first scattered photons originating from a wider range than the initially impinging beam. That is the dominant mode for image generation is the same regardless of the scatter order of the photon.

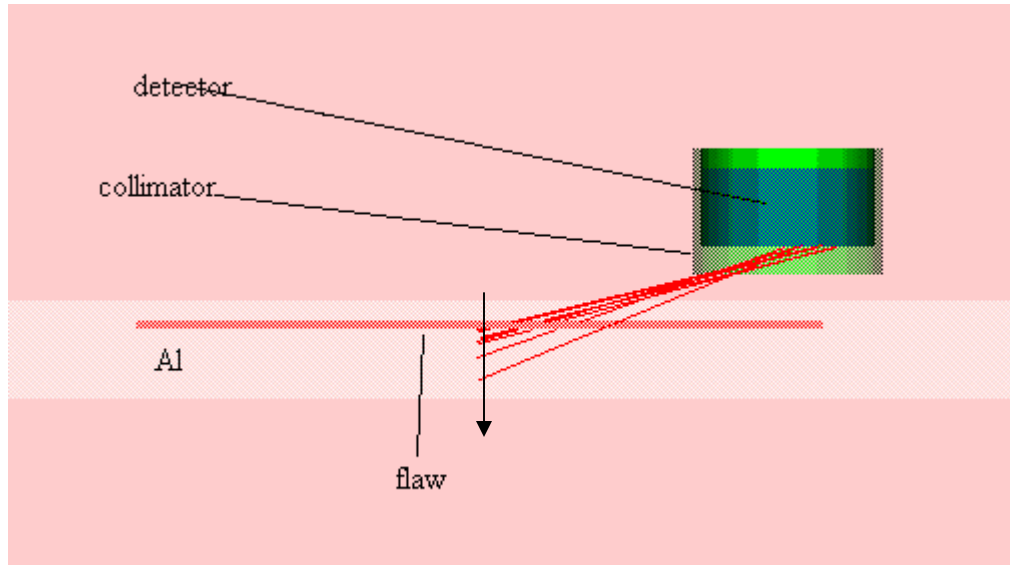


Figure 4.5. First collision components. Black arrow indicates impinging beam axis and line of scatter origination. Note that photons directly traverse the flaw.

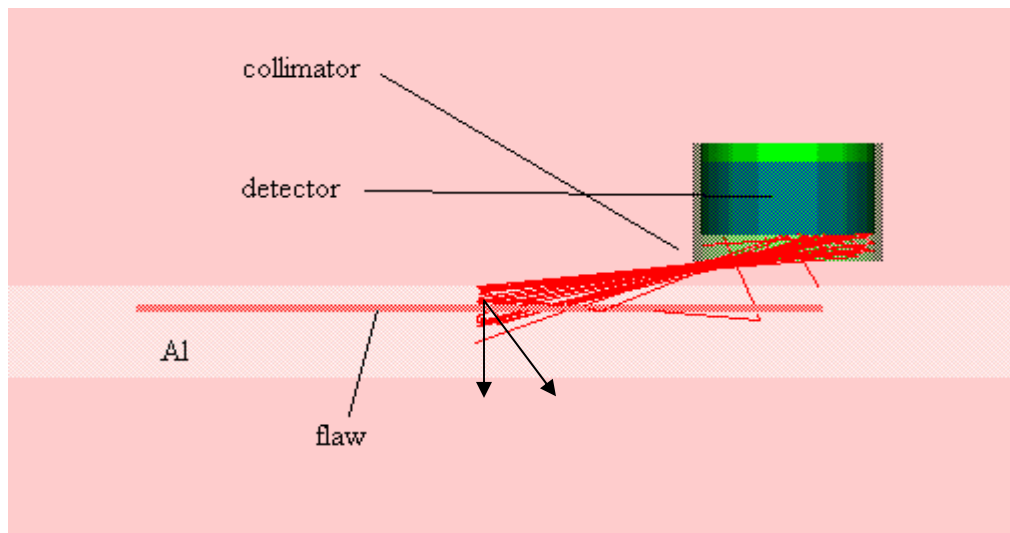


Figure 4.6 Second collisions components. Black arrows indicate approximate effective beam divergence. Note that photons directly traverse the flaw

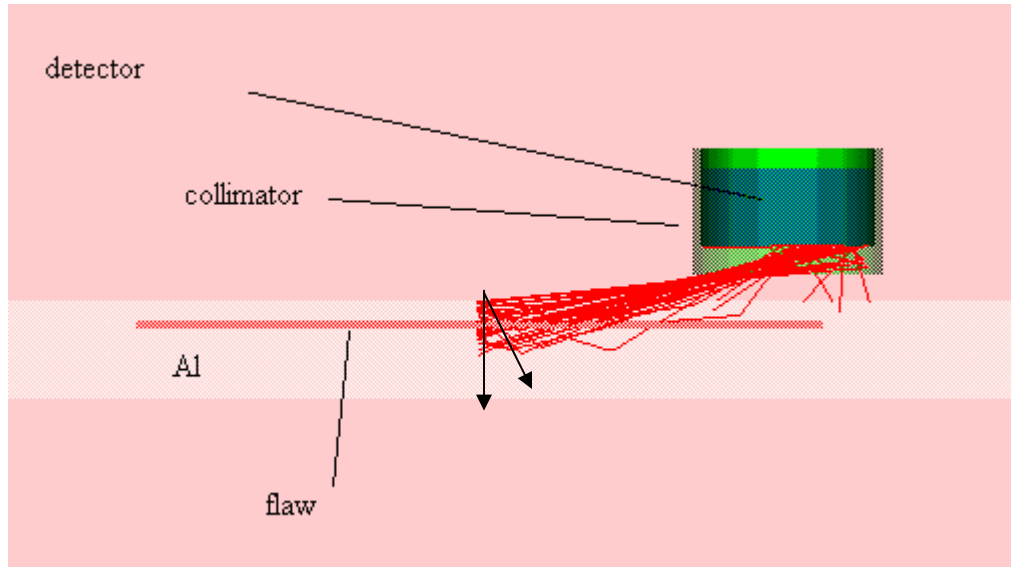


Figure 4.7 Third collisions components. Black arrows indicate approximate effective beam divergence. Note that photons directly traverse the flaw

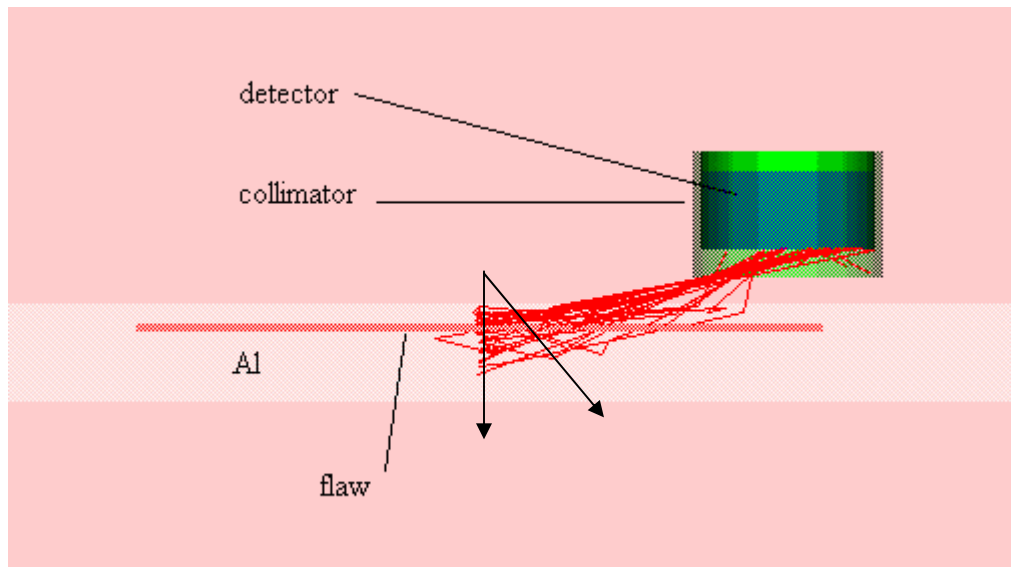


Figure 4.8 Fourth collisions components. Black arrows indicate approximate effective beam divergence. Note that photons directly traverse the flaw

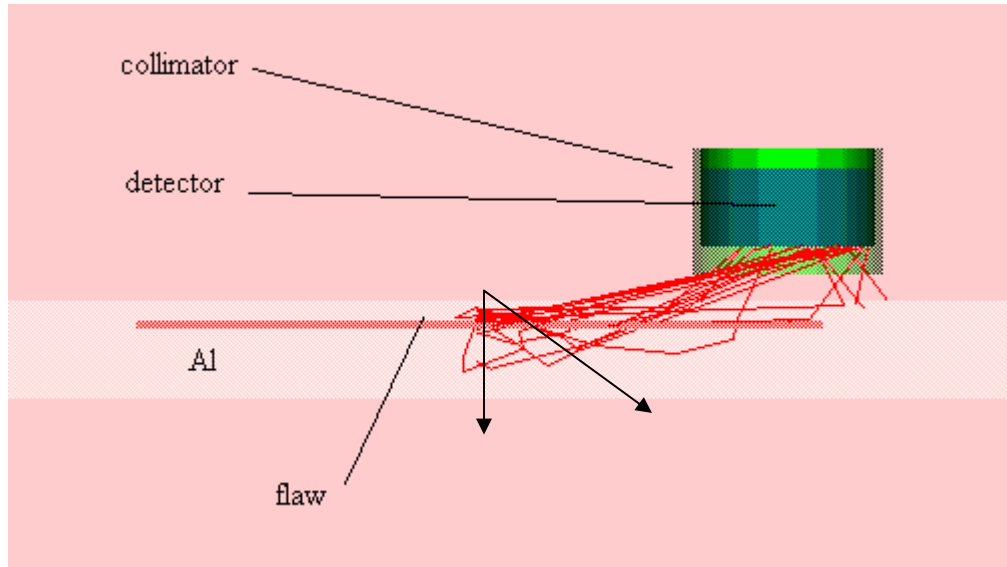


Figure 4.9 Higher order (fifth and greater) collisions components. Black arrows indicate approximate effective beam divergence. Note that photons directly traverse the flaw

The degree to which the effective beam divergence is observed is a function of the relative scatter component contribution to the detector, as dictated geometrically by the collimation configuration, as well as the mean free path of the target material. For relatively high density materials such as aluminum, shown in the figures above, most of the second and third order scatters occur close enough to the initial beam so that neglecting them in an approximation is valid. The relative importance of the first seven scatter components for this simulation, given as percent contribution to the detector current tally, for the simulations depicted above in Figures 4.5 – 4.9, are plotted below in Figure 4.10. Even for this highly collimated situation, contributions of the first three scattering components make up over 70% of the total signal. Furthermore, comparison of this data against a similar MCNP5 run without the flaw channel reveals that the majority of the contrast contribution and thus the important part of the signal comprised mostly first and second scatters as shown below in figure 4.11. This is indicative of the proposed

contrast providing mechanism. As scatter order increases so does the total path length of a photon in the target material. As path length increases (with scatter order) the relative attenuation differential afforded by the flaw (since it remains the same size) decreases. Thus higher order scatter components have lower relative contrasts even though they may represent larger portions of the total signal.

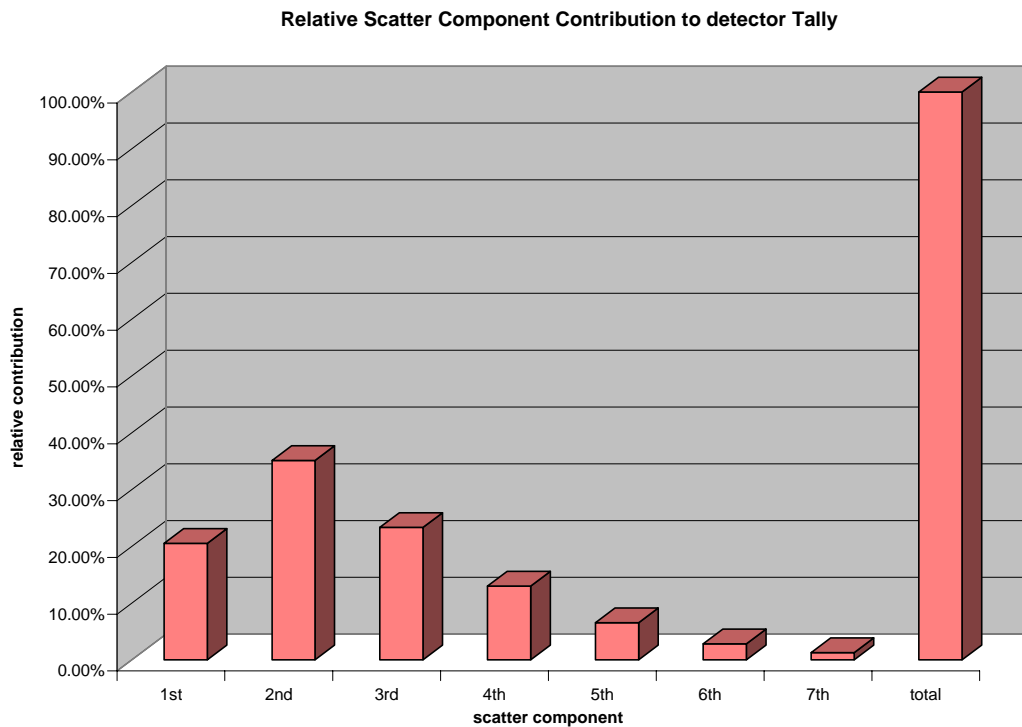


Figure 4.10. Scatter component contribution to detector current tally for geometry of Figures 4.5-4.9.

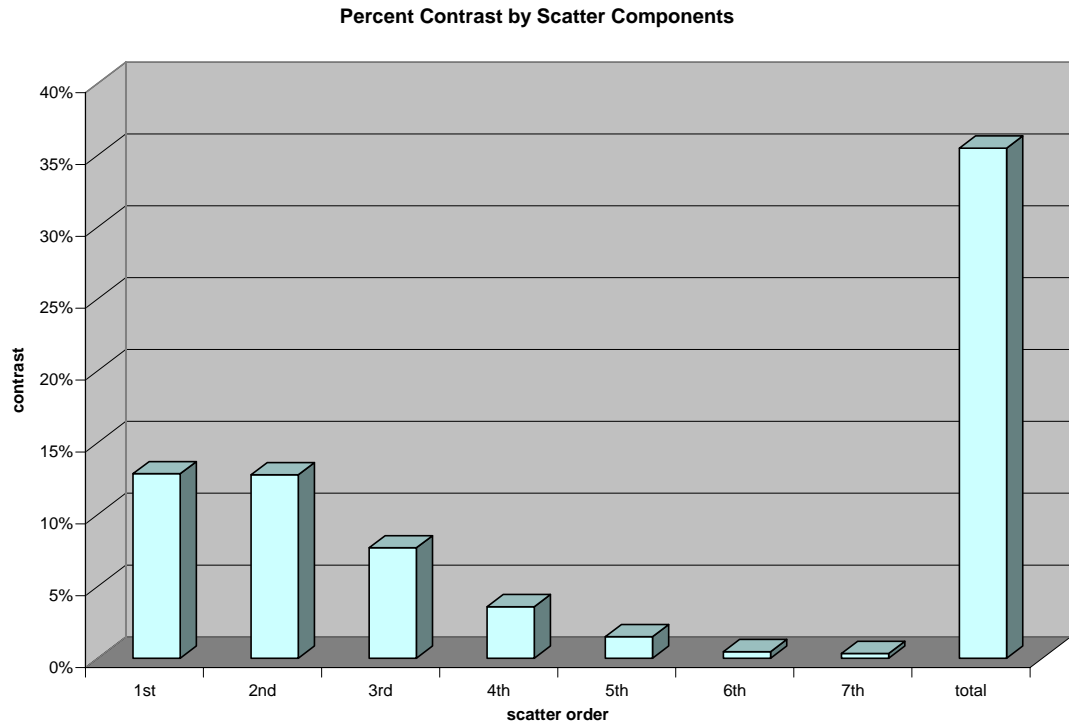


Figure 4.11. Relative contrast by scatter order. This is the contrast that would be observed if each scatter component could be isolated and individually considered.

Additionally, a directional distribution of the tally collision component breakdown (for the simulation discussed above) reveals that for each scatter component considered, up to seventh, the vast majority of the detected photons impinge upon the detector at an angle of thirty degrees or less to the horizontal, just as the once scattered photons do. This indicates that even high order scatter events do not bring the photon significantly far away (geometrically: i.e. – the scattering angles do not vary by more than a few degrees) from the impinging beam axis. If photons in general, were to scatter farther before being deflected into the detector, we would observe a more significant deviation in angular direction components as scatter order increased. There is, as expected, a noticeable increase in detected photons entering further away from the horizontal with increasing

scatter order. However, the majority of photons enter at relatively the same range of angles as the once scattered photons, implying that they traverse the flaw at a similar angle and are thus similarly attenuated by the flaw. The important photons, as defined above and in Figure 4.10 and Figure 4.11, are shown in Figure 4.12 to be composed of more than 90% photons entering within thirty degrees of the horizontal.

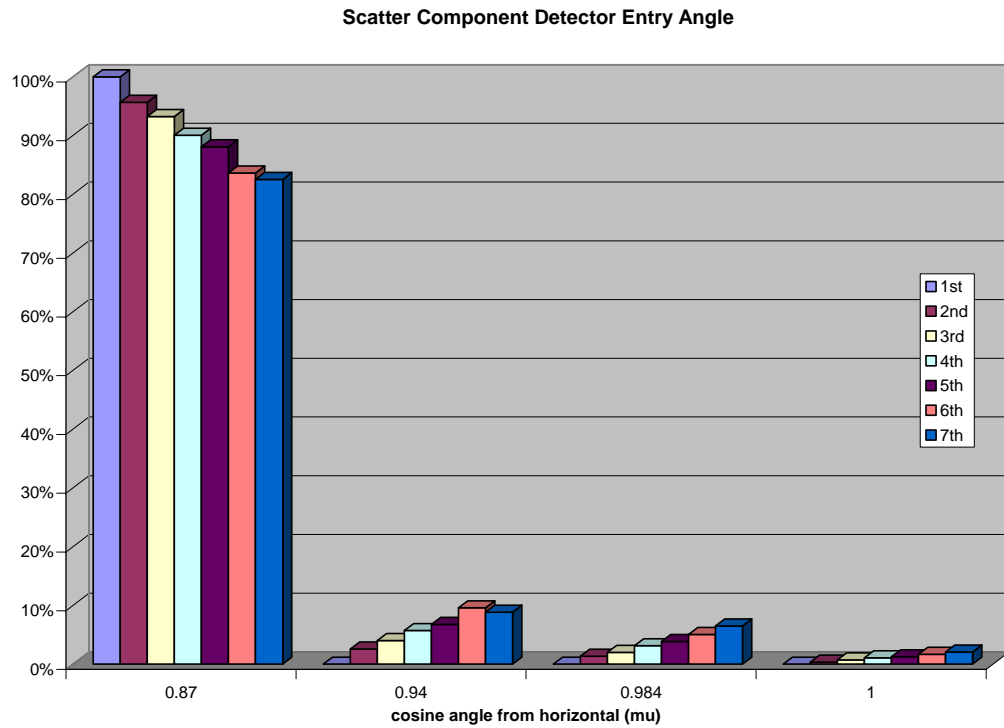


Figure 4.12. Directional distribution of tally components by scatter order.

The following four figures, 4.13 – 4.16, are plots of data taken from MCNP5 simulations. Each shows the percent signal, relative contrast, and contrast contribution of each scatter component (up to seventh) of the signal. The four plots are taken from four separate simulations each of a 40 x 40 x 5.08 cm aluminum target with a 0.08 cm high and 1 cm wide flaw channel 0.1 cm below the aluminum surface. Each simulation was modeled with a 5.08 cm diameter NaI detector 2.9 cm from the target aluminum surface

and offset from the impinging beam (center-to-center) by 9 cm. The collimation in each of these runs was varied as 1 cm, 1.32 cm, 1.5 cm and 2.32 cm extension past the NaI surface. In these plots, the percent signal of each component is calculated by dividing the signal strength of that component by the total signal strength. The relative contrast is calculated by dividing the difference between the nth components of flawed versus non-flawed scenarios by the appropriate component of the non-flawed scenario. This relative contrast represents the contrast that would be observed if the detector was only sensitive to the nth scatter component of the backscattered field. The contrast contribution in these plots is calculated by dividing the signal difference of the nth scatter component by the total signal difference. This represents the contribution to the contrast generated by each scatter component.

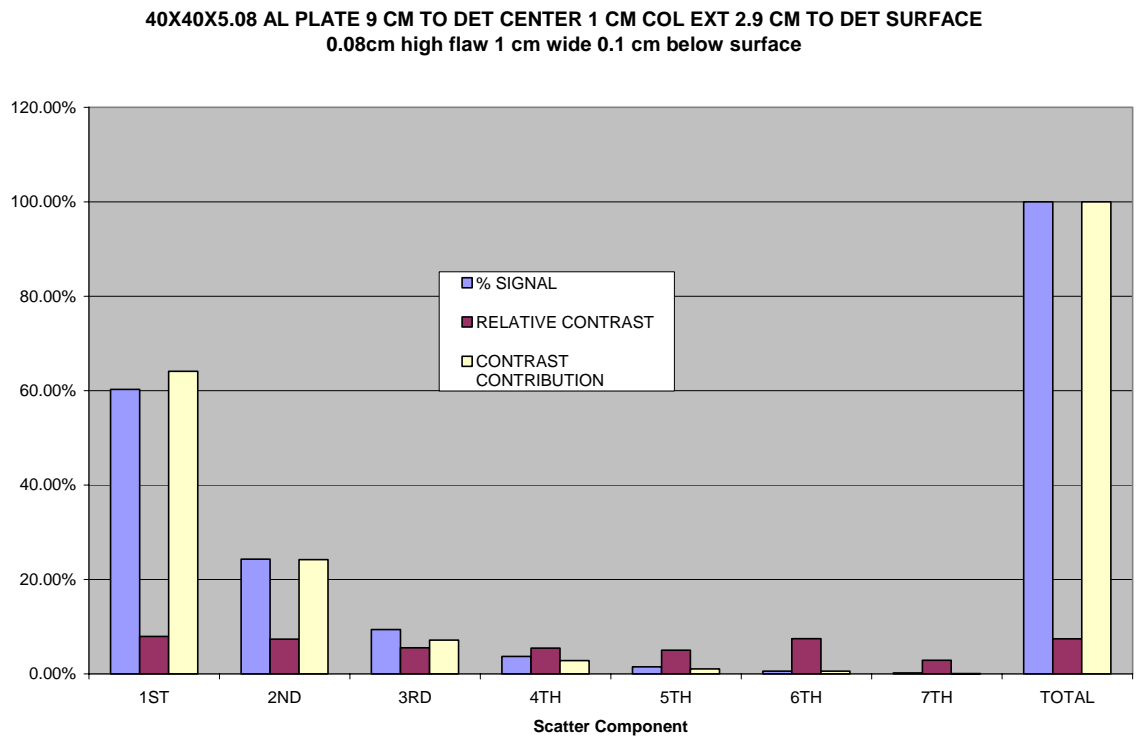


Figure 4.13. Percent signal, relative contrast and total contrast contribution by scatter components for 1 cm collimator extension.

**40X40X5.08 AL PLATE 9 CM TO DET CENTER 1.32 CM COL EXT 2.9 CM TO DET SURFACE  
0.08 cm high flaw 1cm wide 0.1 cm below surface**

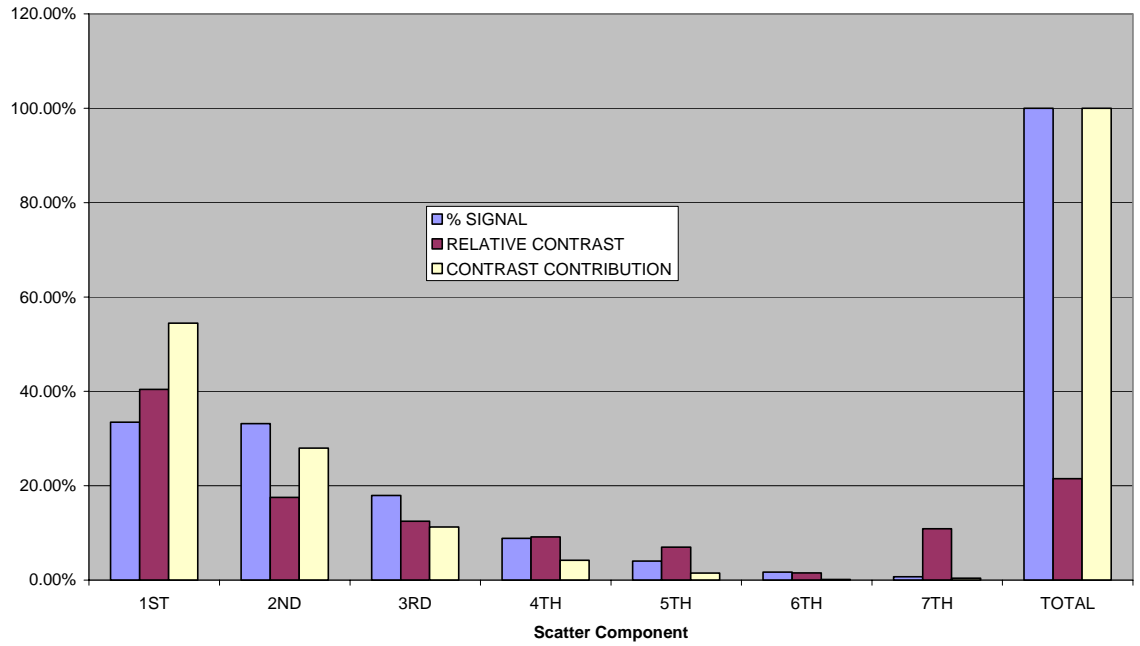


Figure 4.14 Percent signal, relative contrast and total contrast contribution by scatter components for 1.32 cm collimator extension

**40X40X5.08 AL PLATE 9 CM TO DET CENTER 1.5 CM COL EXT 2.9 CM TO DET SURFACE  
0.08 cm high flaw 1cm wide 0.1 cm below surface**

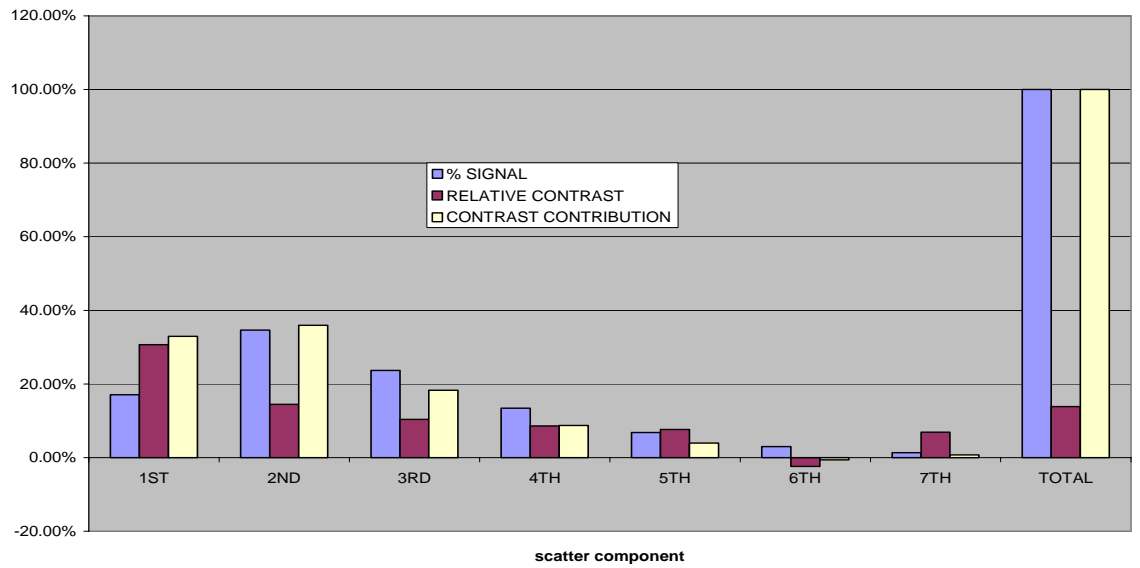


Figure 4.15. Percent signal, relative contrast and total contrast contribution by scatter components for 1.5 cm collimator extension

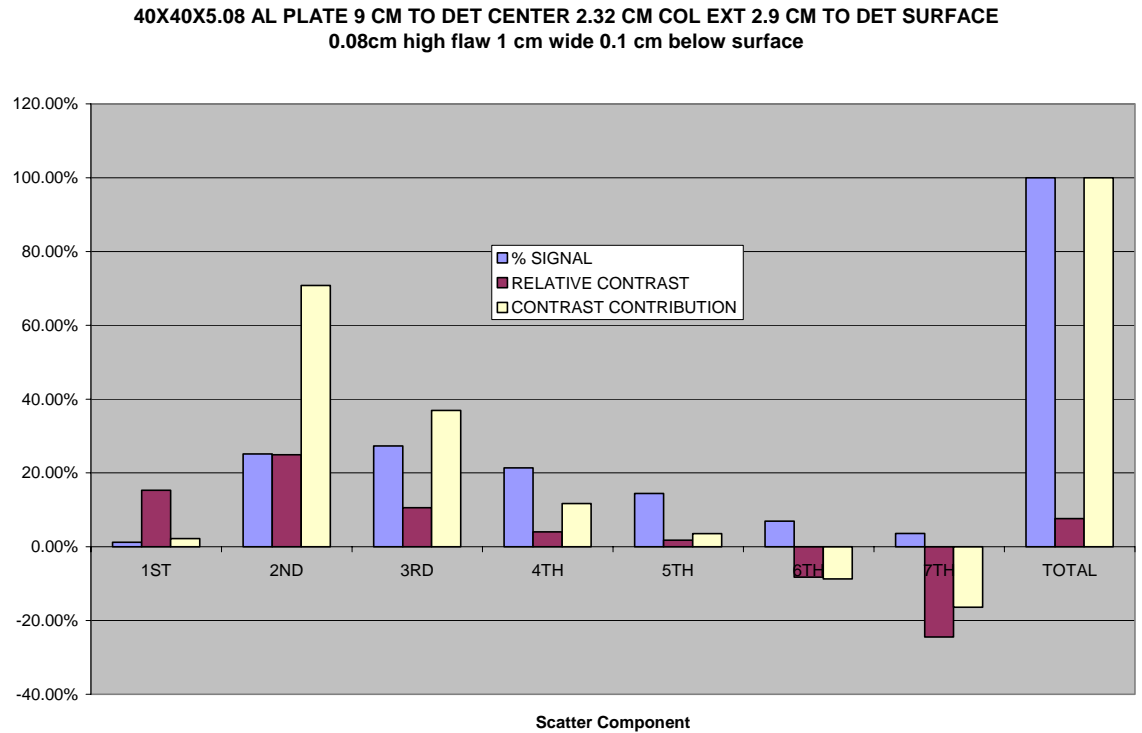


Figure 4.16. Percent signal, relative contrast and total contrast contribution by scatter components for 2.32 cm collimator extension

As these plots demonstrate, the relative contrast of the first collision component is usually (with exceptions for extremely over-collimated and under-collimated cases) the largest. This is because for these cases, the first collision path length is the shortest and thus the flaw represents the largest relative attenuation difference. As scatter order increases, relative contrast percentages generally decrease. This is due to the relatively longer path length of multiple scattered photons in the target material and consequently lessened effect of the attenuation difference caused by the flaw. In fact, as the figures also indicate, for scatter components on the order of 5 or more, the resultant signal is considered noise and can detract from the desired contrast. The above plots also indicate, as expected, that increased collimation increases the signal contribution of higher order scatters. This is accomplished mostly by eliminating shallow low order

scatter components geometrically from entering the detector. The contrast contribution is a function of both the relative contrast and the signal contribution of each scatter component of the signal. Consequently, even though a particular scatter component may have the highest relative contrast, it may not represent the dominant contrast contribution if it does not compose a significant percentage of the total signal. Similarly, the fact that a particular scatter component dominates the signal or even the contrast does not imply that it necessarily produces the largest relative contrast. The justification for including higher order (second, third, and fourth) scatter components even though they may have lower relative contrasts than the first scatter component is that the advantage of decreased scanning time provided by the stronger signal outweighs the disadvantage of lower contrast.

The scattered photons viewed by an RSD configuration are those specific photons which interacted in or traveled through a specific region of interest. In radiography by selective detection, collimators and detector placement are coordinated so that only certain components of a backscattered signal are detected. In many cases, this amounts to using the collimators to discriminate against all interactions occurring above a specific region of interest. This allows a signal originating from deeper within a sample to be collected and relative differences caused by small or deep flaws to become observable. In the RSD imaging modality, this collimation-induced specificity for signal components is referred to as focusing. By focusing to a specific depth, the modality effectively discriminates against all photons having scatters above this depth. The depth to which a RSD configuration is focused is described by a critical reference scattering plane (CRP) which is an imaginary plane located at the depth at which the first significant primary

scatter contribution to the detector occurs. The concept of a CRP is demonstrated by the schematic presented in Figure 4.17. In this figure, below, the CRP is shown as a dark horizontal line. The effect of the collimator on once scattered photons originating from above this plane and below this plane is shown.

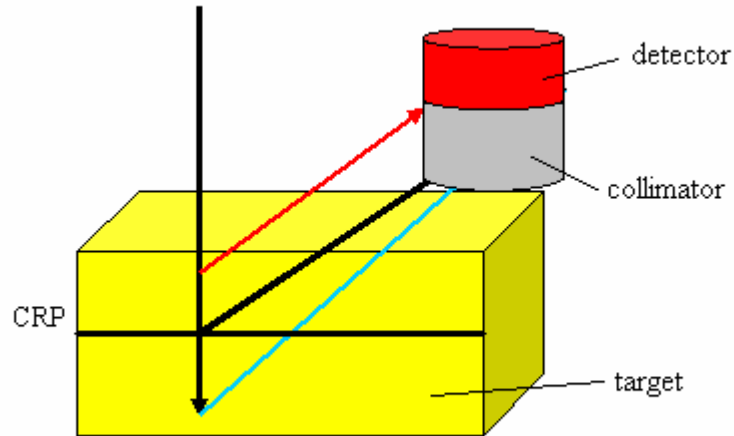


Figure 4.17 Schematic of CRP. Photons at and below CRP can pass under collimator and enter detector. Photons scattering from above CRP are blocked by the collimator.

Figures 4.18 – 4.21 demonstrate how a particular collimation configuration focuses to a specific depth by discriminating against shallower components of the returning scatter field. These figures are again SABRINA photon track plots of MCNP5 simulations. The target is eight inches (20.32 cm) of SOFI foam on an aluminum substrate. Each figure shows the CRP location by a dark horizontal line at the site of the first important scatter event. Each scenario simulated has a collimator sleeve to sample separation of 1.14 cm. Thus a 5 cm collimator extension implies a distance of 6.14 cm from detector (NaI) surface to sample surface. In Figure 4.18, the collimator is fully withdrawn so that photons scattering from all depths in the target may impinge upon the

detector. In Figure 4.19, the collimator is extended 5 cm past the NaI. This forces the CRP to a depth of 5.2 cm below the foam surface. In this figure it is evident that no scatters occurring above the CRP are reaching the detector. Figure 4.20, shows the effect of further increasing the collimator extension to 10cm past the detector surface. Simple geometrical calculations reveal that the CRP is now 11.6 cm below the SOFI surface and, as indicated in the figure, this is the minimum depth that photons must penetrate before being able to directly scatter into the detector. Figure 4.21, features still further collimation as the collimator is extended 14 cm past the NaI surface. Here the CRP is moved to a depth of 16.7 cm and, as the SABRINA track plot demonstrates, no primary scatter events occur above this plane and enter the detector.

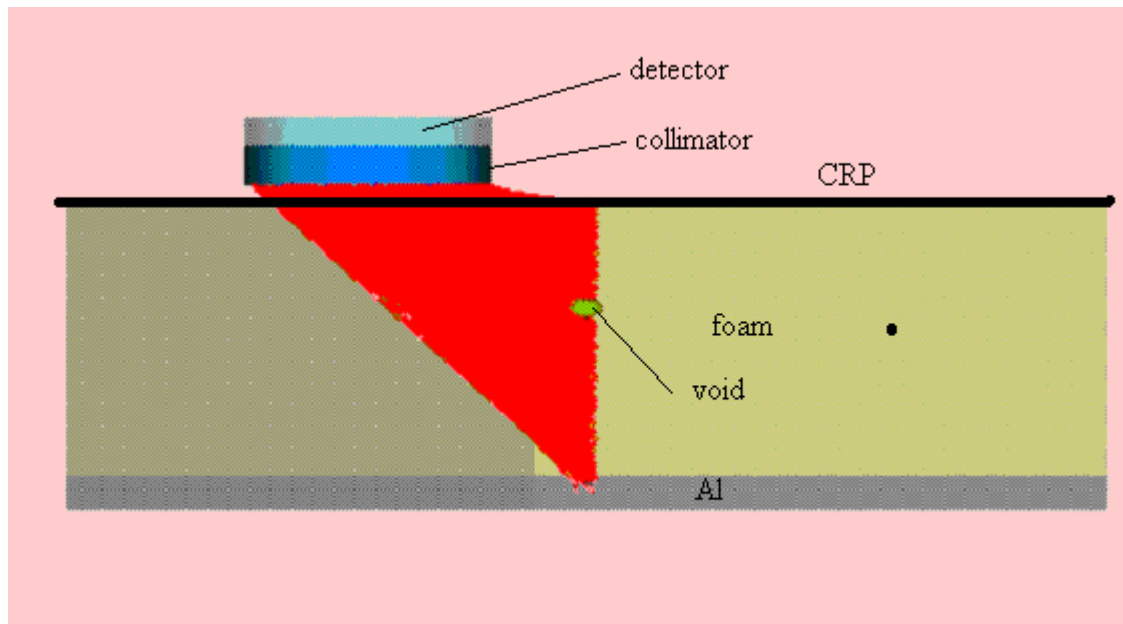


Figure 4.18. Severely under-collimated. first scatters. 5.08 cm radius NaI 1.14 cm from SOFI. Dark line indicates CRP above which no first scatters can enter the detector.

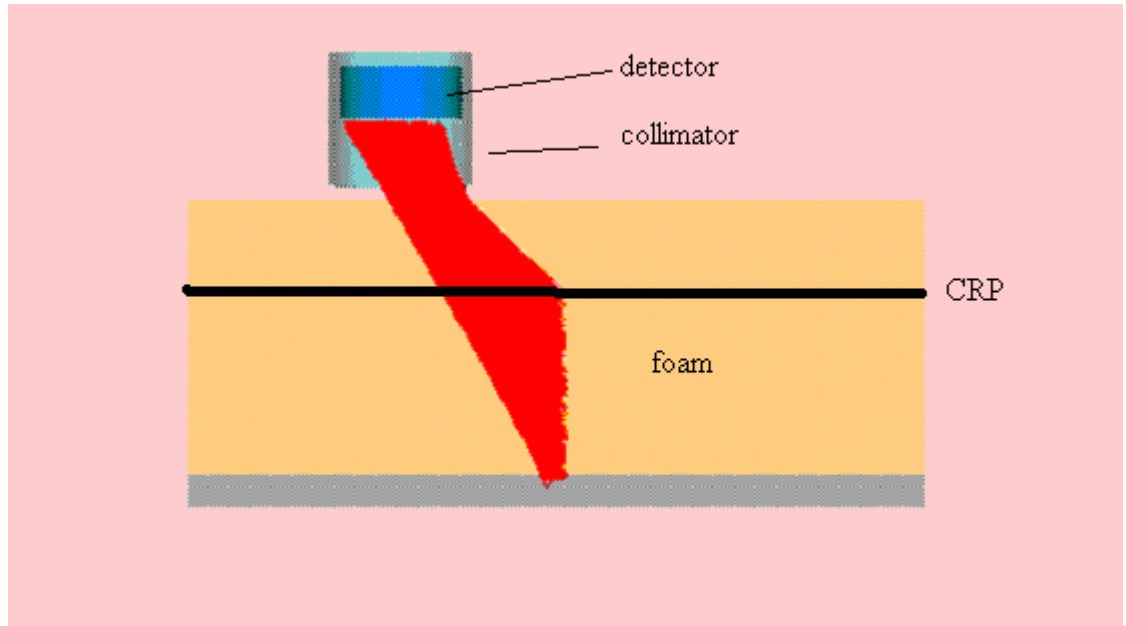


Figure 4.19. First Scatters. NaI 6.14 cm from SOFI 5 cm collimator extension. Dark line indicates CRP above which no first scatters are tallied.

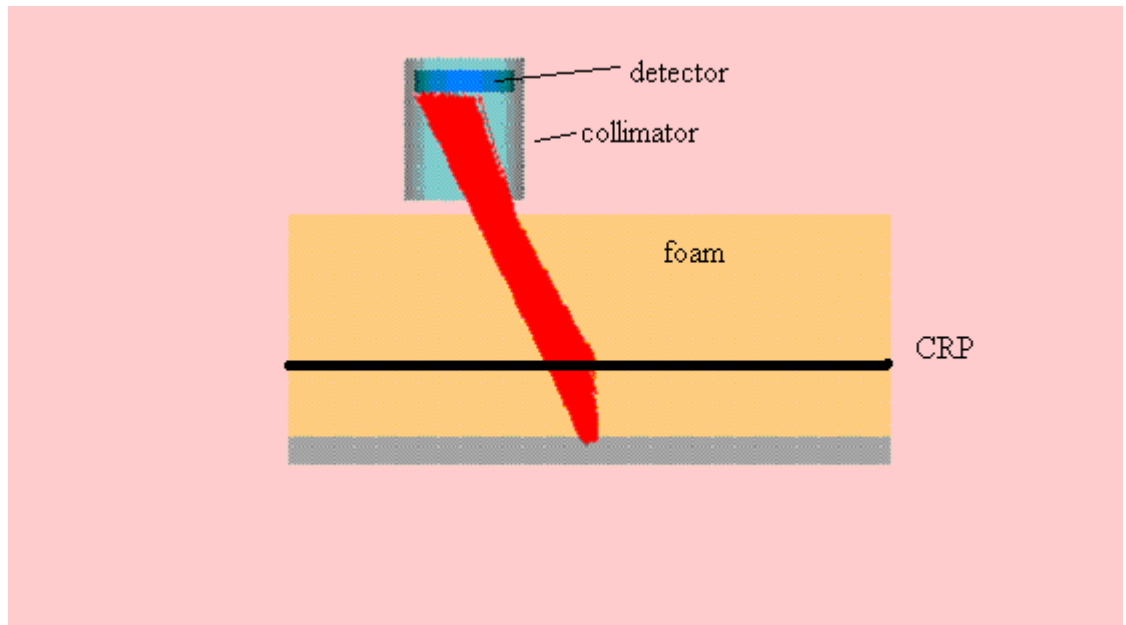


Figure 4.20. First Scatters. NaI 11.14 cm from SOFI 10 cm collimator extension. Dark line indicates CRP above which no first scatters are tallied.

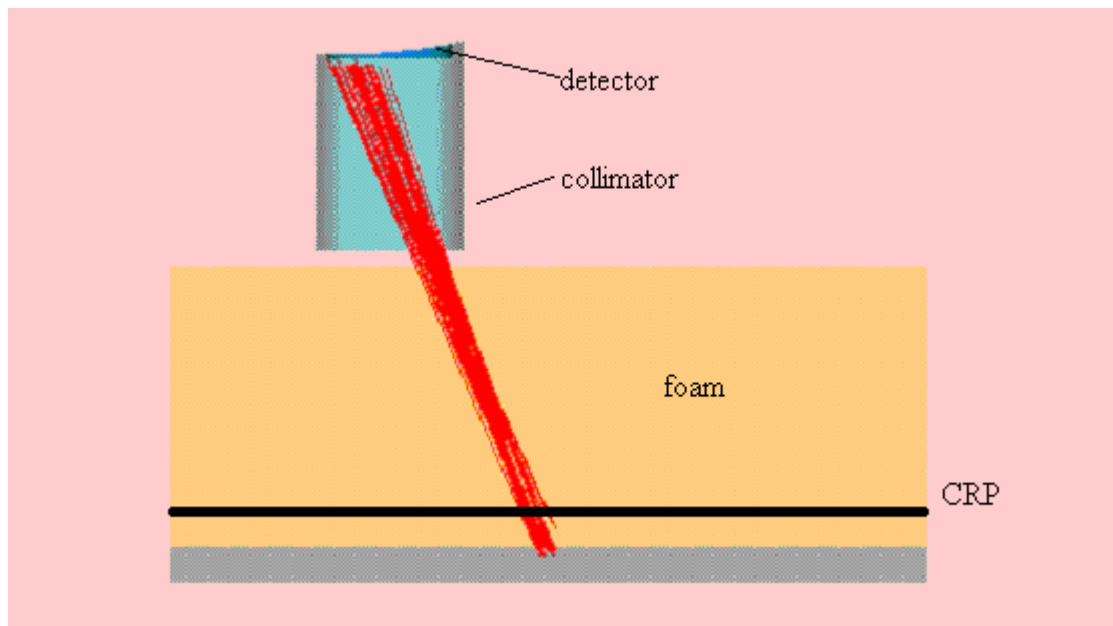


Figure 4.21. First Scatters. NaI 14.15cm from SOFI 14cm collimator extension. Dark line indicates CRP above which no first scatters are tallied.

RSD modalities can often be modeled as one scatter phenomena in that the photons behave much like the once scattered photons in a traditional Compton imaging system. Essentially the physics of RSD can be considered similar to traditional CBI, except that the photons having scatters above a selected depth are discriminated against. In this idealization, RSD methods effectively remove a specified amount of material from the surface of a sample and thereby view the lower layers, below the CRP.

### **Photon Transport Model**

#### **Introduction and Concept**

A rough analytical model has been developed under consideration of experimental observations, MCNP simulation, and photon transport physics. The purpose of this model is to facilitate visualization and understanding of the phenomena leading to an image as well as to approximate detector responses and system optimization parameters

for various types of materials and flaws. The model used to describe the current system is a simplified “one scatter” model, shown below in Figure 4.22.

In this model, each potential first scatter site along the length of the impinging beam axis is considered and the integrated relevant path length leading from each element to the detector is then calculated. The difference between the attenuation of this path for flaw versus no flaw conditions is then taken to approximate a contrast ratio. This model facilitates quick calculations and serves as a good analytical model upon which to base optimization parameters.

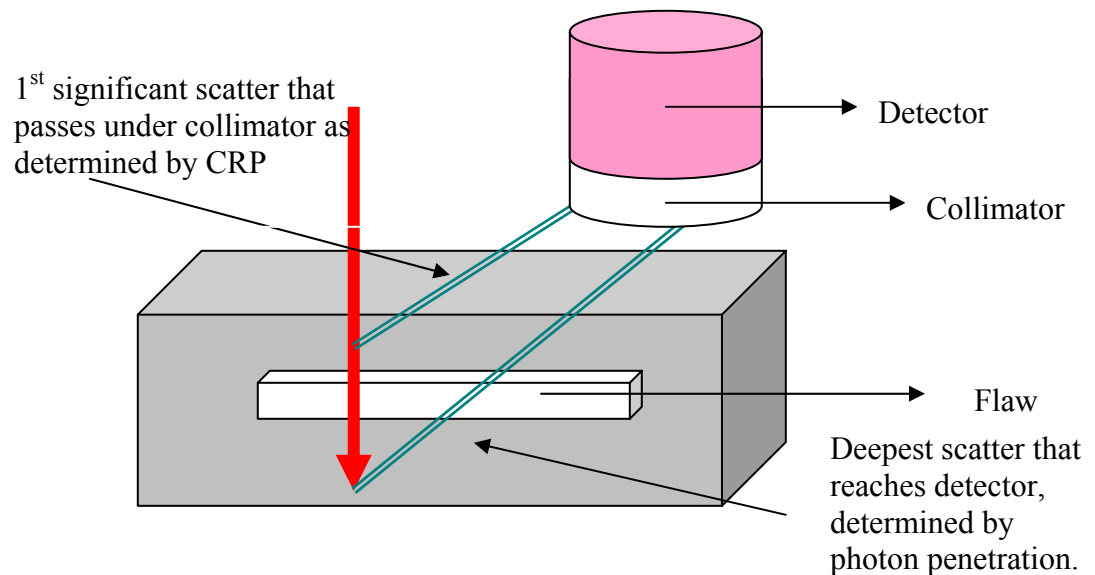


Figure 4.22 One scatter photon transport model. Double lines indicate upper and lower bounds from important scatters.

Here the signal difference between flawed and non flawed regions of a sample can be visualized as a difference in attenuation. The photon beam potentially crosses a flaw twice, as shown above, once impinging and once after scattering. The difference in attenuation of the photon beam over its entire path (incident and scattered) between flawed and non-flawed regions is the primary contributor to the signal difference observed in the detector. In this model the lack of scattering within a volume due to a

low density flaw can be shown to be equivalent to an increase in attenuation of the photon beam that otherwise would have scattered within that volume and returned to the detector. That is, the photons which do not interact in the low density flaw continue to penetrate through the sample where eventually they will interact. When they do interact, it will necessarily be deeper within the sample and they will necessarily have a longer distance to travel through the material to the detector. Consequently these photons will have a greater probability of being attenuated on the way to the detector than their counterparts which interacted in the shallower volume of a non-flawed sample. *[This is, however, contingent upon flaw orientation and detector and collimation configurations. If the system is configured such that the selected portion of the back scattered field traverses the flaw again on the way out, the overall effect on attenuation may be an increase or decrease, depending upon flaw height and material interaction characteristics, as discussed later in this chapter].*

Analytical calculations can easily be performed based upon the simplified one scatter model. In this one significant scatter model, the attenuated photon intensity at each point along the incident beam path (shown as the thick, red arrow) is scattered and further attenuated towards the detector. The integral of this path over all scattering points then results in a final once scattered intensity at the detector. The detected signal intensity then has the following form:  $Ae^a e^b B(y)$ . Here A is the original photon intensity and the exponential terms, a and b, account for the attenuation between the source and the first scatter and between the first scatter and the detector, respectively and B(y) is a function which accounts for the angular cross-section of the scatter and the solid angle subtended by the detector. The percent difference between this integrated intensity for a flawed

versus a non-flawed region in then taken to be the percent contrast. More mathematical detail of this treatment is in Appendix B.

While in reality a detected signal is composed largely of multiple scattered (2<sup>nd</sup> order and higher) photons, the usefulness of the simplified once scattered transport model is that it provides a means of understanding and visualizing contrast generating mechanisms and thus augments our ability to predict and understand trends, optimization and relevant image features such as shifts and shadows.

### **Support /Evidence and Characteristics**

This photon transport model of the RSD modality is based largely upon experimental observations and supported with MCNP5 simulations, SABRINA track plots, and analytical calculations. Trends observed in detector response arising from parameter variations such as flaw type and orientation and collimation configuration strongly suggest a scatter model of this type. Specifically, the image contrast, positive and negative (depending upon flaw type and orientation) as well as collimation induced contrast trends and pixel shifts observed in acquired images all lead to and are well described by the proposed transport model. Figure 4.23 and Figure 4.24 are SABRINA generated track plots of MCNP5 simulations. The simple linear tracks shown here support the premise of the once scattered transport model, i.e. – that contrast is primarily generated by a differential in attenuation experienced by photons as they directly traverse a given flaw. Figure 4.23 is a plot of a highly collimated detector over an aluminum plate with a scattering-type flaw channel (modeled as C<sub>2</sub>H<sub>8</sub>O<sub>2</sub> plastic). As the plot shows, many of the detected photons suffer multiple scatters. However, for the purpose of generating image contrast, even these high order scatter photons behave essentially as primary or first scatter photons. That is, the majority of the photons, regardless of scatter

order, traverses the flaw in approximately the same manner with approximately the same angle and consequently results in similar contrast. Figure 4.24 is a similarly produced SABRINA track plot except that the collimation is much less pronounced. In this scenario the photons similarly traverse the flaw directly and thus generate an image contrast based upon the differential in scattering and attenuation characteristics provided by the flaw. As the Figures 4.23 and 4.24 demonstrate, the attenuation process and contrast mechanics are essentially the same for all important photons, regardless of their scatter angle and order.

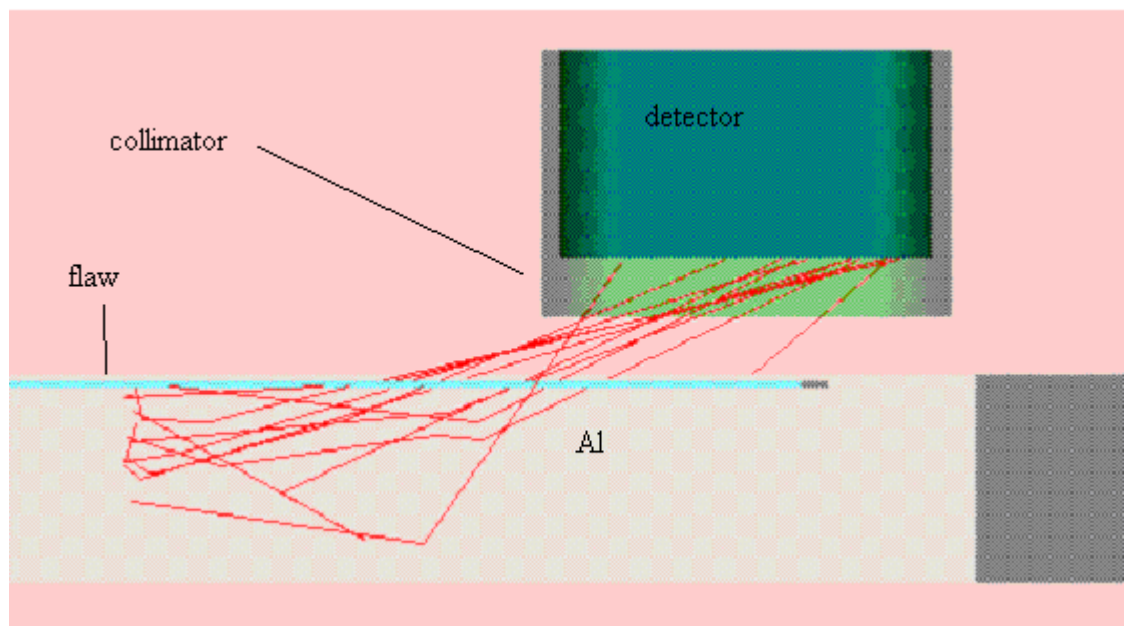


Figure 4.23. SABRINA generated photon track plot. Aluminum plate with shallow scattering type flaw. Severe collimation.

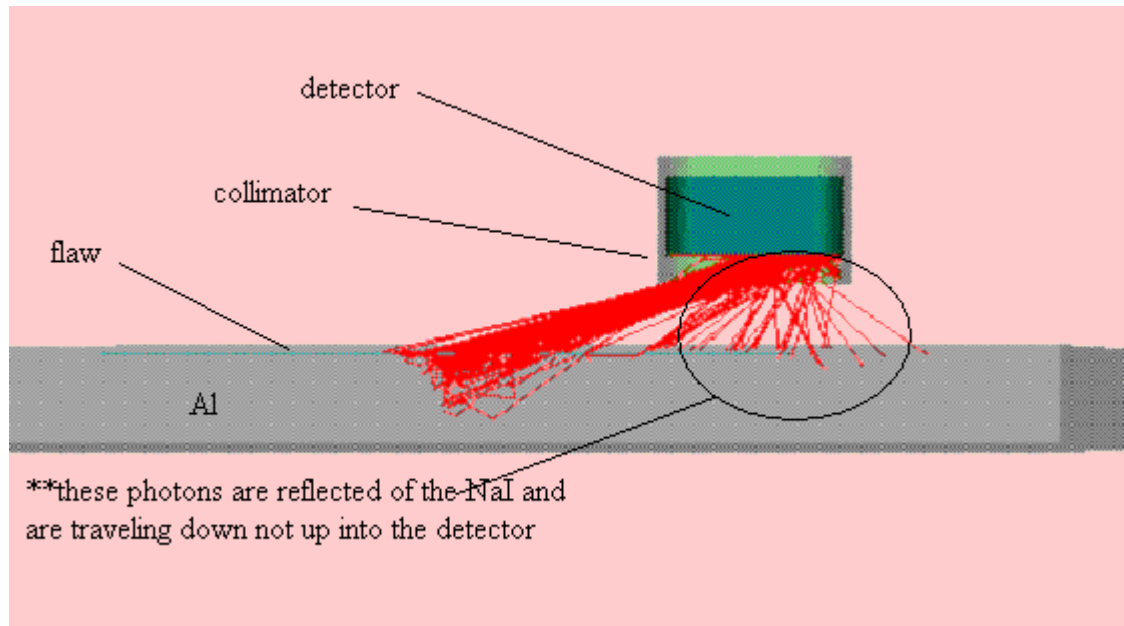


Figure 4.24. SABRINA generated photon track plot. Aluminum plate with shallow scattering type flaw. Less collimated.

### **Image contrast (bright vs. dark images)**

Images generated with the RSD imaging modality display flaws as either bright (high intensity) or dark (low intensity) regions of a sample. Bright and dark regions are a result of relatively more or relatively less photons, respectively, reaching the detector due to the presence of a flaw. This, in turn, is usually caused by a lack of or increase in photon beam attenuation resulting from the presence of a flaw. In the proposed transport model, this differential attenuation is a function of both flaw type and orientation as well as detector and collimator configurations. That is, the intensity of a detected signal is not uniquely a function of electron density of the region of the sample where the incident photon beam impinges. The explanation for this is that, RSD techniques are sensitive to the photons' exit paths through the media, which depending upon system geometry and flaw depth, can be the source of significant attenuation. The contrast between exit paths

of important contributing photons due to collimation in RSD imaging modalities is illustrated in Figure 4.25

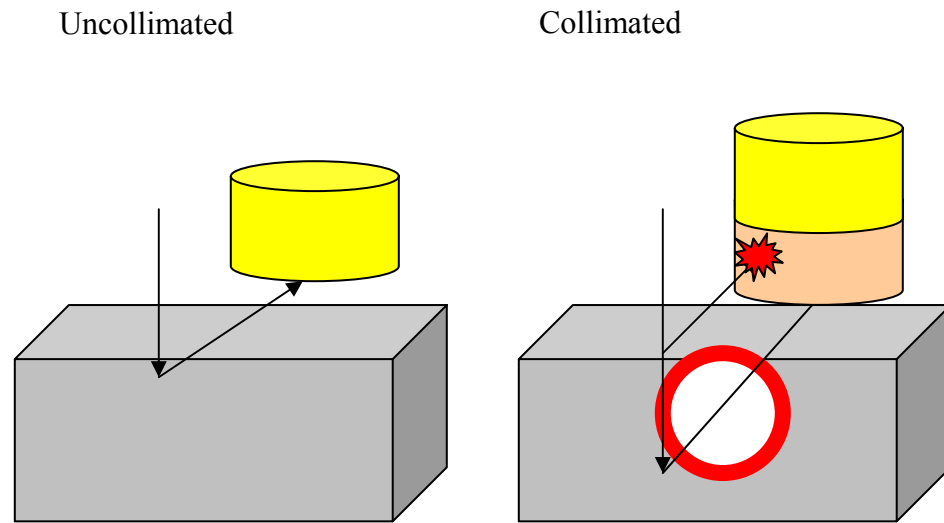


Figure 4.25 Difference in important photon exiting paths caused by a focusing collimator extension.

The additional distance traveled in the material by collimated RSD contributing photons, highlighted by the (red) circle in the figure above, provides additional influences on the contrast presented by collimated RSD images.

Considering relevant parameters in flaw type and orientation and collimation configurations, most relevant imaging scenarios can be idealized by eighteen simple models. The parameters are critical reference scattering plane (a function of collimation configurations), flaw type, and flaw orientation (length). The collimator can be set so that the flaw lies either above or below the critical scattering reference plane. (This imaginary plane, again, represents the depth at which the first important scatter occurs that can pass under the collimator and enter the detector.) The flaw, relative to the object

media, can be low density (void), high density scatterer or absorber. The orientation of the flaw can be such that both the incident and exiting photon field pass through it, only the incident field passes through it, or only the exiting field passes through it. These eight characterizing parameters henceforth referred to by the following letter designations:

D – deep, the flaw is below the critical reference plane

Sh-shallow, the flaw is above the critical reference plane

V- void, the flaw is a void

Sc- scatter, the flaw is a scattered (higher density)

\*low density scatterers are treated as voids

A-absorber, the flaw is an absorber (higher density)

\*qualitatively, low density absorbers are either treated as weak absorbers or as voids and treatment is contingent upon flaw dimensions and relative attenuation characteristics between flaw and target medium. This scenario was not considered in detail.

L-long, the flaw is oriented so that both incident and reflected photon beams pass through it

I-incident, the flaw is oriented so that only the incident photon beam passes through it

E-exit, the flaw is oriented so that only the reflected beam passes through it on its way to the detector.

These parameters can be organized into eighteen permutations relative to a control, non flawed sample. They are specified by three letter designations such that the first letter indicates flaw type (V/A/Sc), the second letter indicates the collimation

configurations (D/Sh) and the third letter indicates the flaw orientation (L/I/E). The permutations are thus:

VShL, VShI, VShE, VDL, VDI, VDE, ScShL, ScShI, ScShE, ScDL, ScDI, ScDE,  
AShL, AShI, AShE, ADL, ADI, ADE

They are depicted in the following Figures 4.26 – 4.37:

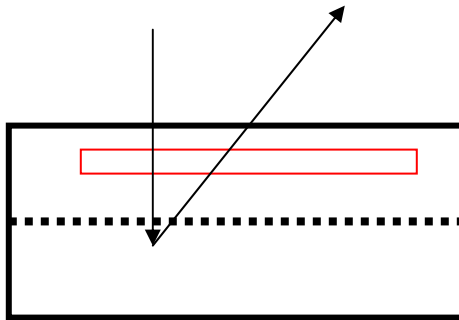


Figure 4.26. VShL: Void Shallow Long. More photons reach a depth at which they can scatter to the detector (below reference plane) due reduced attenuation on the way down. More photons reach the detector on the way out due to lack of attenuation on the way out. BRIGHT

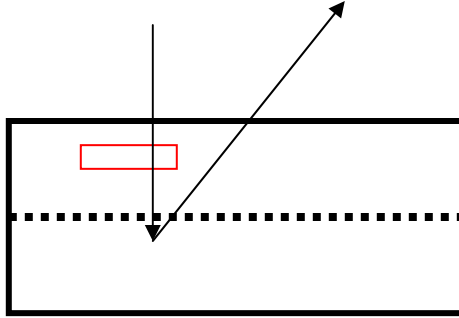


Figure 4.27. VShI: Void Shallow Incident. More photons reach a depth at which they can scatter to the detector (below reference plane) due to reduced attenuation on the way down. BRIGHT

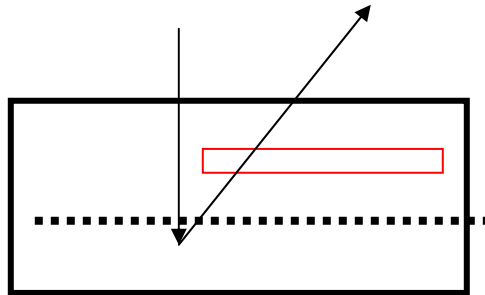


Figure 4.28. VShE: Void Shallow Exit. More photons reach the detector on the way out due to reduced attenuation on the way out. This is also the cause of shifts and shadows: BRIGHT

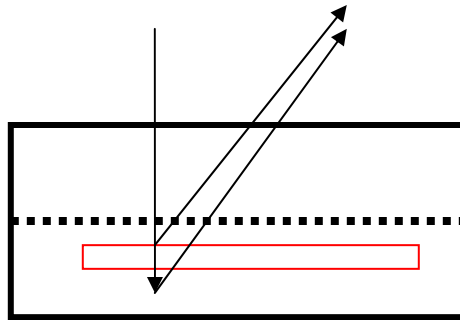


Figure 4.29. VDL: Void Deep Long. This scenario can either be viewed as bright or dark and is contingent upon the combination of two main mechanisms. The first mechanism is the lack of scattering at the flaw site due to the lack of material. This mechanism is similar to traditional Compton backscatter mechanism with a specified amount of material removed from the top by preferential discrimination of the collimator. This mechanism tends to lead to a dark image as expected by a void type flaw in traditional Compton backscatter radiography. The other major mechanism is the increase signal intensity due to the decreased attenuation of the exiting photons due to the flaw. In this mechanism, the incident photons that traverse the flaw scatter below it and experience a lessened attenuation on the way out due to the presence of the flaw. This mechanism tends to produce a bright image. The interplay between these two mechanisms and thus the overall contrast (bright or dark) of the image is very sensitive to parameters such as flaw height and depth, detector and collimator configurations and the attenuation properties (scattering to absorption ratio and over mfp) of the target material

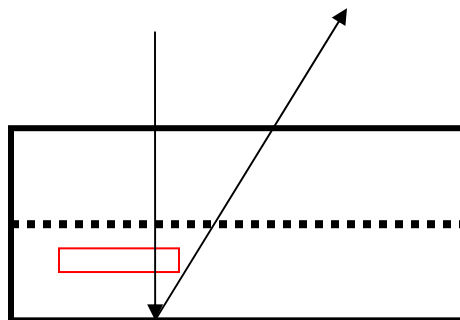


Figure 4.30. VDI: Void Deep Incident Almost same effect as VDL but dark because photons are effectively transported deeper by the flaw and now travel further out through the material. Again similar to traditional CBI: DARK

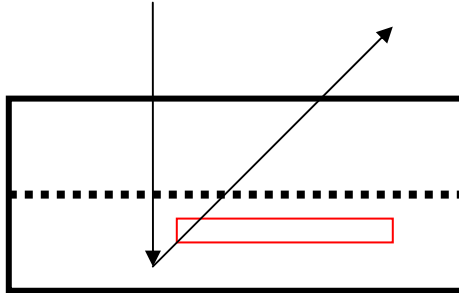


Figure 4.31 VDE: Void Deep Exit. More photons reach the detector on the way out due to reduced attenuation on the way out: BRIGHT

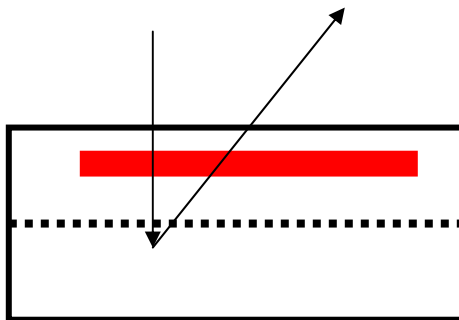


Figure 4.32. ScShL: Scatterer Shallow Long. Less photons reach a depth at which they can scatter to the detector (below reference plane) due to additional attenuation on the way down. Less photons reach the detector on the way out due to additional attenuation on the way out. DARK (note: if scatterer is pure scatterer or very low density, the opposite effect may be observed and these flaws are treated as 'voids'.)

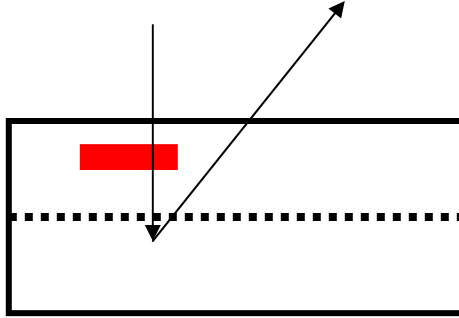


Figure 4.33. ScShI: Scatter Shallow Incident. Less photons reach a depth at which they can scatter to the detector (below reference plane) due to additional attenuation on the way down. DARK

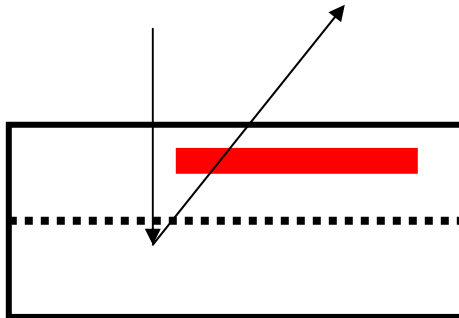


Figure 4.34. ScShE: Scatter Shallow Exit. Less photons reach the detector on the way out due to additional attenuation on the way out: DARK

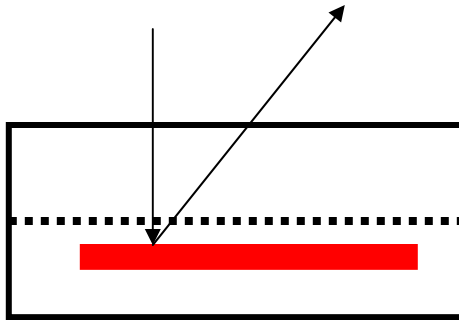


Figure 4.35. ScDL: Scatter Deep Long. More photons are scattered at a shallower depth: BRIGHT

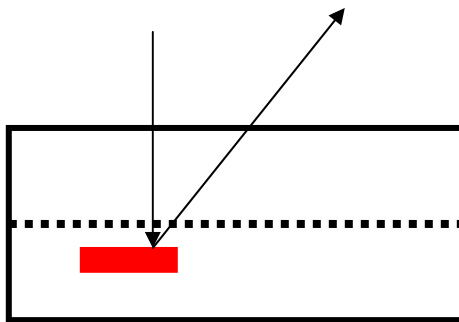


Figure 4.36. ScDI: Scatter Deep Incident. More photons are scattered at a shallower depth: BRIGHT

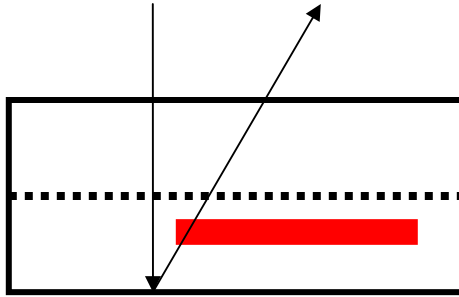


Figure 4.37. ScDE: Scatterer Deep Exit. Additional attenuation from denser material on the way out: DARK

The six scenarios considered with an absorber type flaw result in photon paths identical to those for the six scatter type flaws depicted above and are, for the sake of reducing unnecessary redundancy, not shown. Flaws of dense absorber material will always produce a dark image because whether the dominant process is transmission or reflection dense absorber materials always decrease intensity relative to no flaw.

As the figures above indicate, the relative intensities, high or low, are a primary result of the differential in attenuation provided by a flaw. The mechanisms by which a flaw can perturb the degree of attenuation, as illustrated above, include both primary attenuation differences resulting from the portion of the flaw traversed by the photon field (incident and/or exit) as well as secondary differences resulting from the effective translation in scattering depth, either deeper (void) or shallower (scatterer), resulting from the presence of a flaw. Besides changing the path-length (and consequently the degree of attenuation) of an exiting photon beam, translating the scattering position (in depth) changes the solid angle subtended by the detector and thus produces second order effects on the photon intensity reaching the detector.

The scenarios presented above are first scatter simplifications meant to aid in the understanding of important contrast generating mechanisms and physical processes occurring within the imaging modality. In real world applications, results deviate to varying degrees from these models due to a number of second order effects. Namely, geometries which select for higher order collision components and geometries which are more accurately described by a combination of two or more of the scenarios described above rather than just one. In these situations, bright and dark images as well as expected absolute contrast become very sensitive to flaw, target, photon beam, and detector characteristics and dimensions. Thus, while these scenarios accurately describe a wide range of true applications, there are many which are not perfectly described by this very simplified one scatter linear model.

Further support of this model is provided by the agreement, between predictions based upon rough analytical calculations, experiments, and MCNP5 simulations, of the percent contrast for the simplified scenarios described above. The percent contrast (relative to a control no flaw scenario) for each experimental, analytical and MCNP5 simulations for a few of the scenarios is listed in Table 4.1 below. Several important differences between the calculations, MCNP5 models and experimental results should be noted however. The transport model, upon which the calculations are based are 2-D geometry and only roughly approximate the real world 3-D scenarios. Additionally, for ease of calculations, the impinging photon beam is treated as monoenergetic. The experimental results also include real world uncertainties and efficiencies that neither MCNP5 the calculated results consider.

Table 4.1. Relative contrasts as calculated and observed experimentally

Configuration	1 scatter	MCNP5	Experiment	Bright/Dark Agreement
VDL*	33.8%	22.3%	Bright	Yes
VShL	54.2%	29.7%	Bright	Yes
VDE	15.9%	17.1%	Bright	Yes
VDI	-22.9%	-21.1%	dark	Yes

\* 2.54 cm radius NaI detector 2.9 cm from sample surface, 9 cm centerline-to-centerline from impinging photon beam. 0.15 cm high void channel flaw 0.65 cm deep, 1.5 cm collimator extension.

\*\* MCNP5 data has error of less than 1%.

### **Collimation trends (optimization)**

Both experiments and Monte Carlo simulations reveal inverse parabolic plots of contrast versus collimator extension for a wide range of flaw types and system configurations. The trend shows contrast to increase exponentially as collimation extension is increased from no extension up to a critical optimal extension length. The contrast then remains roughly constant as the collimation is increased slightly and then begins to decrease exponentially as the collimator extension is further increased. Figures 4.38<sup>26</sup> and 4.39<sup>28</sup> are plots from previous publications of MCNP and experimental data, respectively, and both reveal this trend.

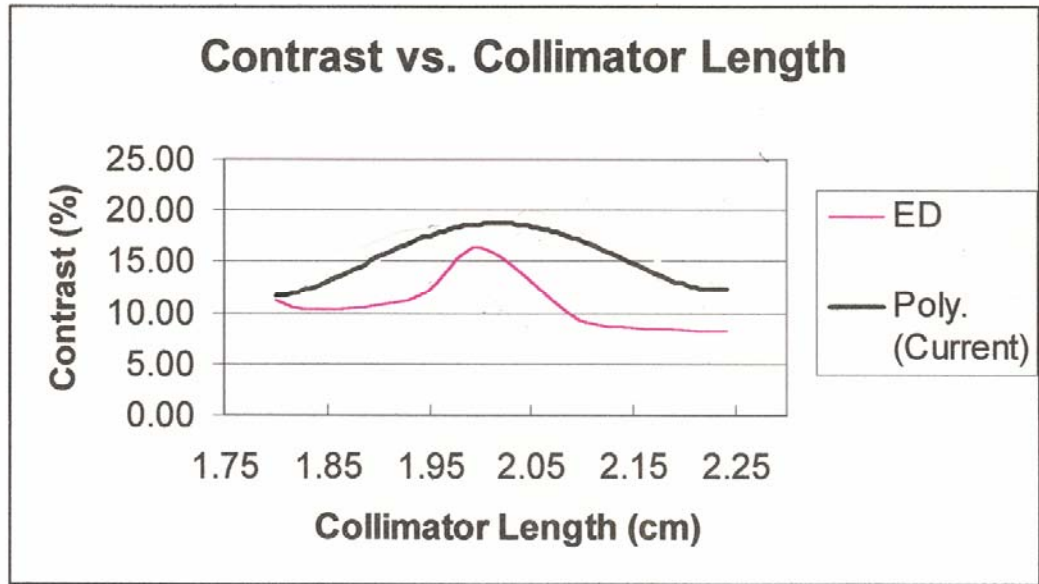


Figure 4.38 MCNP data plots of contrast vs. collimation length. This data is taken from an MCNP run with a 2 inch square detector located 5.96 cm center-to-center from the impinging beam (radius 0.5 cm). The detector height is 6 cm and the void flaw channel is 0.3 cm below the aluminum surface. Analytical calculations based upon first scatter geometry predict an optimum collimation length of 1.98 cm which matches well with the MCNP derived current tally optimum.

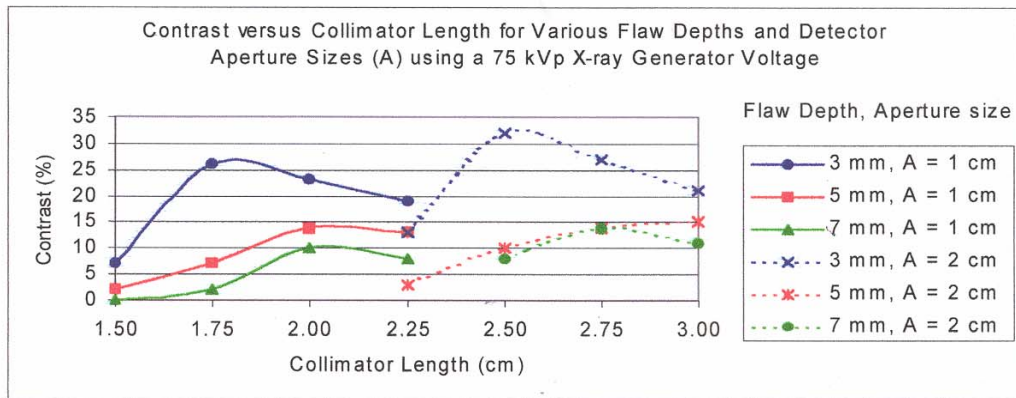


Figure 4.39 Experimental data points of contrast vs. collimation length. This data was taken experimentally and the results have not been verified in this study. The trend, however, assumes the predicted shape for contrast vs collimation curves.

This trend also supports and is well described by the simple direct scatter transport model. To illustrate, consider the simple, ideal case of a regular void type flaw of arbitrary dimensions positioned anywhere within a sample. ( Note that as the collimator is extended, for any particular geometry, the critical reference scattering plane is moved accordingly deeper and the combination will henceforth be referred to as a movement of the reference plane.)

As the reference plane is lowered from the surface of the object to the top of the flaw, image contrast should increase since the scatters in the material above the flaw contribute only to noise and thus reduce the relative contribution of the important scatters. This increase in attenuation should be roughly logarithmic (inversely exponential) since the photon is attenuated exponentially and thus each additional unit of depth into the sample contributes exponentially less photons to the signal. The trend then, as the reference plane moves from the sample surface to the top of the flaw should look approximately like Figure 4.40. This trend is derived analytically, based upon the first scatter model, and is further detailed in Appendix C.

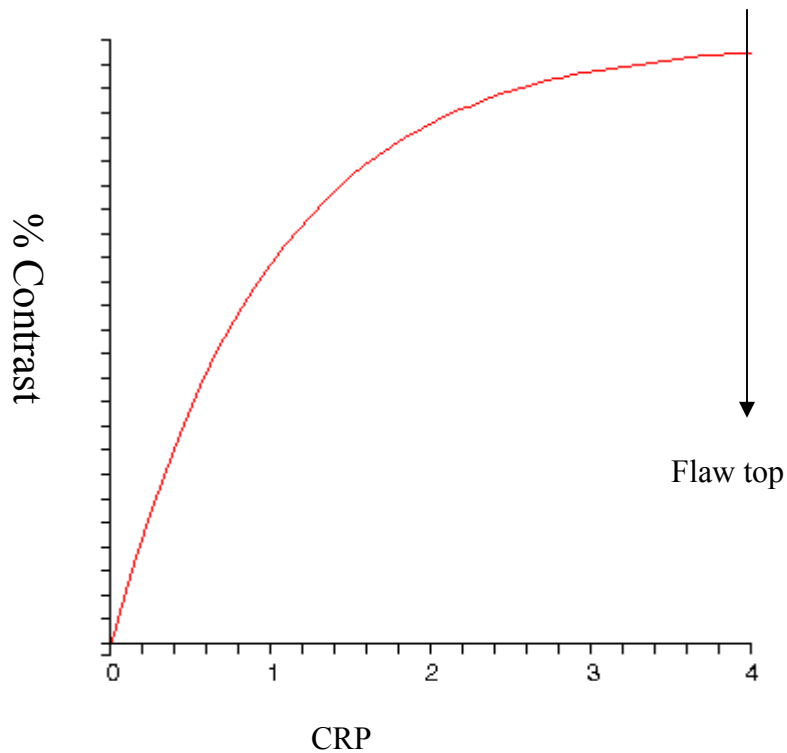


Figure 4.40 Analytically derived Contrast trend as CRP is moved from sample surface to flaw top.

As the reference plane moves from the top of the flaw towards the bottom of the flaw, the contrast should remain about constant since no scatters occur within the void region of the flaw and consequently no photons are eliminated by varying the reference plane within this region. The trend will not be exactly flat in this region however, because increasing the collimator extension within this region does affect the contribution of important multiple scattered photons and thus we expect, and observe, a slight downward slope within this region. Also, of note is that if the flaw is anything other than a void, i.e. a scatterer or an absorber, this downward slope will be more exaggerated since important scatters will occur within the flaw height region.

Once the reference plane reaches the flaw (void) bottom and is moved towards the bottom of the sample or to the maximum penetration depth of the incident photon beam,

we expect the contrast to decrease. This decrease is due to the fact that the photons below the sample, which are now being discriminated against by the collimator, are important photons in that they traverse the flaw and contribute to the signal differential. Since a relatively constant (assuming little variance in the K-N cross-section and solid angle) portion of these photons which interact below the flaw contribute to the signal, we expect and observe the contrast to taper off approximately as the signal does, i.e. - exponentially. This trend is shown below in Figure 4.41 as the reference plane moves from the flaw bottom towards the maximum photon penetration depth.

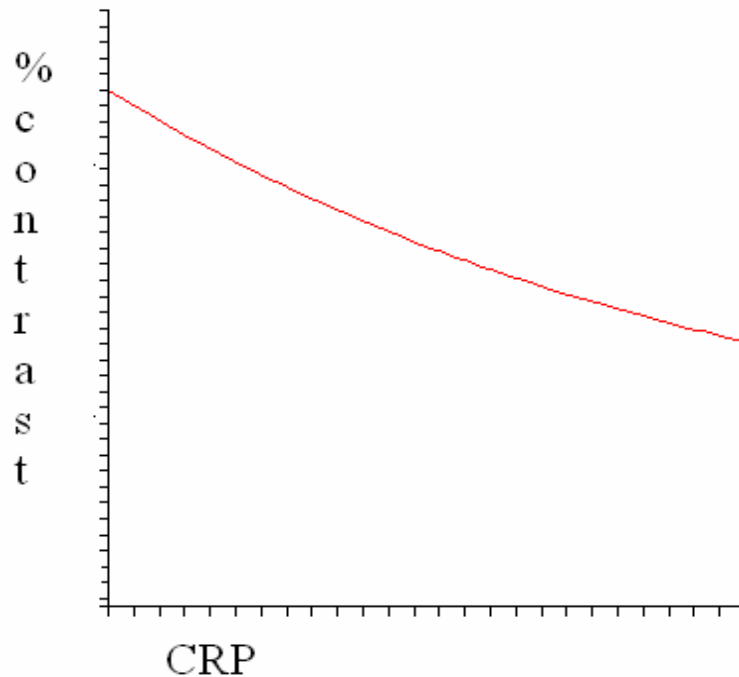


Figure 4.41 Analytically derived contrast trend as CRP moves below flaw bottom

Combining the three segments described above results in a similarly shaped curve with similar inflection points observed in both experiments and MCNP5 simulations.

Furthermore, it can be demonstrated that the peak in the curve, the optimum collimation

length, corresponds to the depth of the top on the flaw, and that the width of the plateau in the trend corresponds approximately to the height of the flaw.

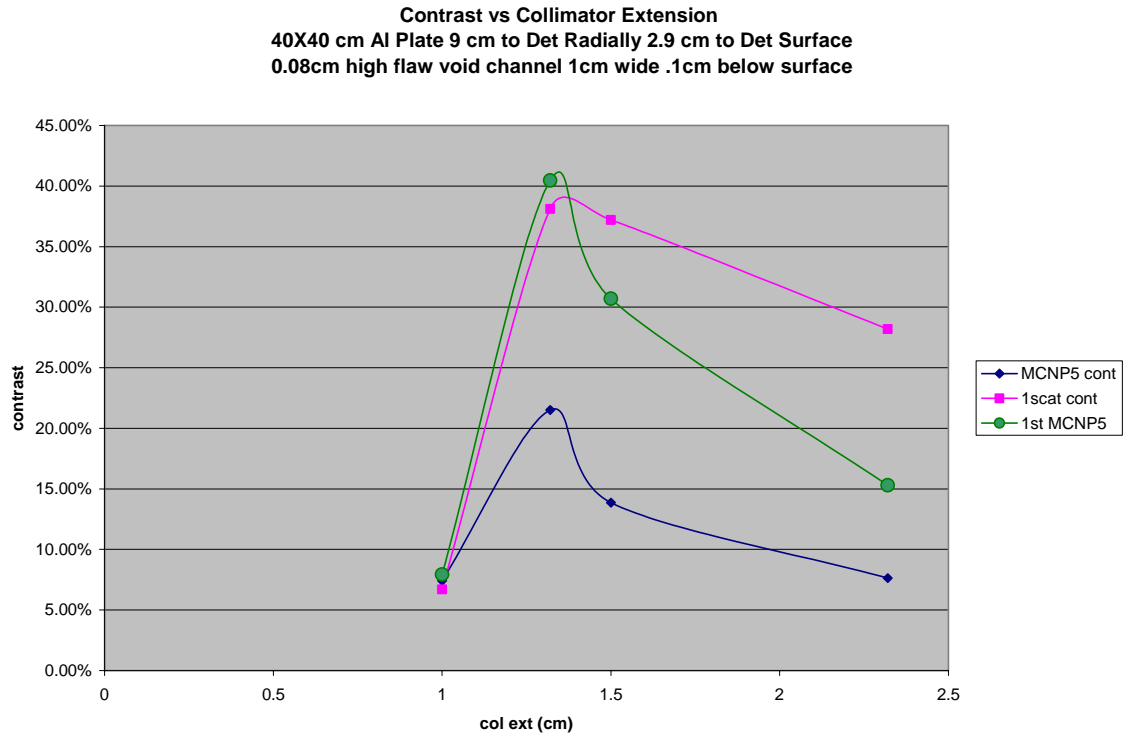


Figure 4.42 Contrast vs Collimator extension trend. MCNP5 simulations and 1st scatter model.

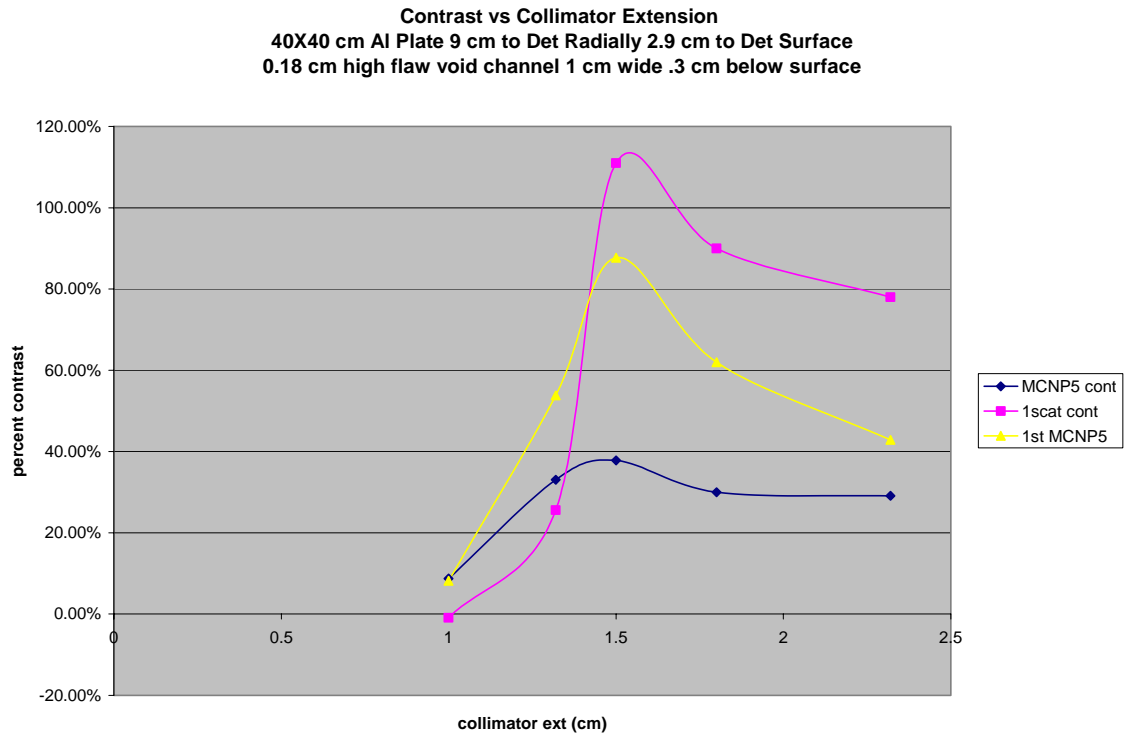


Figure 4.43 Contrast vs collimation extension. MCNP5 simulation data and 1st scatter model approximation.

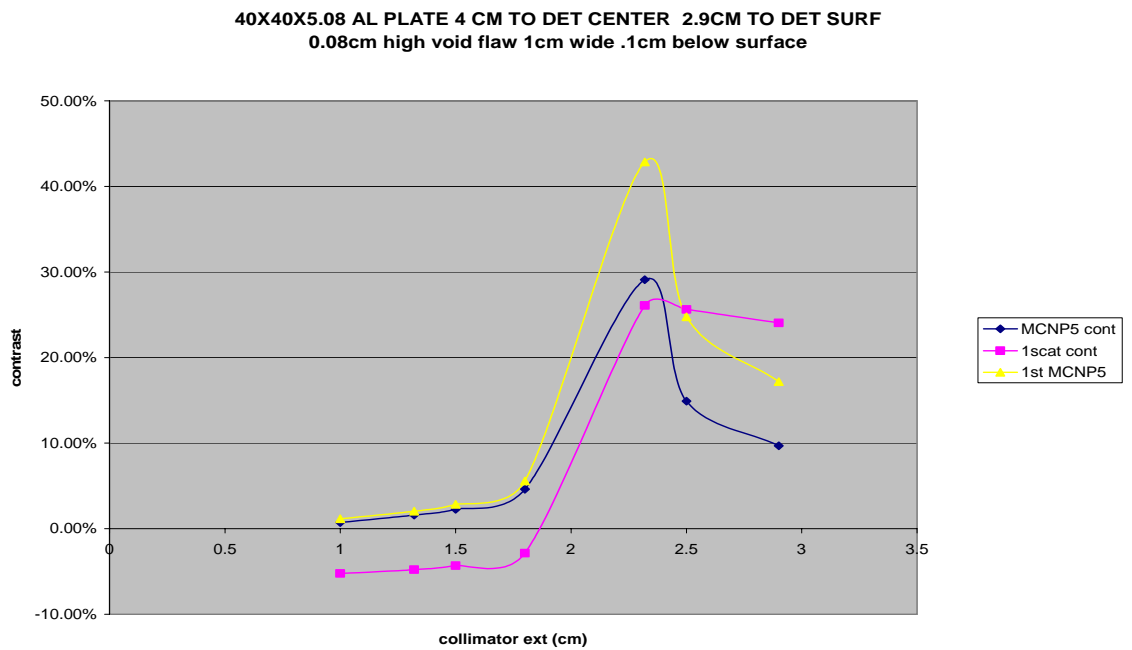


Figure 4.44 Contrast vs collimation extension. MCNP5 simulation data and 1st scatter model approximation.

Figures 4.42 – 4.44 reveal this trend for two flaw geometries for both MCNP5 data and for 1<sup>st</sup> scatter analytical calculations as described in Appendix B. Data for Figure 4.42 was acquired for a 40 x 40 cm aluminum plate, 5.08 cm thick. The detector is a NaI crystal located 9 cm centerline-to-centerline from the beam and 2.9 cm above the aluminum surface. The flaw was a .08 cm tall void channel 1 cm wide and located at 0.1 cm below the surface. The collimator extension for the trend was varied from 1 cm to 2.32 cm. The MCNP5 data plotted is from a current tally crossing the detector surface. The 1<sup>st</sup> scatter data is calculated analytically as described in appendix B. The mfp used was taken from the average mfp as calculated by MCNP5. Figure 4.43 was similarly derived except that the flaw channel was changed to a height of 0.18 cm at a depth of 0.3 cm. Geometry for data shown in Figure 4.44 is identical to that of Figure 4.42 except that detector to photon beam centerline-to-centerline spacing was changed from 9 cm in Figure 4.42 to 4 cm in Figure 4.44.

As the plots demonstrate, the trend, including inflection points (as described in appendix B) and optimal collimation length assumes the predicted shape for both the analytical calculations and the MCNP5 simulations. Further the trends, MCNP5 and calculated display identical optimal collimation length, indicating that the contrast generating mechanism is indeed a first scatter type phenomena. That is, the contrast is generated by the attenuation differences as the flaw is traversed directly by the photons. The calculated data and the MCNP5 acquired data, while displaying the same trend, do not match up identically. This is expected. The discrepancy between the first scatter analytical model and the MCNP5 data is attributed to two main factors. The first being that while MCNP5 uses an impinging x-ray beam with the true energy distribution the

analytical calculations assume an appropriate mono-energetic photon beam. Thus all properties and attenuation characteristics, which are treated as continuous in MCNP5, are treated as a one group approximation in the calculations. The other reason is that MCNP5 data is for total detected signal while the analytical model considers only 1<sup>st</sup> scattered photons. Thus, as previously demonstrated and thus expected, the analytical calculations display higher contrasts than the MCNP5 simulation because the analytical model only considers 1<sup>st</sup> scattered photons which typically have the highest contrast.

Also of note is that for Figure 4.38 and Figures 4.42, 4.43 and 4.44 (Figure 4.39 is excluded because it is used only to demonstrate the trend and the exact experimental data points have not been reproduced or confirmed in this study) the optimal overall contrast is achieved at the same collimation configuration dictated by the optimal first scatter configuration. This is true even for situations when the true first scatter contribution is below 10% of the signal (e.g. for data in Figure 4.44 1<sup>st</sup> scatter component at the optimum collimation length represents only 1.2% of the total signal). This supports the two main premises of the proposed photon transport mechanism. The first scatter component of a signal has the highest relative contrast and thus contributes a larger than expected (from overall signal fraction) contrast contribution. The significant higher order components of the signal behave essentially the same as first scatter components for the purposes of providing detectable image contrast.

A more comprehensive analytic explanation of this trend in contrast versus collimation, as handled by the transport model is included as Appendix C.

**Image pixel shifts and shadows**

Pixel shifts observed in the images between various detectors serve as an important proof of principle tool for validating the transport model. A clear angle and thus a projection is realized between the detector and the investigated object. The model predicts that, much like optics, a relative shift will be observed between images taken from different view points, i.e. different detectors. The phenomena responsible for both pixel shifts and shadows, or more appropriately, pixel shifts of shadows, are demonstrated in the following schematic labeled Figure 4.45. As the illustration indicates there are four important variables which determine the pixel shift observed by a particular detector. These include the thickness of the sample (or the penetration depth of the effective impinging photon beam), the depth of the flaw within the sample, the position of the detector (both x and y components) and the collimation extension past the detector surface. In Figure 4.45 these variables are labeled as  $t$ ,  $d$ ,  $R$ , and  $c$ , respectively, and the shift in shadow relative to the true flaw location is given as  $s$ .

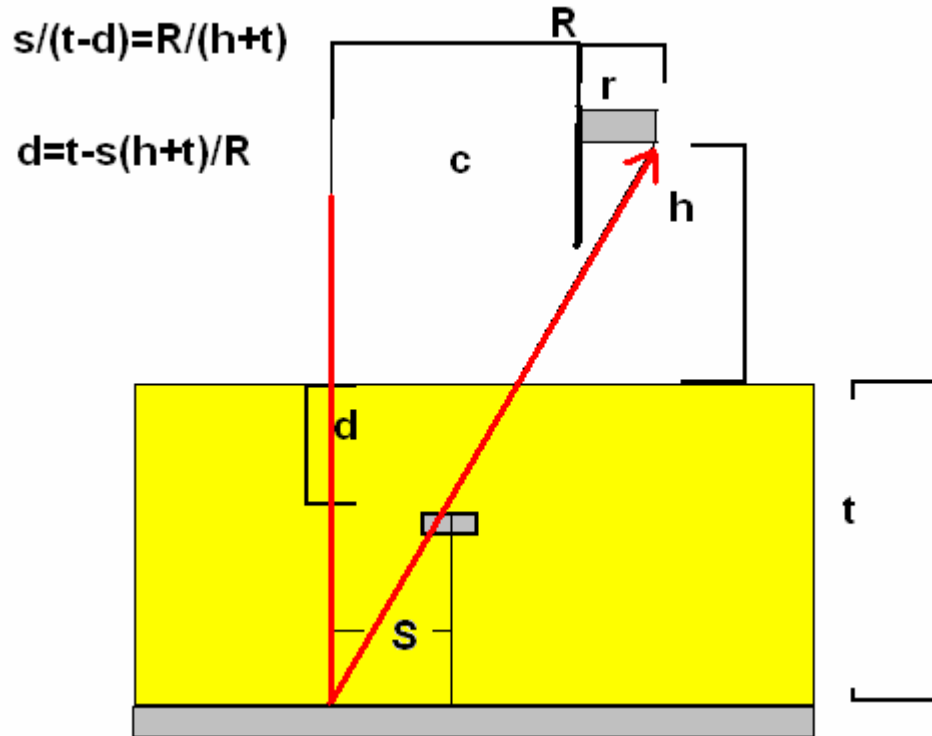


Figure 4.45 Geometrical considerations for shadow pixel shifting relative to detector position.

The following set of images, Figures 4.46 and 4.47, demonstrate, according to the above schematic, the shadow pixel shifts as observed by the various detectors. In each image, the arrow points in the direction that the effective shadow is cast. This is away from the position of the detector. That is, the shadow image is formed when the flaw is between the incident beam and the detector, thus the image appears on the opposite side of the flaw as the detector. Thus the arrow points from the detector position towards the beam.

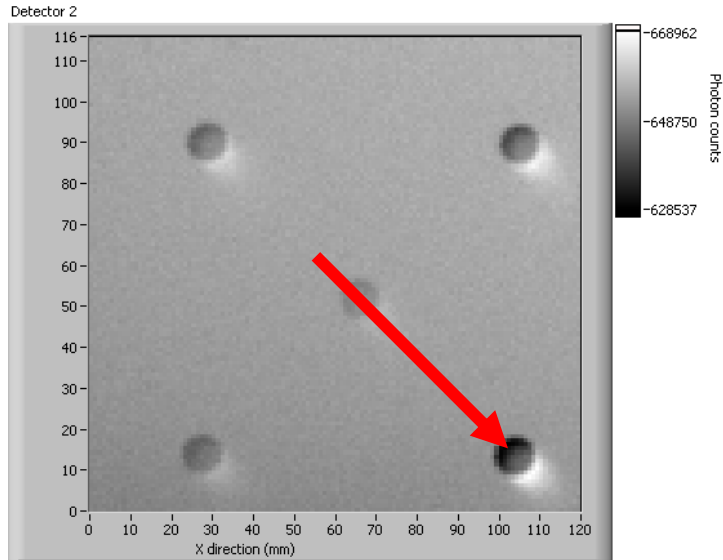


Figure 4.46 Bright shadow cast by void in Al seen by detector in lower right hand corner.

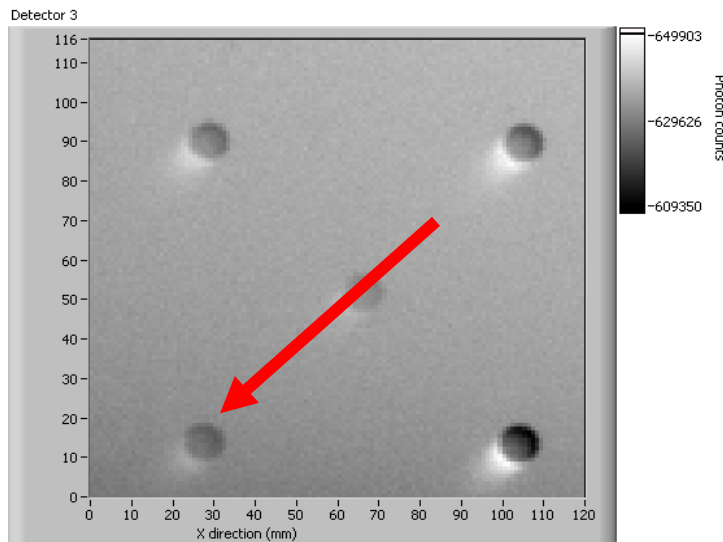


Figure 4.47 Bright shadow cast by void in Al seen by detector in lower left hand corner.

### Signal intensity

Total signal intensity in the RSD imaging modality is observed to decrease markedly with increased collimation. Considering the exponential attenuation of the incident signal this should be expected based upon the same arguments presented above

in the collimation extension section. As collimation is increased and the critical scattering reference plane is consequently moved deeper into the sample, more of the scattered signal is being discriminated against. As the scattered signal varies as interaction rates which vary with incident photon flux, the characteristic exponential attenuation is also observed in the signal intensity decrease with collimation extension.

### **Applications and Limitations**

To date, RSD imaging modalities have been successfully applied to various materials including, SOFI foam, aluminum, plastics, landmines buried in soil, concrete, drywall, and reactor insulation. Each of these materials possesses unique interaction and attenuation properties and presents specific important flaw types. Therefore, each specific imaging task represents its own unique problems and inherent limitations.

## CHAPTER 5 BACKSCATTER FIELD DISTRIBUTION AND DETECTOR PLACEMENT

### **Backscattered X-ray Signal Profile**

The backscattered photon field is distributed according to the appropriate differential scattering cross-section. Thus, the backscattered photon distribution should be symmetric about the axis of the impinging beam. The signal profile should also be peaked at 180 degrees (direct backscatter) and sinusoidally taper off towards a minimum at 90 degrees. The sharpness of the peak and speed of the tapering are functions of the incident photon energy, with the scatter profile becoming more isotropic as energy is decreased. The unmodified (i.e. – without consideration of atomic form factor) Klien-Nishina cross-section for a 55 keV photon beam is presented below (Figure 5.1) as a function of scattering angle. The backscattered photon flux through a plane parallel with the surface of foam target (w/ Al substrate) is presented below as Figure 5.2. This plot is taken from data acquired via MCNP5 simulations. The foam target in Figure 5.2 is eight inches thick with a one inch aluminum substrate. The tally plane is 1 cm above the surface of the foam. The impinging photon beam is 75 keV peak spectra with a 0.5 cm diameter. In Figure 5.2, as expected from the shape of the differential scattering cross-section, the highest backscattered photon flux is directly above the source (180 degrees scattering angle). This plot, however, represents the flux across a surface and is thus more exaggerated than the Klien-Nishina cross-section because the flux is dependent upon both the relative fraction of photons scattered into a particular solid angle as well as

the relative orientation of the reference plane to the incident photons. Since photons scattered at smaller angles (to the horizon), i.e. closer to 90 degrees than to 180 degrees across the reference plane at more severe angles (further away from perpendicular), these surfaces have less effective area and thus will display lower fluxes than the scattering cross-sections would otherwise dictate. Additionally, since the tally is taken across a plane rather than a sphere, the photons reaching the outer mesh voxels are geometrically attenuated by the  $1/r^2$  law and thus the fluxes are further reduced.

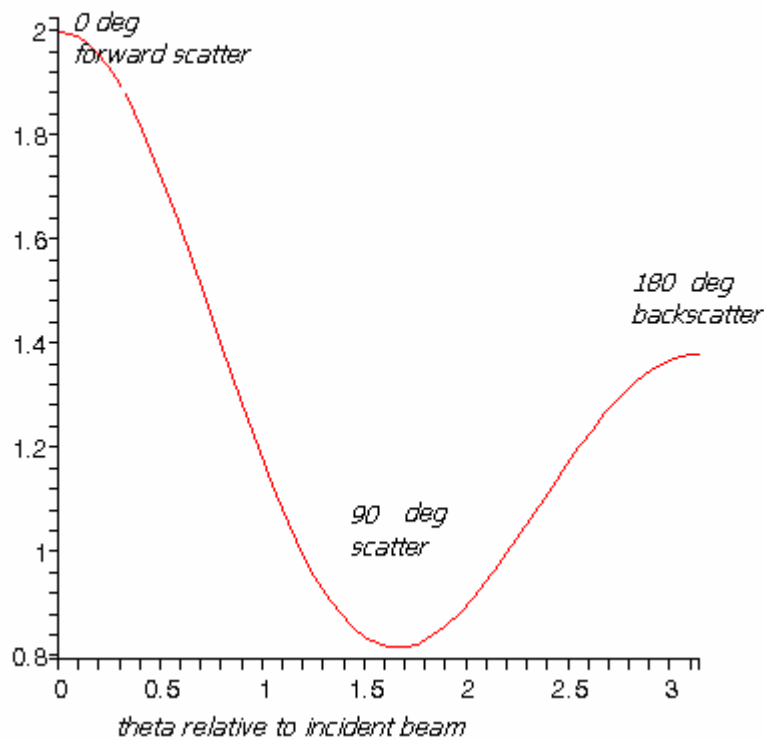


Figure 5.1 Klein-Nishina differential scattering cross-section for 55 keV photon

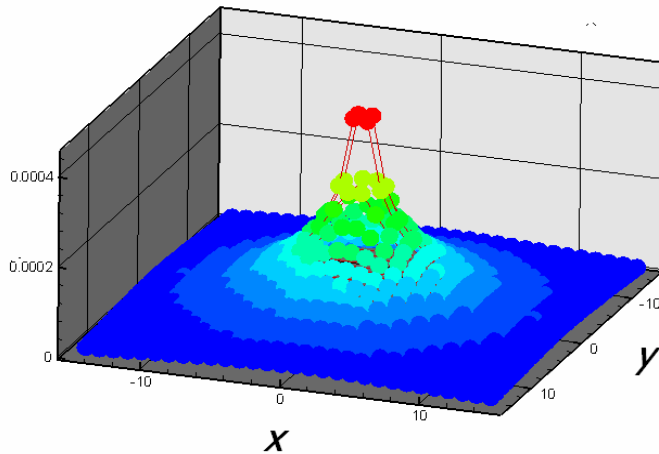


Figure 5.2 Backscattered photon flux across a plane parallel to SOFI sample surface

As the transport model indicates (chapter 4), the primary cause of a detected signal differential (i.e. – image contrast) is a change in the scattering/attenuation characteristics of the photon field as a result of a ‘flaw’ in the imaged target material. Since to a first approximation, the presence or absence of a flaw changes only relative interaction rates within a specific volume (about the flaw) and has no effect on the directional distribution of the scattered photon field, we would expect that the same signal (i.e. – same relative contrast) could be detected from any particular solid angle component of the backscattered photon field. In fact, for a perfectly symmetrical flaw in a uniform medium, this is indeed the case as illustrated in Figure 3. Figure 3 is a plot of relative differences (% contrast) in photon fluxes across a meshed tally plane oriented parallel to a target sample surface. The target, as in Figure 5.1, is a SOFI foam material on an aluminum substrate. The data for the plot is taken from 2 MCNP5 simulations. The first simulation utilizes a 15 x 15 cm mesh tally taken over an eight inch thick sample of SOFI on a one inch aluminum substrate. The second simulation is identical except that a one

cm diameter spherical void flaw is placed two and a half cm below the sample surface. In both cases the incident photon beam is 55 keV peak and the mesh tally plane is located 1 cm above the surface of the foam. The backscattered photon flux through the mesh tally for simulation 1 is shown above as Figure 5.2 and the backscattered flux for simulation 2 (with the flaw) would have an identical relative distribution. The percent difference between these two simulations is presented below as Figure 5.3. As the plot shows, relative differences in the signals are essentially the same across all voxel elements of the mesh plane. The high and low peaks observed towards the outer edges of the plot are statistically insignificant and are a result of the relatively few number of photons crossing the outer mesh elements.

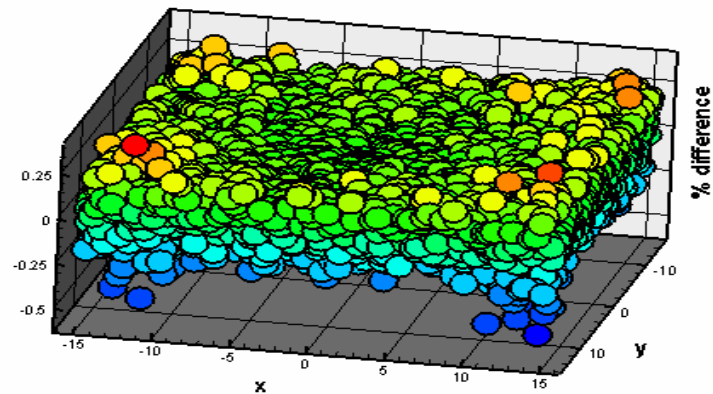


Figure 5.3 Percent difference in signal due to void flaw in SOFI as a function of scatter field component. Notice that the contrast is evenly distributed across the entire scatter field.

### Detector Placement Considerations

The ideal scenario described above in which the same relative contrast is obtained regardless of scatter component selected does not indicate that detector placement and orientation are irrelevant for image acquisition. On the contrary, in real situations, detector orientation and appropriate selection of scatter-field components are of

paramount importance in generating meaning images and accurate detection of flaws.

The reasons for this are manifold. In many real imaging scenarios, the signal perturbation caused by a flaw, particularly a deep flaw, is masked by the relative contribution of the material above the flaw. Thus the signal originating from this region must be effectively discriminating against. In the RSD imaging modality, this discrimination is accomplished by selecting the appropriate scatter component based upon geometrical collimation as shown in Figure 5.4. Simple trigonometry indicates that the further away (laterally) from the incident photon beam, and the smaller the diameter of the detector, the easier it is to effectively collimate to a specific depth below the surface of a sample. This concept, however, is checked by the fact that the signal intensity, as shown in Figures 5.1 and 5.2, is strongest closer to the photon beam. Additionally certain scanning applications necessitate tightly packed detector configurations in order to fit into specific geometries. Furthermore, most realistic flaws are not uniform and symmetrical and thus will exhibit varying degrees of differential attenuation (and thus various percent contrasts) depending upon the specific scatter field components selected for and its specific (and unique) path through the flaw and the target material. Detector configuration is also crucial because in a many situations, an imaged sample will have natural artifact and contours in it. These artifacts can, depending upon detector positioning and configuration, obscure important flaws either geometrically, or by saturating the local contrast or by casting a shadow (also geometric in nature) over an important region.

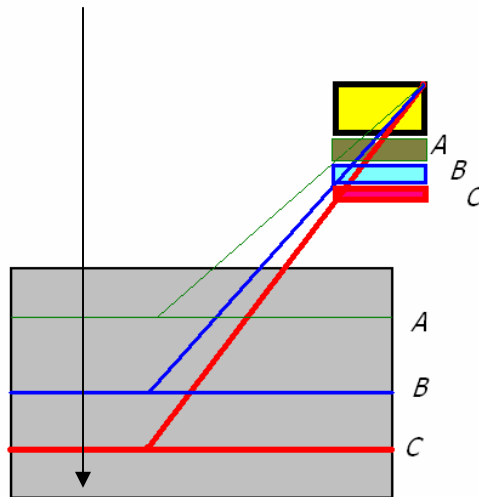


Figure 5.4 RSD focusing. Each collimation configuration A, B, C selects for photons originating at and below each specific depth A, B, C, respectively.

Thus each specific imaging task requires a unique balance to be reached between maximizing signal intensity (thus reducing scan time) and optimum detector placement for focusing. Realistic spatial constraints, which are also task-specific, must also be considered. Consequently each new imaging task presents a unique problem and requires a unique solution with tailored detector configurations for optimum image generation and flaw detection. The more freedom the detector assembly provides for varying detector configuration the easier and more effective imaging optimization becomes. A new detector assembly should allow for detectors to be able to move both laterally and vertically with respect to the photon beam and should also provide a means for the detector surface to be pivoted about an axis perpendicular to its longitudinal axis. This pivoting will allow for the detector face to always be oriented so that the important scatter field components impinge upon it normally. Consequently, the detected photon

flux will be increased, ultimately leading to a decrease in scanning time. Additionally, if the photons strike the detector normally, more of the photons which scatter at the surface of the detector will scatter into rather than out of the detector and thus more efficient energy deposition will result.

## CHAPTER 6 RSD OPTIMIZATION AND IMAGING CHARACTERISTICS

### **Optimization Principles**

RSD modality optimization is achieved with consideration given to both sample material and flaw type and configuration. The degree to which each of these commands specificity varies based upon the physical parameters such as MFP and scattering to absorption ratio of the photons interacting in the sample material as well as the relative interaction properties and orientation of the flaw. Since a detected signal contrast is due primarily to a differential in attenuation caused by a flaw, certain flaw types, such as high density absorbers and scatterers in a low density media, are detectable in a variety of configurations and thus need not be perfectly optimized for. Other flaw types such as small cracks and delaminations or slight density fluctuations are more difficult to detect and can only be done so under optimized conditions.

Variable parameters of the system include detector spacing, collimation extension and rotation, incident photon energy, and photon beam spot size. Geometric variables such as collimation and detector configurations, as previously described, function to select specific components of the backscattered photon field originating from scatters occurring in specific regions of a sample. These parameters are usually adjusted to focus a detector on an important region where a flaw is suspected or crucial to sample integrity. Photon beam spot size is directly related to the resolution required to detect a flaw. The photon beam spot size must be approximately equal to the pixel size to achieve meaningful results. Situations where the spot size is much larger than the

pixel size result in blurred images due to an effective averaging out of the region impinged upon by the larger beam. Such configurations lead to an inability to effectively detect small flaws. Since decreasing the spot size and with it the pixel size of the acquired image, increases total scan time, a balance must be reached between resolution and realistic scan time.

Photon beam energy is optimized both for flaw type and depth as well as for substrate material. The correct degree of penetration and scattering is important to image a flaw. The incident spectrum must penetrate to and scatter back from at least the depth of the flaw and also interact enough to provide a meaningful backscatter signal.

### **SOFI Foam**

The spray on foam insulation (SOFI) material provided by Lockheed Martin presents a unique imaging challenge. The SOFI is applied over a contoured aluminum substrate. The aluminum substrate contains bolts, nuts, flanges and other structural components which effectively absorb contrast away from the actual foam and thus make flaws more difficult to detect. The low density of the foam, roughly  $0.03 \text{ g/cm}^3$ , results in a large fraction of the incident photon beam penetrating all the way to the aluminum substrate. The imaging process thus becomes complicated by a strong transmission-type phenomena with an effective source distribution located at the aluminum substrate surface. Figure 6.1 depicts the two important pathways for a photon to reach the detector. Photons can either interact in the foam and scatter directly into the detector (B) or they can penetrate the foam and reflect off the aluminum substrate towards the detector (A). The relative probability of each of these pathways is a function of flaw parameters, foam thickness, incident energy spectra, and detector and collimator configurations. For high

density flaws, photons may also interact within the flaw itself and thus be scattered towards the detector. This enhances flaw contrast and greatly simplifies the imaging process, however in practical applications there is rarely a high density flaw in the SOFI material.

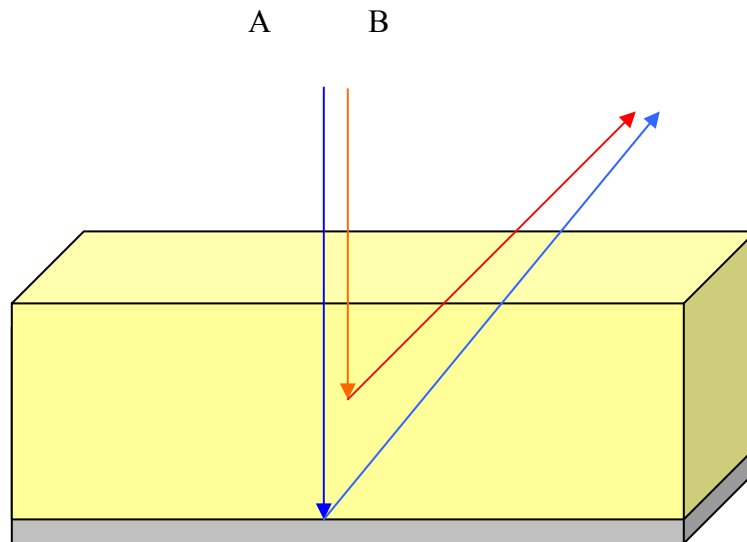


Figure 6.1 Two important paths of a backscattered photon

Figures 6.2 -6.4, below, catalog the effect of both collimation and energy on the relative detector contributions from each of these pathways for a few scenarios. The data for this plot is taken from several MCNP5 simulations. Each simulation models an eight inch thick sample of SOFI divided into four, two inch layers. The SOFI is mounted to a one inch thick aluminum plate. The parameters varied were incident beam spectra peak energy, detector to sample distance (height) and collimation extension. The data presented below comprises 6 MCNP5 simulations. Three different detector and collimator configurations were each run at 60 keV and 75 keV peak spectra. The detector and collimation configurations are described in the plots below as X-Y. In this format, X

describes the distance from the NaI surface to the SOFI surface (in cm) and Y describes the collimation extension (in cm) past the NaI surface. The absence of a Y indicates that the collimator is flush to the NaI surface. Thus, the three geometries simulated: 5.14, 5.14-4 and 1.14, describe 5.14cm from NaI to SOFI with flush collimator, 5.14 cm from NaI to foam with 4 cm collimator extension and 1.14 cm from NaI to SOFI with flush collimator, respectively. Figure 6.2 is a SABRINA generated plot of the geometry and shows the numbering scheme for foam layer reference. Figures 6.3 and 6.4 plot the relative detector (energy deposition) contribution from photons having their deepest collision (thus max penetration depth) in each layer of foam as a function of collimation configuration, for 60 keV and 75 keV incident photon spectra, respectively. These plots reveal, as expected, that increasing collimation causes the contribution from photons scattered in the deeper layer of the SOFI to become more important. It is important to realize that the net backscattered photon field (for each incident beam spectra) is identical for each geometrical variation. What changes is the portion of that field which reaches the detector and thus becomes the detected signal. That is, the geometrical configuration does not change the actual backscattered field, merely which part of it we detect.

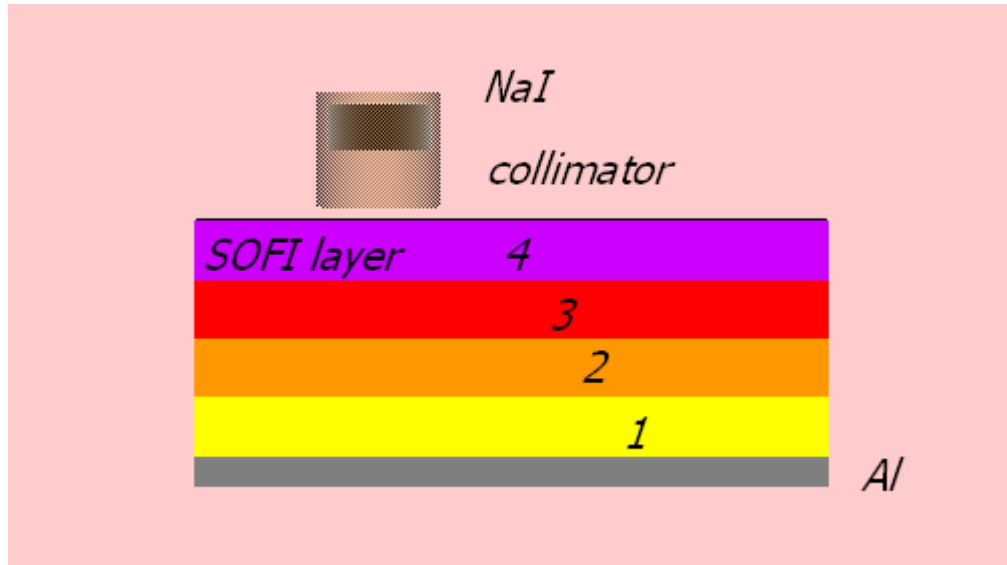


Figure 6.2 MCNP5 simulated geometry. Four, two inch thick layers of SOFI on aluminum substrate.

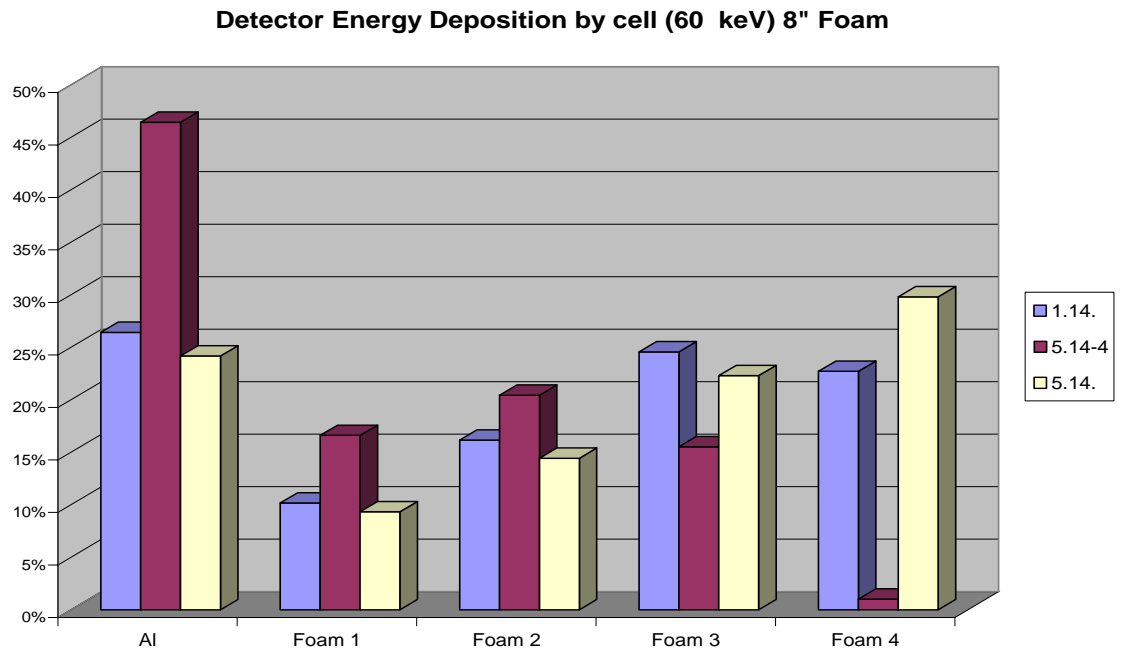


Figure 6.3. Detector contribution by cell as a function of collimation. 60 keV incident spectrum.

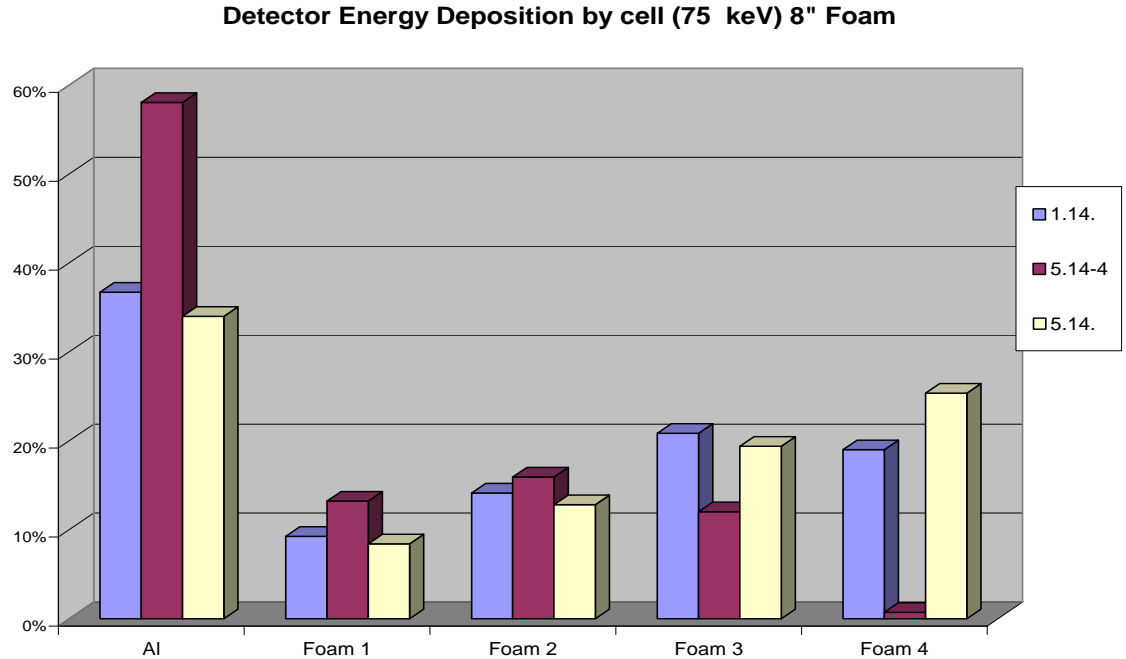


Figure 6.4. Detector contribution by cell as a function of collimation. 75 keV incident spectrum

### **Voids in foam**

Void-type flaws are the most difficult to image in the SOFI material because the relative density between void (air) and foam is very slight,  $0.03 \text{ g/cm}^3$  versus  $0.001 \text{ g/cm}^3$ . For these flaw types, optimization of the system is crucial in order to acquire meaningful images. The source of the signal difference between void and non-void regions of a foam sample is the lack of interaction within the flaw volume relative to the non-flaw region. This lack of interaction due to the void flaw has two effects: it causes less scatters at the flaw location to be directed towards the detector and it causes more scatters from lower regions, including reflection off the aluminum substrate, to occur and thus be directed towards the detector. Consequently, depending upon the interplay between these two mechanisms, dictated by collimation configuration, a void-type flaw can be imaged as either a bright or a dark region. That is, the system can focus on either

the weaker scatter field returning from the flaw region or the stronger scatter field returning from below the flaw region. This is completely determined by collimation configuration. If the flaw is above the CPR, then the scatters occurring at the flaw site and above are discriminated against and thus the dominant mechanism is the increased signal originating from below the flaw. Again, the reason for this increased signal is the lack of attenuation caused by the flaw, effectively transporting more photons deeper into the sample. If the flaw is below the CRP then (because of exponential attenuation of the signal) the dominant contrast generating mechanism is the lack of scatters occurring at the flaw site. In this situation the flaw is imaged as dark. In an uncollimated configuration, the flaw (assuming it is not too deep or too small, in which case it would not show up on the uncollimated image) will be imaged as a dark region. As the collimator is increased so that the CRP approaches the top of the flaw, the flaw will be imaged as an increasingly dark image. Once the collimator is increased so that the CRP is below the flaw, the flaw will be imaged as a bright region as the secondary (increased penetration) effect begins to be dominant.

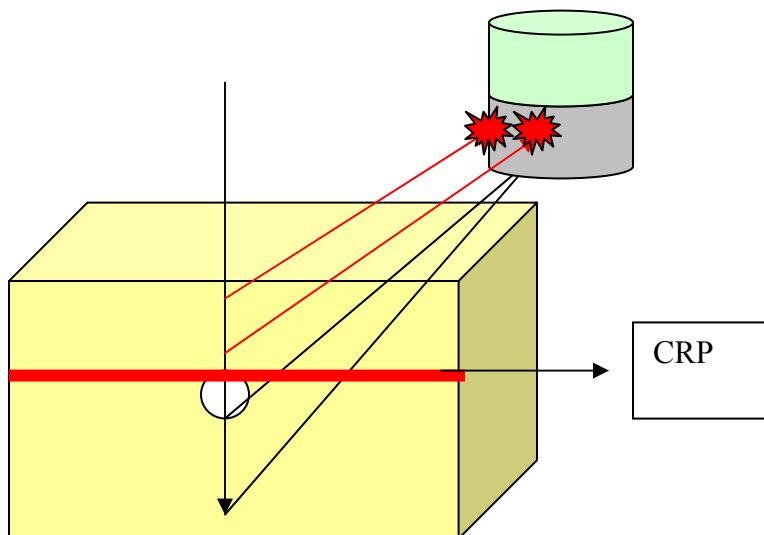


Figure 6.5 Void-type flaw in SOFI. CRP is optimally set to be just above flaw.

With collimation set as in figure 6.5, the scatters originating from above the flaw, which are identical in both flawed and non-flawed situation, are eliminated from the signal. The detected signal is thus composed of photons interacting at the flaw depth and below. In a void flaw situation virtually no photons interact at the flaw depth and thus the photon beam is transported, unattenuated, deeper into the sample by the height of the flaw. This, as mentioned above, results in a dark image of the void-type flaw. The mechanism can be thought of as either of two ways. The first idea is that, relative to the non-flawed sample, there are less interactions and thus less scatters occurring at the flaw region and thus there is a weaker signal coming from this region. The second concept is that the photons that do not interact at the flaw depth interact instead at a distance deeper into the sample, and this, relative to where they otherwise (in a non-flawed sample) would have interacted, they have a longer path and thus experience greater attenuation

upon exiting the sample towards the detector. This represents the optimum configuration for imaging void-type flaws in SOFI. Over-collimation and relying upon the secondary increased signal (bright image) is not as effective since it represents a significantly weaker signal.

The following Figure 6.7 illustrates several void type flaws imaged in foam at the indicated depth and collimation settings. Since a void is usually imaged as a dark region and is effectively filtered out once the critical scattering reference plane is below it, it is believed that the dominant effect which leads to detection of flaws is their lack of scattering rather than their increased transmission. If, however, a void in SOFI is sufficiently large and collimation is properly configured, the increased transmission effect can be observed and a void flaw will be imaged as a subtle bright area. This can be seen below in Figure 6.6. This figure represents a foam calibration panel (Appendix D). In this panel the upper two holes are at substrate level (eight inches) and the lower two holes are at mid-plane level (four inches) below the foam surface. In each of these images, dark regions represent flaws below the CRP and bright regions represent flaws above the CRP (over-collimated) as discussed above.

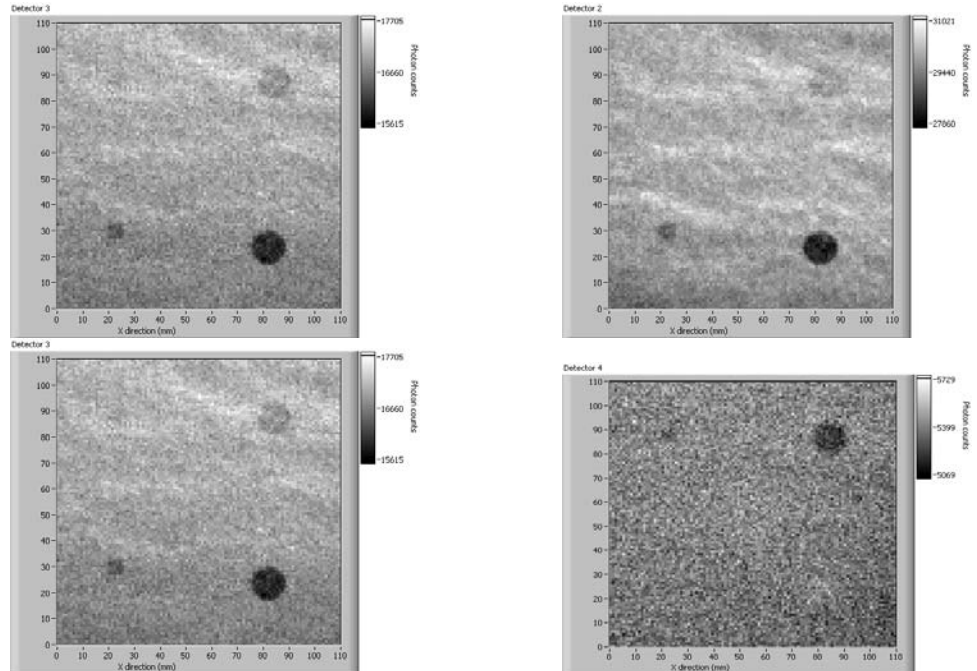


Figure 6.6 Images of foam calibration panel with varying degrees of collimation. Collimation increases clockwise from lower left.

In Figure 6.7, below, the scattering phenomena caused by a void-type flaw in SOFI foam are shown. Scatters which occur above the flawed area are identical in either flawed or non-flawed cases and thus contribute to noise if they are not filtered out. The area between the two thick (dark) converging arrows, originating at the void, represents the region from which no scatters occur. The lack of scatter from this region due to a void-type flaw represents lessened detected signal intensity and thus a dark image of the flaw. These un-scattered photons will, however, suffer a collision somewhere deeper within the foam. From these deeper collisions, the photons not only see the detector through a smaller solid angle (to a first approximation due to increased distance), but also must travel through more material on the way towards the detector. The path difference caused by a void on a photon which consequently interacts deeper within the sample is shown by the two (color) thin arrows.

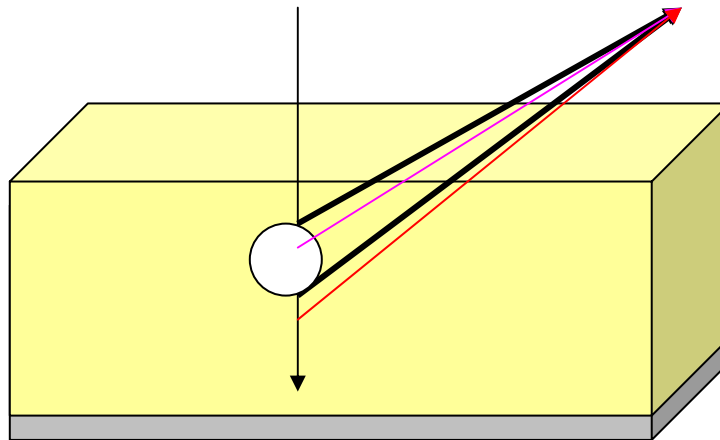


Figure 6.7 Void-type flaw in SOFI. Thin arrow demonstrates the path difference induced by the lack of scatter at the void site.

### **High density absorber and scattering type flaws**

Detection of high density, especially absorbing, materials in a SOFI-like substrate is a trivial task. The density of such materials, lead or aluminum for example, is several orders of magnitude larger than the substrate and consequently stands out as a contrast regardless of the configuration setting. The detector responses to optimization routines and various geometrical configurations used for high density flaw detection is, however; of significant academic interest as it elucidates the photon transport processes occurring in this RSD imagine modality.

Unlike void type flaws in SOFI, whose presence can often be effectively filtered out by lowering the critical reference scattering plane sothat they lie above it, high density type flaws, in SOFI, because they have strong affects on both transmission and reflection, can not be similarly filtered out. This is shown below in figure 6.8. If the collimator is set to discriminate above the blue line (labeled 1), the photons shown in blue

(top arrow) will still experience significant relative attenuation as they pass through the absorber and upon subsequent reflection (off the AL) they will be detected as a decrease in signal intensity. If the collimator is set so that it discriminates above the red line (labeled 2), the initial image will be generated by the lack of (absorber) or increase in (scatterer) scattering at the flaw location, shown in red (lower arrow), relative to the non-flawed section.

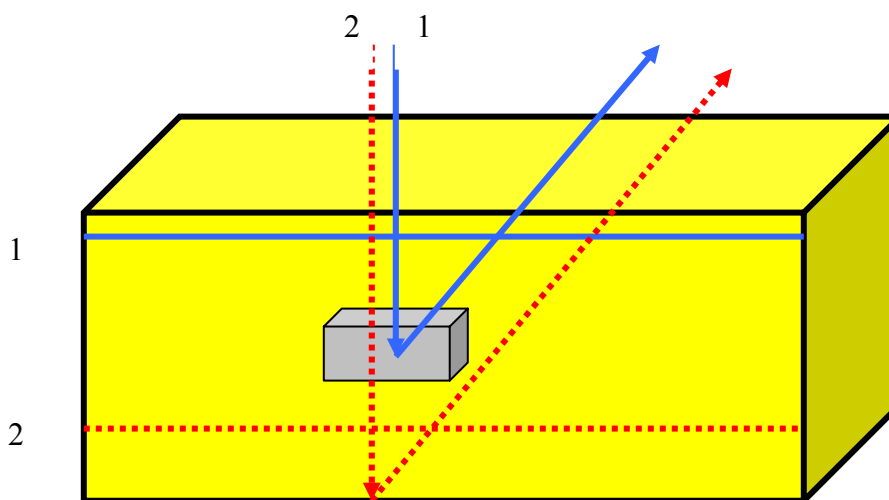


Figure 6.8 Two mechanisms (1-lack of scatter, 2- increased attenuation) for generating low intensity signal from an absorber-type flaw in SOFI.

The dual nature of image generation and the relative importance of each photon pathway are demonstrated in Figure 6.6. This is an image of several thin aluminum inserts in a foam media. Each insert is set at a different depth. Notice that some of the inserts appear as dark and some as bright images. This is due to the phenomena illustrated above in figure 6.8. Each insert necessarily produces both images generated by the photon path represented by a solid line and the photon path represented by the

dashed, respectively. For the case of a scattering media, such as aluminum, the solid path (1) will result in an intensity increase (higher scattering) and the red path will generate an intensity decrease (higher attenuation). When under collimated (shown in by the solid scattering reference line) the solid (high intensity scattering) effect is dominant. This is due mainly to the fact that it represents a shorter total path through the material and thus is attenuated less. Other factors increase this effects' dominancy including the reduced solid angle subtended by the detector, the additional scattering that must occur for the dashed effect, and the high scattering to absorption ratio of aluminum. When the collimator is set such that the red line now becomes the critical scattering reference plane, the bright increased scattering signal no longer reaches the detector. Under these settings, the dark, low intensity, signal due to the increased attenuation as the beam passes though the flaw is now observed. In the figure below, Figure 6.9, the collimator is positioned such that the critical reference scattering plane is located between the aluminum inserts. The bright flaws lie below the plane and thus increase scattering towards the detector and the dark flaws are shallower and lie above the plane and thus represent only an increase in attenuation.

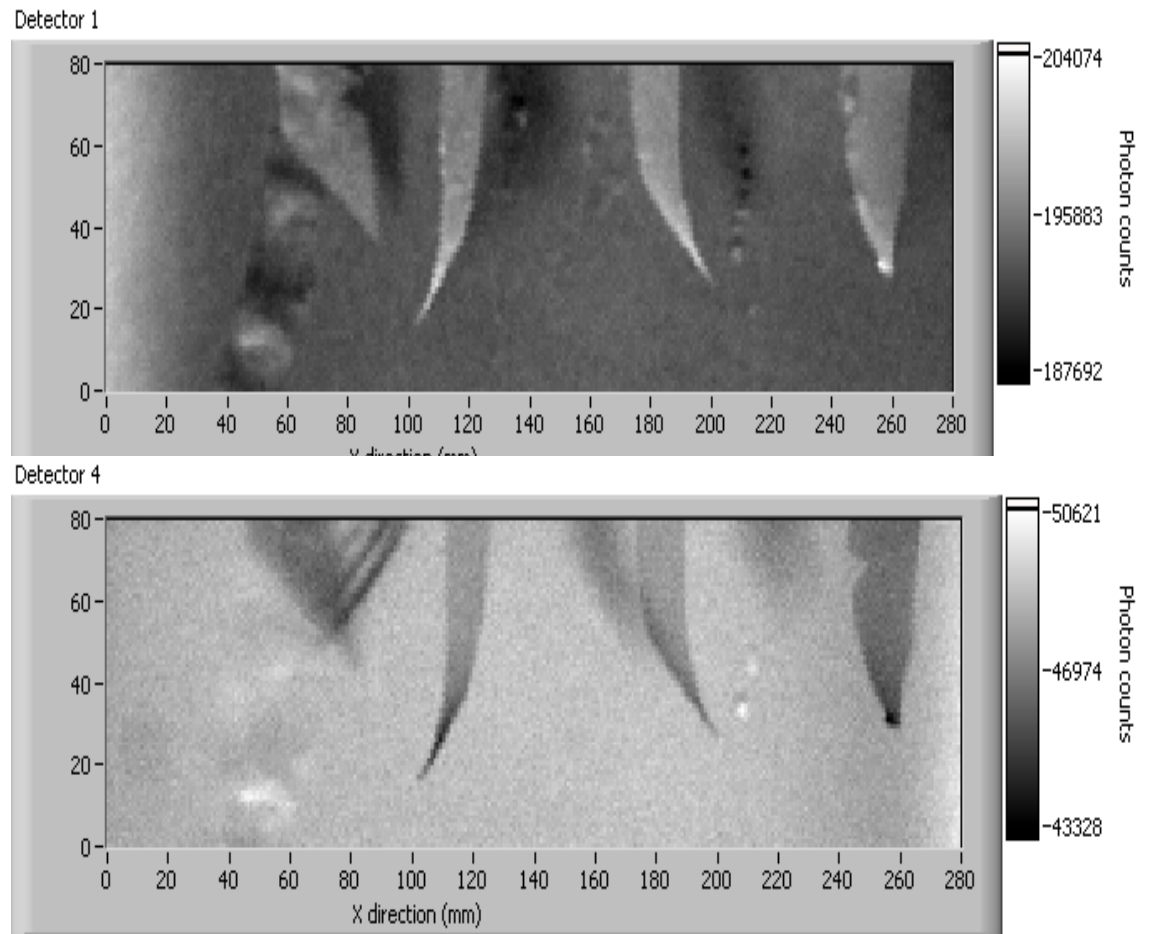


Figure 6.9 Scan of depth staggered aluminum inserts in SOFI. Bright inserts are above CRP and dark inserts are below CRP.

### Shadows

Shadows observed in images acquired of the foam material are a result of high density flaws in the material through which an exiting photon traverses on its way back to the detector. These are different than the dark images observed from over-collimated images of high density flaws. The over-collimation produced dark images, as described above, are a result of attenuation of the primary photon beam before it scatters back towards the detector. These images occur when the incident beam impinges directly

above the actual flaw. Dark shadow images, on the other hand, are produced by the scattered photon beam on its way toward the detector. These images are displaced by a distance dependent upon the detector geometry. Since these shadow images result from photon exit path attenuation, they can not be filtered out by collimation. The mechanism describing both the shadow phenomena and its relative displacement is illustrated below in figure 6.10. In this schematic, the double arrow indicates the shift between the position of the actual flaw (dashed line) and the position of the shadow image (impinging beam). As shown, shadows are not created when the beam is directly over the flaw, but rather when the flaw is between beam and detector. In this geometry, the photon beam traverses the flaw, after scattering, as it travels towards the detector.

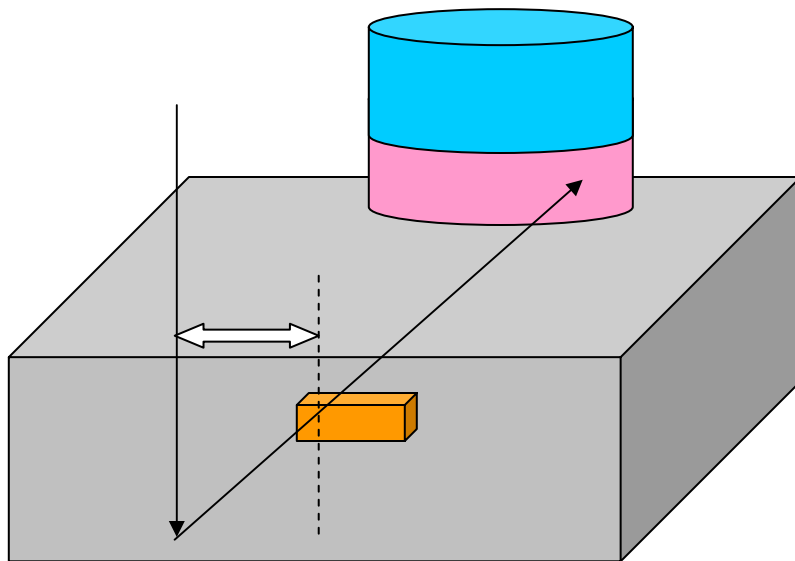


Figure 6.10. Mechanism for shadow image generation. Dashed line represents true flaw position, solid arrow indicated shadow image detection position.

These shadows can be readily observed in figure 6.9 above as well as in many of the following foam images. In the image of the aluminum inserts in SOFI, Figure 6.9, a dark shadow can be seen associated with each insert. In these images it is evident that regardless of flaw position relative to the CPR, the shadow is always a dark image.

Theoretically, based upon the proposed mechanisms, voids in foam should produce bright shadow type affects. However, experiments done with the current system have not yet been able demonstrate this. Most likely the slight change in attenuation due to the flaw on the exiting photon beam is on the order of magnitude of the inherent noise in the system and thus can not be resolved.

The following figures represent typical images acquired of the SOFI foam material. Descriptions are included to point out certain features and characteristics.

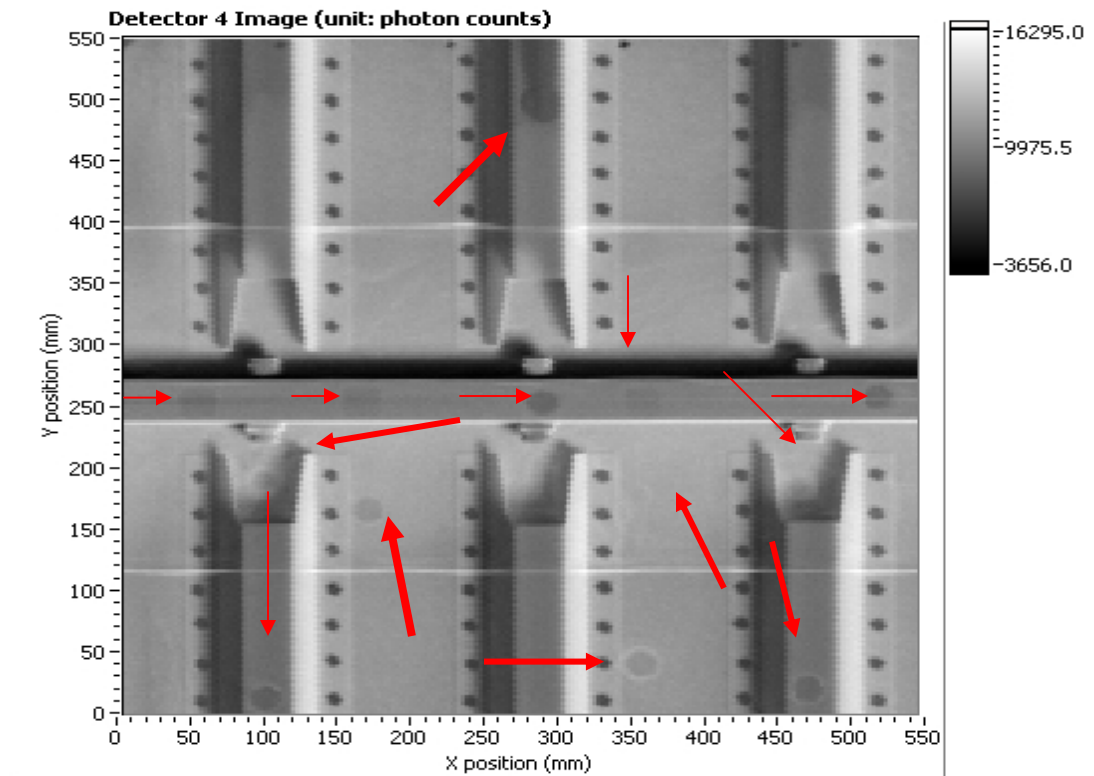


Figure 6.11 SOFI panel with contoured aluminum substrate. B&W

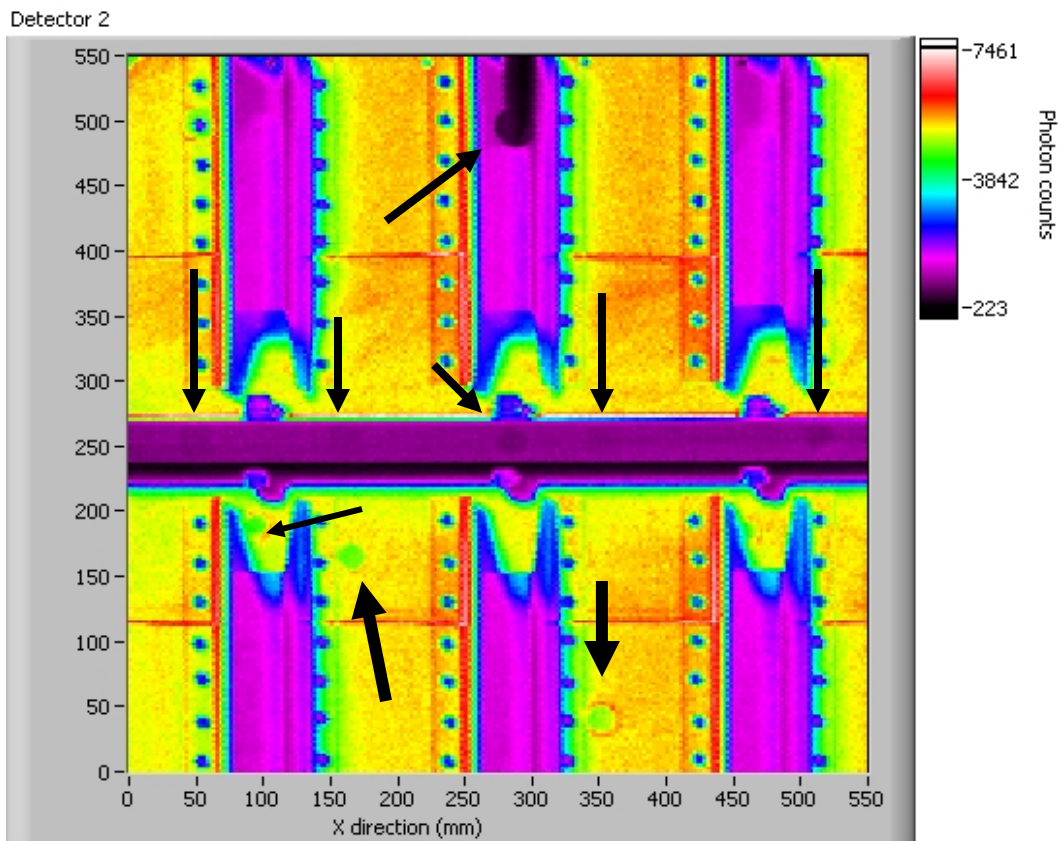


Figure 6.12 SOFI ramp panel with contoured aluminum substrate. Color.

Figures 6.11 and 6.12 demonstrate the difference in contrast between gray scale and color scale images of the same scan. Each is taken at 60 keV on ramped flange panel 2 (Appendix D) with artificially inserted flaws. Notice, however, that some flaws shown in the gray scale image are not in the color image. This is due to the different projection of the detectors. The flaw in the middle stringer, for example, is not seen in the color image because from that detector's viewpoint the aluminum stringer hides the flaw. Figure 6.13 is an image of a bolt and stringer panel under SOFI.

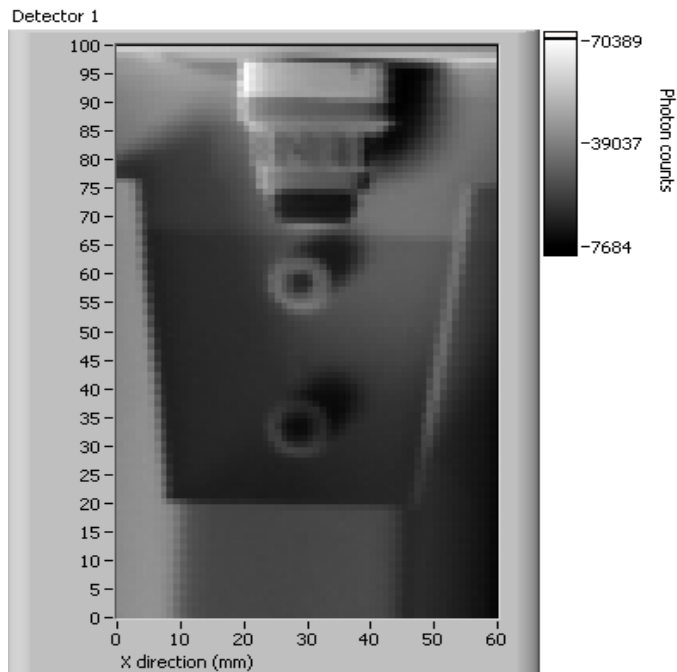


Figure 6.13 Bolt of flange panel under SOFI.

### Aluminum

System optimization for imaging aluminum objects precedes in much the same manner as for foam objects. Geometrically, the mechanisms are the same and thus similar collimation length and detector positioning must be considered. The density of aluminum, however, is orders of magnitude larger than that of the SOFI material thus the incident photon energy must be accordingly adjusted and the beam is not expected to penetrate as far. Additionally, in aluminum the important flaw types are almost always void type flaws, manifested as cracks, holes, or fractures. The photon spectrum used to investigate aluminum samples was typically 75keV peak energy. The effective mean-free-path of this spectrum in aluminum, calculated by MCNP5, is about 1 cm.

Since the density differential between aluminum ( $2.7\text{g}/\text{cm}^3$ ) and void (air  $.001\text{g}/\text{cm}^3$ ) is so large, imaging large ( $\sim 1\text{cm}$  photon beam chord) voids is easily accomplished with this modality and collimator focusing is often not necessary unless the flaw is deeper

than about half of a centimeter. These large void type flaws while often trivial to image, are of fundamental import because of the insight they lend to the imaging process and photon transport mechanics involved.

In aluminum objects, it is easier to see how important flaw alignment and detector geometry is and what effects they have on the resultant images. The same flaw depending upon configuration can be imaged as either a dark or bright region. This is related to whether the flaw provides an incident photon beam with relatively more or relatively less aluminum to travel through before reaching the detector. This phenomenon is illustrated in the following sequence of figures. The following images were taken of a 1 inch thick aluminum plate with three channels, each 1 cm wide by .1 cm high and located at 0.3 cm, 0.5 cm and 0.7 cm below the surface respectively. Each image in Figure 6.14, below, was acquired from a different detector during the same scan. The incident energy was 75 keV peak. The flaws are oriented at 45 degrees so that they either subtend a direct line between the source and the detectors (detectors 2 and 4) or they lie perpendicular to such a line (detectors 1 and 3). Detectors 2 and 4 view the flaw much as the VDL scenario described in chapter 4. In this configuration, the flaw is imaged as a high intensity, bright region because, the shadow effectively overlaps directly the flaw so that the combined entry and exit path of the photon, due to the presence of the void channel, represents a lesser attenuated path. The image of detector 4 is a highly over-collimated case and image degradation is obvious. In this view (detector 4) only a portion of the flaw channel is evident. This is due to the collimation induced geometry. The flaw will only be imaged as bright as long as the reflected beam passes through only the flawed channel on its way towards the detector. As the collimation

increases, the angle becomes more severe and this distance, across the increases. At a point the detector will be positioned so that the exiting photon beam goes through not only a portion of the channel but also a portion of the unflawed aluminum plate. At this point the contrast will be either lost or the flaw will be imaged as dark. This is illustrated below in figure 6.15. Essentially, when scanning a channel flaw aligned with the detector, at some point the mechanism changes from VDL to VDSH (as described in chapter 4). At this point the high intensity signal will be lost. As collimation increases and the angle becomes more severe, this changing point becomes a larger part of the flaw, much as optical shadow length increases with angle of light projection.

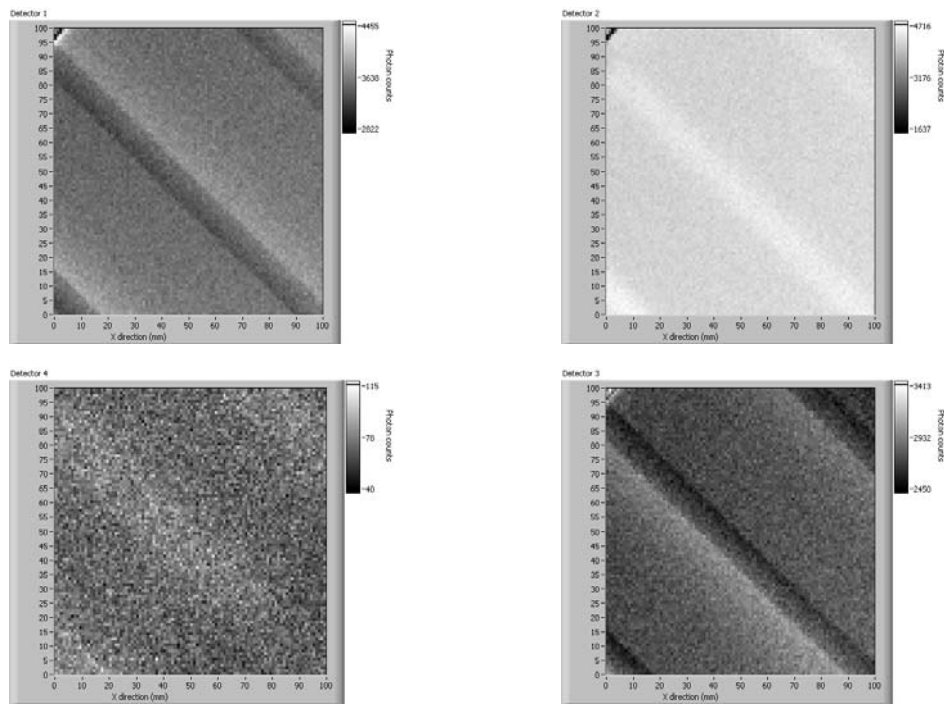


Figure 6.14 Clockwise from upper left, detectors 1,2,3,4.

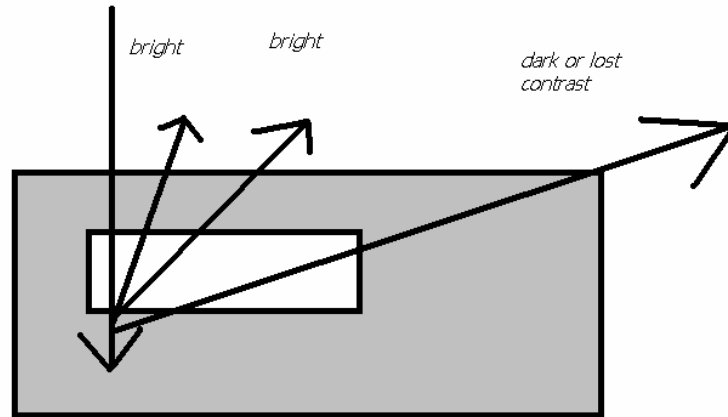


Figure 6.15. Photon exit paths across a void channel.

Detectors 1 and 3 are oriented perpendicularly to detectors 2 and 4. In Figure 6.14 the channels are imaged as dark, low intensity regions in these detectors. In this situation the channels, relative to the detector and source orientation are no longer long channels since they are not aligned along the detector to source axis. This configuration forces the flaws to be imaged by the VDSH mechanism. Also of interest is the bright shadow flanking these images from detectors 1 and 3 in Figure 6.14. These bright shadows are produced by the mechanisms previously discussed (also see VDE, chapter 4) and are located on the opposite side of the flaw as the detector is. That is, they are produced when the flaw is between the detector and the source and thus appear to be directed away from the detector.

Similar to absorbers in foam, voids in aluminum cast shadow type images. The images are similarly produced and similarly displaced from the actual flaw position. The

shadow images of a void, however, are a bright region. This bright region of high relative photon intensity is caused by the lack of attenuation afforded by the void when it is between a photon scatter site and the detector. This is the same phenomenon illustrated in Figure 6.7 above for foam. Since the shadow is caused by the void being between the detector and the incident beam, it is necessary and expected that each detector will see the shadow at a different location. The shadow should extend directly from the flaw towards the detector. This is observed and shown below in Figures 6.16. This again is an aluminum sample plate. This plate had holes drilled into it. The four images correspond to the four different detectors and the bright shadow is accordingly displaced in each one.

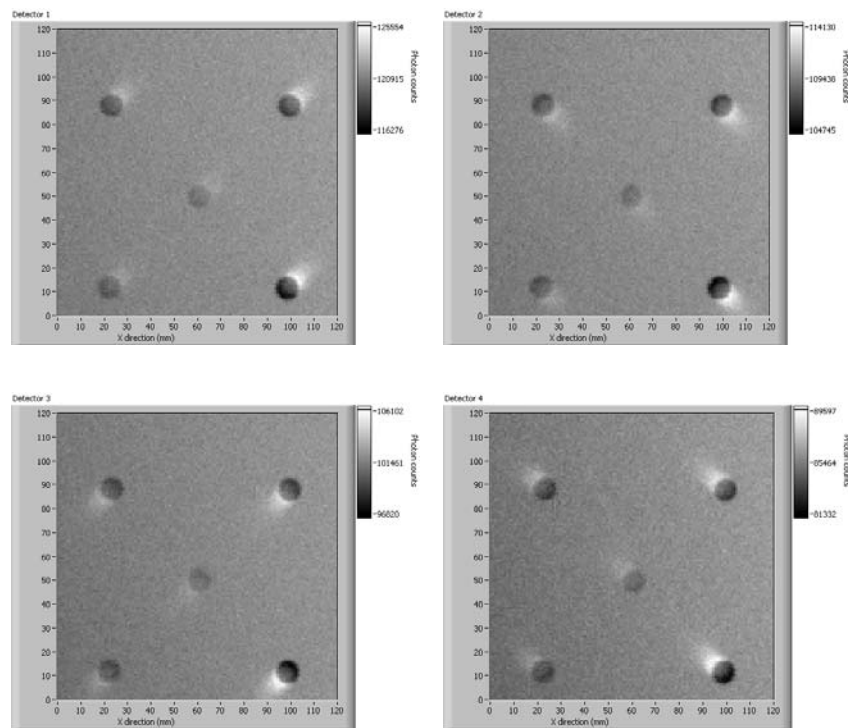


Figure 6.16 Shadow shifting with detector position

As noted in the foam example, since the shadow effect is related to the exiting photons path, it can not be collimated out. The actual image of the flaw however, since it is the incident path that affects this, can be collimated out. This is seen below in Figure 6.17. Here the collimator is set so that the critical scattering reference plane is below the deepest flaw. Thus the dark image of the flaw is not observed and only its shadow projection is seen.

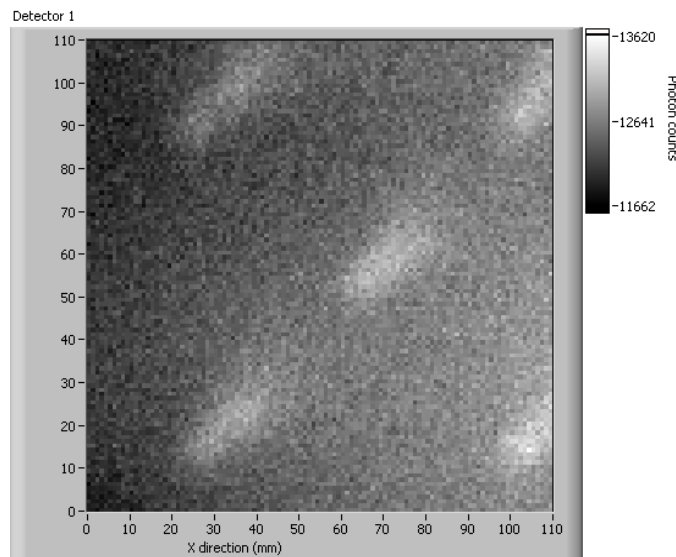


Figure 6.17 Bright shadow images of aluminum flaw plate. 5 cylindrical void flaws at various depths are imaged as bright with severe over-collimation.

The shadow effect is the mechanism responsible for producing bright images of the channel-like flaw observed above in Figure 6.14. When the detector and flaw are thus aligned, the shadow of the flaw identically overlaps the actual flaw and thus a bright image (if the attenuation deficit is significant) can be obtained. Notice that in Figure 6.11, there is a bright area at one end of the channel and a dark image at the other end. The shape and intensity profiles of the flaw shadows are directly related to the

dimensions of the flaw and the offset is directly related to the depth of the flaw. These relations, as detailed in the schematic given as Figure 6.18, are contingent upon the detectors viewpoint relative the flaw as well as to the effective penetration depth of the impinging photon beam.

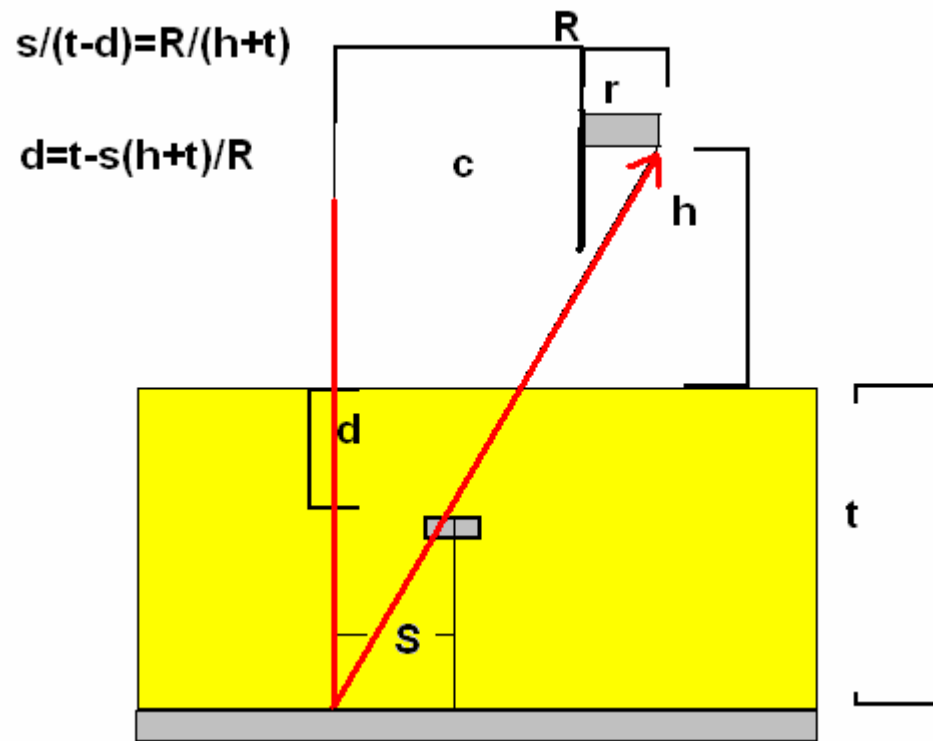


Figure 6.18 Schematic of flaw shadow and detector orientation relationship

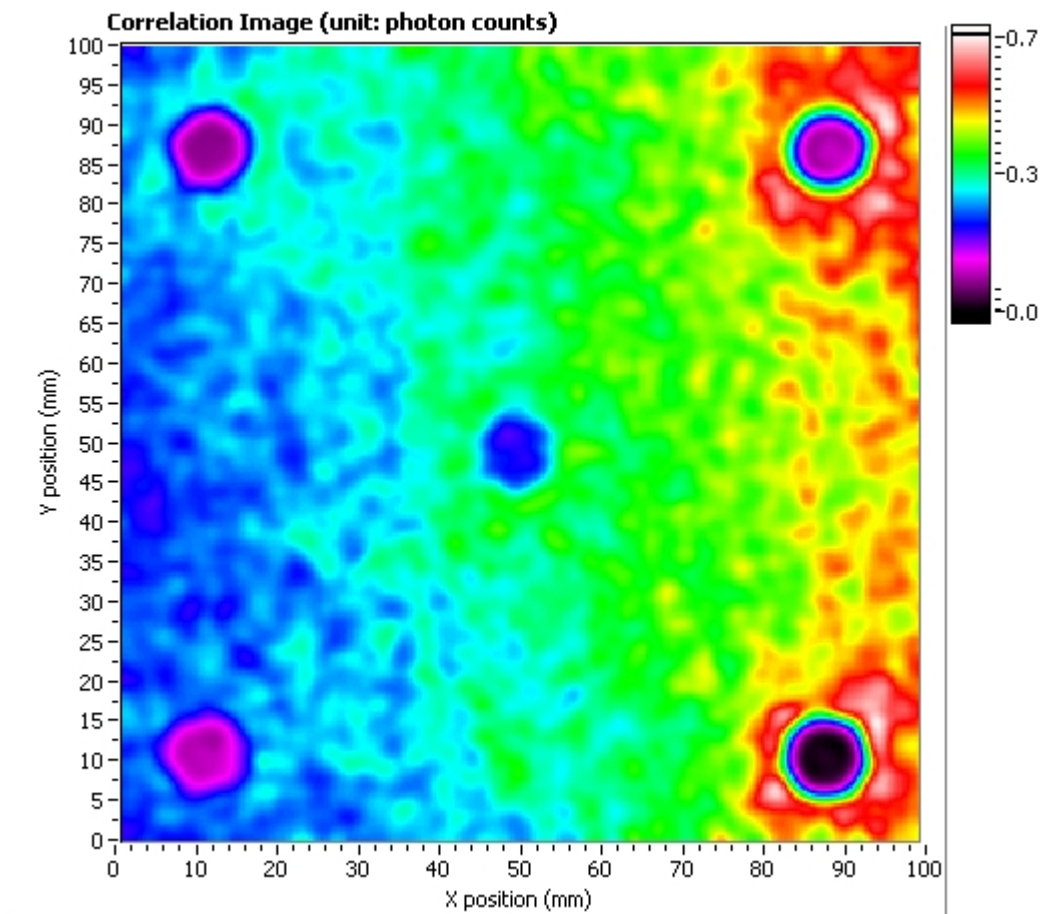


Figure 6.19 Correlated (processed) image of sample aluminum plate

Figure 6.19 demonstrates the correlation routine of the LABVIEW image processing program used to interpret the images<sup>33</sup>. This represents a simple correlation where each detector is weighted equally. If each detector is similarly collimated so that they each have a symmetric view of the imaged object (as in Figure 6.19, above) the effect of the correlation is to effectively remove shadowing effects. The long, streaking shadows observer about each flaw in the single detector views becomes a small halo around the flaws in the correlated view. This is essentially an effect of adding the contrast of each separate detector together to generate a final correlated image.

The following set of Figures, Figures 6.20- 6.22, demonstrates the effect of increasing collimation on the acquired image in aluminum samples. The target, again, is

sample plate #2 (Appendix D). Each Figure, 6.20-6.22, is acquired with from the same detector (detector 4) with the same incident energy spectrum (75 keV peak). Figure 6.20 is taken with the collimators withdrawn so that the CRP lies above the aluminum surface. This is essentially an uncollimated image. The figure shows that the shallower two flaws are imaged as dark regions with high intensity shadow regions. The next two deepest flaws are again imaged as dark regions, but this time (although barely visible in flaw C) there is no associated high intensity shadow. This is because the flaws are deep enough that the signal from the aluminum above them, since it is not collimated out, overwhelms the slight high intensity signal that originates from below the flaw. Flaw E, the deepest one, is not even observed, for the same reason.

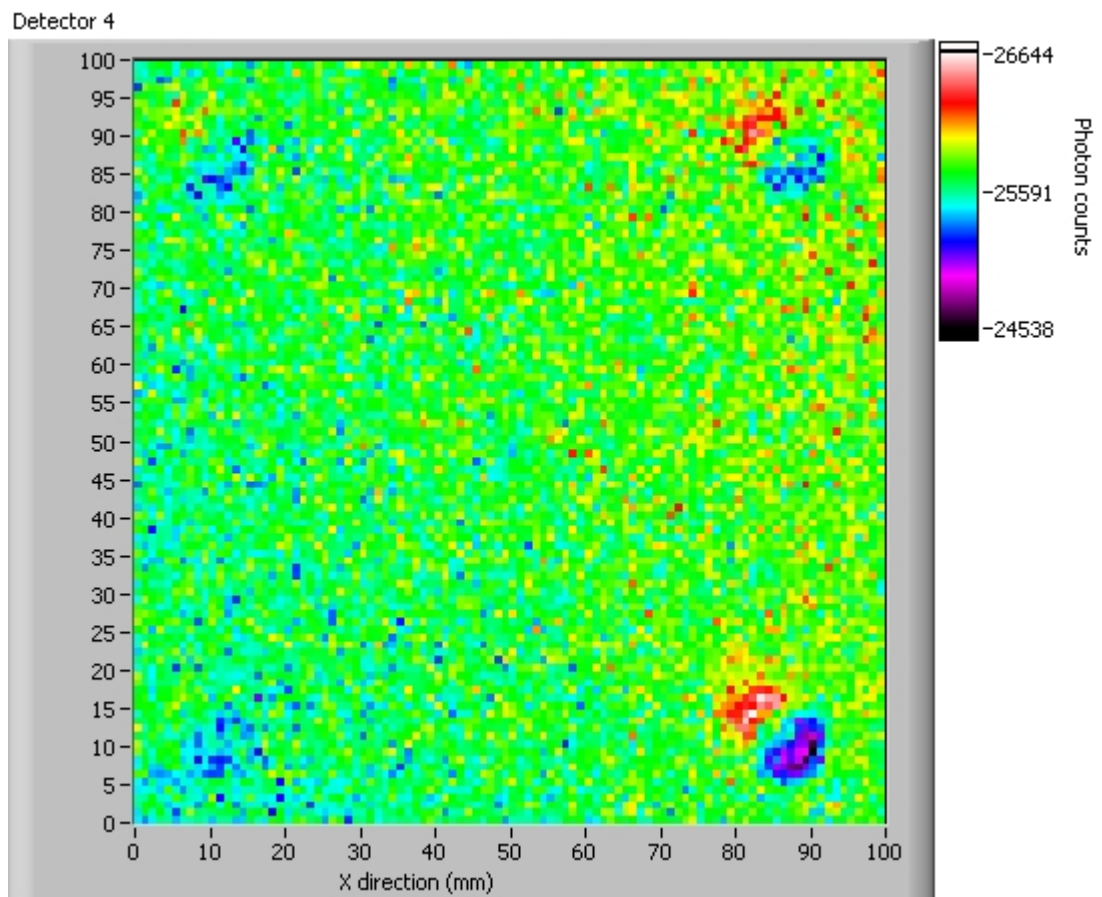


Figure 6.20 Uncollimated image of aluminum flaw plate.

Figure 6.21 is acquired with the collimator set so that the CRP is just above the bottom of flaw A. Here each flaw, as optimally expected is presented as a dark, low intensity region, with an associated high intensity, bright shadow. Notice that flaw A, which should have the most intense bright and the most intense dark image, has a barely observable dark image. This is due to the fact that the collimator is set of just barely above the bottom of this flaw. Such collimation, by discriminating against all scatters above the CRP, effectively images the flaw as if it were only as high as the distance between the CRP and the flaw bottom. The bright shadow, however, is not degraded with over attenuation since, as mentioned before, it is an effect of the emergent scattered beam, not the initial impingent beam.

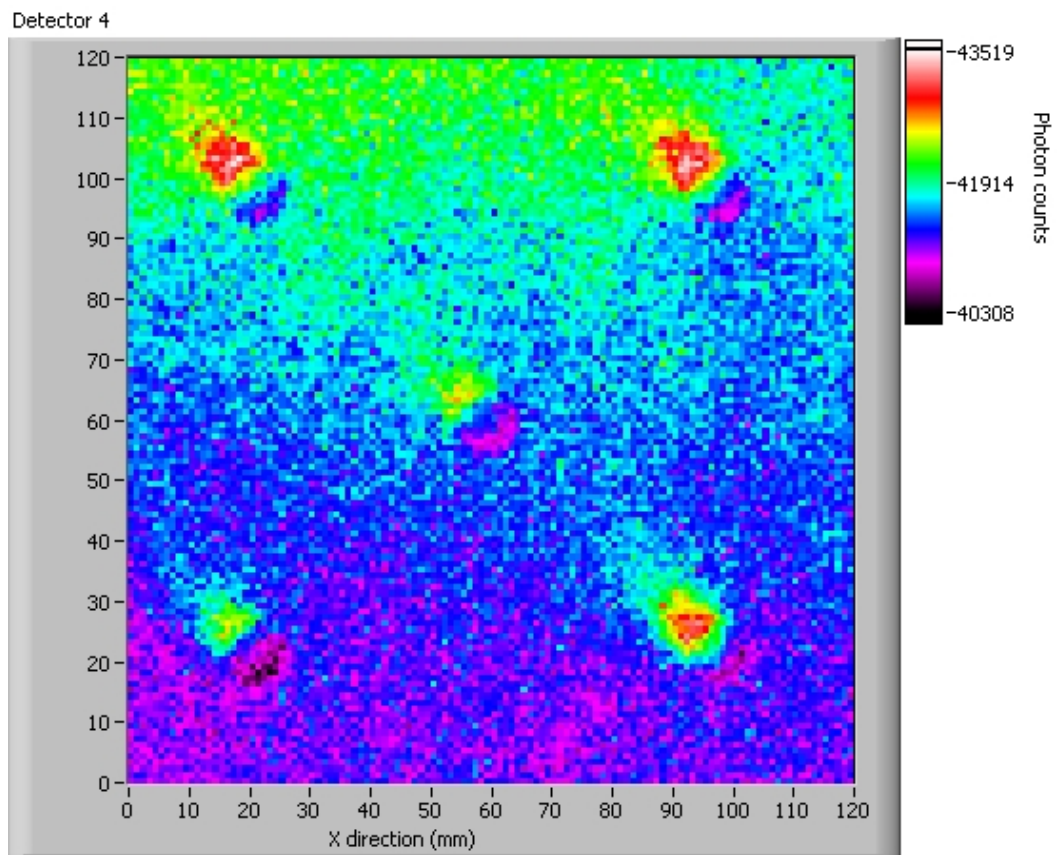


Figure 6.21 Collimation set to discriminate just above shallowest flaw. Flaw depth increases from lower right, counterclockwise to center.

Figure 6.22 shows an image acquired with the geometry severely over-collimated. In this image, the CRP is set below the bottom of the deepest flaw, Flaw E. As shown, each flaw is observed only as a bright region. This is because the true image of the void, the dark region is completely collimated out, thus only the bright shadow is detected. The bright, high intensity regions are slightly offset, since they are shadows, from the actual void flaw location.

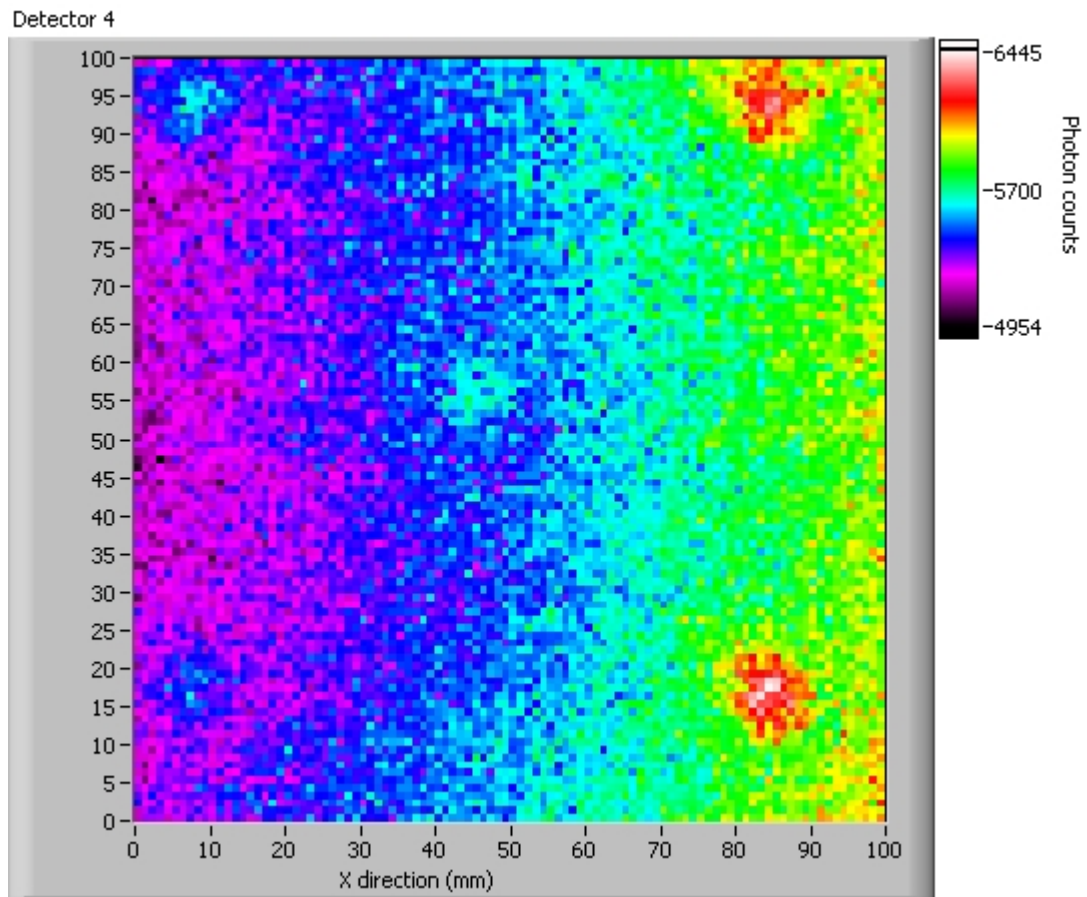


Figure 6.22 Over-collimated image of aluminum sample plate.

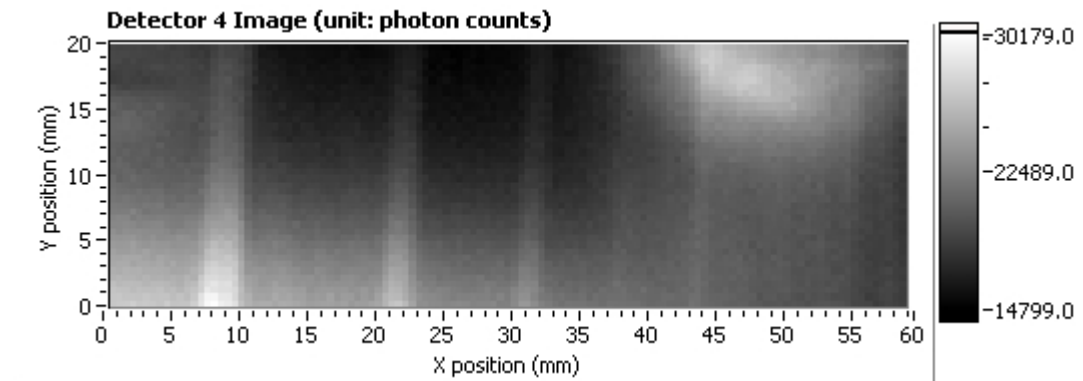


Figure 6.23 Over-collimated image of small channel aluminum plate.

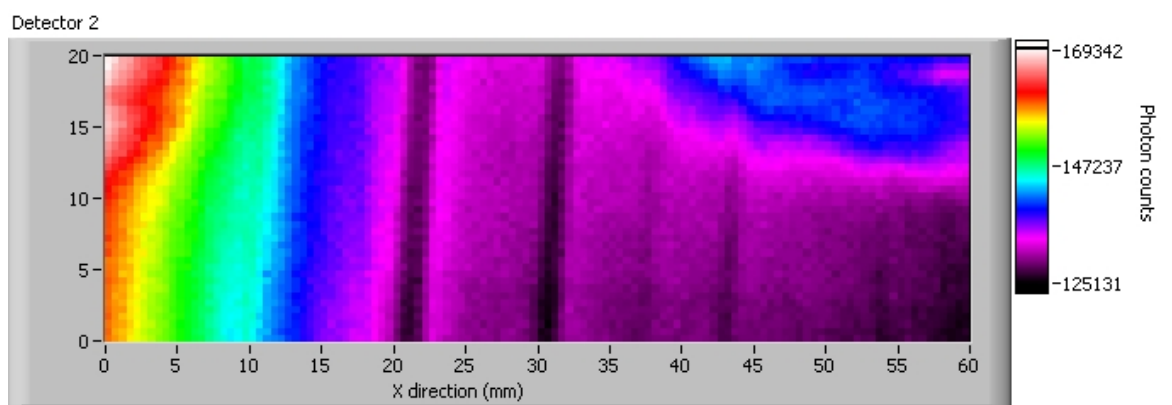


Figure 6.24 Under-collimated image of small channel aluminum plate.

Figures 6.23 and Figure 6.24 are taken with 75 keV peak incident spectra. They are of a small channel aluminum plate (Appendix D) with void-type flow channel machined at various depths. Figure 6.23 and 6.24 are over- and under- collimated, respectively. Due to previously discussed mechanism, the channels are thus imaged as bright and dark regions for the over-collimated and under-collimated cases, respectively.

### Plastic

The extremely high scattering to absorption ratio of most plastic materials makes imaging subsurface flaws without collimation focusing nearly impossible. Even without surface features, the initial scattering from a plastic surface often saturates the signal, masking the effects of any subsurface features. The addition of a collimator, however,

allows for this surface and shallow scattering to be removed from the detected signal increasing the relative signal contribution of deeper penetrating photons which interact with the void region. The drastic effect of proper collimation focusing is shown below in Figure 6.25. Both of these images are of the same plastic sample plate with a 1 cm wide by .15 cm high flaw running down its center. For the first image on the left in Figure 6.25, no collimator is used and only the surface is imaged. In Figure 6.24, a collimator is set to focus on the flaw, by moving the critical references scattering plane to just above the flaw surface. In this configuration, the subsurface channel now becomes apparent.

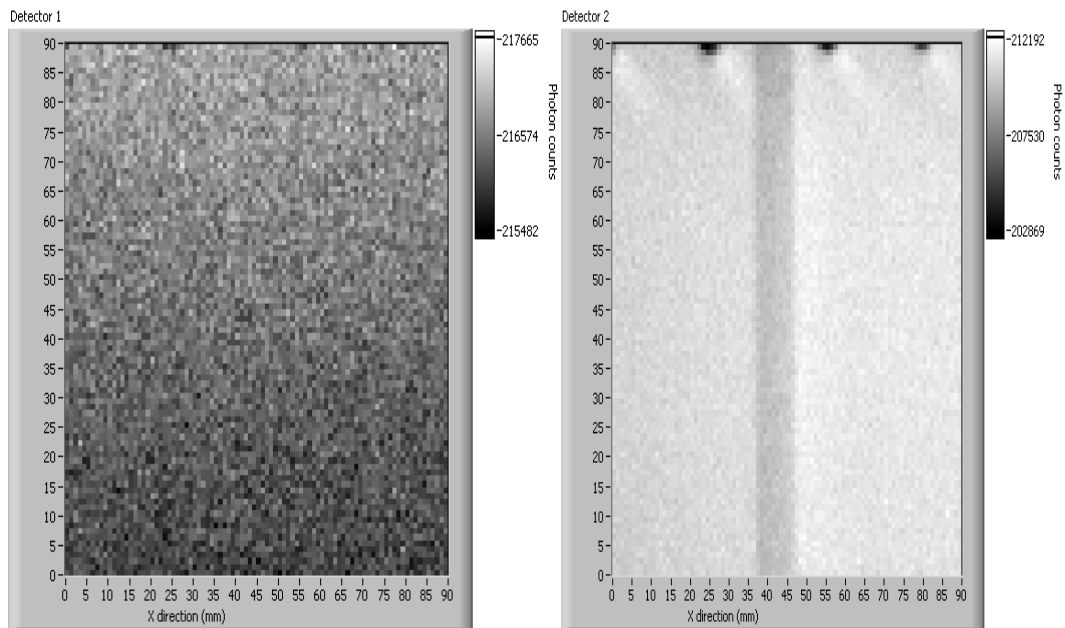


Figure 6.25 Plastic flawed plate #1, uncollimated on left, collimated on right.

The high scattering and lack of absorption in plastics also requires low photon energy be used. Typically 55 to 60 keV peak incident spectra provide the best results for imaging plastic type materials. Despite the differences in interactions properties between plastics and aluminum, the governing mechanism and hence the optimization processes

are similar to those of aluminum. Dark shadow type regions on the close end of flaws are not as dark in plastic since the absorption is markedly less pronounced in this material.

### **Concrete and Gypsum**

Imaging of concrete and gypsum samples usually indicated scanning for objects concealed behind walls. For this type of scenario, higher photon energies (up to 100 keV peak) are typically used and collimation setting is configured so as to focus past the  $\frac{1}{2}$  inch to 1 inch of wall material which is usually represents impedance to imaging.

Additionally, for instance, when collimation extension alone is not sufficient to focus to the desired depth or when higher count rates are desired, above that which the properly collimated detector receives, closing the detector to sample gap has a similar effect, but functions by a different mechanism, as increasing the collimation length. The Klein-Nishina cross-section dictates scattering angle distribution peak towards zero (forward) and 180 (backward) degrees. Thus as the sample to detector distance is decreased, deeper penetrating photons, having scatters closer to 180 degrees are preferentially detected. As energy is increased near the 100 keV peak which is often used form imaging concrete (represents the limit of the current Nylon generator capabilities) the backscatter angular distribution peaking towards 180 degrees becomes more pronounced and this method of focusing becomes more effective. The following figures are indicative of typical results achieved with the current RSD imaging modality on various concrete and gypsum targets.

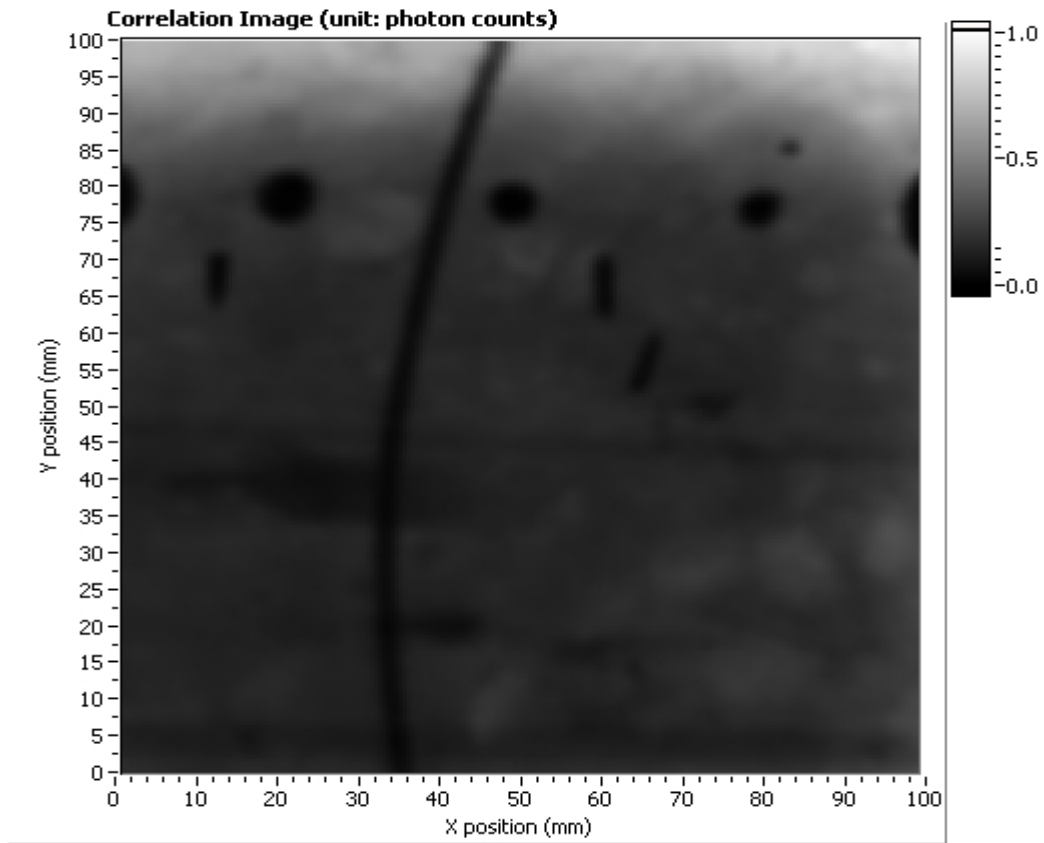


Figure 6.26 Correlated image of LANL block

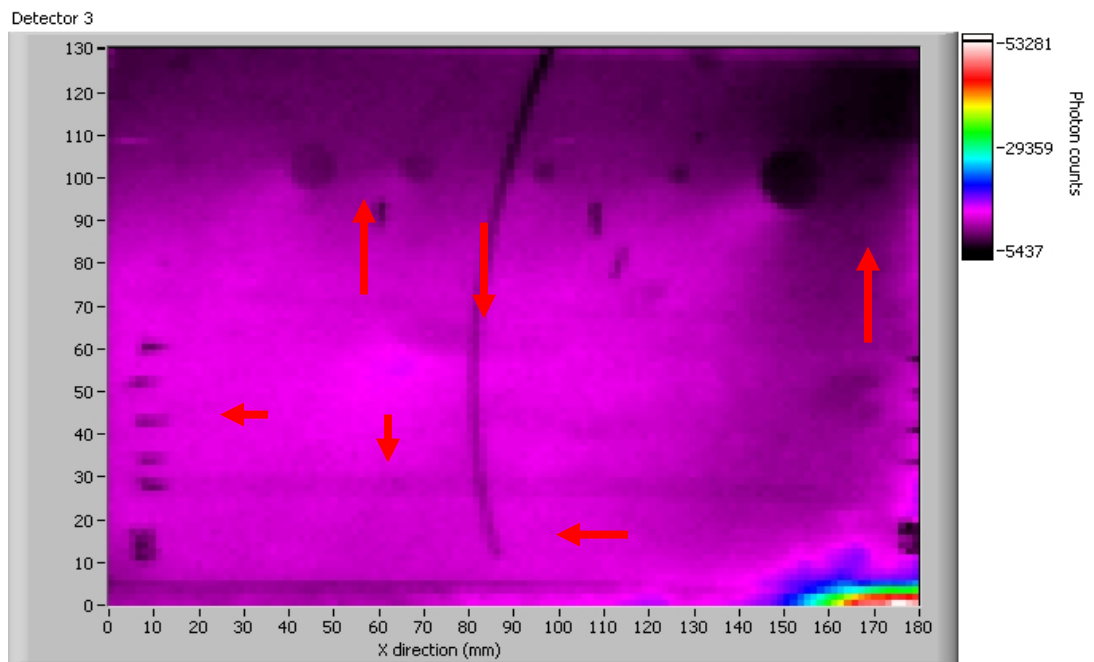


Figure 6.27 LANL block color image.

The two images above (Figures 6.26 and 6.27) are taken of a concrete sample block from Los Alamos National Laboratory. The sample is referred to as LANL block and is described in Appendix D. The various flaws present and detectable include nylon wire, lead arrows, plastic and steel at depths from almost flush to up to 2 inches below the surface.

Figure 6.28 is an image of various objects (radio, glass graduated cylinder, acrylic rod) placed within a concrete cinder block. Figures 6.29 and 6.30 are images of similar objects behind 1 inch of drywall.

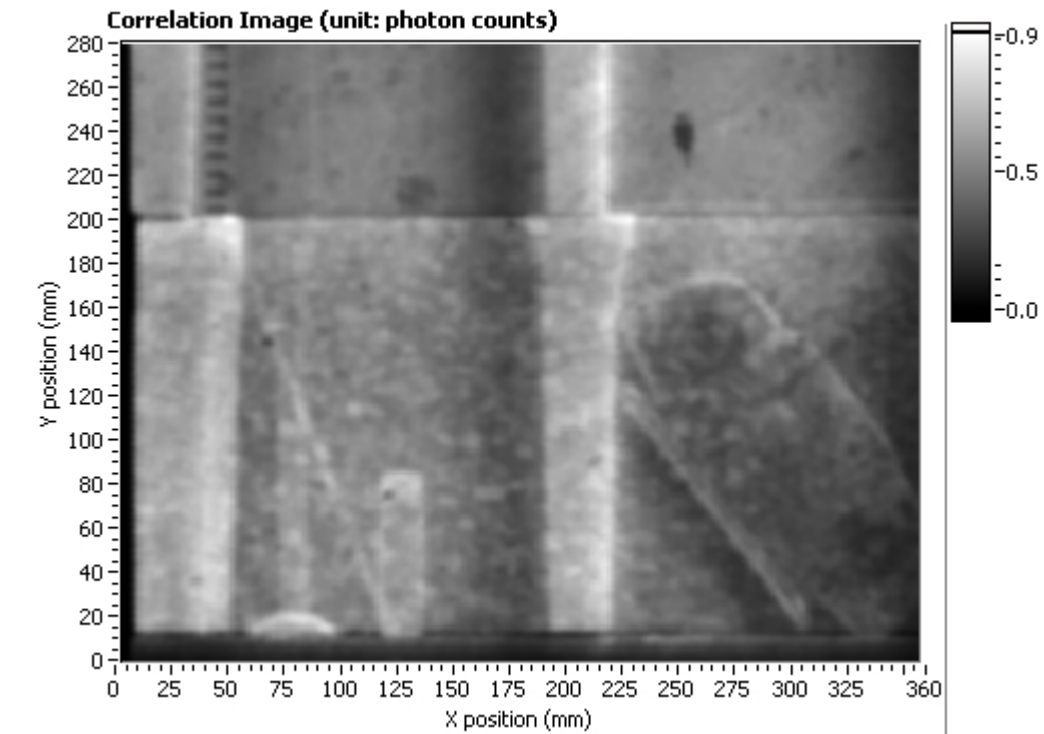


Figure 6.28 Clock radio, glass tube, wire, and acrylic rod inside cinder block.

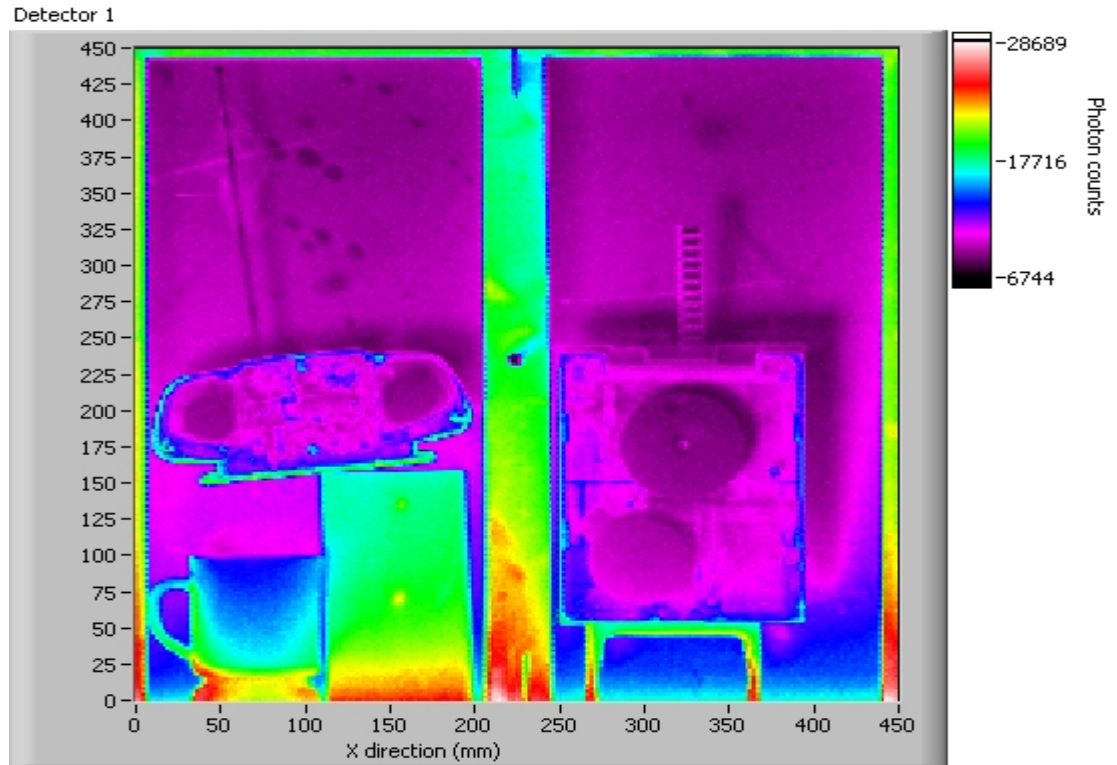


Figure 6.29 Various objects behind 1 inch of gypsum.

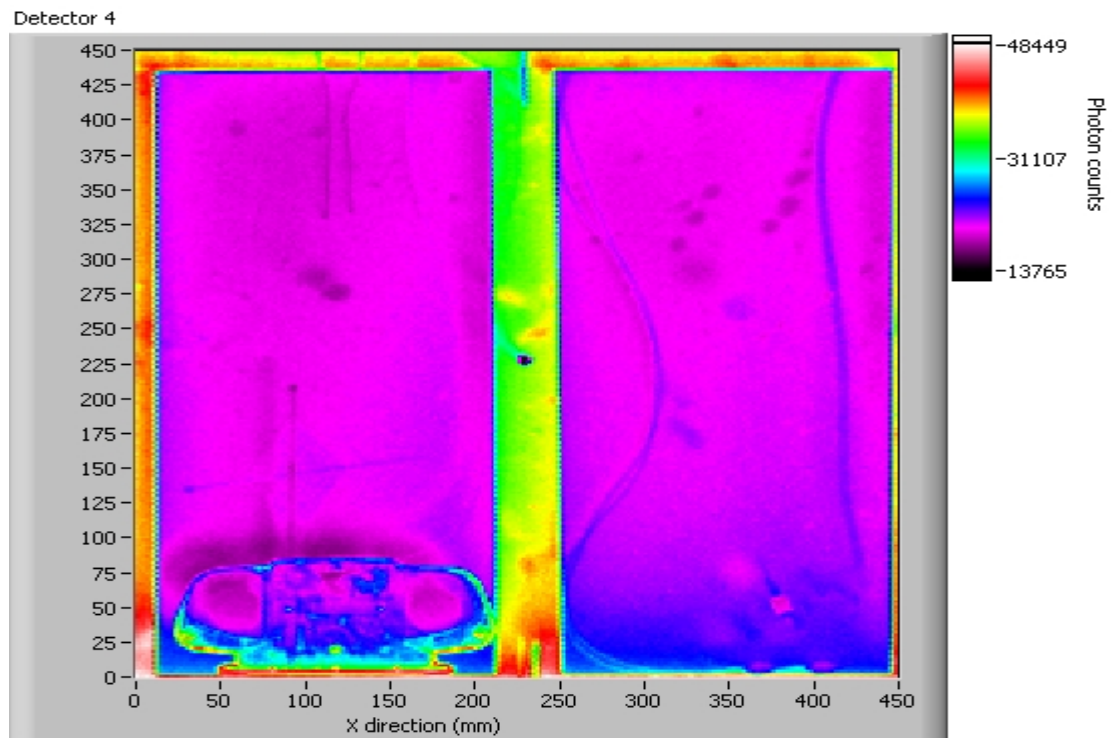


Figure 6.30 Miniature stereo, glass, fiber optic cable, copper wire, behind 1 inch of gypsum (drywall).

## Reactor Insulation

The problem of imaging the reactor insulation panels, provided by Westinghouse, is similar to that of typical concrete and gypsum problems in that there is a layer behind which the infrastructure is to be investigated. For the reactor insulation, the layer is a thin stainless steel sheet. The structure of the panel is such that behind this sheet is several layers of corrugated steel foils. Important flaws in this material were described to be boric acid residue on the opposite side and crushed or disengaged foil components on the interior.

The following figures, Figures 6.31 through 6.36, demonstrate various views and characteristics of the reactor insulation panel and the system's imaging capabilities.

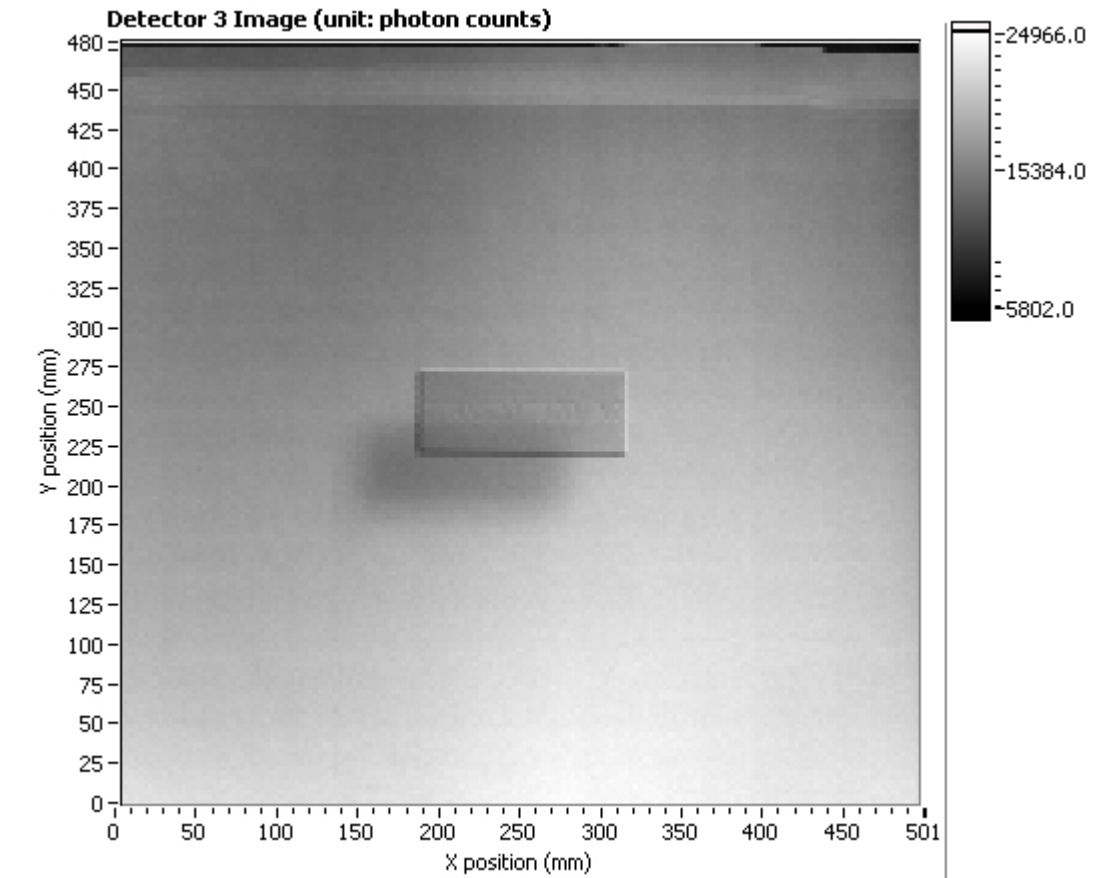


Figure 6.31 Reactor insulation panel image showing steel nameplate and shadow also corrugated interior foil structure evident.



Figure 6.32 Steel reactor insulation panel with boric acid residue.

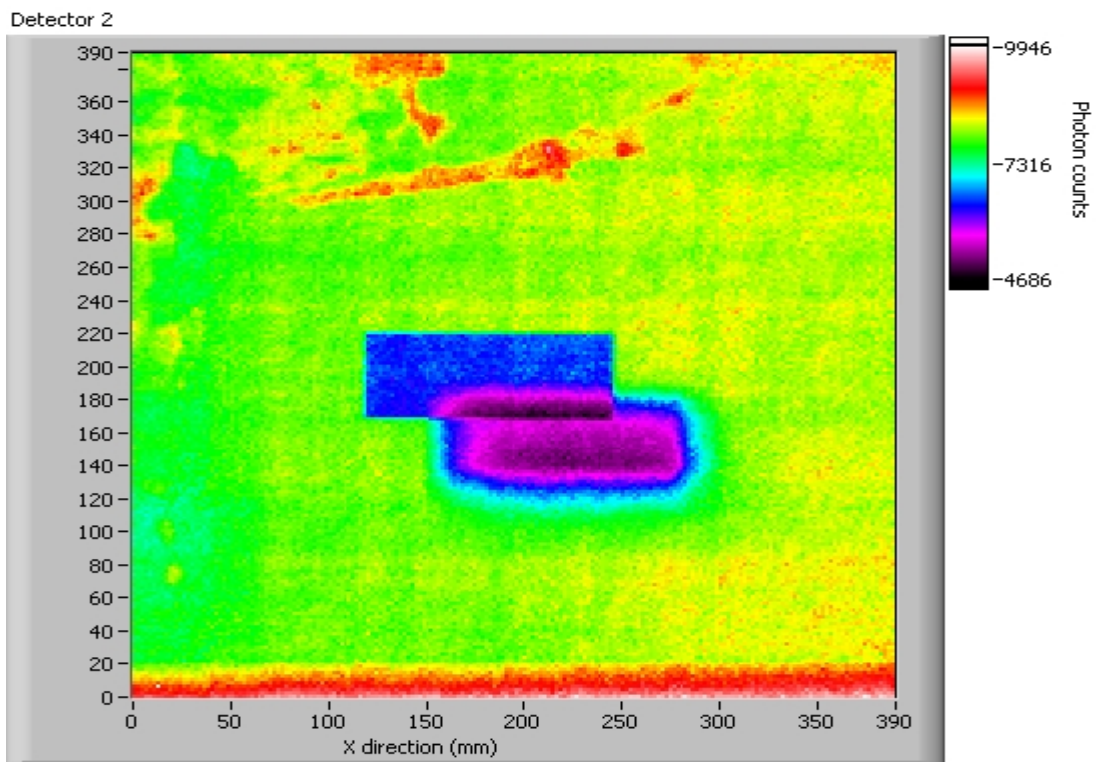


Figure 6.33 Color image of insulation panel, boric acid on far side clearly evident.

## Reactor Insulation

The problem of imaging the reactor insulation panels, provided by Westinghouse, is similar to that of typical concrete and gypsum problems in that there is a layer behind which the infrastructure is to be investigated. For the reactor insulation, the layer is a thin stainless steel sheet. The structure of the panel is such that behind this sheet is several layers of corrugated steel foils. Important flaws in this material were described to be boric acid residue on the opposite side and crushed or disengaged foil components on the interior.

The following figures, Figures 6.31 through 6.36, demonstrate various views and characteristics of the reactor insulation panel and the system's imaging capabilities.

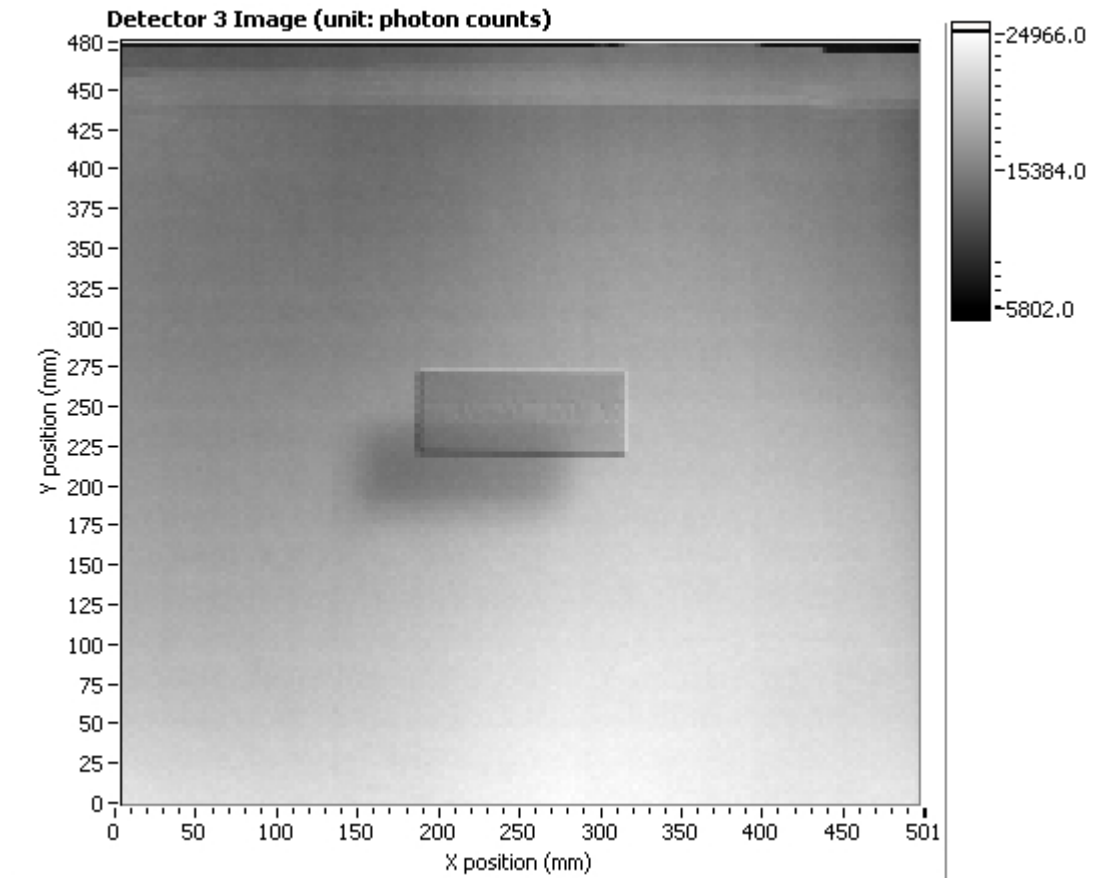


Figure 6.31 Reactor insulation panel image showing steel nameplate and shadow also corrugated interior foil structure evident.

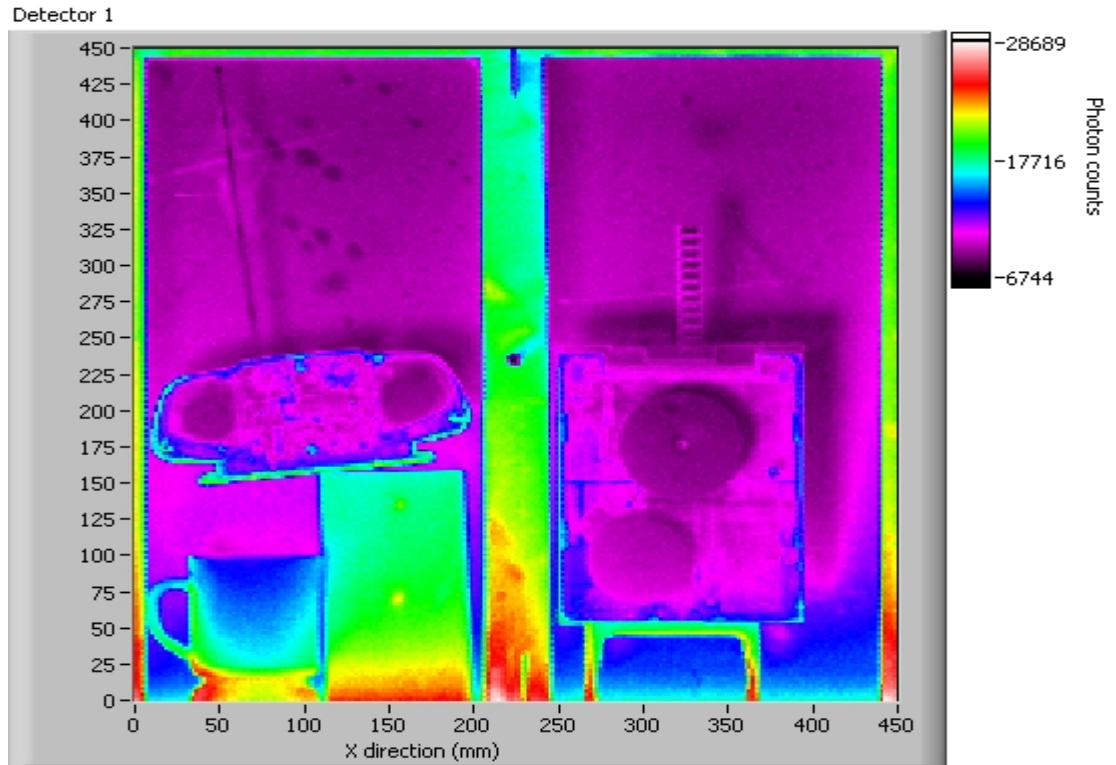


Figure 6.29 Various objects behind 1 inch of gypsum.

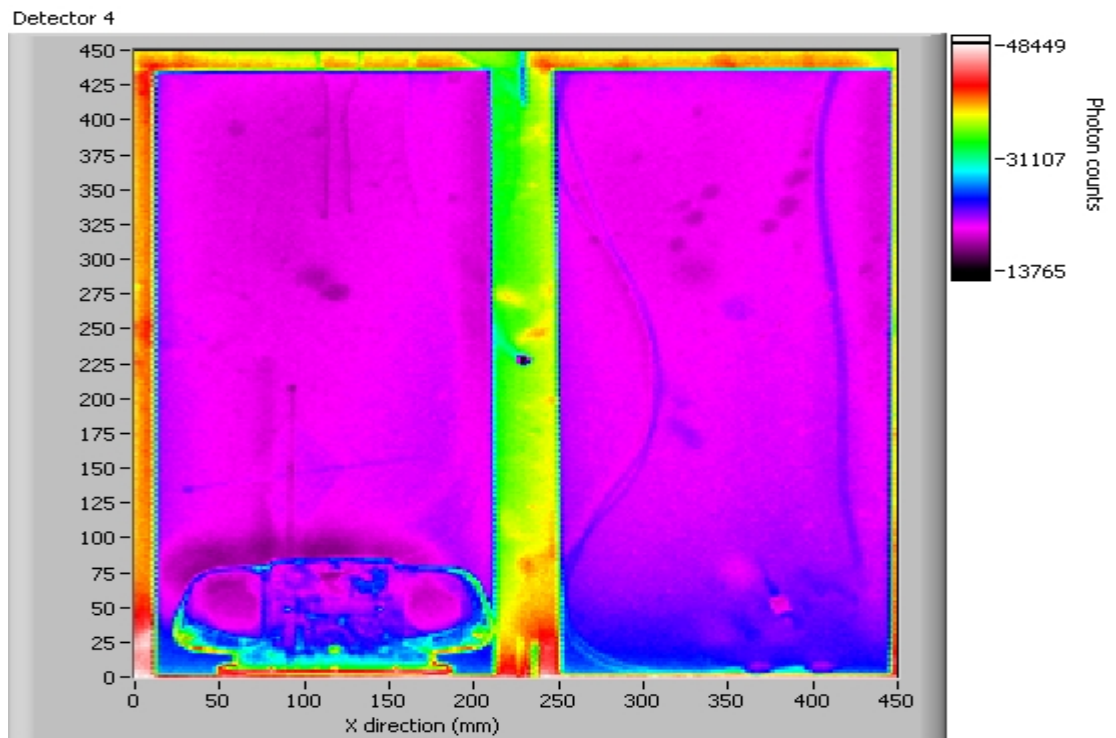


Figure 6.30 Miniature stereo, glass, fiber optic cable, copper wire, behind 1 inch of gypsum (drywall).

The two images above (Figures 6.26 and 6.27) are taken of a concrete sample block from Los Alamos National Laboratory. The sample is referred to as LANL block and is described in Appendix D. The various flaws present and detectable include nylon wire, lead arrows, plastic and steel at depths from almost flush to up to 2 inches below the surface.

Figure 6.28 is an image of various objects (radio, glass graduated cylinder, acrylic rod) placed within a concrete cinder block. Figures 6.29 and 6.30 are images of similar objects behind 1 inch of drywall.

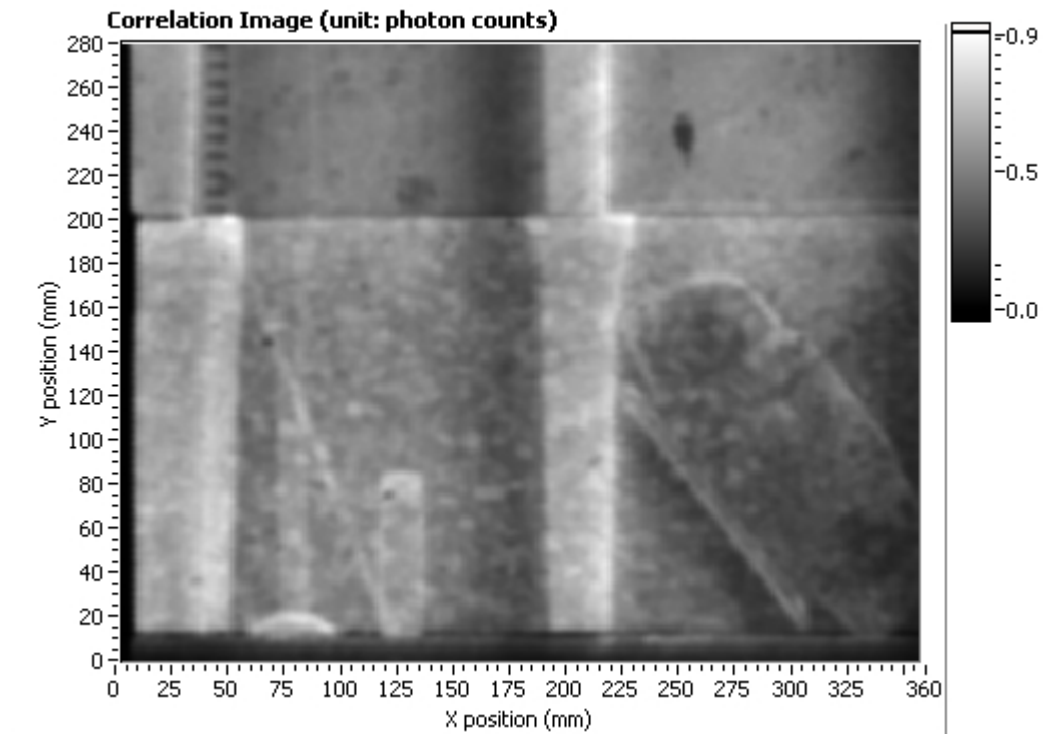


Figure 6.28 Clock radio, glass tube, wire, and acrylic rod inside cinder block.

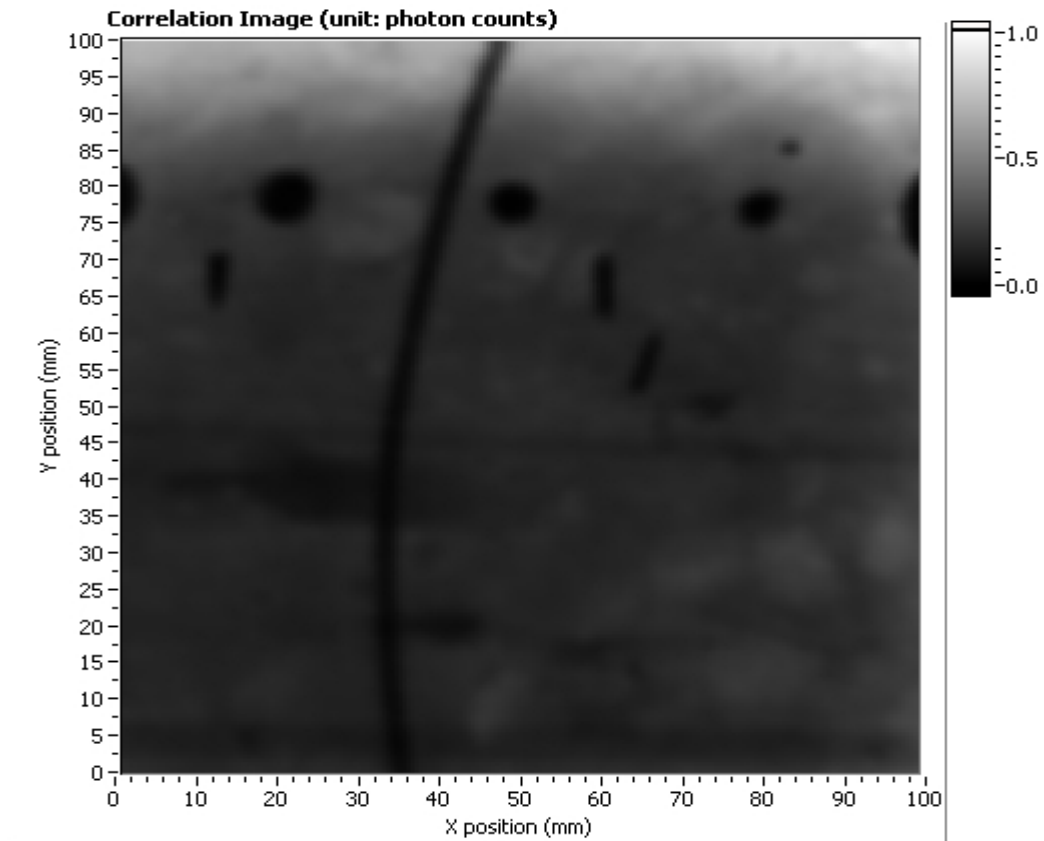


Figure 6.26 Correlated image of LANL block

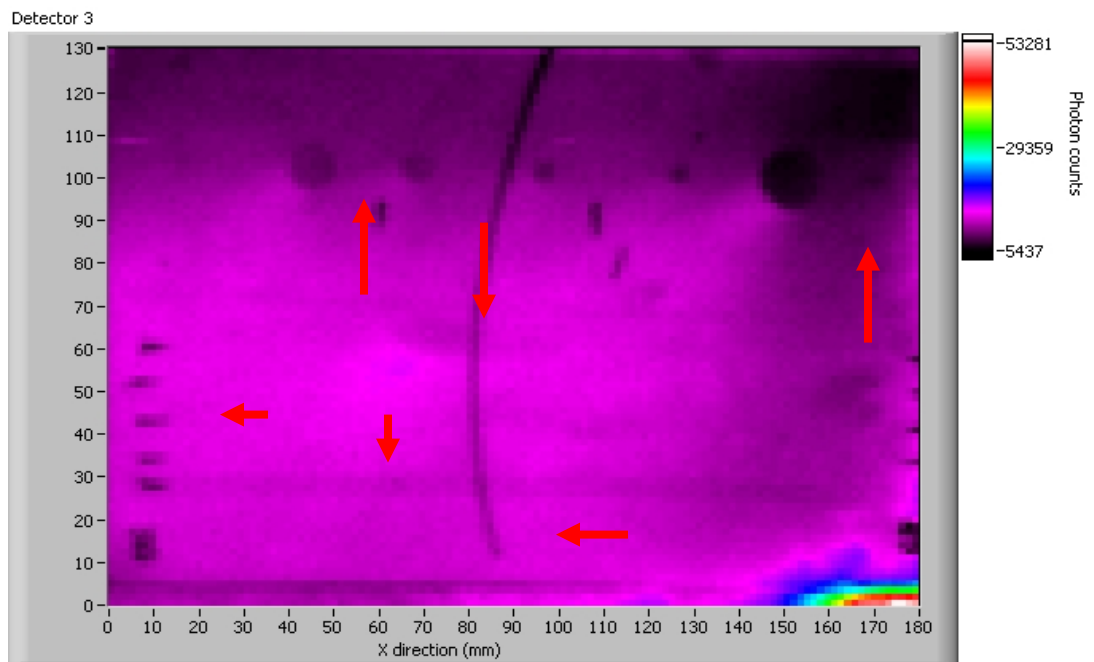


Figure 6.27 LANL block color image.

are similar to those of aluminum. Dark shadow type regions on the close end of flaws are not as dark in plastic since the absorption is markedly less pronounced in this material.

### **Concrete and Gypsum**

Imaging of concrete and gypsum samples usually indicated scanning for objects concealed behind walls. For this type of scenario, higher photon energies (up to 100 keV peak) are typically used and collimation setting is configured so as to focus past the ½ inch to 1 inch of wall material which is usually represents impedance to imaging.

Additionally, for instance, when collimation extension alone is not sufficient to focus to the desired depth or when higher count rates are desired, above that which the properly collimated detector receives, closing the detector to sample gap has a similar effect, but functions by a different mechanism, as increasing the collimation length. The Klein-Nishina cross-section dictates scattering angle distribution peak towards zero (forward) and 180 (backward) degrees. Thus as the sample to detector distance is decreased, deeper penetrating photons, having scatters closer to 180 degrees are preferentially detected. As energy is increased near the 100 keV peak which is often used form imaging concrete (represents the limit of the current Nylon generator capabilities) the backscatter angular distribution peaking towards 180 degrees becomes more pronounced and this method of focusing becomes more effective. The following figures are indicative of typical results achieved with the current RSD imaging modality on various concrete and gypsum targets.

allows for this surface and shallow scattering to be removed from the detected signal increasing the relative signal contribution of deeper penetrating photons which interact with the void region. The drastic effect of proper collimation focusing is shown below in Figure 6.25. Both of these images are of the same plastic sample plate with a 1 cm wide by .15 cm high flaw running down its center. For the first image on the left in Figure 6.25, no collimator is used and only the surface is imaged. In Figure 6.24, a collimator is set to focus on the flaw, by moving the critical references scattering plane to just above the flaw surface. In this configuration, the subsurface channel now becomes apparent.

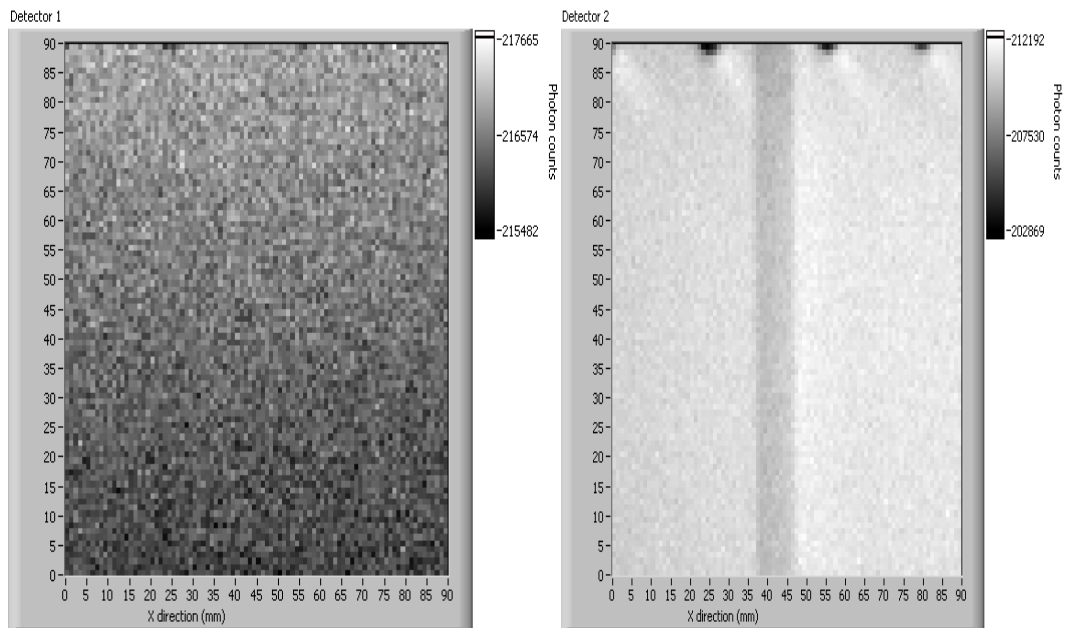


Figure 6.25 Plastic flawed plate #1, uncollimated on left, collimated on right.

The high scattering and lack of absorption in plastics also requires low photon energy be used. Typically 55 to 60 keV peak incident spectra provide the best results for imaging plastic type materials. Despite the differences in interactions properties between plastics and aluminum, the governing mechanism and hence the optimization processes

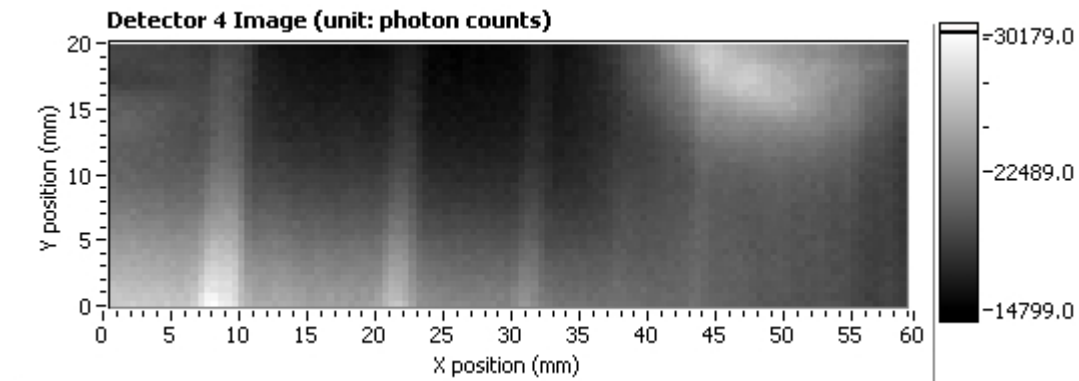


Figure 6.23 Over-collimated image of small channel aluminum plate.

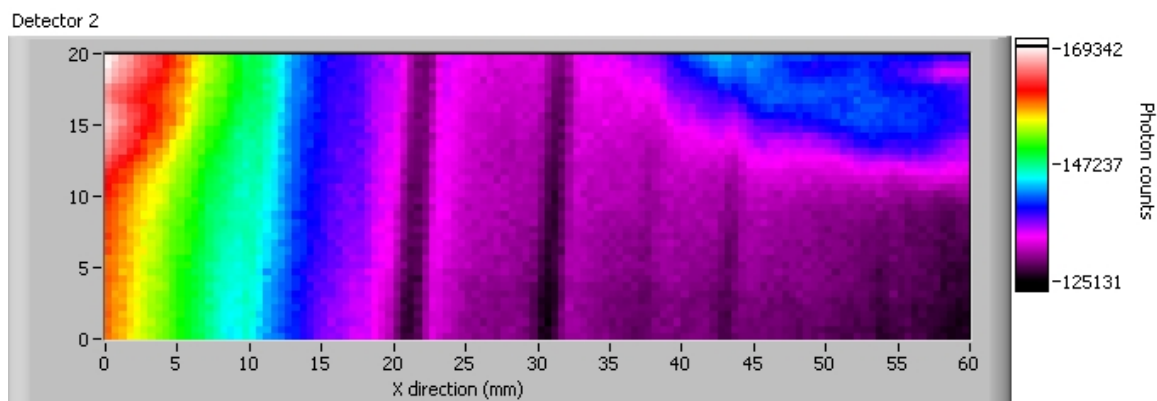


Figure 6.24 Under-collimated image of small channel aluminum plate.

Figures 6.23 and Figure 6.24 are taken with 75 keV peak incident spectra. They are of a small channel aluminum plate (Appendix D) with void-type flow channel machined at various depths. Figure 6.23 and 6.24 are over- and under- collimated, respectively. Due to previously discussed mechanism, the channels are thus imaged as bright and dark regions for the over-collimated and under-collimated cases, respectively.

### Plastic

The extremely high scattering to absorption ratio of most plastic materials makes imaging subsurface flaws without collimation focusing nearly impossible. Even without surface features, the initial scattering from a plastic surface often saturates the signal, masking the effects of any subsurface features. The addition of a collimator, however,

Figure 6.22 shows an image acquired with the geometry severely over-collimated. In this image, the CRP is set below the bottom of the deepest flaw, Flaw E. As shown, each flaw is observed only as a bright region. This is because the true image of the void, the dark region is completely collimated out, thus only the bright shadow is detected. The bright, high intensity regions are slightly offset, since they are shadows, from the actual void flaw location.

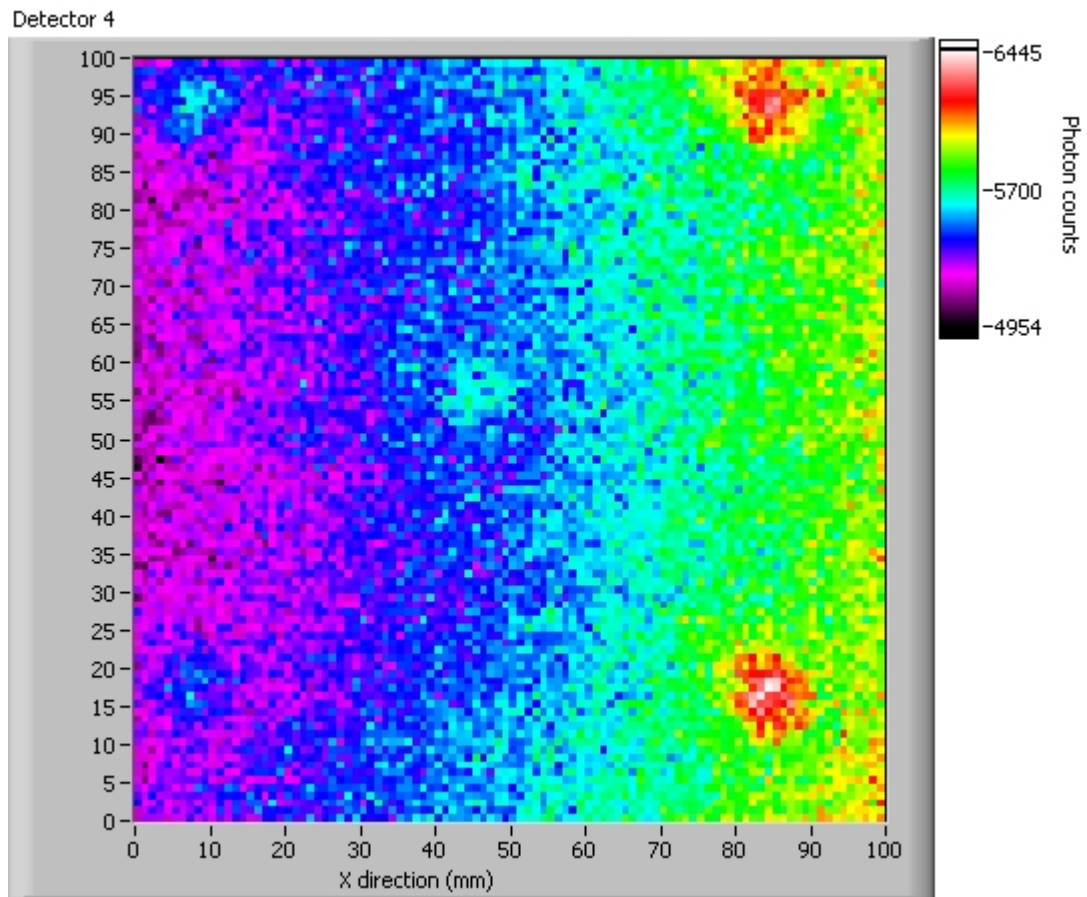


Figure 6.22 Over-collimated image of aluminum sample plate.

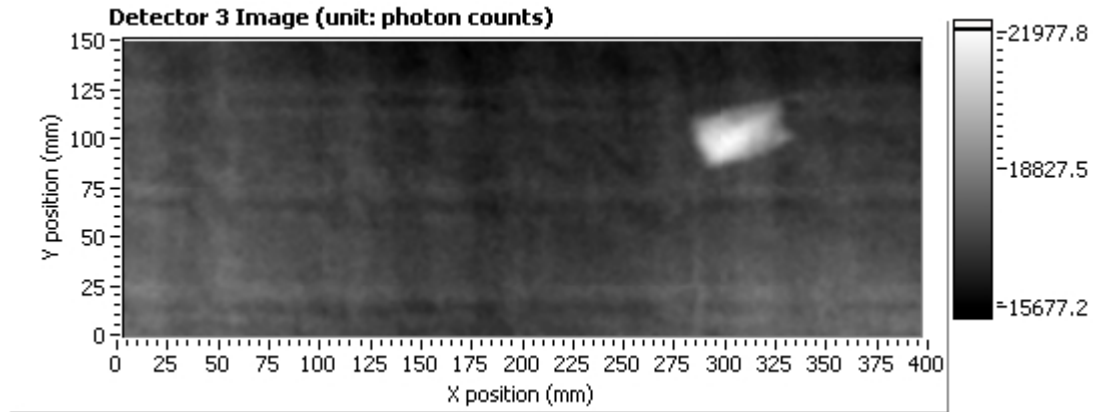


Figure 6.34 Reactor insulation panel correlation image. Plastic bag with boric acid on far side of panel. Interior structure of foil also apparent.

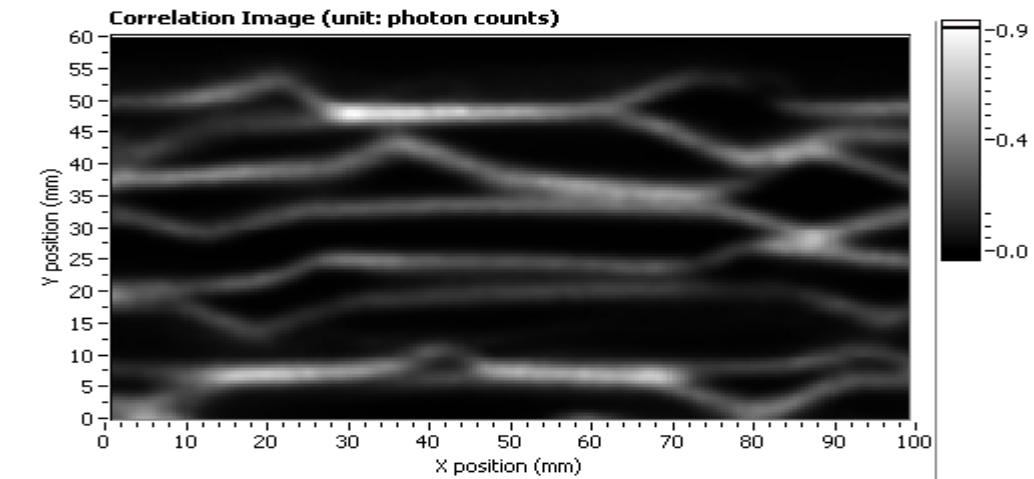


Figure 6.35. Side view of reactor insulation panel, showing several layers of corrugated foil.

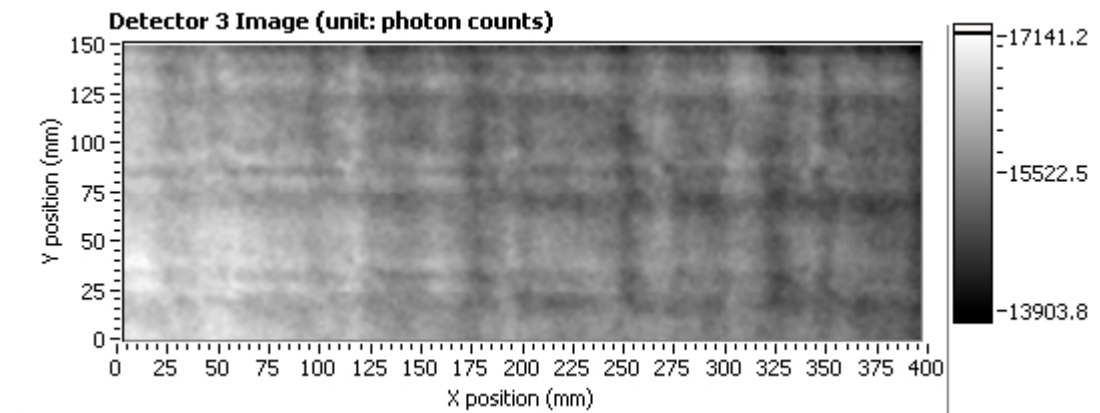


Figure 6.36 Internal structure of corrugated foil inside reactor insulation panel.



Figure 6.32 Steel reactor insulation panel with boric acid residue.

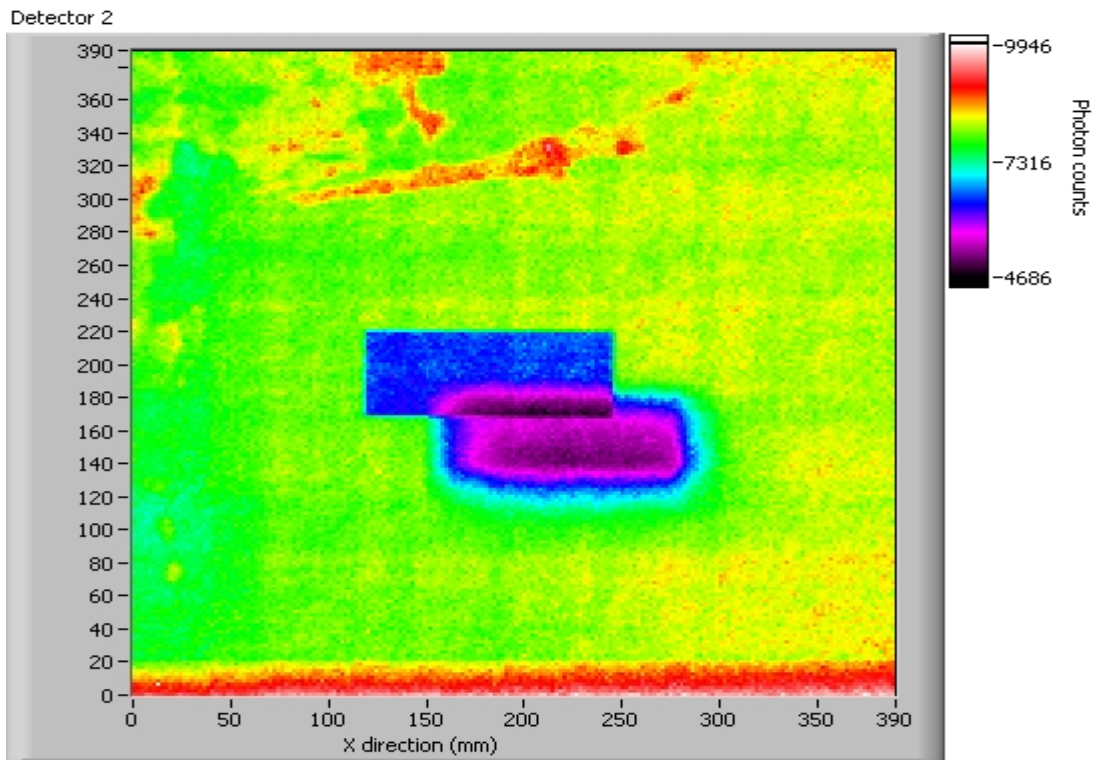


Figure 6.33 Color image of insulation panel, boric acid on far side clearly evident.

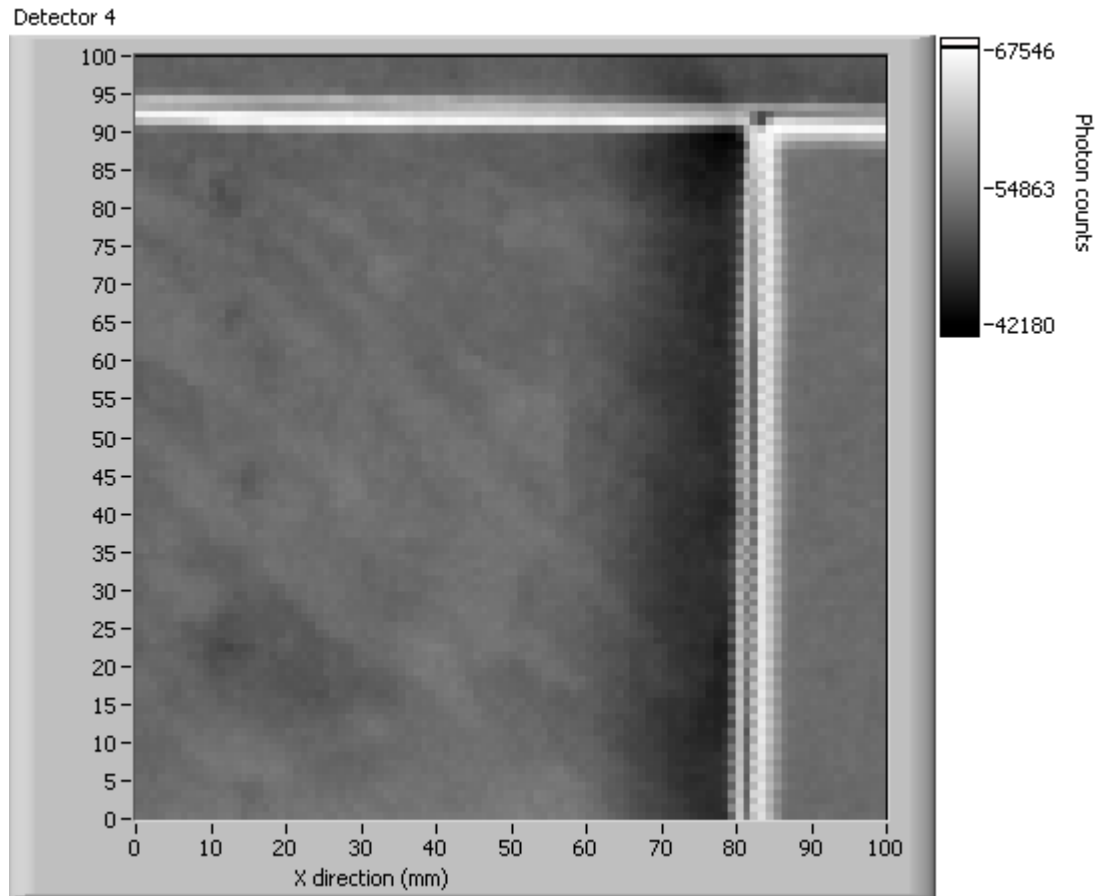


Figure 6.38 Space shuttle insulation tile, under-collimated. Bright smears are glue below CRP, dark circles on left are drilled holes.

Table 7.1 Percent contrast for various flaw types in aluminum. Flaws are .25 inch high by .5 inch diameter cylinder 0.236 inches below aluminum surface. Collimation is configured as in Figure 7.1A.

	Void	Plastic	Lead
5 cm to NaI 4.4 cm ext (Fig 7.1A)	6.06%	13.11%	-77.02%
5cm to NaI 2.4 cm ext (Fig 7.1B)	-8.11%	4.03%	-21.5%

Figure 7.2 shows data from the same three flaws taken at different collimation geometry. In this set of simulations, all parameters are identical except the collimator is extended only 2.4 cm past the NaI surface. As shown in the figure, this affects the shapes and relative shifts of the various spectra. In this set of simulations a small but obvious shift is observed between each spectrum. This is because, for the collimation configuration modeled, the CRP is above the top of the flaw. This allows for differences in both scattering and absorption properties to affect the spectra. The shift is expected based upon interaction characteristics and is similar to that observed in the previous set of simulations as far as the order of spectra. The plastic and void flaws, however, in this configuration, are shifted relative to one another. This is mostly due to the fact that in the plastic flaw, more photons will interact and scatter towards the detector from within the flaw. In the void flaw, the photons which traverse the flaw do not scatter towards the detector until they have reached the aluminum of the flaw bottom. This mechanism affects the spectral shape in two ways. It moves some of the scatters shallower in the material (within the flaw rather than below it) which results in a shorter exiting

In this geometry (Figure 7.1) there is no significant difference between the backscattered spectra taken over the void flaw and that taken over the plastic flaw. This is because, due to the collimation configuration, most photons impinging upon the detector have their first scatter at the flaw depth and below, effectively eliminating the increased signal due to primary scatters in the flaw. Additionally, the geometry is such that the significant attenuation (filtering) is caused by the aluminum traversed by the photon as it exits the target. That is, in this situation the spectral shift caused by the attenuation difference between the plastic-type flaw (modeled as  $C_5O_2H_8$ ) and the void type flaw is not significant when compared to the spectral filtering due to the aluminum target material traversed. The differential signal intensities, given as percent contrast versus non-flawed simulation, are given for each flaw type as modeled (in Figure 7.1) as Table 7.1. As the data indicates, the relative contrast is much higher and thus a more intense shift is expected for the lead flaw relative to both the plastic and the void flaw. The percent contrast ( differential signal intensity) is directly and intuitively correlated to the number of interactions and thus the degree of filtering occurring within a sample. Thus, a geometry which provides higher relative contrasts will necessarily enhance the relative spectral shifts. In the case of the plastic and void flaws in the scenario modeled in Figure 7.1, the contrast is on the order of a few percent. This contrast, when distributed over the entire range of the spectrum does not present itself as an observable shift. The spectral shape then, filtered mostly by the aluminum target medium is thus relatively the same for the three cases (no flaw, plastic flaw and void flaw) and it is merely the overall intensity that results in the detected signal.

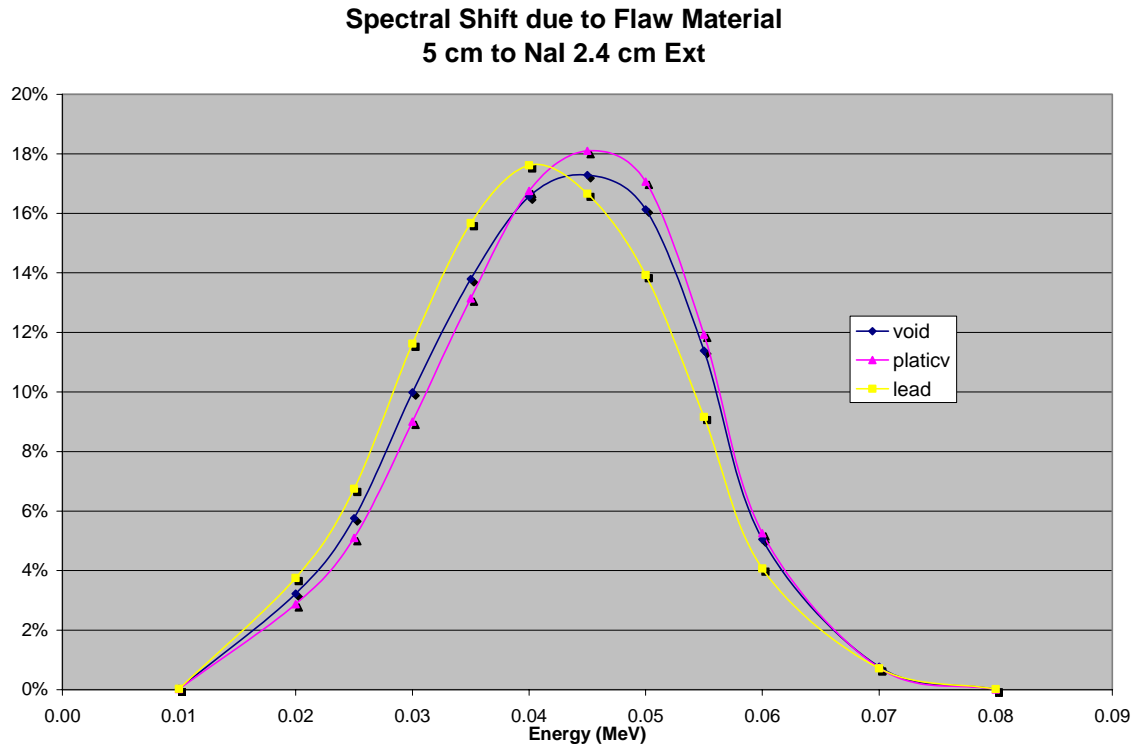


Figure 7.2 MCNP5 generated backscatter spectra of various flaw materials in Al, low collimation

The figures above demonstrate, not only how flaw material can affect spectral shapes, but also the sensitivity to relative photon track lengths through the flaw and target medium. In Figure 7.1, the system is configured so that the CRP is below the flaw. In this situation, most photons must completely traverse the height of the flaw in order to scatter into the detector. Thus the photon beam must cross the flaw twice, once impinging and once upon exiting, in order to reach the detector. Additionally, the severe angle subtended by the detector increases (for the flaw geometry modeled) the exiting photon track length through the flaw as well as through the aluminum target. As shown, the lead flaw has a marked spectral shift relative to the plastic and void type flaws. This is due to the large attenuation, specifically absorption, differences between lead and the other flaw materials as well as to the relative attenuation of the aluminum target medium.

within each energy bin, however, range from about 2-3% for the important relevant energy bins (25-60 keV) to around 10% for the lower and upper limit energy bins.

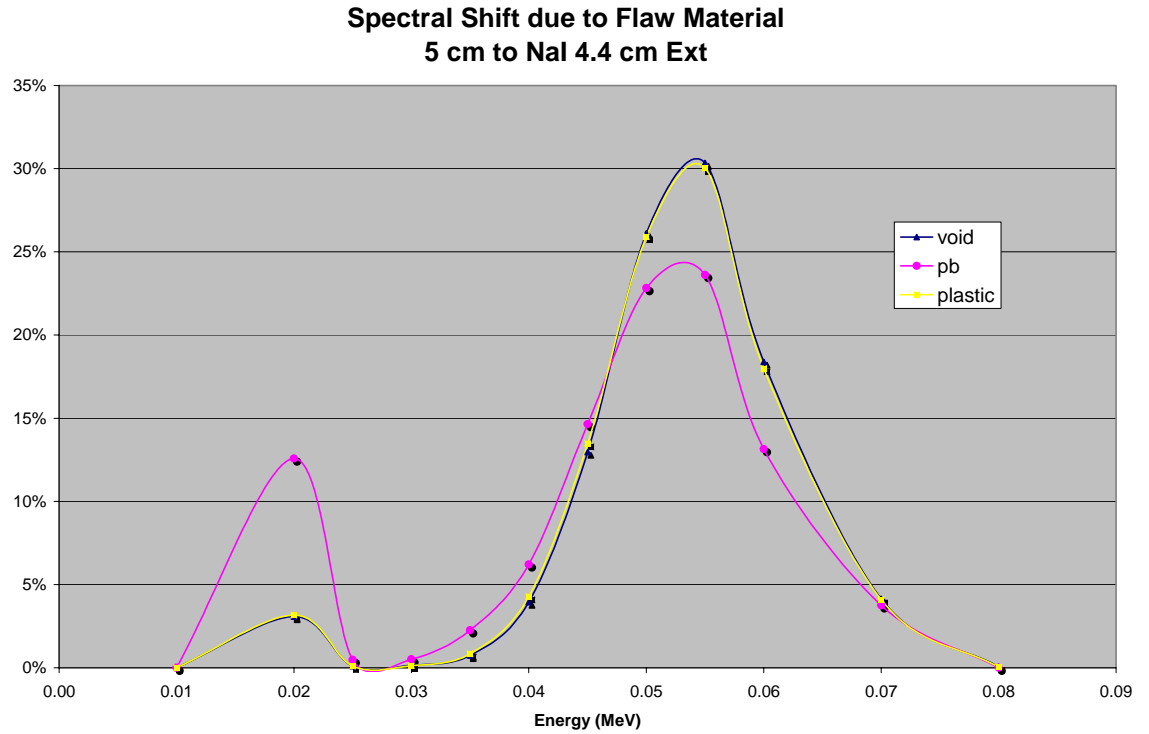


Figure 7.1 MCNP5 generated backscatter spectra of various flaw materials in Al, high collimation

marked than that between aluminum and plastic. This causes the spectral shift of the flawed region (the lead in the foam and the plastic in the aluminum) to be more distinct in the lead/foam case. Additionally, the relative density differential between lead/foam is much more severe than between aluminum/plastic. Thus the lead flaw in the foam represents a more significant portion of the backscattered signal than does the plastic flaw in the aluminum and thus the lead/foam scenario will have a much more exaggerated shift than the aluminum/plastic. This shift, flaw orientation remaining the same, is thus a function of the total relative difference in attenuating properties of flaw versus target material. That is, it is dependent upon the type of filtering caused by the flaw (related to scattering and absorption properties within the relevant energy continuum) and to the amount of filtering (related also to the size and density of the flaw).

The following figures, 7.1 and 7.2 demonstrate the ideal shifts (MCNP5 simulations) observable for various flaw material in an aluminum target medium. The simulation models a 10 inch by 10 inch, 2 inch thick aluminum plate with a ¼ inch high by ½ inch diameter cylindrical flaw at a depth of 0.236 inches (0.6 cm) below the surface. The various flaw materials considered are air (void), lead (Pb) and plastic (C<sub>5</sub>O<sub>2</sub>H<sub>8</sub>). The simulation in Figure 7.1 models a NaI to sample spacing of 5 cm and a collimator extension of 4.4 cm. Figure 7.2 models a 5 cm NaI-to-sample spacing with a 2.4 cm collimator extension. In both configurations the detector is a 2 inch diameter NaI crystal offset, centerline-to-centerline, from the photon beam by 9 cm. The incident photon beam is 75 keV peak (75kVp) and 5 mm in diameter. MCNP5 calculations for these data sets were done with 2E8 particles yielding total uncertainties within 0.5%. Uncertainties

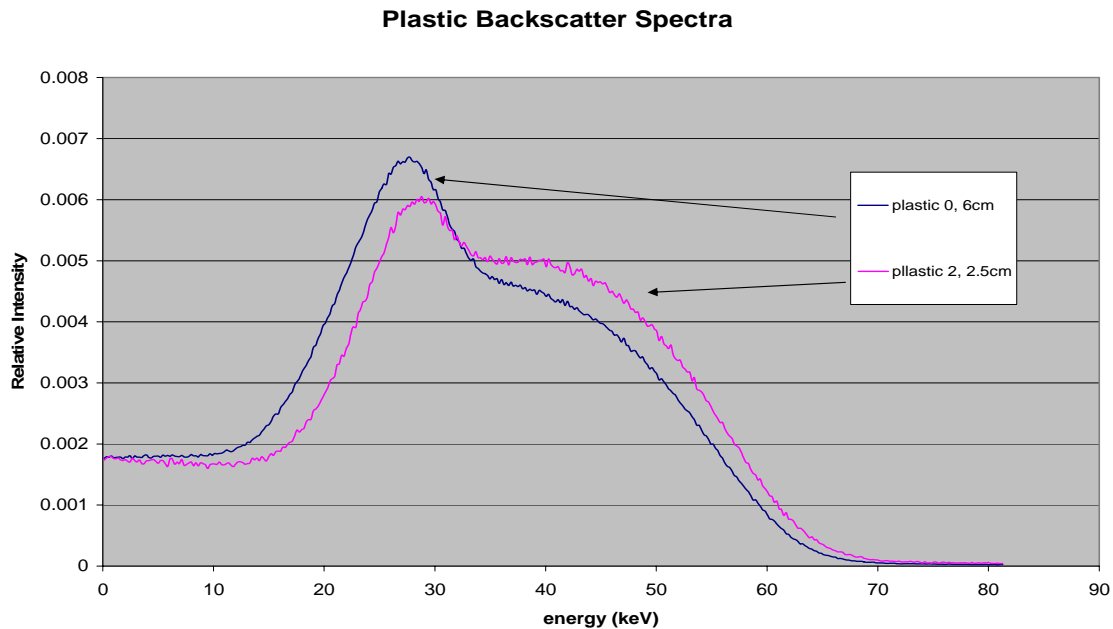


Figure 7.7 Normalized (first moment) experimental data 75 keV backscatter spectra from a plastic target.

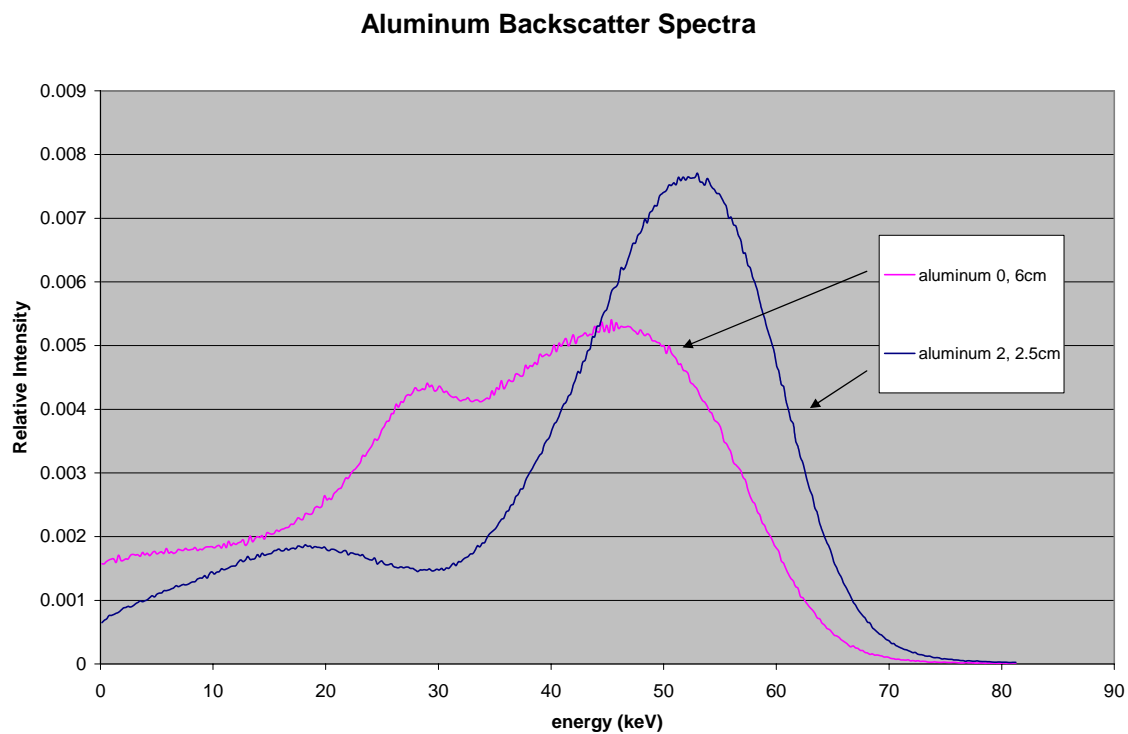


Figure 7.8 Normalized (first moment) experimental data 75 keV backscatter spectra from an aluminum target.

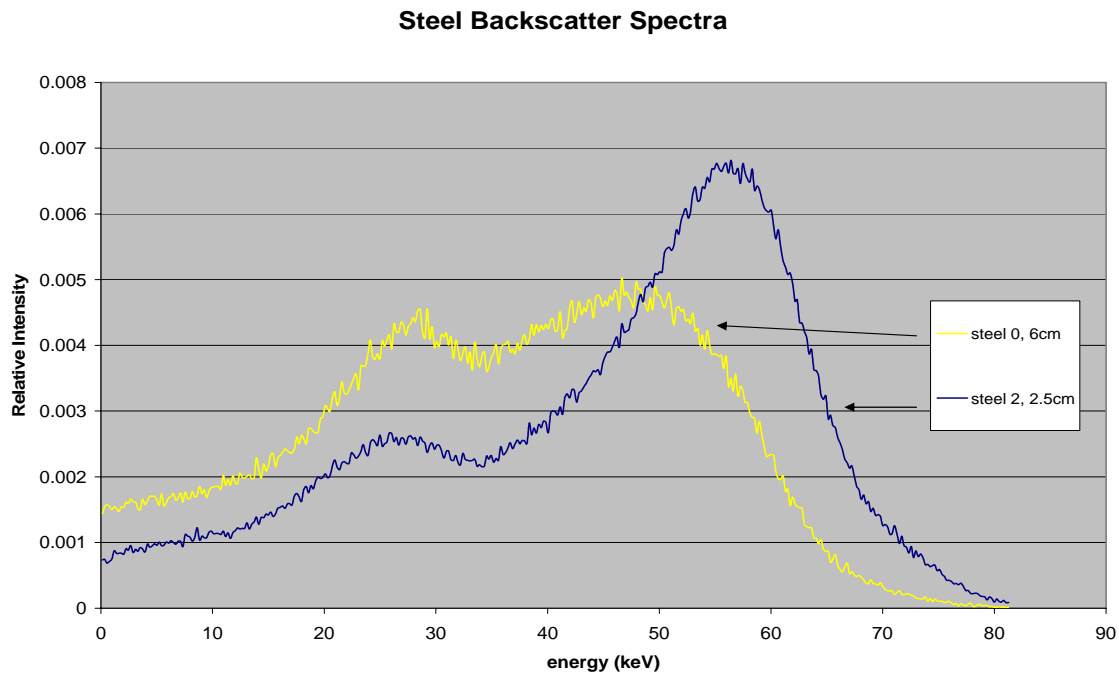


Figure 7.9 Normalized (first moment) experimental data 75 keV backscatter spectra from a steel target.

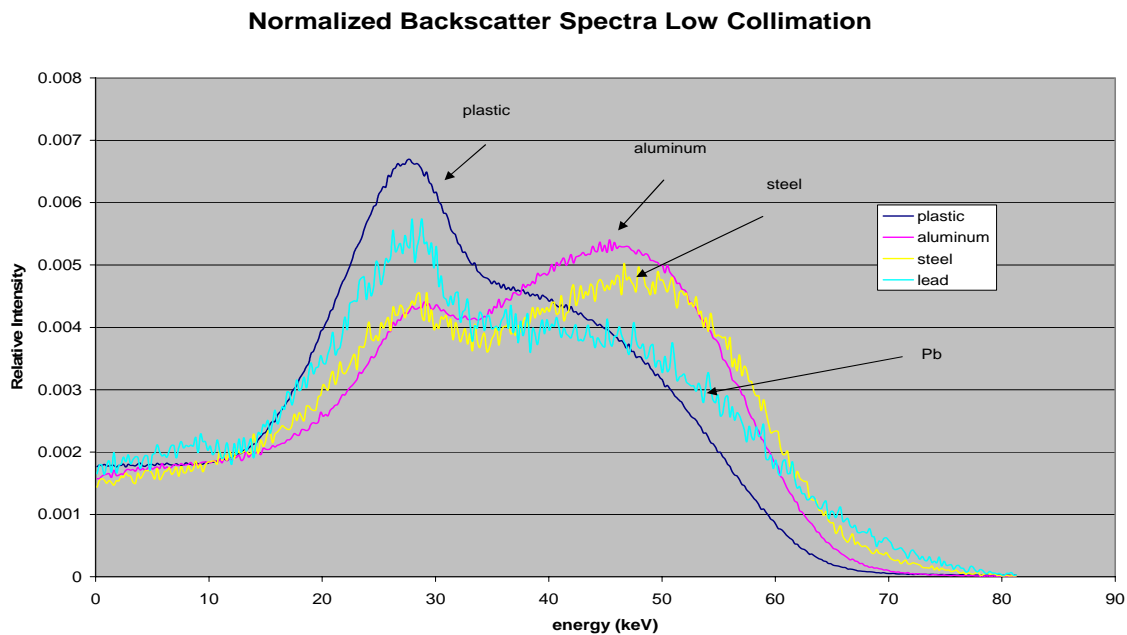


Figure 7.10 Normalized (first moment) experimental data 75 keV backscatter spectra. No collimator extension, 6 cm from NaI to Sample surfaces.

### Normalized Backscatter High Collimation

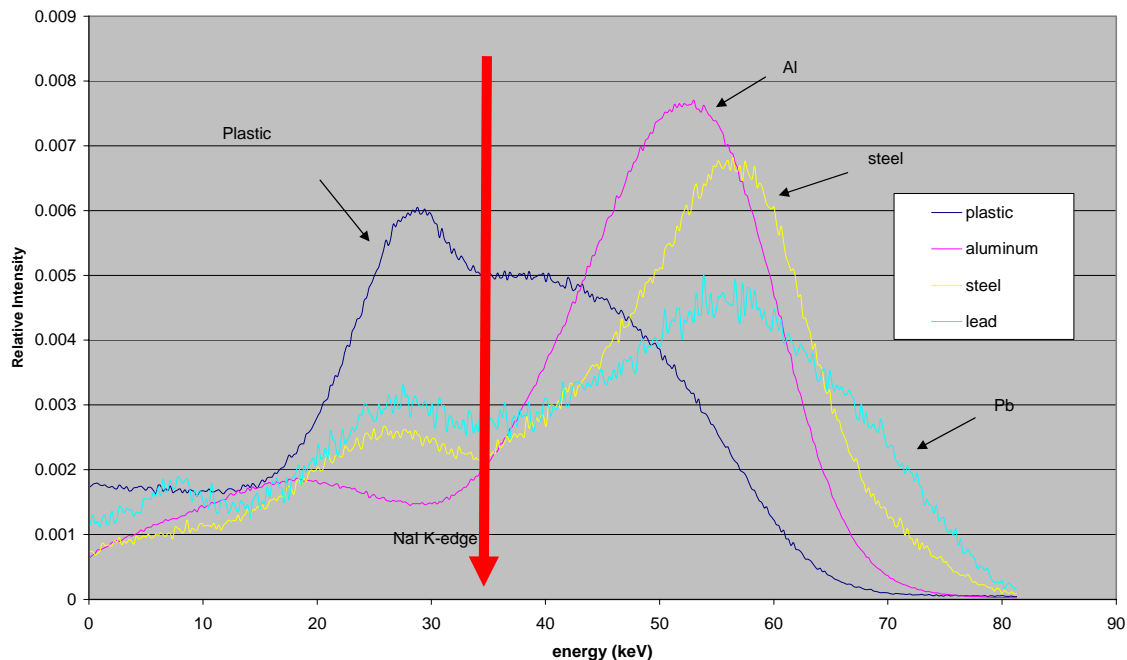


Figure 7.11 Normalized (first moment) experimental data 75 keV backscatter spectra. 2 cm collimator extension, 4.5 cm from NaI to Sample surfaces Arrow indicated k-edge in photoelectric cross-section of iodine.

The figures above, especially the side-by-side comparisons presented in Figures 7.10 and 7.11, show a marked spectral shift as a result of target material. As previously noted, the higher the relative absorption to scattering characteristics of the target material, the more pronounced the effective spectral hardening will be. The aluminum and steel spectra above clearly show significant hardening compared to the spectrum taken off of the plastic sample. The slightly more complicated spectrum backscattered from the lead target material is a result of the absorption edges in the photoelectric cross-section of lead. These edges, shown below as Figure 7.12, result in the lower energy peaking (at  $\sim 10$  keV) shown in Figures 7.10 and 7.11 for lead. Similar to other spectroscopic characteristics, this low energy peaking is accentuated as collimation is increased.

Additionally, the relative flatness of the lead spectrum, compared to those of aluminum and steel, is a result of the relative slopes of each of the absorption cross-sections (versus energy) these plots, for aluminum and lead are shown below as figures 7.12 and 7.13.

The photoelectric cross-section for aluminum is almost three orders of magnitude higher at the low energy end ( $\sim 10\text{keV}$ ) of the plot than it is at the high energy end ( $\sim 100\text{keV}$ ).

In contrast, the cross-section for lead varies by only about two orders of magnitude across the same relevant energy range. This indicates that in aluminum the relative absorption preference for low energy photons is stronger than it is in lead. For this reason, relatively more low energy photons are absorbed in aluminum per high energy photon absorbed and consequently we have a much sharper high energy photon peak in the backscattered spectrum of aluminum relative to lead.

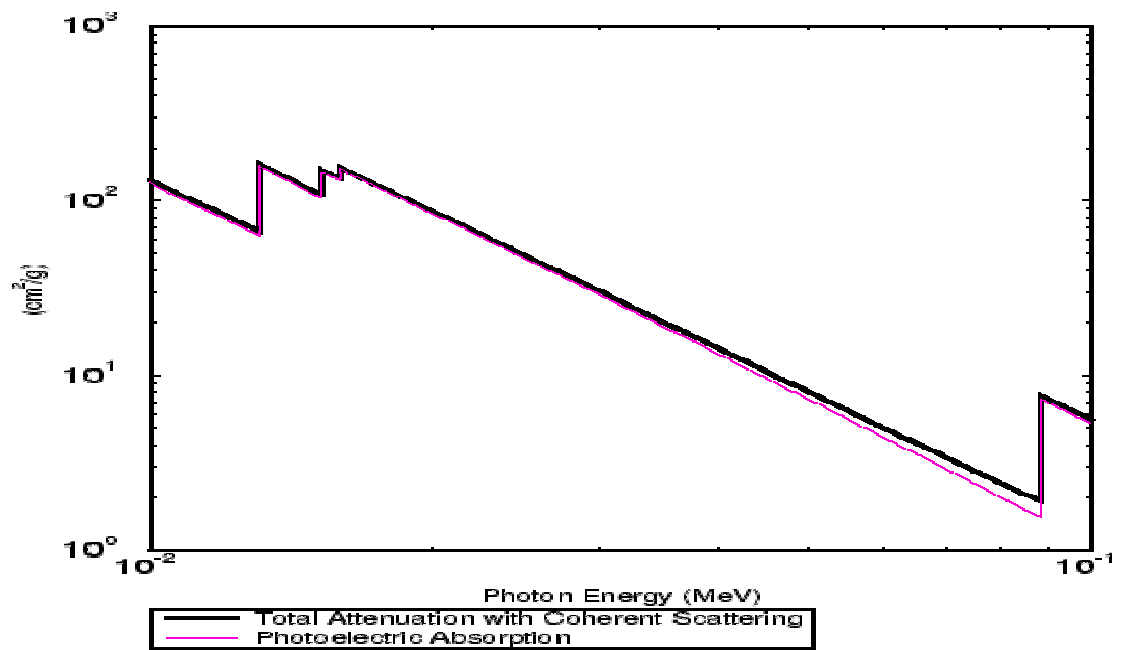


Figure 7.12 Photoelectric cross-sections for lead

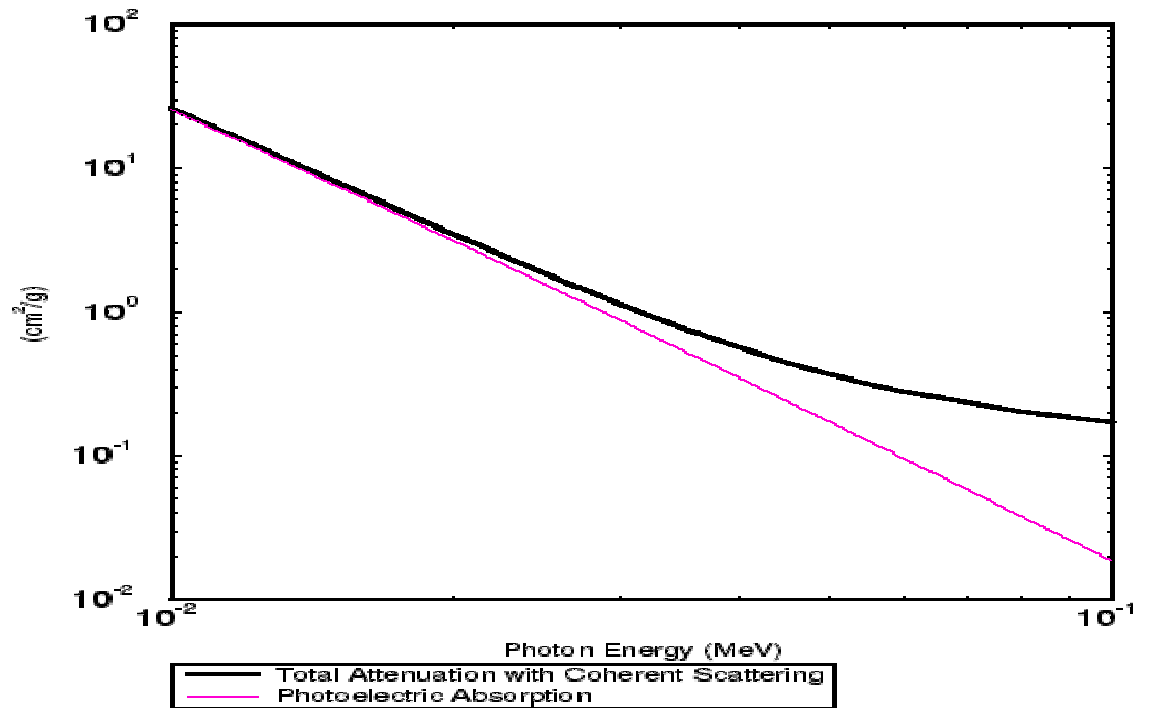


Figure 7.13 Photoelectric cross-sections for aluminum.

### Detector Material

A detected photon must have at least one interaction in the detector material. Usually, if spectroscopic information is to be retrieved from that photon, several interactions or a photoelectric absorption must occur within the detector to ensure significant energy deposition. Of the detector materials and modes considered in this investigation, only the NaI crystal in pulse mode is capable of collecting useful spectroscopic data. This, as described earlier, is because current mode detects a voltage caused by total energy deposition and does not assign any portion of that deposited energy to a particular photon. Additionally, the plastic scintillation material, due to its intrinsic physical properties (also mentioned previously) does not induce many photons to deposit their full energy. The consequence of this is most photons deposit about the same energy in the detector regardless of their actual wavelength.

Energy distributions collected by the NaI crystals are subject to the inherent resolution limit of the crystal, generally taken to be about 5-10 keV. This energy resolution limit is a function of the crystal itself, related to the excitation energy state gaps available within the doped crystal and to the inherent de-excitation or charge collection time of the crystal. Consequently, regardless of front-end or back-end electronics or MCA (multi-channel analyzer) components, energy differences below this limit can not be accurately measured with NaI.

An important feature of the NaI crystal is the sharp negative peak (valley) observed in all experimental and MCNP5 spectroscopic data collected. The valley is observed at about 34 keV in all spectra collected with the NaI and is shown in each of the above figures, but marked with an arrow in Figure 7.11 for clarification. The invariance of this valley to other parameter perturbations, led to the conclusion that it must be a property of the detector material and how it interacts with the incident photons. Consideration of the various cross-sections for both sodium and iodine revealed that the valley corresponded identically and thus must be a result of the K-edge in the photoelectric cross-section of iodine. Figure 7.14 shows the photoelectric cross-section for iodine<sup>32</sup>. The sharp k-edge coincides identically with the valley observed in the NaI acquired spectra. Further investigation of documented NaI spectroscopic properties confirmed this conclusion<sup>34</sup>.

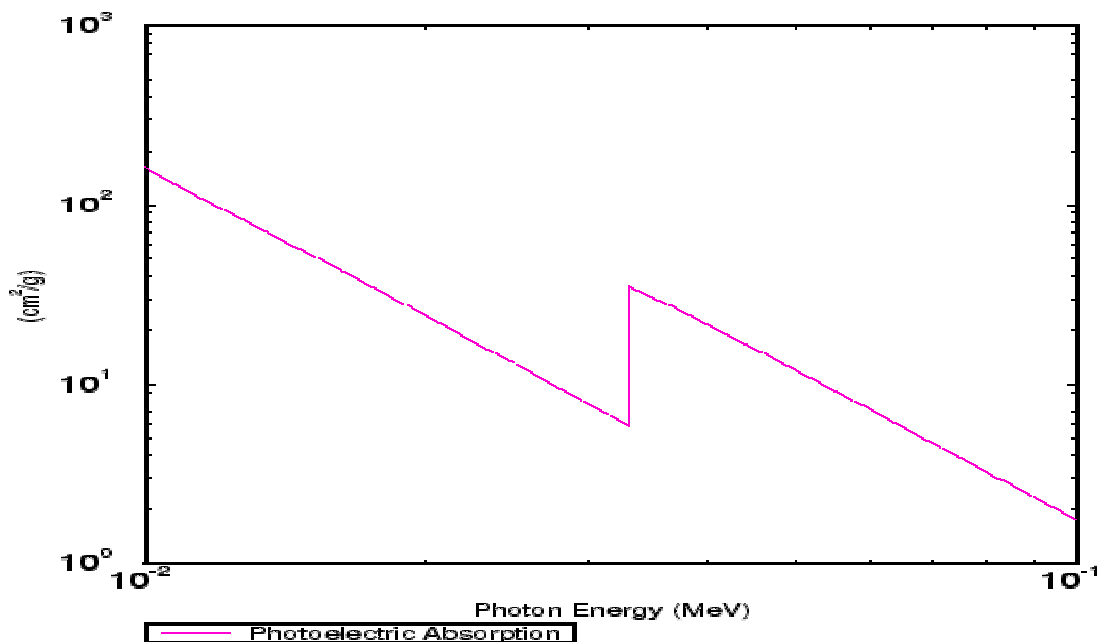


Figure 7.14 Photoelectric cross-section for Iodine. K-edge at  $\sim 30$ keV.

## Detector and Collimation Configuration

### Detector to Sample Spacing

Detected signal spectra were taken for several different sets of system configurations. Each set had a different but constant (within the set) incident energy distribution and collimator extension and a variable detector (NaI surface) to sample spacing. Similar trends for each set were observed. The dominant general trend is a sharpening and hardening (increase in most probable energy) of the detected spectra as detector to sample distance is decreased. This is mostly due to the fact that as distance from sample to detector is decreases the effective collimation is increased and photons from deeper within the sample are preferentially selected for. These photons, since they have traveled further through the target material, are filtered to a higher degree by the

target material and thus demonstrate stronger filtering effects in the spectral shapes. For the case in Figure 7.10, the dominant filtering effect is absorption of the low energy end of the spectrum which produces the observed spectral hardening. To illustrate this trend one section of a set in the series is shown below in Figure 7.15 which depicts trends observed experimentally for target to detector surface distance variation.

In this set the collimator is fixed at 1.5 cm past the NaI surface. The collimator fins are fixed at zero degrees. The set is taken with a 75 keV incident spectrum on an aluminum sample. Spectra were taken as the NaI to sample surface distance was varied from 8.5 cm to 2.5 cm. In this particular set the dominant trend is the shift towards higher energy. Other sets show similar trends and are included in Appendix E for completeness along with complimentary MCNP5 simulations.

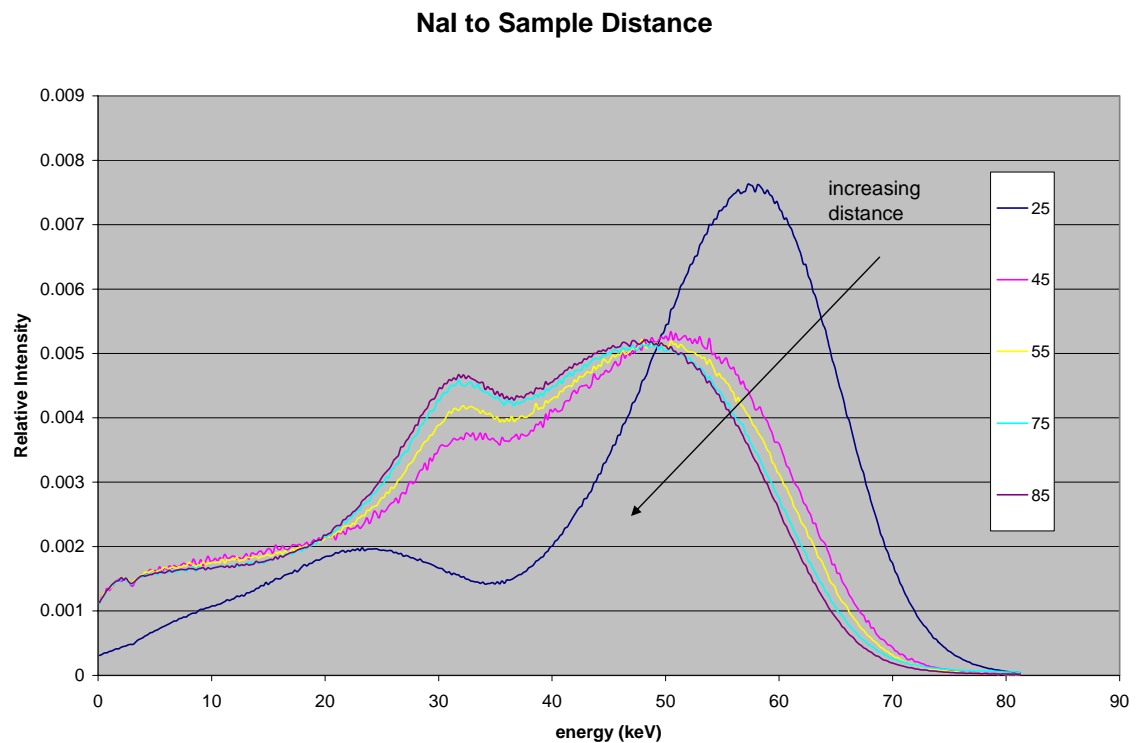


Figure 7.15 Normalized experimental spectral shifts for various detector to sample distances over aluminum.

### **Collimation Extension**

Parallel experiments were done to investigate the effect of varying collimation extension. In these sets, incident energy distribution and detector to source spacing were held constant while collimation extension was varied. These experiments revealed similar, if more exaggerated, trends as the experiments done by varying detector to sample spacing. In these sets the same sort of sharpening of the detected spectra was observed as the collimator extension was increased. This sharpening was similar to that observed previously in that it is apparently caused by both a hardening of the low energy end and a softening of the high energy end of the spectrum.

The mechanisms responsible for spectroscopic shifts and trends in both detector spacing and collimation length extension experiments are identical. The same physical process leads to the energy shifts observed in both experiments and the degree to which the process alters the spectroscopic properties of the detected signal is determined almost purely by geometrical configurations.

The hardening in energy observed on the low energy end of the detected spectrum is due to filtration by photoelectric attenuation. As shown for aluminum in Figure 7.13 above, the photoelectric effect is the dominate mode of interaction by several orders of magnitude at the low energies considered in these investigations (up to about 30 keV).

When a poly-energetic photon beam passes through a media, the lower energy components are preferentially removed since their removal (i.e., photoelectric absorption) cross-section is much larger than that of the high energy photons. Consequently, it is the higher energy photons which have a greater probability of interacting in a media and then returning to the detector. The further a photon beam travels through a material or the more interactions a photon has in a material, ultimately the same thing, the greater the

probability of a photoelectric absorption event occurring. Thus, we would expect deeper penetrating and higher order scattering detected photon fields to reveal larger up-shifts in energy for the low energy components of their distributions. The up-shift referred to here is actually a preferential elimination of the low energy portion of the spectrum which causes the renormalized distribution to appear shifted upwards in energy.

Decreasing detector-to-sample spacing as well as increasing the collimator extension both function to select high order scattering and deeper penetrating backscattered photons. Increasing collimator length, based upon previously verified geometrical arguments, results in the detected signal comprising increasing contributions of deeper penetrating photons. This is shown below in Figure 7.16. As the collimator extension is increased, the critical scattering reference plane moves deeper below the object surface. All scatters occurring above this plane are discriminated against allowing the deeper penetrating photons to be a more prominent part of the detected signal. Similarly, as the detector to sample spacing is decreased, as shown in Figure 7.12, the angle and solid angle subtension to the detector change. The change in the angle is such that photons, scattering in the sample and exiting towards the detector must, geometrically, travel further and thus be attenuated more in the sample before impinging upon the detector. The change in solid angle also functions, though less dramatically, to select for deeper penetrating photons as illustrated in Figure 7.11.

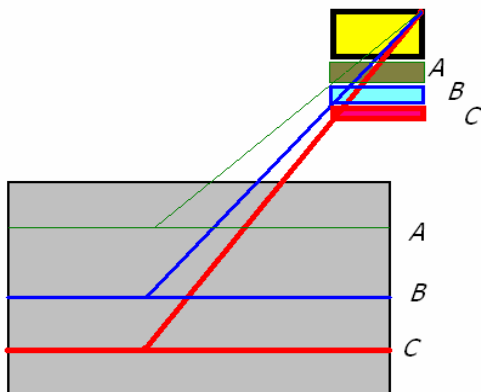


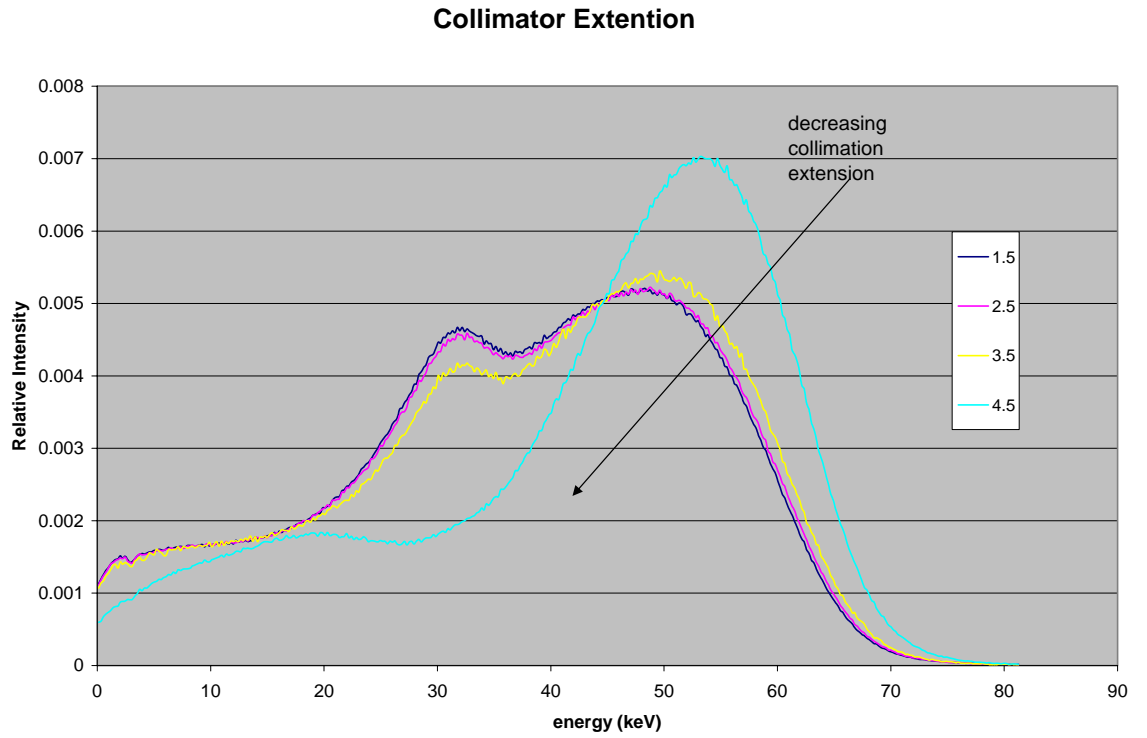
Figure 7.16 Collimator extension and CRP. As collimator is extended from position A to B to C, the critical scattering reference plane moves from A to B to C, respectively. All primary scatters occurring above the CSP do not reach the detector.

The slight softening of the high energy side of the spectra is a result of the energy lost in scattering. Compton scattering, which is the more dominant and relevant phenomena for backscatter scenarios requires that a recoil electron, for momentum conservation, inherit a portion of the incident photon's energy. Thus, the backscattered distribution is expected to be downshifted in energy by at least the amount of energy lost during scattering. Furthermore, this energy loss should increase with increased number of scatterings, increased backscattering angle, and increased initial photon energy.

This shift and the trends describing it are much less obvious than the up-shift in energy at the opposite end of the spectra. At the energies considered in these investigations, up to 75 keV peak, energy lost in a Compton collision is slight. Even in the limiting case of the largest energy photon (75keV) backscattered at 180 degrees, the

energy lost is only 12 keV, and thus the scattered photon returns with an energy of 58keV. Since this shift is barely within the energy resolution of the NaI detectors and because the detected scatters, being mostly first and second order collisions suffer collisions of less than 180 degrees, the shift due to scattering angle is not well distinguished. The shift due to number of scatterings, however, does appear to be detected by the NaI resolution limit and is observed in the expected direction. As collimator extension is increased or as sample-to-detector spacing is decreased, as described above, higher order scatter components are preferentially selected. Thus the softening in energy, due to multiple scatters is observed to increase with both of these parameters.

The following Figures 7.17 and 7.18 show the spectral shifts caused by increasing collimation as NaI-to-sample distance is held constant. Figures 7.17 and 7.18 show the effect as measured and as simulated via MCNP5, respectively. In this set, the NaI to sample distance was held fixed at 8.5cm. The collimator fins were fixed at zero degrees. The spectra were again taken off an aluminum sample with a 75 keV incident photon beam spectrum. The collimator sleeve, for this set, was extended from 1.5 cm to 5.5 cm past the NaI surface.



7.17 Normalized experimental spectral shifts as a function of collimation extension.

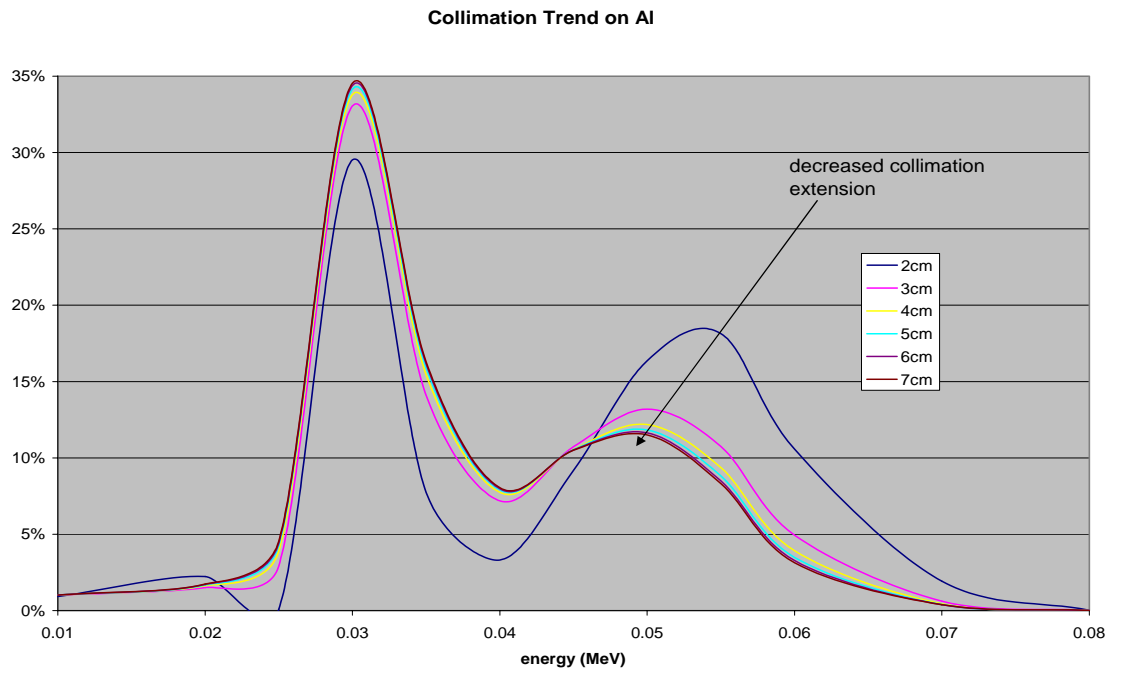


Figure 7.18. Normalized MCNP5 spectral shifts as a function of collimation extension

### **Monte Carlo Verification**

Monte Carlo simulations were conducted to analyze the trends caused by detector and collimator configurations, initial photon energy spectra, flaw type and configuration and target material. The trends observed from Monte Carlo collected data closely agree with those experimentally collected. Additionally, tally component break down by both penetration depth and scattering order support the mechanism proposed above for causing the spectral shifts.

Tally break down by collision component shows that spectra composed of larger fractions of higher order scattering components demonstrate larger shifts, on both ends of the spectra. For completeness, MCNP5 generated spectra along with tally scatter breakdown are compared with similar experimentally recorded spectra in Appendix E.

### **Applications**

Spectroscopic information can be used a guide to visualize the degree of collimation and thus approximate the focusing depth set by the collimation and geometrical configurations. Since the mechanisms resulting in trends due to collimation and detector geometrical configurations are well understood and since the degree of collimation has already been correlated with depth focusing through the previously developed RSD transport model, it is intuitive that the spectral trends observed will serve well as an approximate depth focusing gauge. This gauge of course is relative and must be appropriately calibrated. That is, it is the shift in spectral shape rather than merely the shape itself which is roughly related to focus depth.

Additionally, spectral information can be used to assess the relative absorption and scattering properties of a material. Material compositions can theoretically be estimated based upon the relative shift observed in a backscattered spectrum. This can be

accomplished by establishing a relative scale based upon backscattered spectra from materials of known properties taken at a specific and constant energy and collimation configuration.

The work done in evaluating the spectroscopic trends and the mechanisms responsible for them in this study represent only an initial qualitative investigation. There is much more analysis to be carried out to further detail these mechanism and possible quantitatively relate spectral trends to the variables described above. Additionally, the use of spectroscopy to ascertain relative importance (to image contrast) of various energy regions within the detected backscatter signal is an application that should be investigated in further detail. The concept is that certain regions of a spectrum will exhibit greater shifts and this higher relative contrast between flawed and non-flawed regions of a sample, thus using energy windows to preferentially select these regions may increase overall contrast and decrease scan time.

One of the important obstacles hindering a complete analysis of the backscattered spectra and its trends is that there are always several mechanisms which are filtering the detected spectra simultaneously. It is experimentally impossible to truly isolate one mechanism at a time as each is a strong function of system geometry and thus when one parameter is varied other parameters are often varied as well. If one particular mechanism is not completely dominant, deconvolving the trends with respect to the appropriate mechanism can become very complicated.

## CHAPTER 8 CONCLUSIONS

Development of an accurate qualitative photon transport model and the indicative comprehensive understanding of the phenomena involved in this new imaging modality have led to more effective use of the system and increased awareness of possible future modifications to further increase the performance of the system and its range of applicability. The system has been proved effective on a variety of materials for a wide range of flaws and defects. Additionally, future modifications should increase the systems applicability to other materials and imaging tasks.

### **Applications**

Currently the backscatter X-ray imaging system has proven to be effective in the NDE of materials ranging from ultra-low density materials such as SOFI to higher density materials such as aluminum, steel, and concrete. Key limiting factors in the performance and applicability of the system include scanning speed, detector and x-ray generator head size and impingent x-ray beam energy. The scanning speed is limited by the availability and delectability of an adequate backscattered photon signal. Ideally each pixel should comprise at least 30,000 counts for good image quality and statistical validity. This signal in turn is limited by the current available from the x-ray generator. Image resolution which is a function of pixel size is also a factor in determining scanning speed. Increasing number of pixels a particular image is divided into increases resolution, obviously an artifact smaller or about the size of a pixel will not be well detected, and increases scanning time. Thus a balance must be reached for each

particular scanning application between speed and resolution. The size of the detector and x-ray generator assembly determine the type of areas which can be scanned. While many applications effectively involve scanning one side of a plane and are not susceptible to size constraints, many other application require tight detector configurations in order to scan in between various structures of a target. Besides electron current limitations, the x-ray generator also imposes limitations on the maximum peak energy spectrum available. This in turn limits the depth into a particular material which can be imaged.

### **Recommendations for Further Developments**

#### **Detector Configuration**

With the possibility of new, smaller detector components (e.g.- 0.11 inch YSO detectors mounted onto state of the art miniature photomultiplier tubes ~ 3" in length from Hamamatsu) comes the possibility of modifying the current imaging system to achieve a broader range of applicability. Rather than the current rigid detector mounting system with fixed detector orientations and positions, a new mounting system is proposed to allow 2 more degrees of freedom in detector positioning. That is, rather than the detector to sample geometrical configurations being a pure function of detector to sample spacing and collimation extension, the new system should allow for the detector to be moved both laterally (radially in and out) and vertically (up and down) with respect to the X-ray generator and mounting base. Additionally, the detectors (or at least the detector heads) should be mounted on a pivot so that their orientation relative to the backscattered photon field can be varied. Such modifications would permit the imaging system to be applicable to a new class of situations with tighter, smaller geometries for which the current system, because of its large and rigid detectors, is not practical. Additionally, a

larger range of detector mobility will allow for more accurate and more efficient selection of backscattered photon field components.

Analysis of the backscattered signal components via MCNP5 and supported with experimental observations and analytical calculations has led to a more thorough understanding of the imaging processes and firmer grasp of the various components of the backscattered photon field and the importance of the information that they carry. As a result of this analysis, a transport model has been developed to detail the mechanics and processes leading to a contrast generated image of various flaws in a target. Application of this model has further led to the understanding that while the fundamental physics of the imaging process remain the same, the optimal detector and collimator configuration is often task specific and the more freedom and versatility of the detector configuration the easier and more efficient image acquisition becomes.

### **Detector Materials and Operation Modes**

Detector material type and operational mode are an integral part of the system and can have a marked effect on the acquired image quality. Since it is the photon interactions within the sensitive volume of a detector with lead to a signal and thus an image. Each detector material has its own unique interaction characteristics and thus, to some extent, should produce slightly different images of a given scenario.

Although plastic scintillator type detectors were considered in this investigation, a more thorough investigation into their capabilities is worth while. In particular, the nature of the plastic detectors, their large photon mean free path and fast response time, makes them inclined to be operated in current rather than pulse mode. Since their photon stopping power makes them virtually useless in spectroscopic applications, there is no real value in operating them in pulse mode. A current mode operation would take better

advantage of their fast response time and allow for extremely high count rate and potentially faster scanning times. Additionally, plastic scintillators are more rugged, less expensive and can easily be manufactured into a variety of shapes.

YSO detectors are also worth considering. YSO are more rugged, and have faster response times than NaI. P.I.N. diode detectors are smaller and can handle extremely high counts. Current state-of-the-art P.I.N. diode components and their properties may be a worthwhile investigation for future applications.

### **MCNP5 simulations to be considered**

Monte Carlo simulations are a powerful tool to quickly assess the potential of various detector and impinging photon beam geometries and to test the range of applicability of the system and the detectability of various classes of flaws. Among the more promising configurations that should be simulated and analyzed are those which tilt the detector surface at various degrees with respect to the horizon. Currently only simulations with the detector face parallel with the sample surface have been evaluated. The potential benefit of angling the detector face, as previously discussed, include faster scanning times and more efficient photon collection. Additionally, Monte Carlo simulations should be run with the photon beam impinging at an angle. This may prove especially useful in analyzing carbon-carbon laminates and other striated type materials. The theory here is that a small delamination often does not present significant electron density changes in the transverse direction and possible a photon beam directed along the delamination flaw may experience more significant attenuation differential than a similar beam impinging normally to the flaw length. Other simulations that may be of interest include various detector materials and incident photon beam energies.

### **Optimizing geometrical variables**

Geometrical and configurational variables of the system include detector to sample vertical spacing, detector to source radial separation, collimation extension and detector surface angle relative to both incident beam direction and target surface. The perturbations in the backscattered spectroscopy and photon field has been investigated for the first three variables listed and the effect of the last has been mostly speculation with minimal experimental or analytical data. It is clear that each of these variables affects the properties of the detected backscattered photon field and thereby can affect the quality of the image generated by the preferential collection of these photons.

Current data indicates that these variables do not function independently of one another. That is, the portion of the total backscattered photon field observed by the detector is an intimate non-linear function of all of these variables. Thus, while the relative effect of each of these variables can be isolated for specific scenarios, the combined net effect of all of them is important to the configuration which results in the optimum balance between the highest quality image and the fastest image acquisition time. Further investigation into the interplay between each of these variables has potential to increase the understanding of the imaging system and increase the efficiency of focusing optimization routines.

APPENDIX A  
SELECTED SABRINA GENERATED PHOTON TRACK PLOTS

The following figures are SABRINA plots with these geometric specifications:  
0.6 cm from lead collimator to aluminum sample surface 4.3 cm from NaI to Al.  
5.05 cm radius detectors 9 cm centerline-to-centerline from the beam.

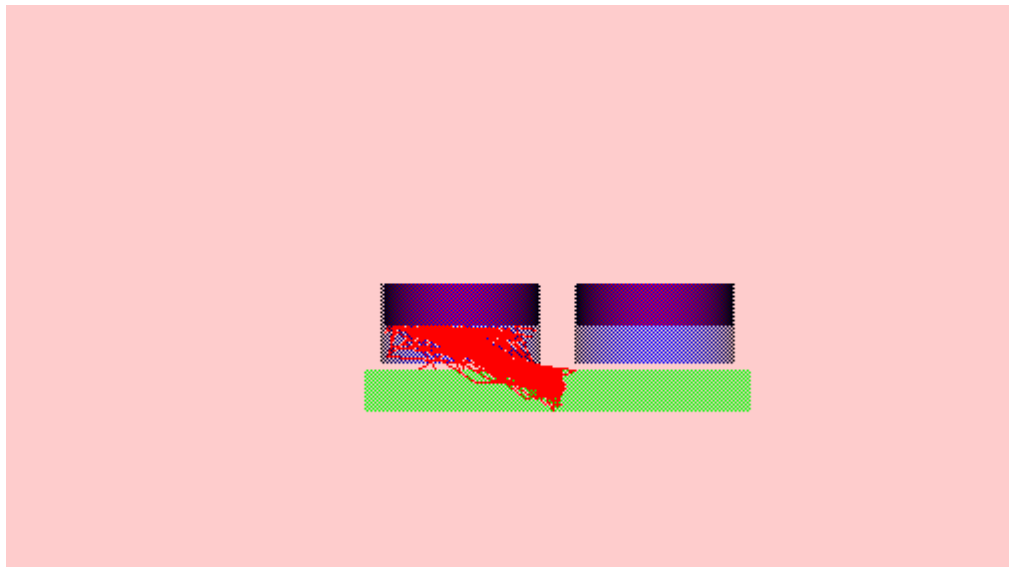


Figure A1. Photons having four or less collisions (void flaw)

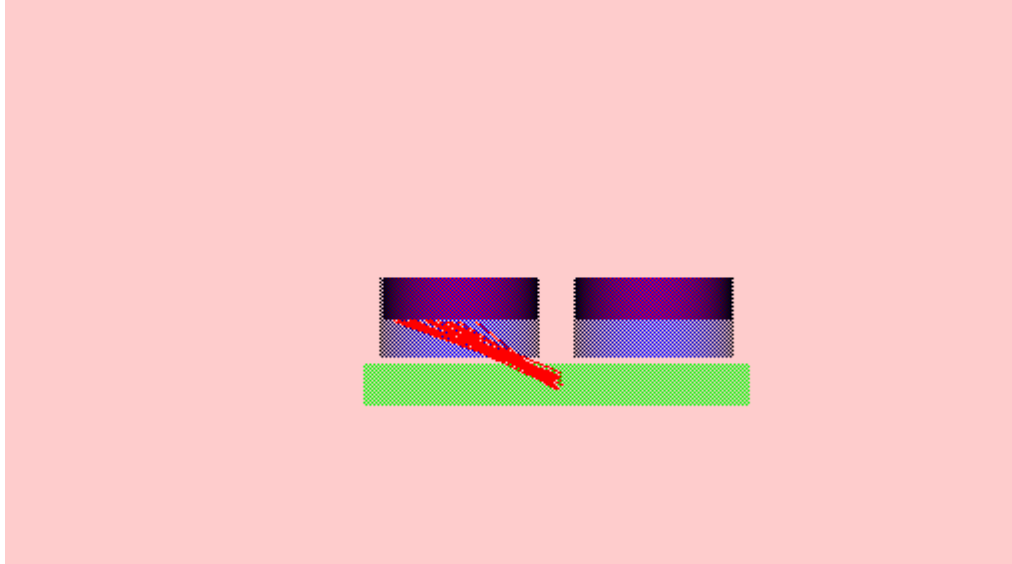


Figure A2. Photons having one collision (void flow)

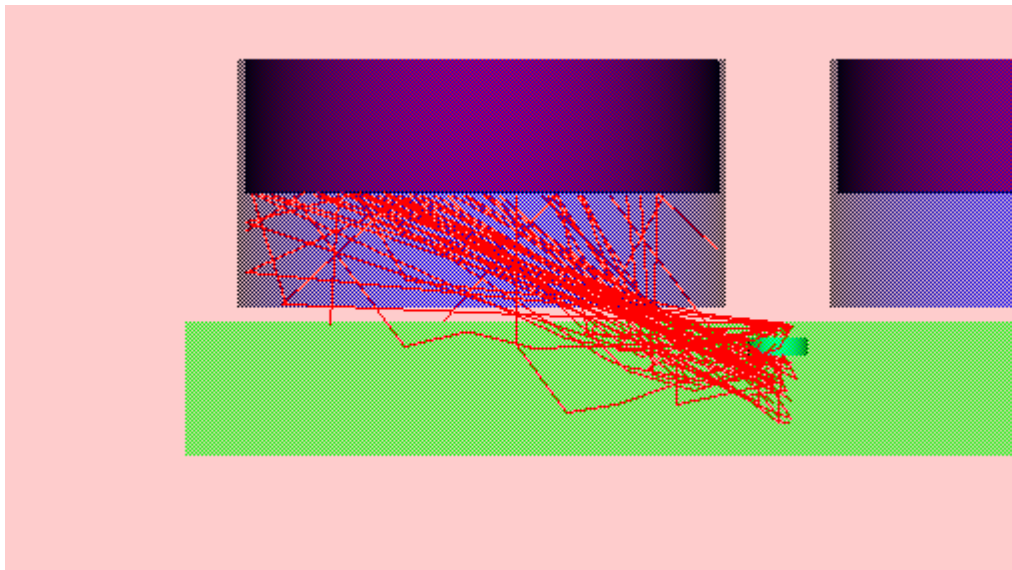


Figure A3 All photons entering detector (history filtered for clarity-void flow)

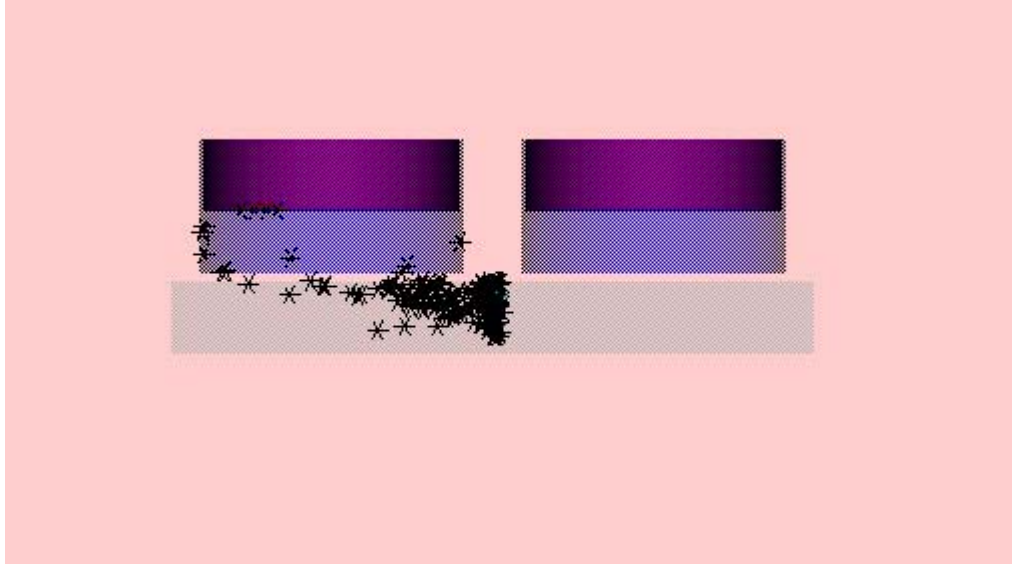


Figure A4 All photons entering detector. Scatter sites marked with black X (plastic flaw).

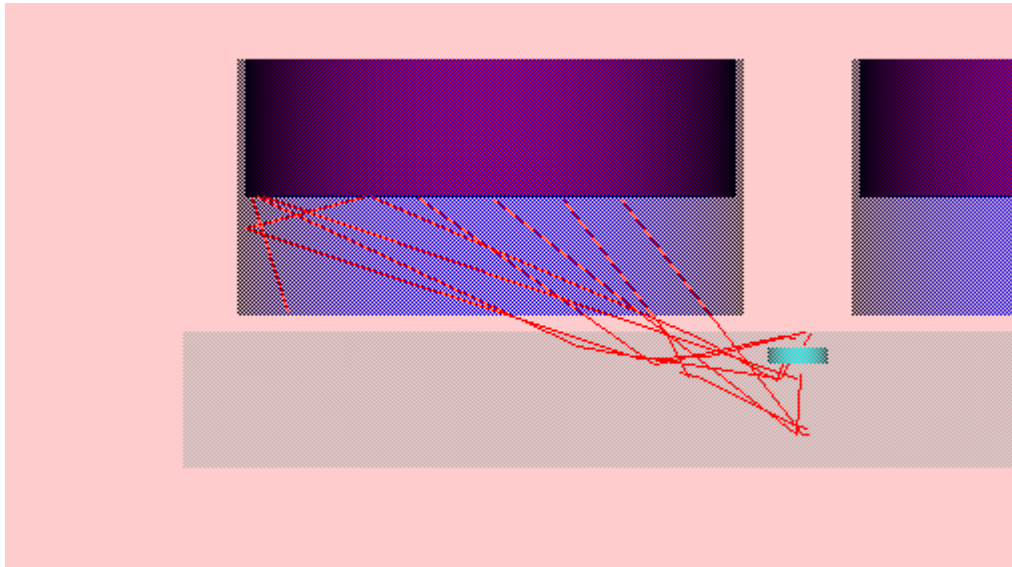


Figure A5 All collision components, history filtered (plastic flaw)

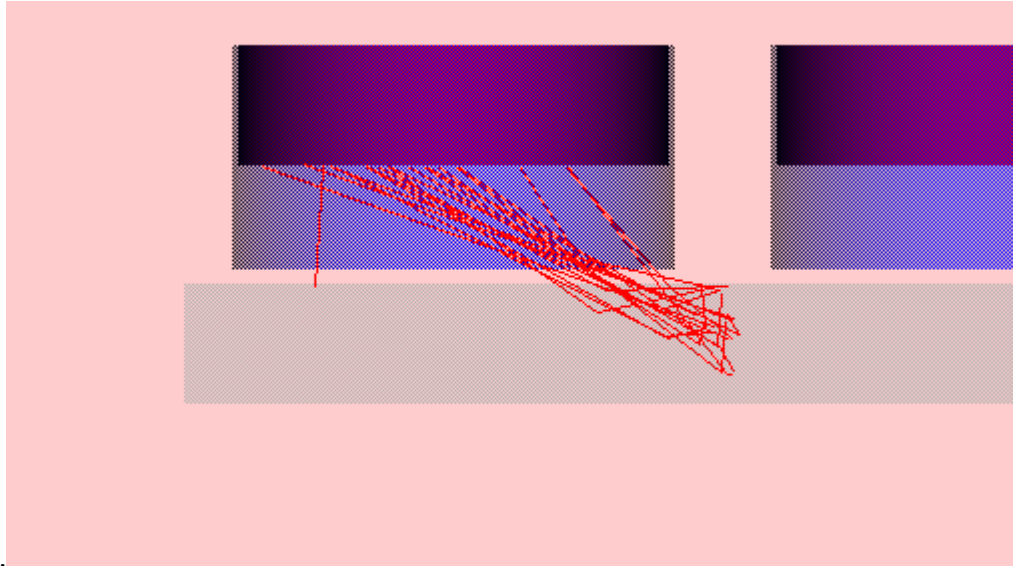


Figure A6 No flow first through fourth collision components

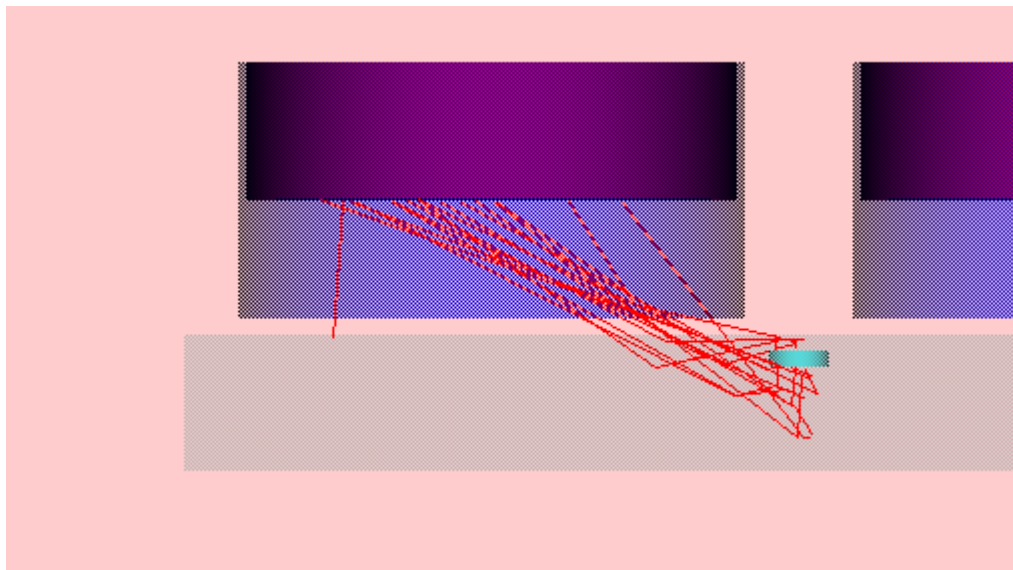


Figure A7. Plastic flow first through fourth collision components

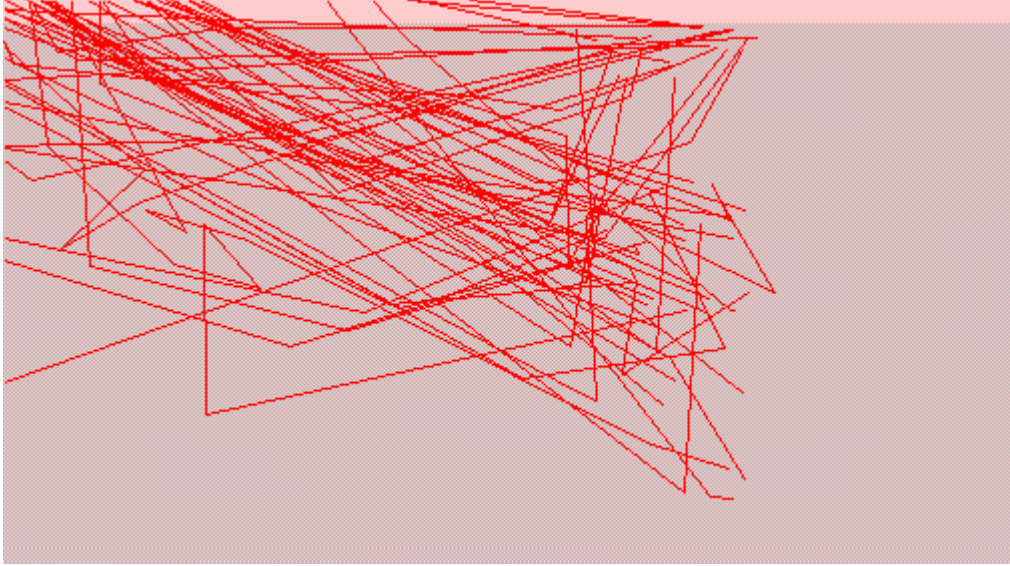


Figure A8. No flaw all collision components, zoomed in view.

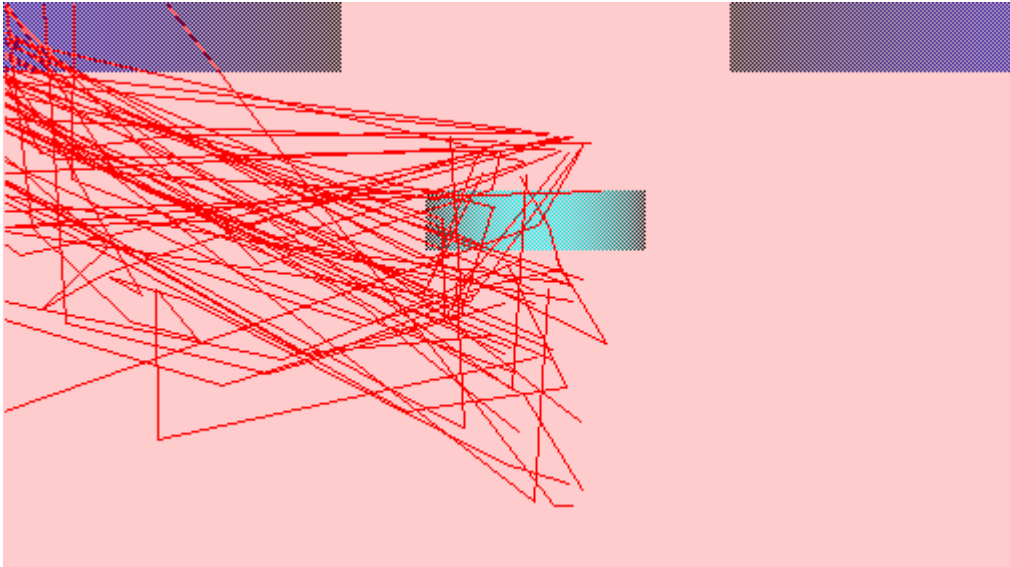


Figure A9 Plastic flaw all collision components zoomed in view

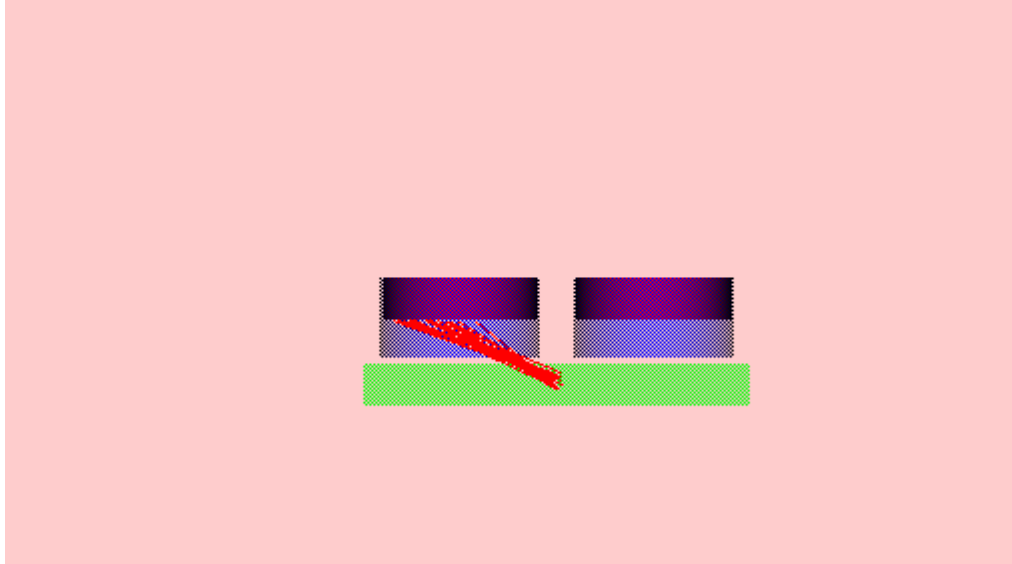


Figure A10 Plastic flaw first collision components

**The following figures are SABRINA plots with these geometric specifications :**  
**Lead collimator 2.6 cm from aluminum sample surface 4.3 cm from NaI to Al. 5.05**  
**cm radius detectors 9 cm centerline-to-centerline from the beam.**

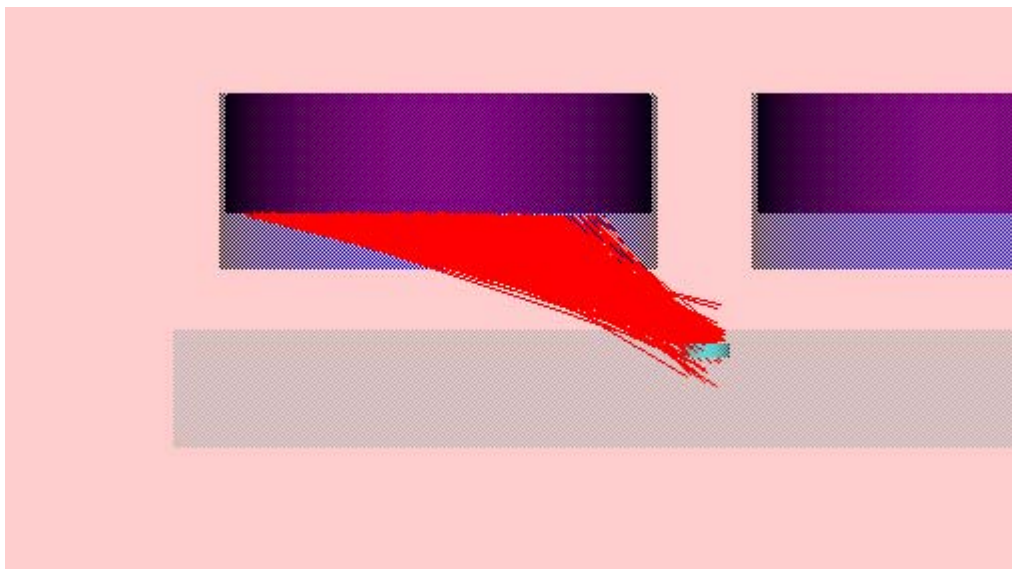


Figure A11 Plastic flow first collision component.



Figure A12 Plastic flow first collision scatter points.

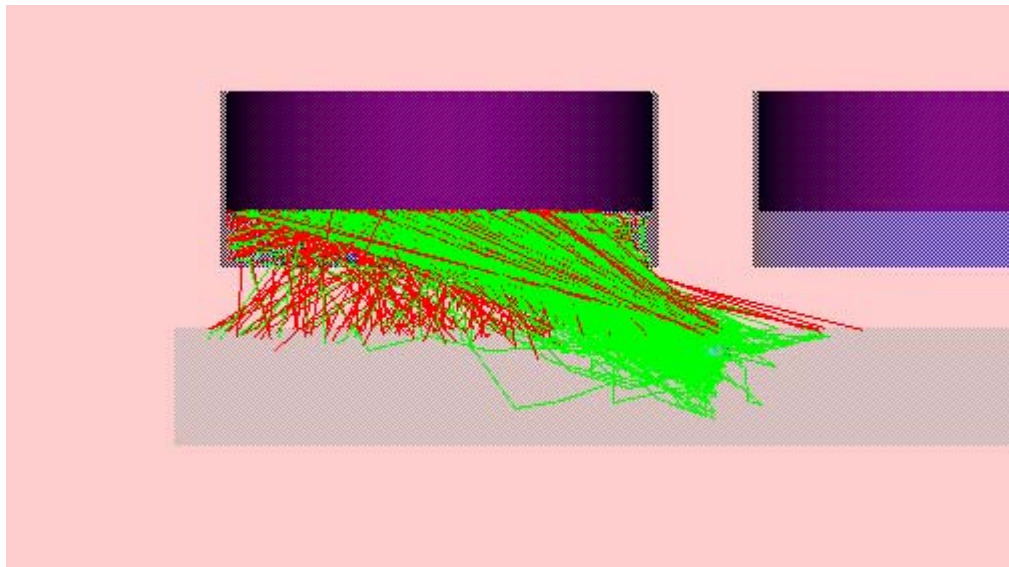


Figure A13 Plastic flow, all scatter components (note many scatters off the NaI surface and down back into Al)

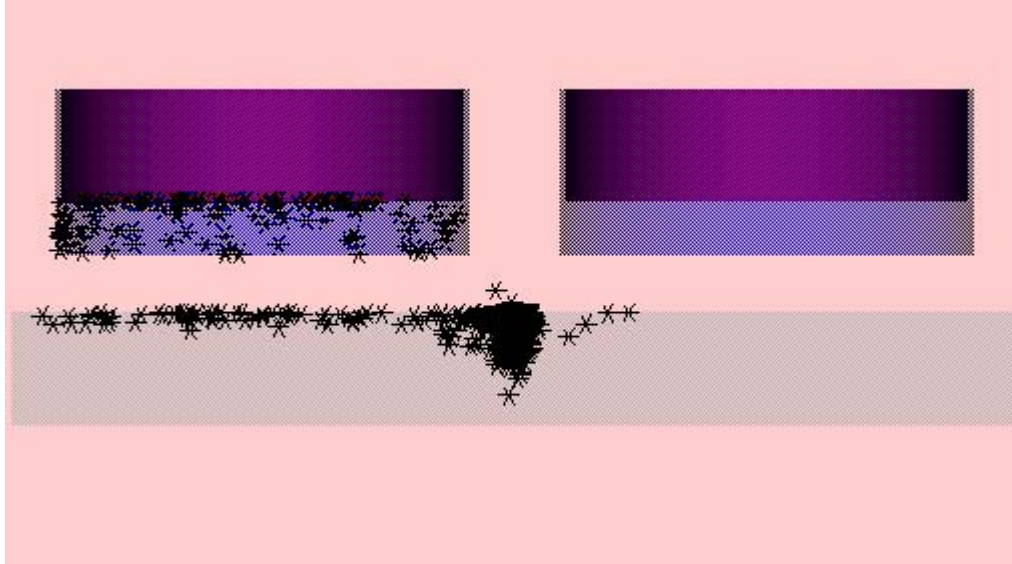


Figure A14 First and Second scatter points

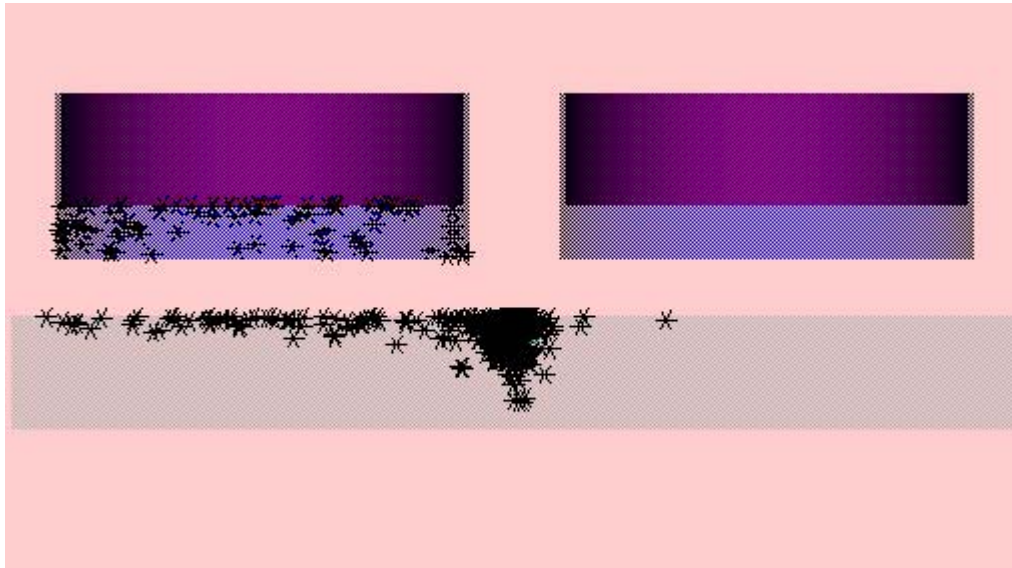


Figure A15 Multiple scatter sites.

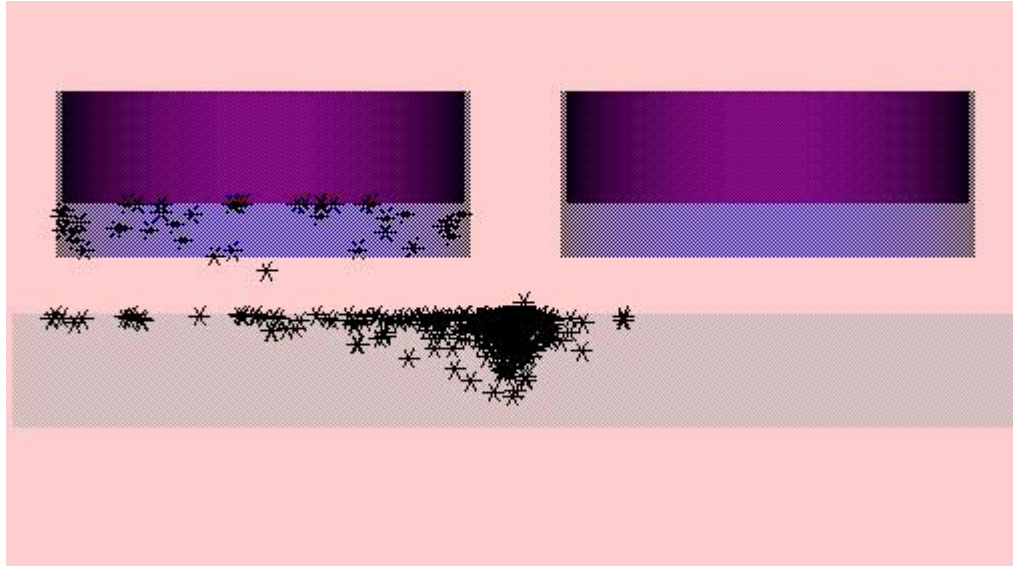


Figure A16 First, second, third scatter points.

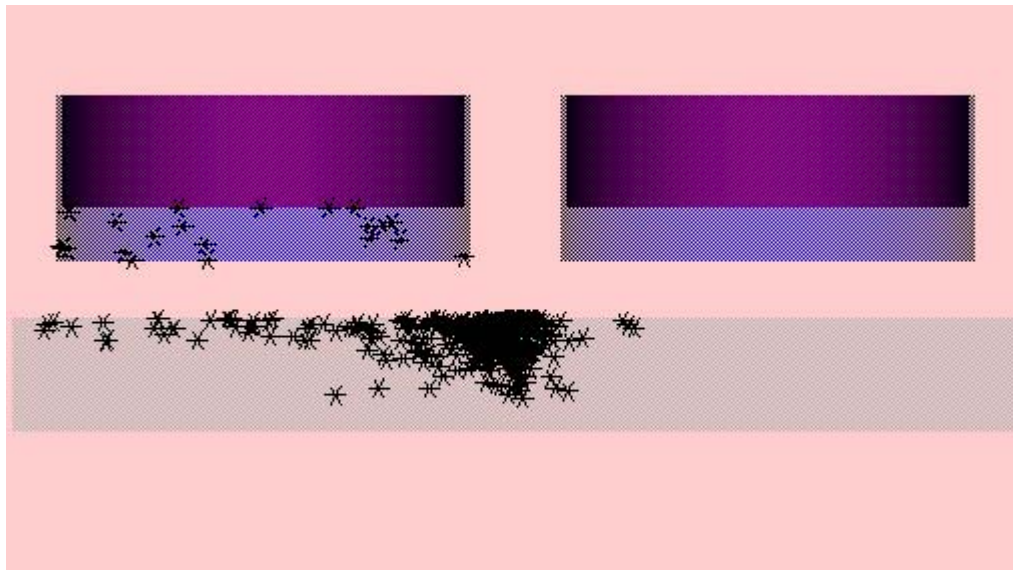


Figure A17 First, second, third, fourth scatter points.

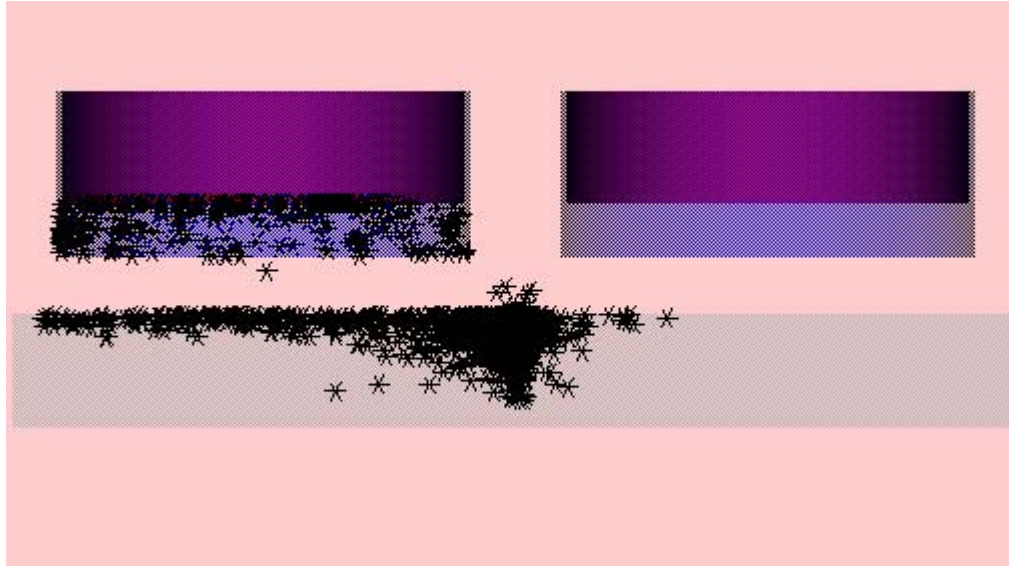


Figure A18 All scatter points.

**The following figures are SABRINA plots with these geometric specifications :**

**4.3 cm to NaI 1 cm to collimator, from Al sample surface.**

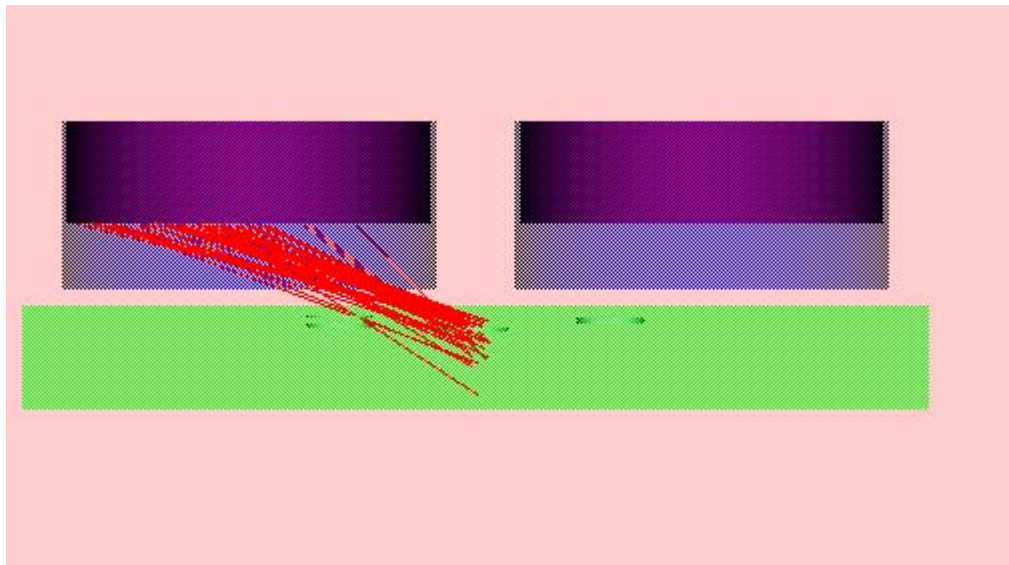


Figure A19 Void flaw first collision components

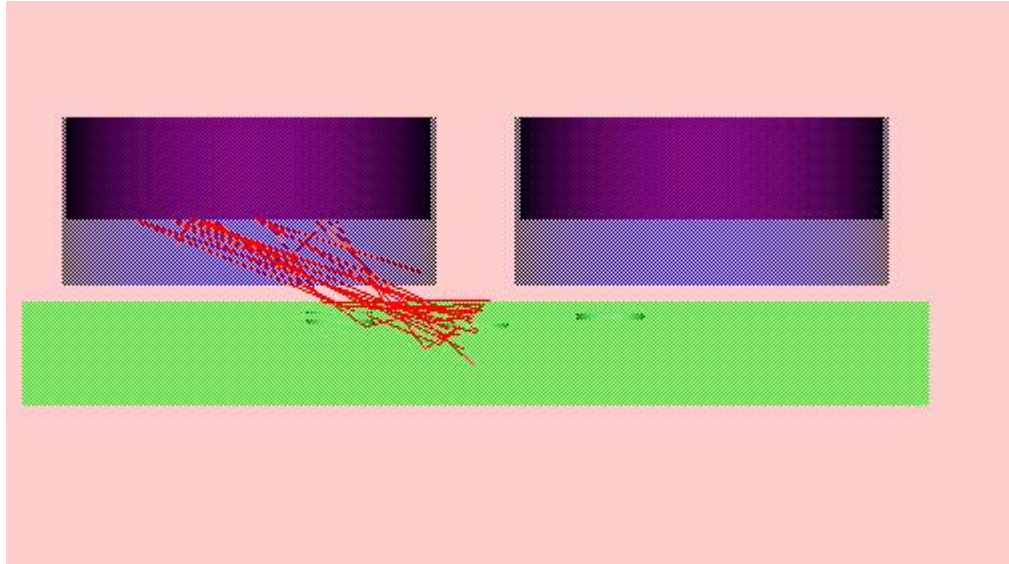


Figure A20 Void flow all collision components.

**The following figures are SABRINA plots with these geometric specifications :  
8.5 cm to NaI 4 cm to collimator, from aluminum sample surface 5.08 cm radius NaI  
detectors 9 cm from beam**

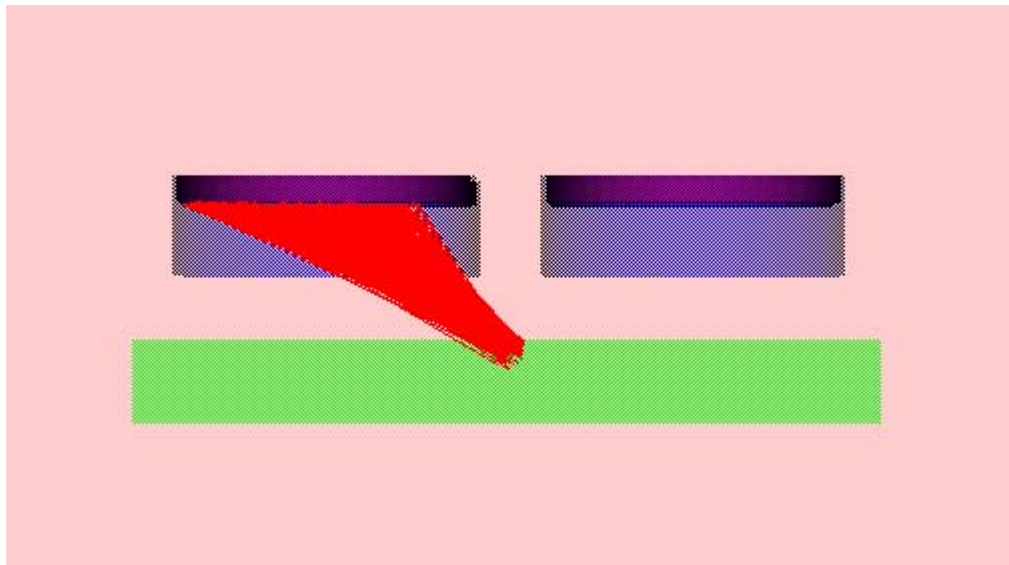


Figure A21 First collision components

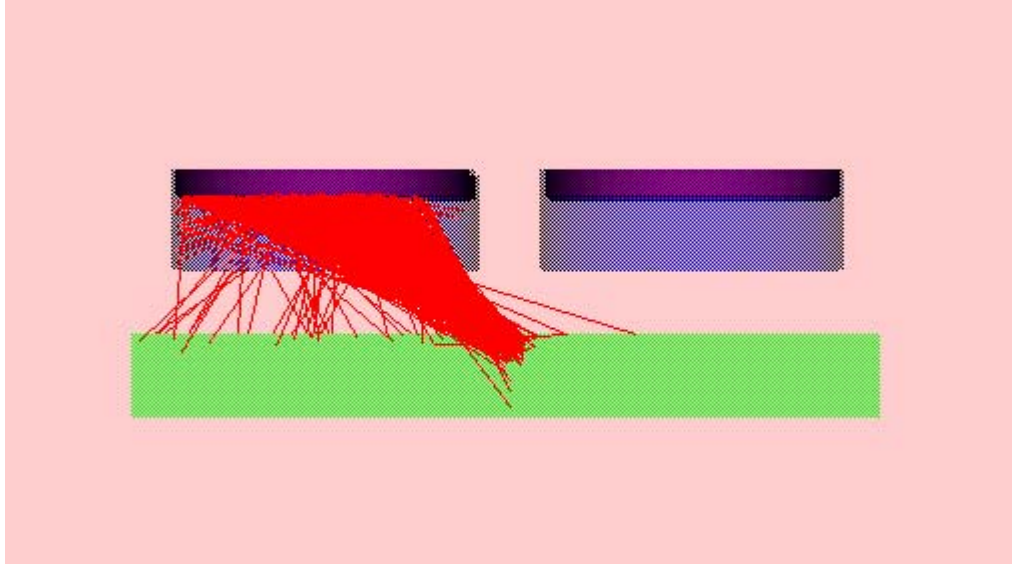


Figure A22 Second collision components.

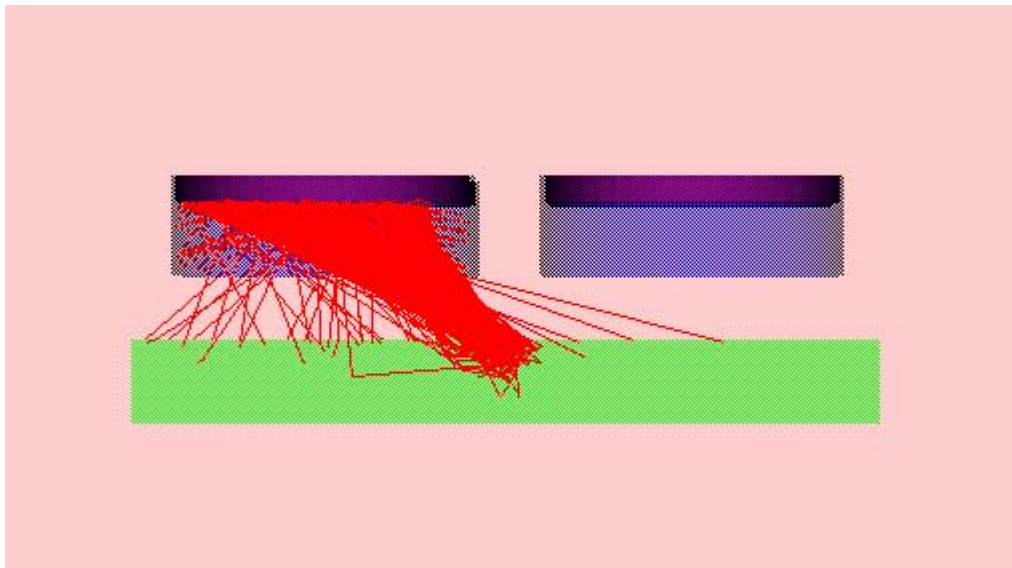


Figure A23 Third collision components

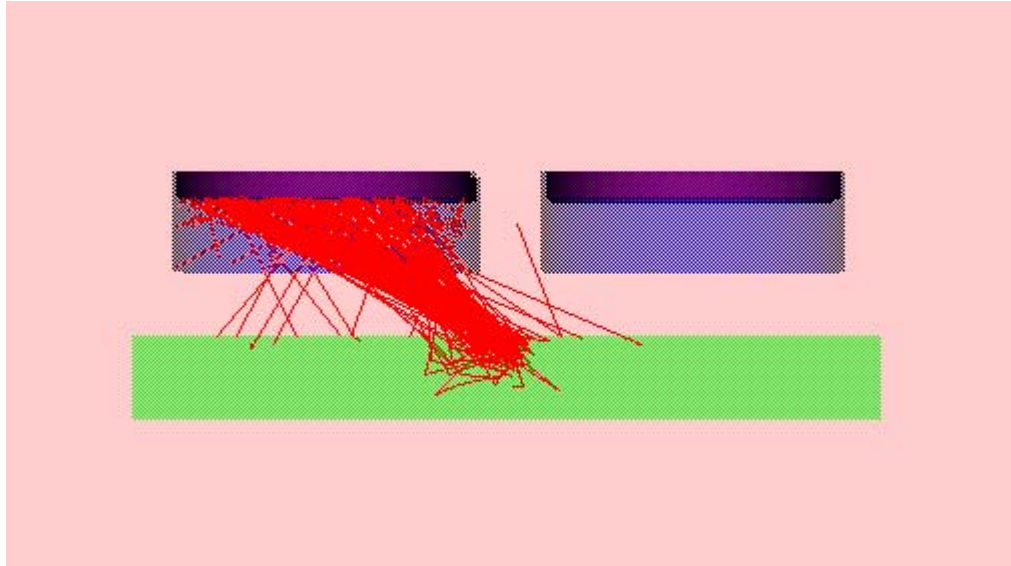


Figure A24 Fourth collision components

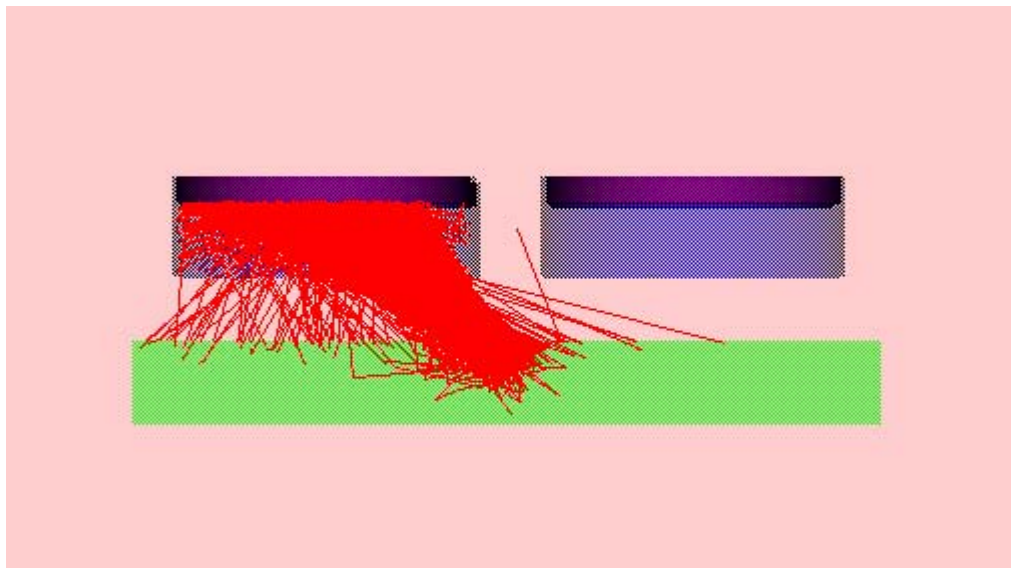


Figure A25 All collisions. (note photons reflecting off NaI surface and scattering down towards Al sample.)

The following figures are SABRINA plots with these geometric specifications :  
8.5 cm to NaI 7 cm to collimator, from aluminum sample surface 5.08 cm radius NaI  
detectors 9 cm from beam

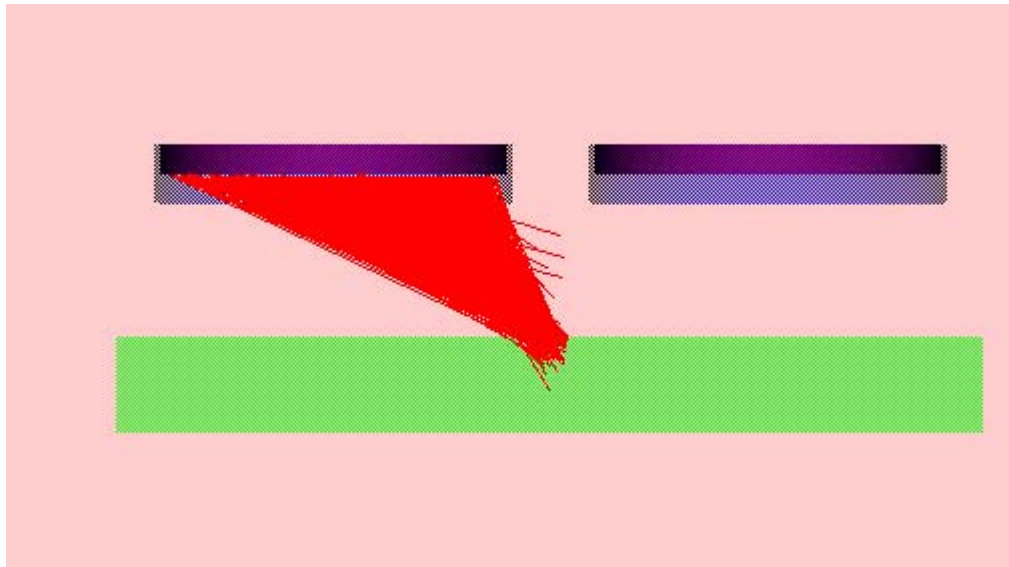


Figure A26 First collision

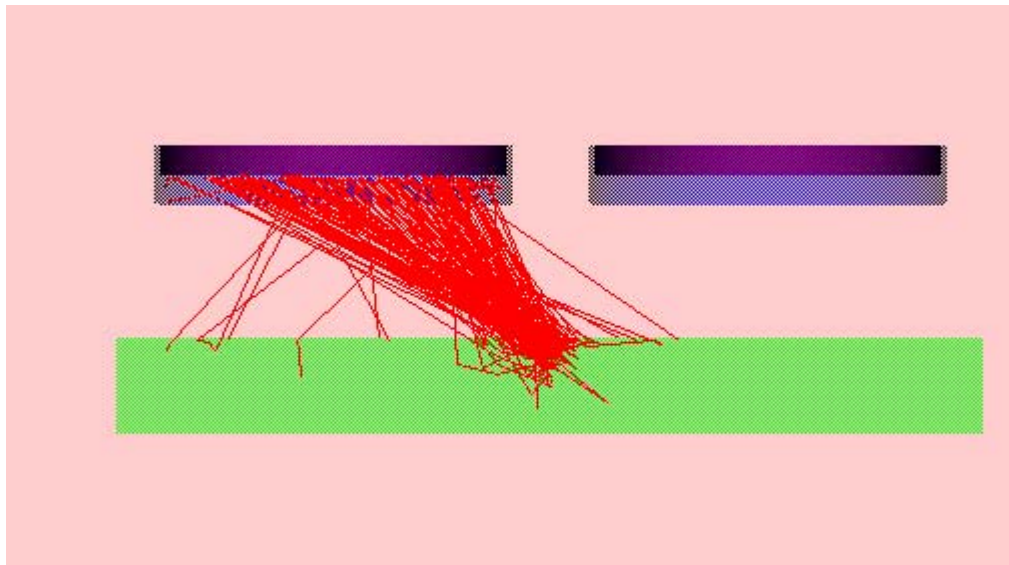


Figure A27 All collisions

Scenarios from chapter 4 (Figures 4.14 A-L)

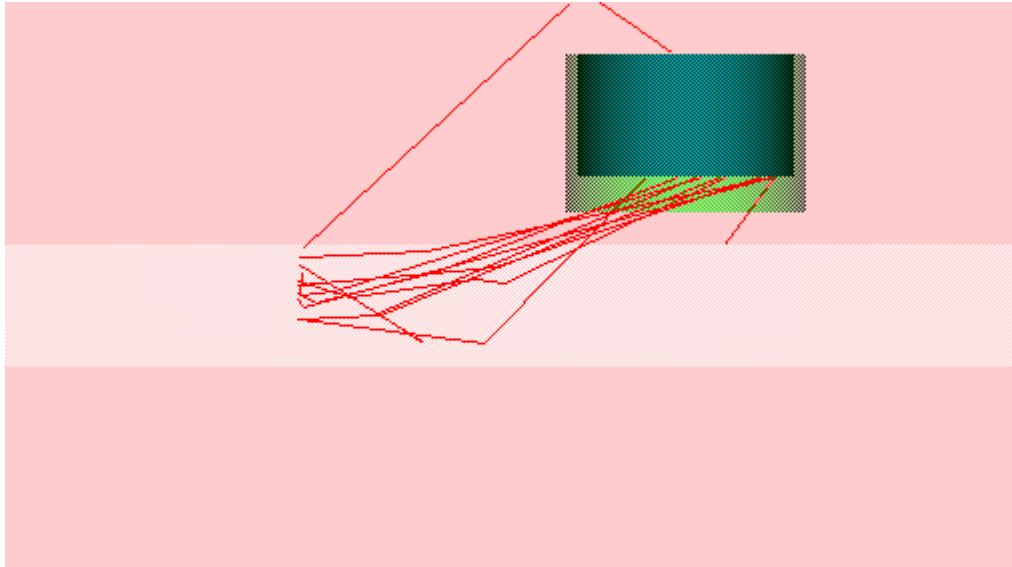


Figure A28. No flaw.

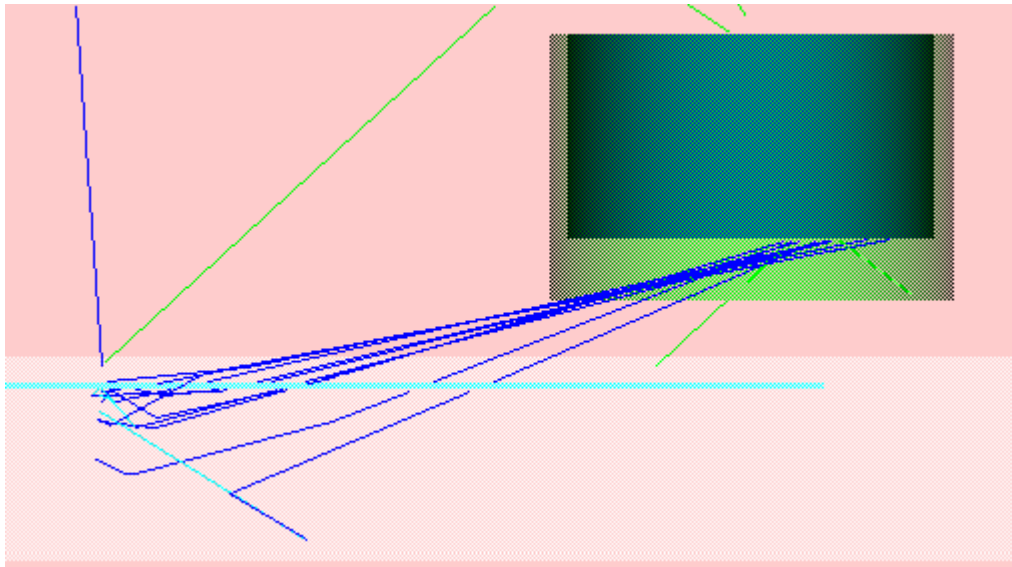


Figure A29. SSL

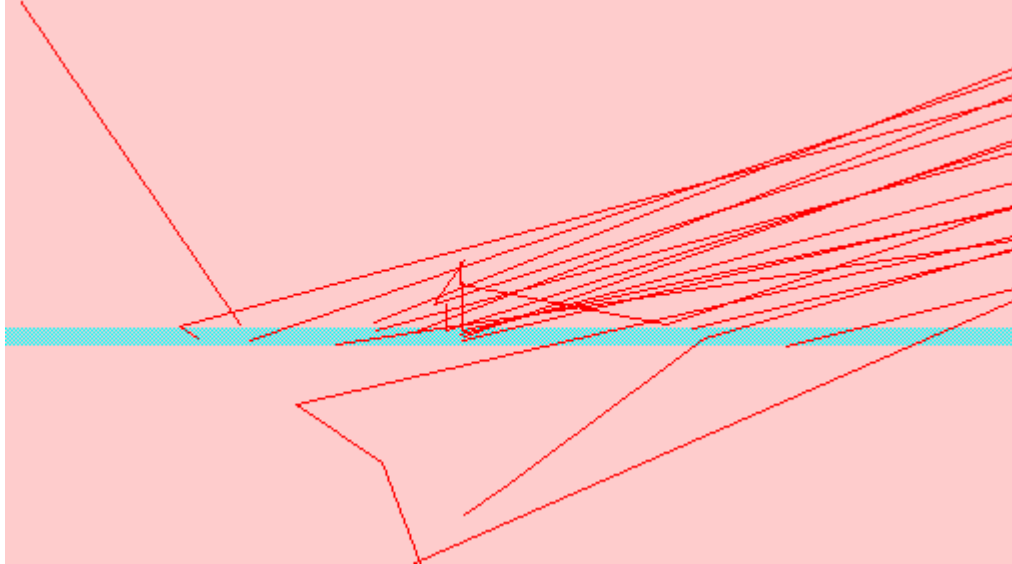


Figure A30. SSL zoomed in view of tracks across flaw and aluminum.

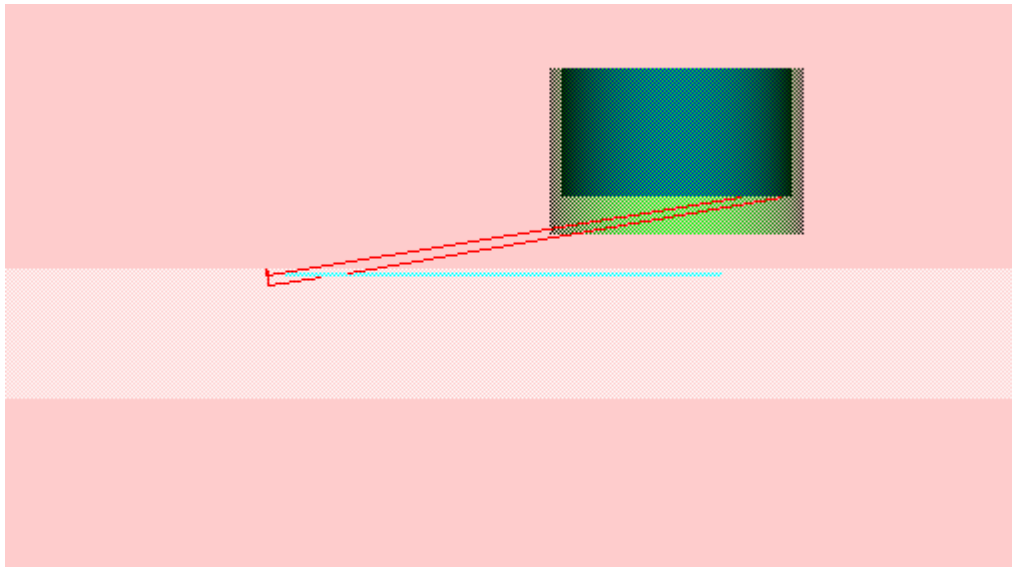


Figure 31. SSL. Flaw is above CRP

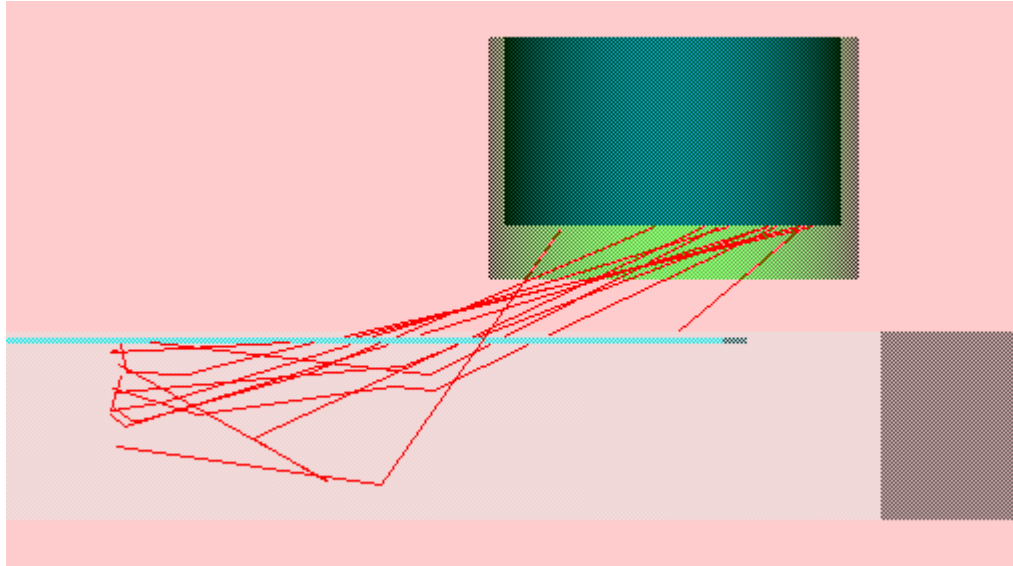


Figure A32. SSL.

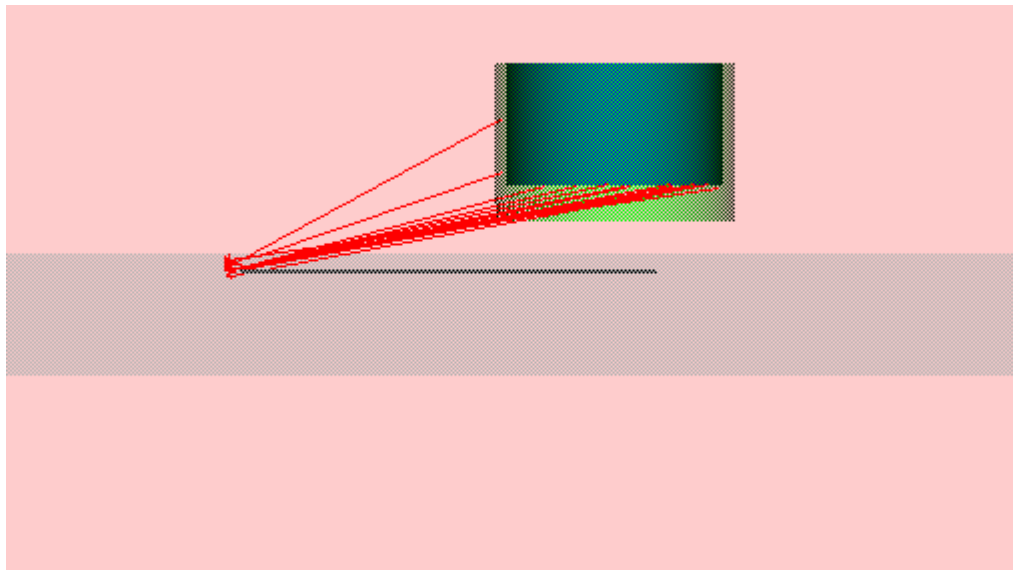


Figure A33. ADL flaw is below CRP.

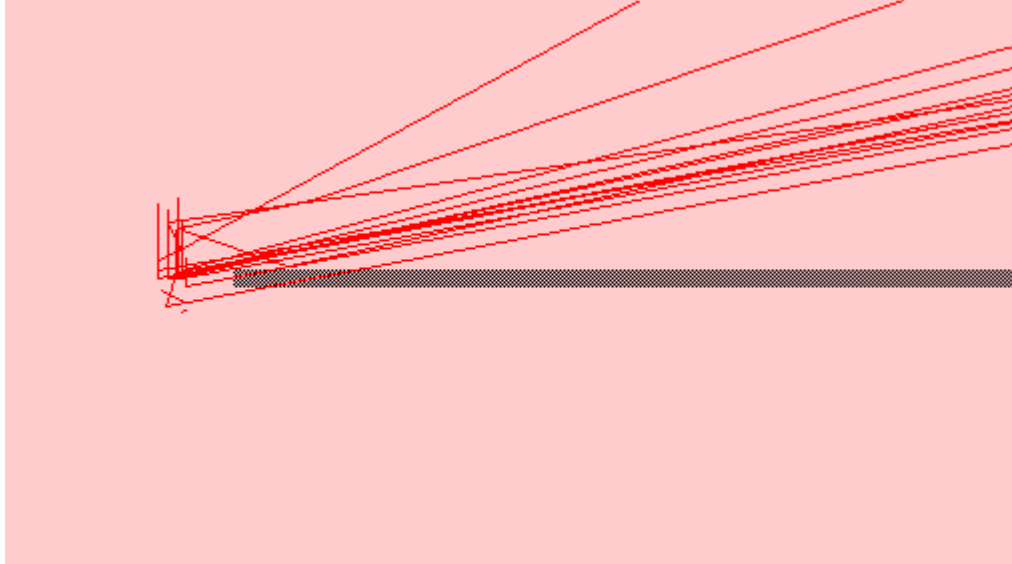


Figure A24. ADL zoomed in view.

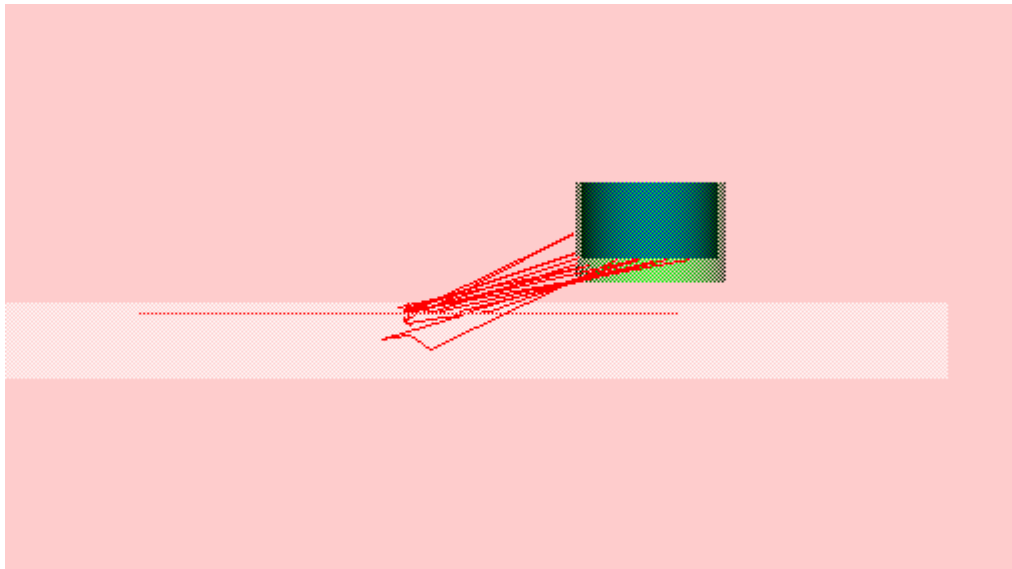


Figure A35. VDL. Flaw is below CRP.

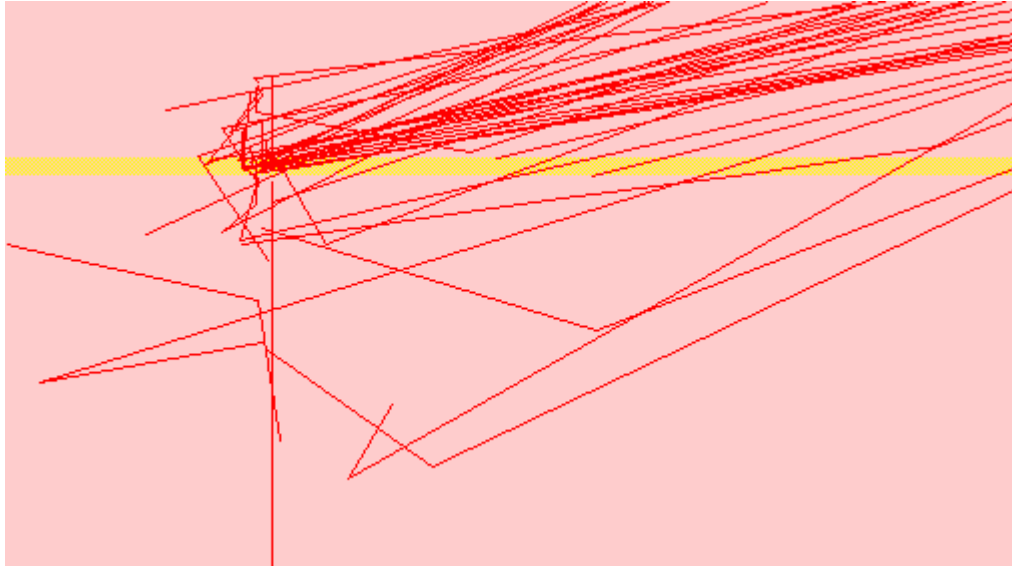


Figure A36 VDL zoomed in view.

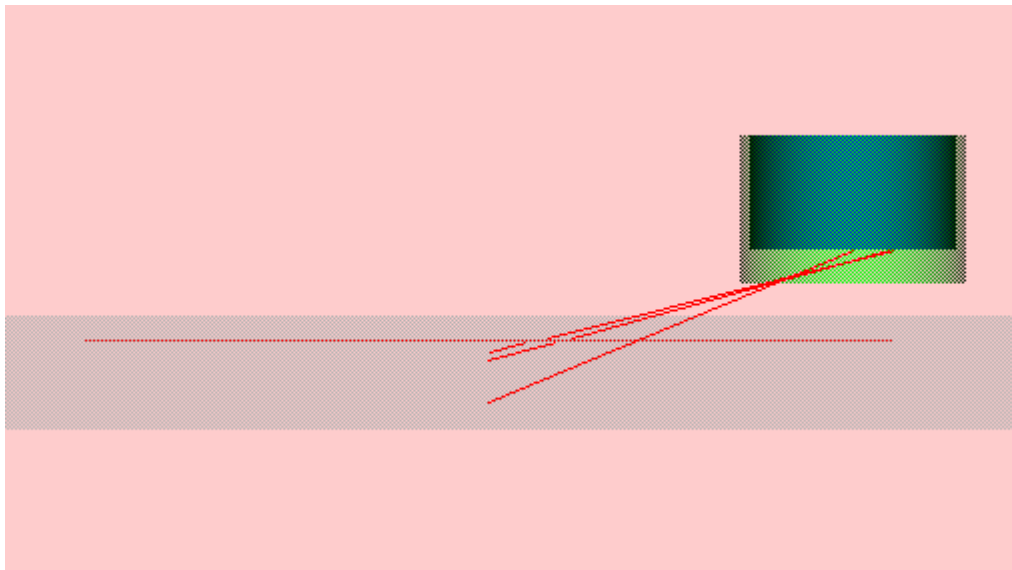


Figure A37. VSL. Flaw is above CRP

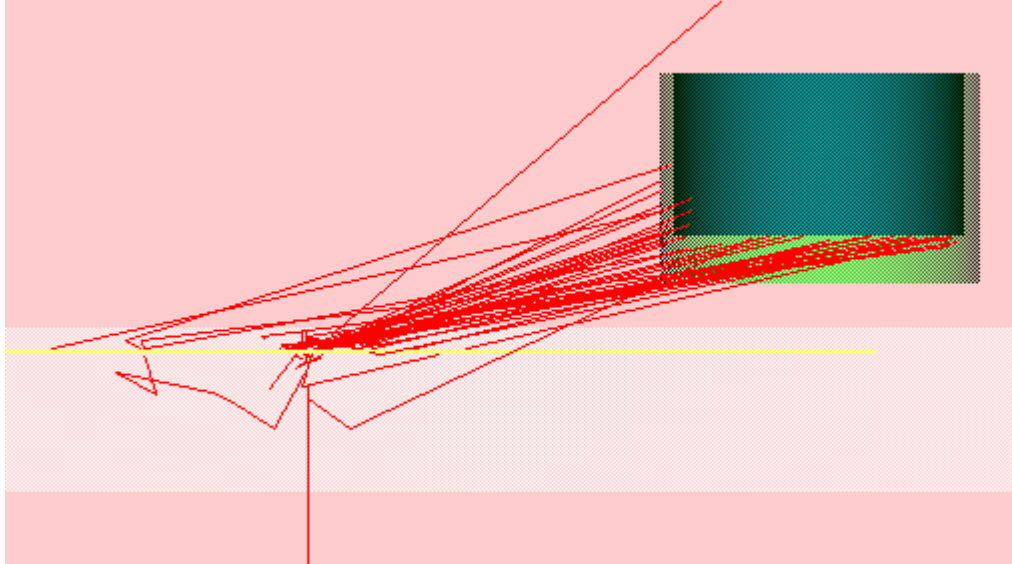


Figure A38. VDL, flaw shown opaque.

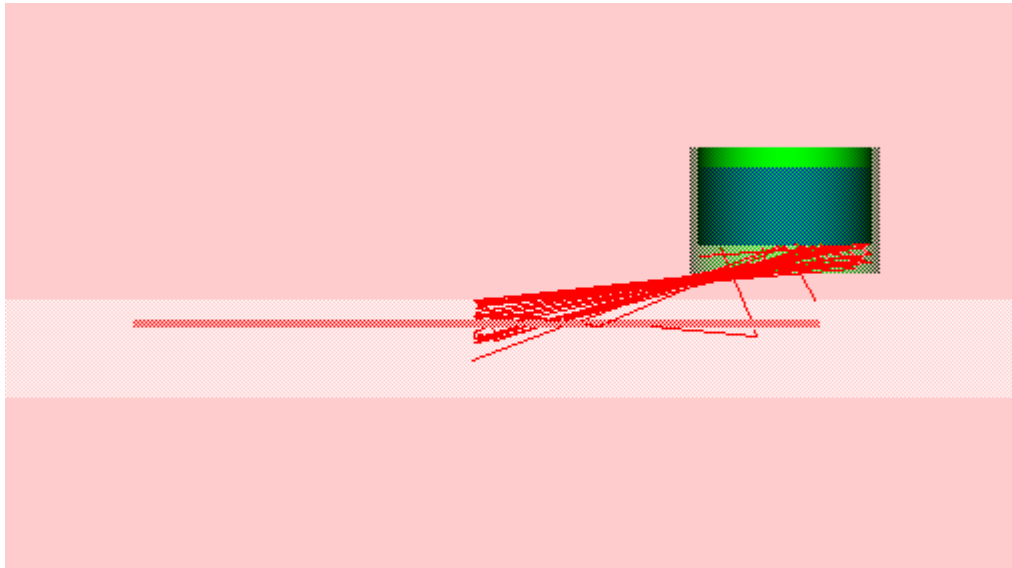


Figure A39. VDL.

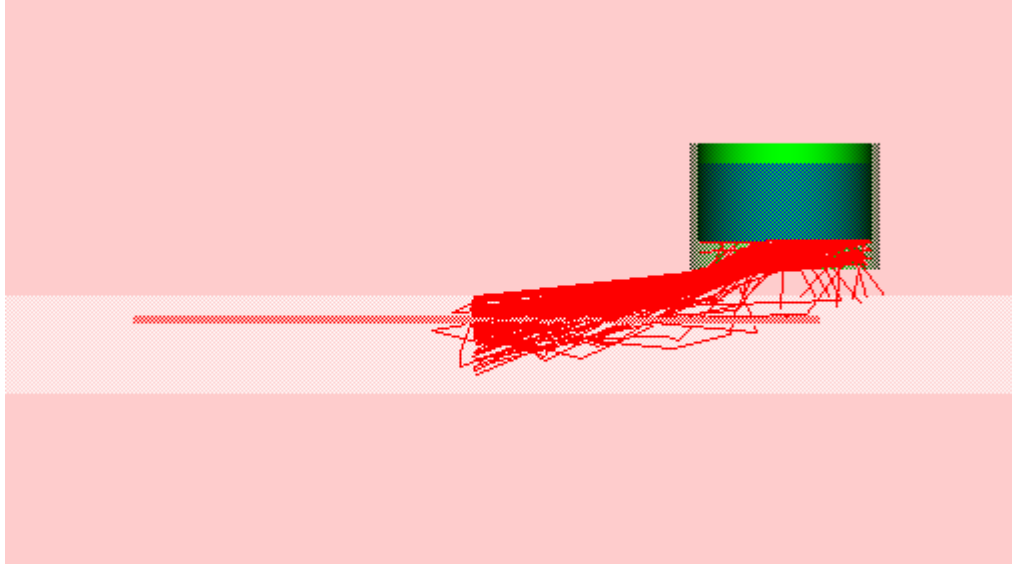


Figure A40. VDL, flow is transparent. Notice that photons of all scatter order traverse the flow directly.

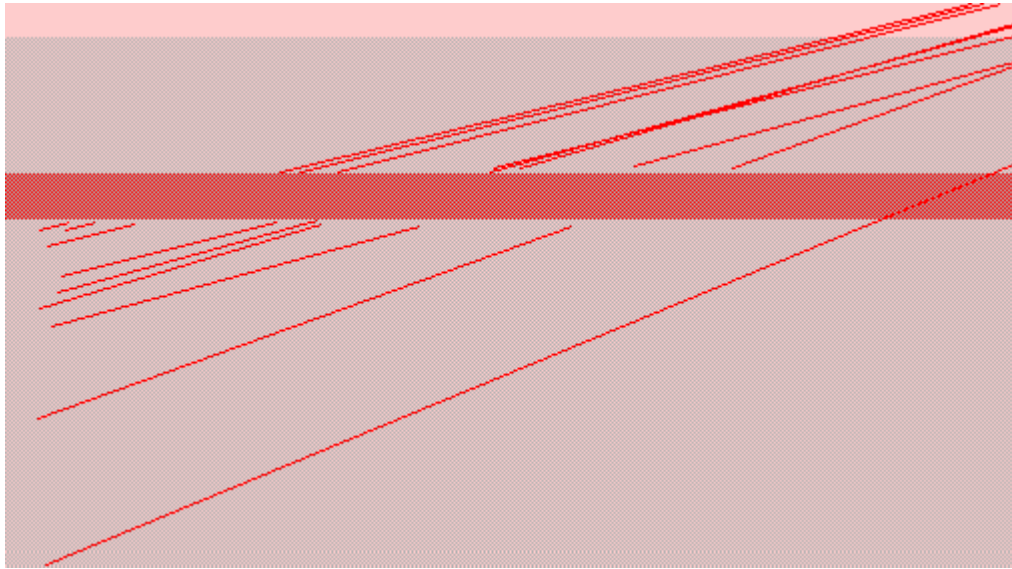


Figure A41. VSL zoomed in view.

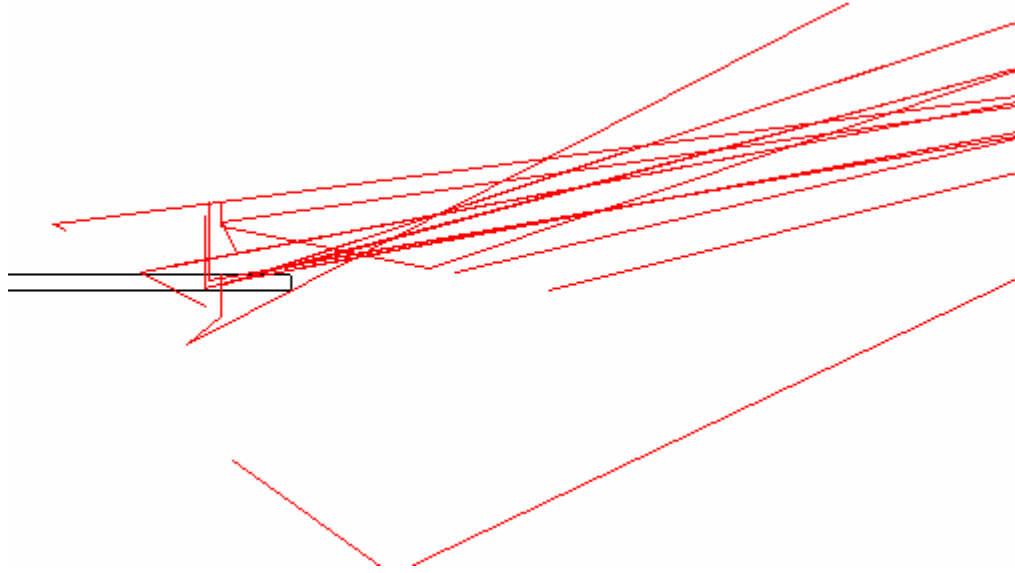


Figure A42. VDE. Aluminum and flaw are both set to invisible to emphasize simple photon tracks.

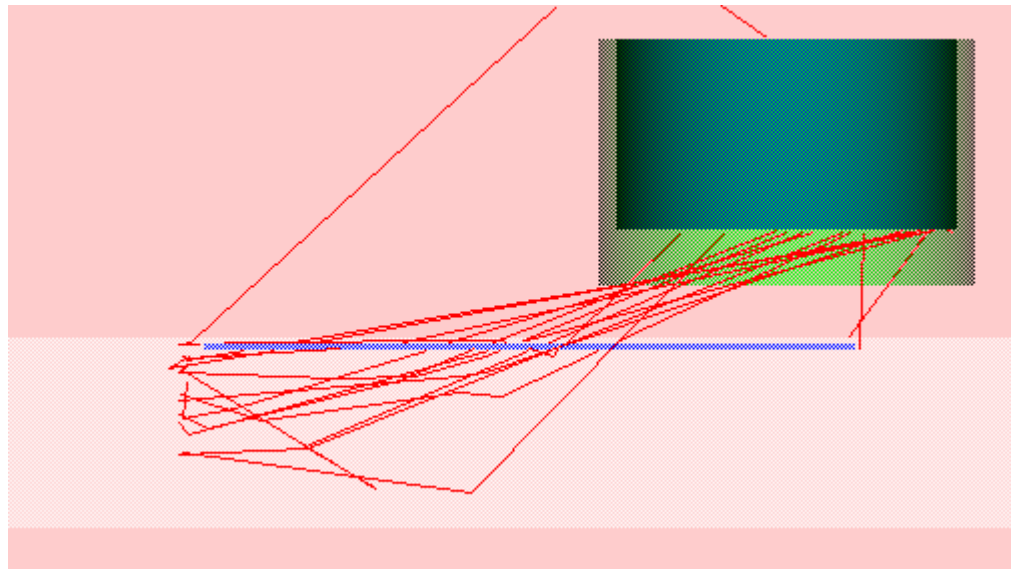


Figure A43. ASL. Photon on far right are reflecting off NaI, going up into it.

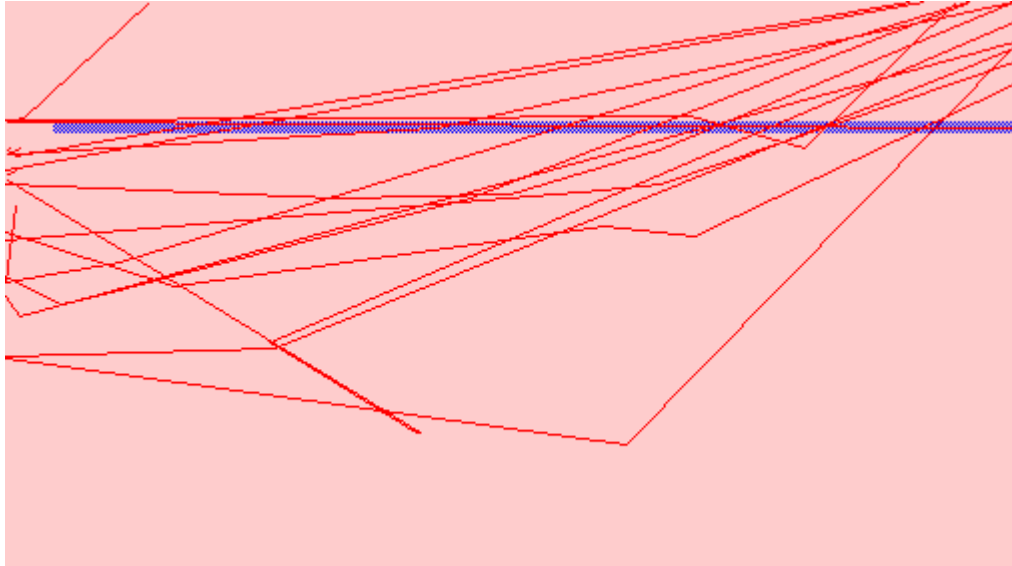


Figure A44. ASL zoomed in view.

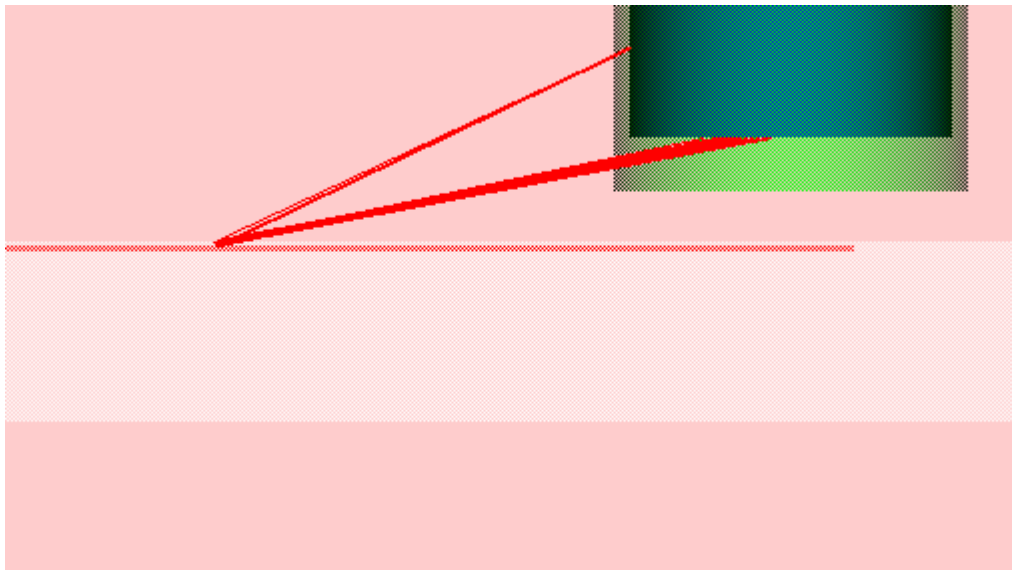


Figure A45. ADL

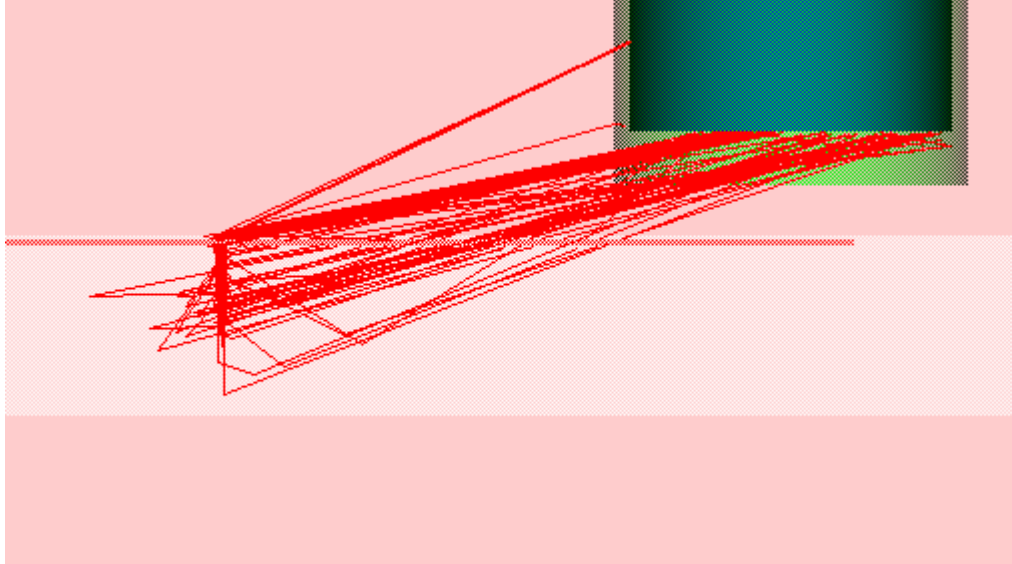


Figure A46. VDL

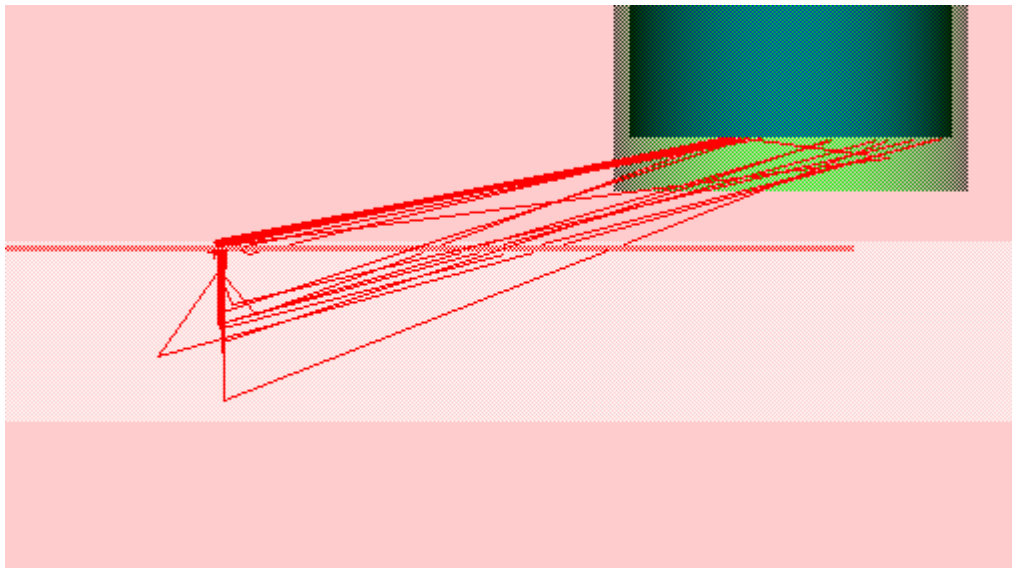


Figure A47. VDL.

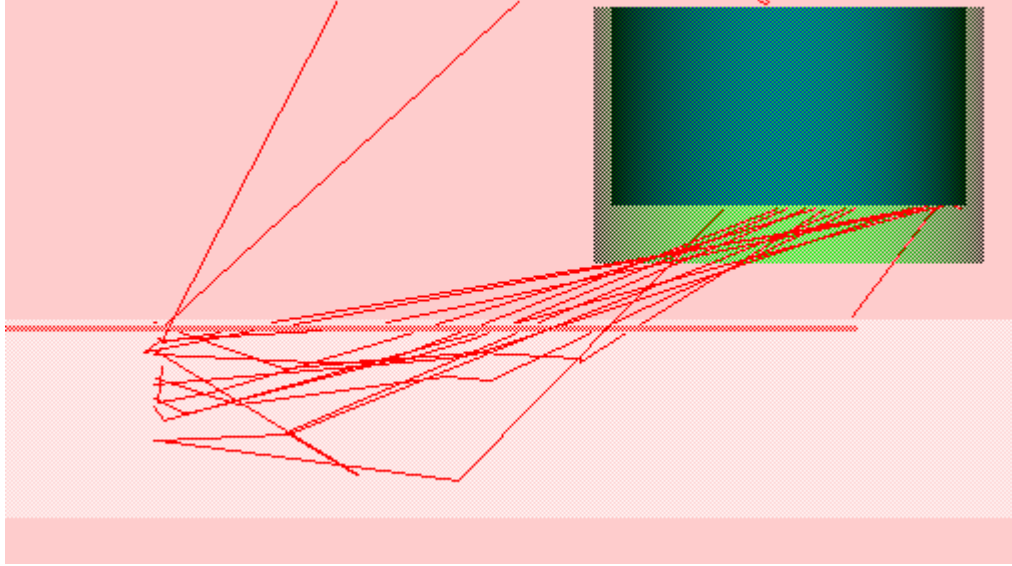


Figure A48. VSL.

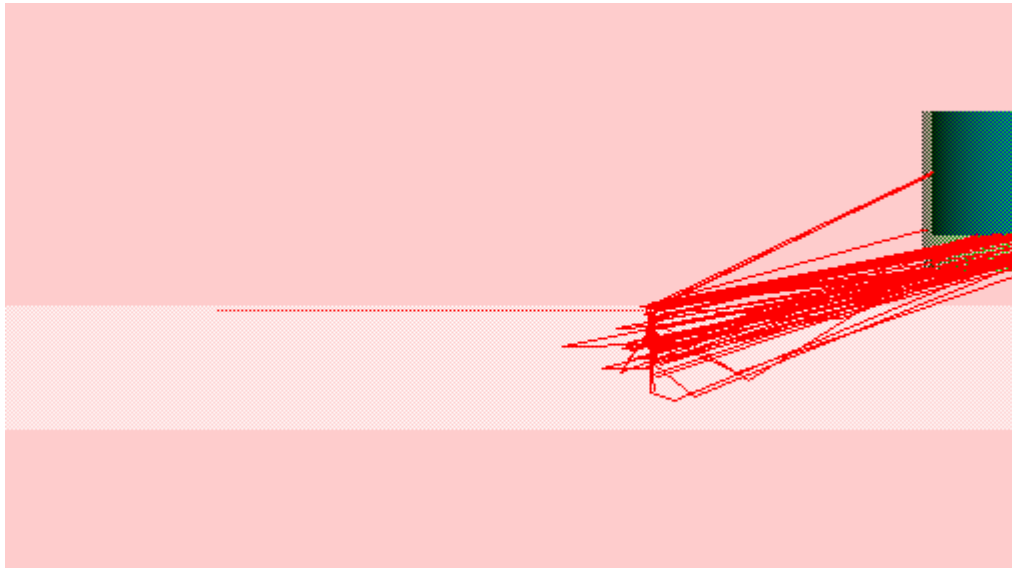


Figure A49. SSL.

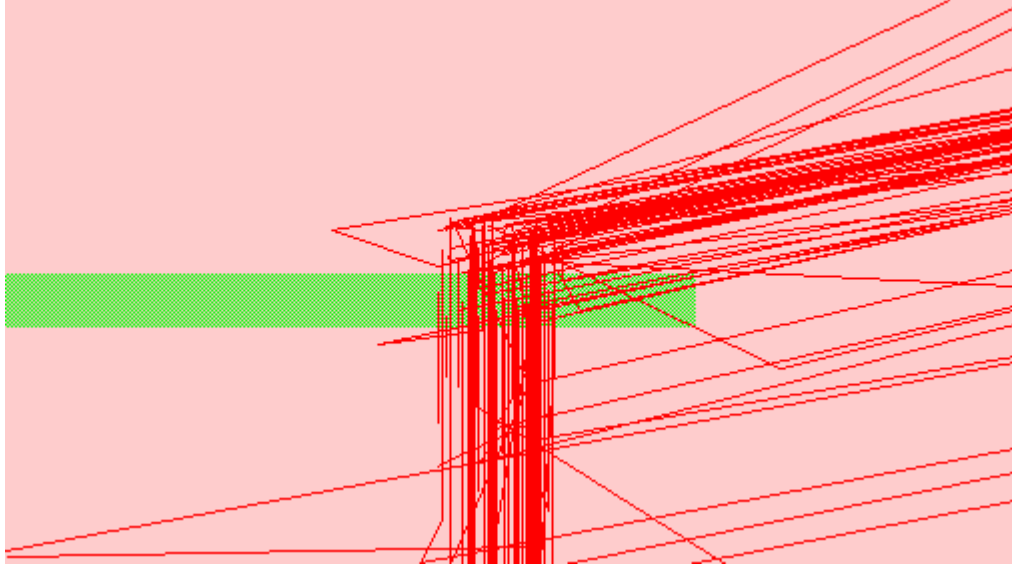


Figure A50. SDI zoomed in view of flaw and photon tracks. Aluminum is set to transparent.

APPENDIX B  
ONE SCATTER SIMPLIFIED PHOTON TRANSPORT MODEL

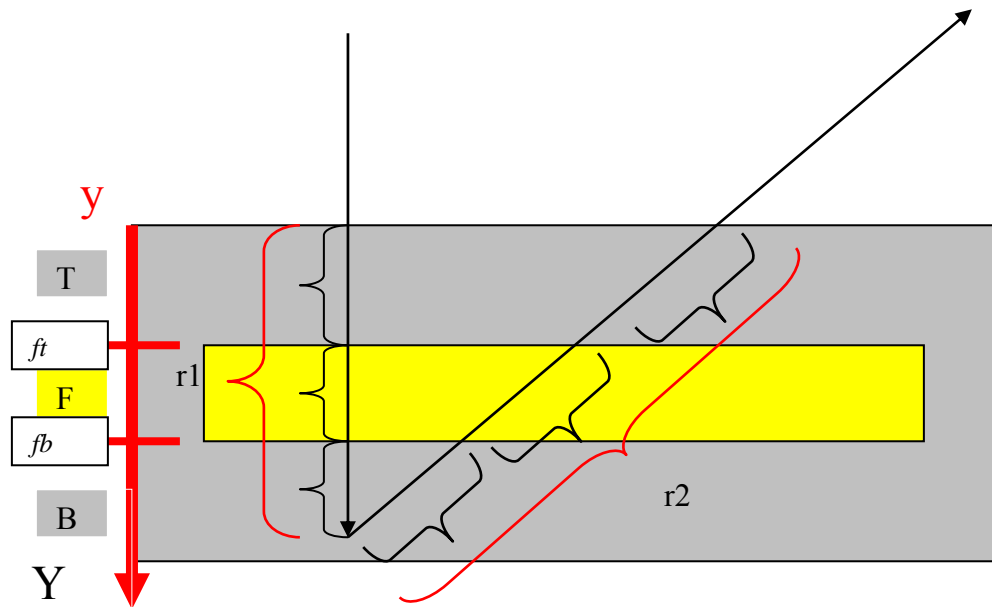


Figure B.1 Typical photon path across a flaw.

In the simplified one scatter transport model the signal differential leading to an image is a result of a difference in attenuation experienced by the incident and reflected photon beams caused by the presence of a flaw. In the schematic above, the flaw, region F is represented by the yellow rectangle. The rest of the target material is divided into two regions, the top, T, and the bottom B. The two portions of the photon path, incident

and exiting are represented by  $r_1$  and  $r_2$ , respectively. The photon can scatter either above the flaw, within the flaw (unlikely for void type flaws) or below the flaw.

The equation detailing the first scatter relative signal intensity returning to the detector from a particular depth in the sample is  $I = I_0 e^{-\sigma_1 r_1} \frac{d\sigma}{d\Omega} \Delta\Omega e^{-\sigma_2 r_2}$  where  $I_0$  is the unattenuated photon intensity,  $e^{-\sigma_1 r_1}$  and  $e^{-\sigma_2 r_2}$  are the attenuation functions for the incident portion and exiting portion of the photon beam, respectively. In this equation,  $\frac{d\sigma}{d\Omega}$  is the differential scattering cross-section per solid angle per electron as defined by the Klien-Nishien relationship as :

$$\frac{d\sigma}{d\Omega} = \frac{r_0^2}{2} \left( \frac{v'}{v} \right)^2 \left( \frac{v}{v'} + \frac{v'}{v} - \sin^2 \theta \right), \quad h\nu' = \frac{h\nu}{1 + \frac{h\nu}{m_e c^2} (1 - \cos\theta)}$$

$\Delta\Omega$  is the solid angle subtended by the detector. The solid angle subtended by the detector is simply approximated by the area of the detector divided by the distance from scatter point to the detector surface, squared. Simple geometric observations reveal the relationship  $r_2 = r_1 / \cos(\pi - \theta)$ , where  $\theta$  is the photon scattering angle. This angle is taken as the median between the largest and smallest scattering angles permitted, by geometrical and collimation considerations, to impinge upon the detector. Each of the photon tracks, incident and reflected, is, for ease of calculations, divided into up to three segments, depending upon the scatter point. These segments include top, flaw and bottom and each is handled with its own interaction characteristics. For most samples the top and bottom segments will be the same material and will consequently be treated with the same cross-sections. The simplicity of these approximations is justified by the fact

that they are applied to both flawed and non-flawed scenarios and since we are concerned with describing a relative contrast (ratio) between the two, the effect of the rough approximations should, to some extent, cancel out. The point is not to provide a realistic model for photon transport as much as to describe the mechanisms responsible for image contrast acquisition and thus flaw detection.

Thus the calculation is divided into three segments; primary scatter in top region, primary scatters in flaw region and primary scatters in bottom region. The first scenario has a scatter in the top region and the exiting photon beam will travel only through the top region towards the detector. The second scenario scatters in the flaw region, this photon beam which travel though the top and part of flaw region before scattering and then through the flaw and top region upon exiting. The third scenario travels though all three regions incident and exiting after being scattered. An uncollimated signal will be composed of all three segments. As collimation is increased, each scenario is cut off in order from the first to the third. Thus a well collimated signal will only comprise (to a first approximation as modeled here) photons which have a primary scatter in the bottom region of the sample. Additionally, depending upon flaw orientation and detector configuration a photon beam may miss the flaw upon entering or exiting the sample and thus may only traverse it once, rather than twice. (These scenarios are discussed in Chapter 4).

The mathematical representation of each of these segments is as follows:

$$\text{For } I = I_0 e^{-\sigma_1 r_1} \frac{d\sigma}{d\Omega} \Delta\Omega e^{-\sigma_2 r_2}$$

Segment 1 (top): for  $y \in [0, ft]$

$$r_1^* \sigma_1 = y^* \sigma_{\text{top}}$$

$$r_2 * \sigma_2 = (r_1 * \sigma_{top}) / (\cos(\pi - \theta))$$

Segment 2 (top & flaw): for  $y \in [ft, fb]$

$$r_1 * \sigma_1 = ft * \sigma_{top} + (y - ft) * \sigma_{flaw}$$

$$r_2 * \sigma_2 = (ft * \sigma_{top}) / (\cos(\pi - \theta)) + [(y - ft) * \sigma_{flaw}] / (\cos(\pi - \theta))$$

Segment 3 (top, flaw & bottom): for  $y \in [fb, Y]$

$$r_1 * \sigma_1 = ft * \sigma_{top} + (fb - ft) * \sigma_{flaw} + (y - fb) * \sigma_{bottom}$$

$$r_2 * \sigma_2 = [ft * \sigma_{top} + (fb - ft) * \sigma_{flaw} + (y - fb) * \sigma_{bottom}] / (\cos(\pi - \theta))$$

The total signal strength is the integrated value of segment 1 + segment 2 + segment 3.

Or

$$I_T = \int_0^Y dy I = \int_0^Y dy [I_0 e^{-\sigma_1 r_1} \frac{d\sigma}{d\Omega} \Delta \Omega e^{-\sigma_2 r_2}]$$

And the contrast is relative signal differential is simply a ratio of the signal strength of flawed to non-flawed areas of a sample.

For the calculations presented in table 4.1. the incident photon spectrum was 75 keV peak. The mfp's for this photon beam used in these calculations in aluminum and in air were taken from MCNP5 simulations as:

9.75E-01 cm, 6.78E-01 cm and 6.09E+03 cm for Al top, Al bottom and flaw void, respectively.

*Different values are taken for Al top and Al bottom to account for the filtering and scattering of photons as they reach further into the sample.*

The geometry considered in these calculations is as follows:

Two inch thick aluminum plate with a 0.15 cm flaw 0.65 cm (1/4 inch) below the surface. The detector is a NaI crystal two inches in diameter. The detector surface is 2.9 cm above the sample surface and the detector is located nine cm centerline-to-centerline

from the photon beam. The collimator extension is set contingent upon the model being calculated.

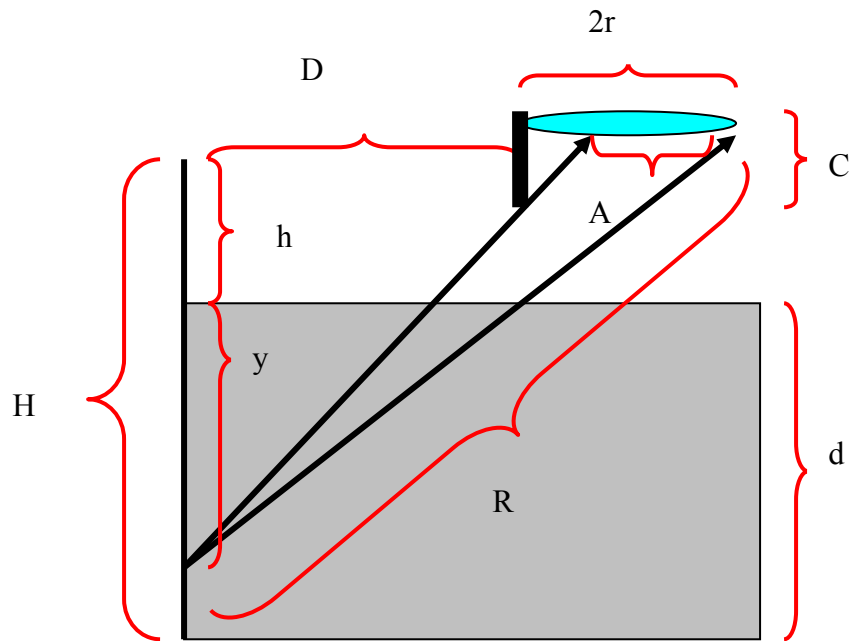


Figure B.2 Parameters used to determine optimal collimation length for focusing to a specified depth.

APPENDIX C  
COLLIMATION DEPENDENT CONTRAST TREND ANALYSIS

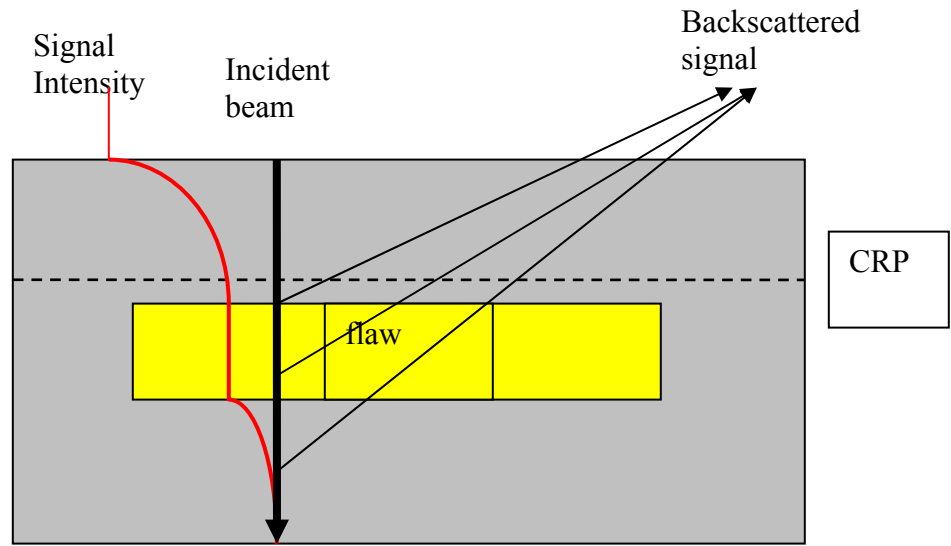


Figure C.1 Signal intensity as a function of depth and across a void type flaw.

$$\frac{dS(y)}{dy} = \Phi_0 e^{-\sigma_1 y} \frac{d\sigma}{d\Omega} \Delta\Omega e^{-\sigma_2 y}$$

$$S(y) = \int_0^y \frac{dS(y)}{dy} dy$$

Or, roughly

$S(y) \propto \int_0^y e^{-y} dy$ , so let,  $S(y) = A \int_0^y e^{-y} dy = (1 - e^{-y})$  so that  $S = A$  (total signal strength)

$$\text{Percent contrast} = 100 * [S_{\text{flaw}} - S_{\text{no flaw}}] / S_{\text{no flaw}}$$

\*From the figure above it can be seen that all scatters occurring above the flawed region are identical for both non-flawed samples (i.e. – above the flaw in the flawed sample is effectively the same as a non-flawed sample). Thus the Absolute difference in signal intensity, for collimation up to the flaw top is a constant.

$$\% \text{ contrast} = d / S_{\text{no flaw}}, \text{ where } d \sim (S_{\text{flaw}} - S_{\text{no flaw}})$$

As the collimator extension is increased in length from zero, the critical reference plane (CRP) moves from sample surface down. As the CRP approaches the flaw top,  $d$

does not change, and  $S_{\text{noflaw}}(y) = \int_y^{\infty} A e^{-y} dy$

$$\text{But, } S_{\text{noflaw}} = \int_0^y A e^{-y} dy + \int_y^{\infty} A e^{-y} dy$$

Thus, percent contrast as a function of  $y$  position of the critical reference plane (or synonymously as a function of increased collimation extension) is

$$\%C = d / \int_y^\infty [\ ] dy = d / (S_{noflaw} - \int_0^y [\ ] dy)$$

$$\text{Or } \%C = d / (S_{noflaw} - \int_0^y [A(1 - e^{-\sigma y})] dy \Rightarrow d / (B - e^{-\sigma y})$$

For  $d$  constant and  $(0 < y < \text{flaw top})$  which corresponds to  $(0 < X_{col} < X_{crit})$ :

Where  $X_{crit}$  is the optimal collimation length corresponding to the depth of the flaw top.

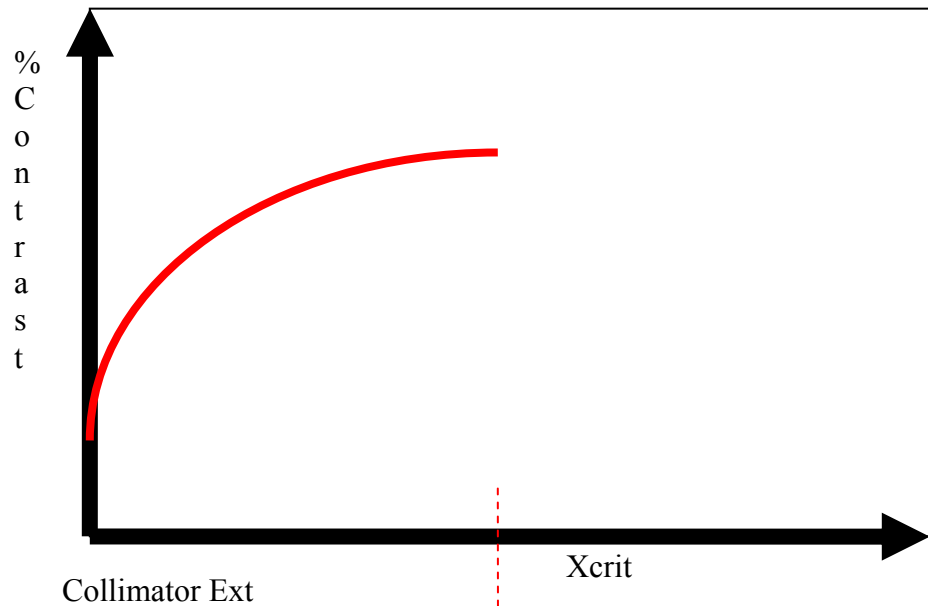


Figure C.2 Contrast versus collimator extension for collimator from zero to critical (optimal) extension. This optimal corresponds to collimating to top of flaw.

Contrast here increases as a function of increasing collimation since the signal being discriminated against, from sample surface to flaw top, is effectively noise (As it is

identical between flawed and non-flawed scenarios) and this its inclusion lessens the contrast.

As the collimator is extended from  $X_{crit}$  towards  $X_{bottom}$  (corresponding to CRP being at flaw bottom) almost no signal is lost as very few photons interact within the flaw (assuming void type flaw)

Thus the contrast trend within this region appears as follows:

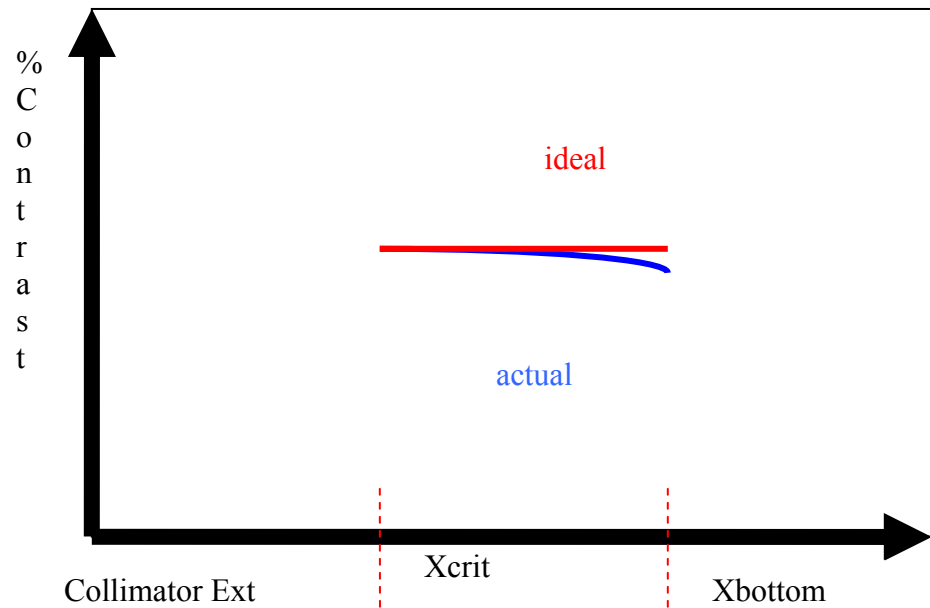


Figure C.3 Contrast versus collimator extension for collimator from critical (optimal) extension to flaw bottom.

In reality some photon do interact within the void and more importantly, some photons which interact deeper and would otherwise scatter into the detector (as the source has a definite diameter) are lost. This makes the real trend in this region slightly sloped downward (observed experimentally) in comparison with the theoretically predicted flat line.

As collimation is further increased so that the CRP moves down from the flaw bottom, all signal being discriminated against is useful as theses photons pass through the flaw. The importance of these photons, however, decreases exponentially as a function of depth since the incident photon beam intensity reaching these areas is exponentially attenuated as a function of depth. This means that as you collimate to deeper within a sample you are cutting out less important signal per additional unit of depth collimated out. Thus in this region, the contrast appears as follows:

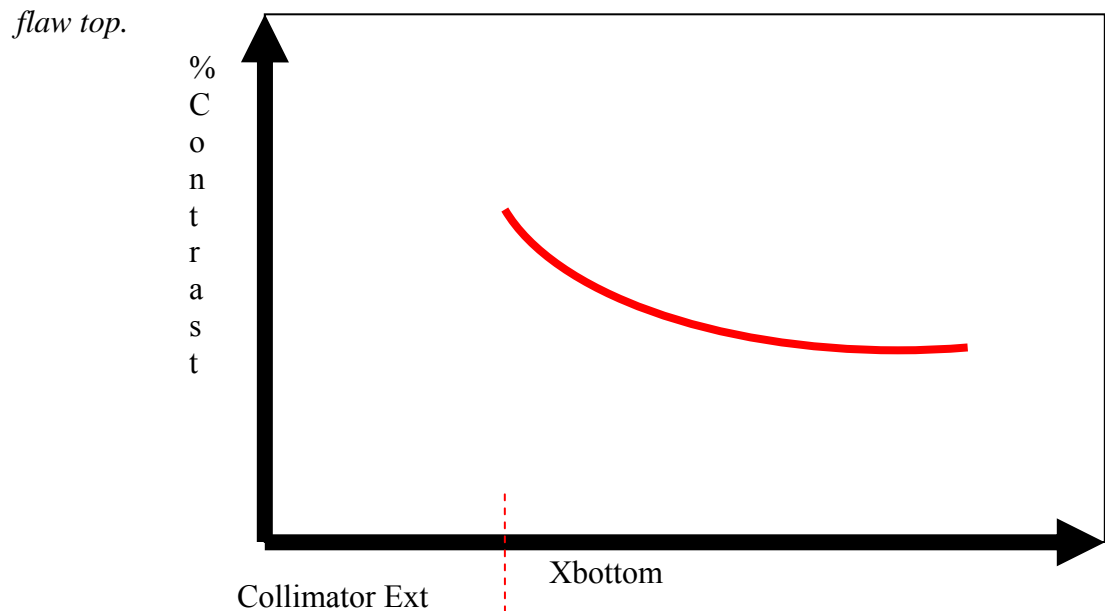


Figure C.4 Contrast versus collimator extension for collimator extension corresponding to flaw bottom to maximum extension.

The entire trend of contrast versus collimator extension (or identically contrast versus CRP position) is as follows:

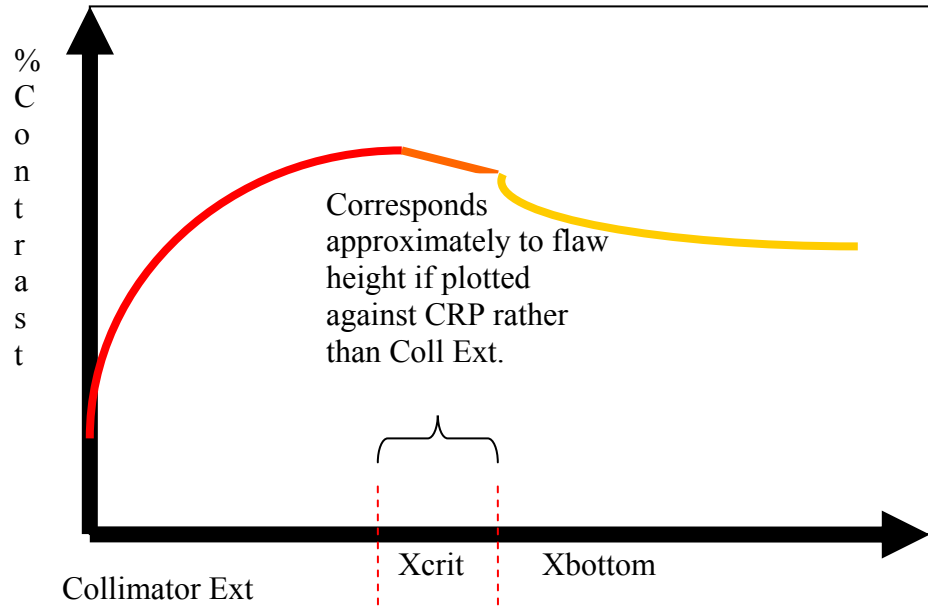


Figure C. 5 Contrast versus collimator extension .

*as shown in chapter 4, data from experiments and MCNP5 simulations agree with this trend.*

## APPENDIX D IMAGED SAMPLE DESCRIPTIONS

### Foam

Three main SOFI foam type samples were evaluated. The first type is a calibration panel. This is an eight inch thick piece of SOFI mounted on a ten by ten inch aluminum substrate. There are four bored out voids within the SOFI a large and a small ( $\frac{1}{2}$ " and  $\frac{1}{4}$ " diameters, respectively) at each substrate level and midplane level (four inches below surface.) The second sample type is a ramp panel. This is a large (usually one meter by one meter) contoured piece of aluminum substrate with various flanges and bolts with 2 to 8 inches of SOFI foam applied to it. There are often other inserted objects and/or naturally occurring voids and delaminations within the foam as well. The third type of sample are smaller (ten by ten inch with 2 to 4 inch thicknesses) foam blanks. These are blank foam panel not mounted. These were cut and various objects were inserted into them to help develop depth correlations.

### Aluminum

The aluminum samples scanned included for the most part the machined aluminum test plates. There are four of these. Two of the plates had voids machined into them and two of the plates had void channels machined into them. Of the void non-channeled plates, one was machined with five,  $\frac{1}{4}$ " high flaws positioned at various depths and one had cylindrical voids with various heights. Of the channeled plates, one had three 1 cm

wide by .1 cm high channels at various depths ( ) and one had 5, 1 cm high .1 cm wide channels at various depths ( ).

#### Plastics

The main plastic sample imaged was a machined plastic plate with three, 1 cm wide by 0.1 cm high channel flaws running the length of the plate at various depths ( . )

#### Reactor Insulation Panel

The Reactor Insulation Panel was supplied by Westinghouse. It was a one meter by one meter by eight inch thick hollow panel of stainless steel. Inside were several layers of corrugated stainless steel foils. Boric acid and Boric acid residue was placed on various places of this sample for several images.

#### Concrete & Gypsum

The Concrete sample was supplied by LANL. It is a solid concrete block with various “flaws” (e.g. fishing line, lead pointers, plastic and copper wires, steel pipe) inserted at various positions and depths.

#### Ceramic Space Shuttle Thermal Tiles

The Space Tiles were provided by NASA. They are small 6 inch by 6 inch by 3/8 inch ceramic tiles with a ceramic mesh outer binding. Flaws in the tiles included glue drops and delaminations, both at mesh to ceramic interface.

APPENDIX E  
SPECTROSCOPIC TRENDS

Aluminum Flaw plate 1: 1.5 CM to PERP collimator fins. 3 cm to NaI Experimental Backscatter  
Spectra Flaws A and E 60 & 75 keV peak specs.

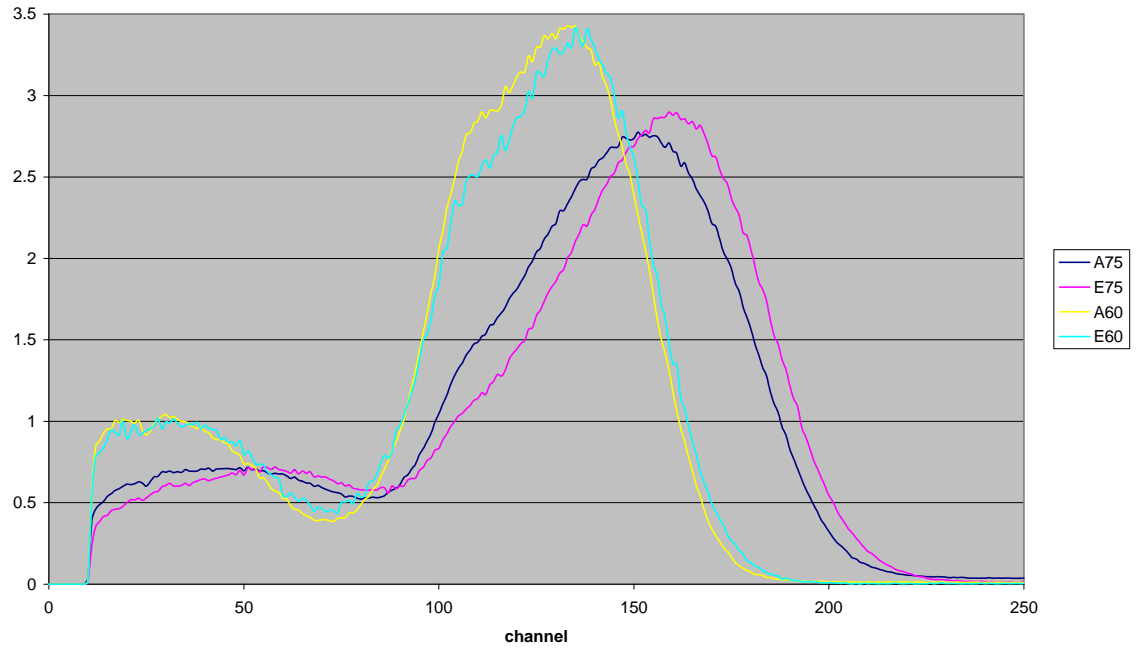


Figure E1 Spectroscopic trend for flaw depth by incident energy spectra.

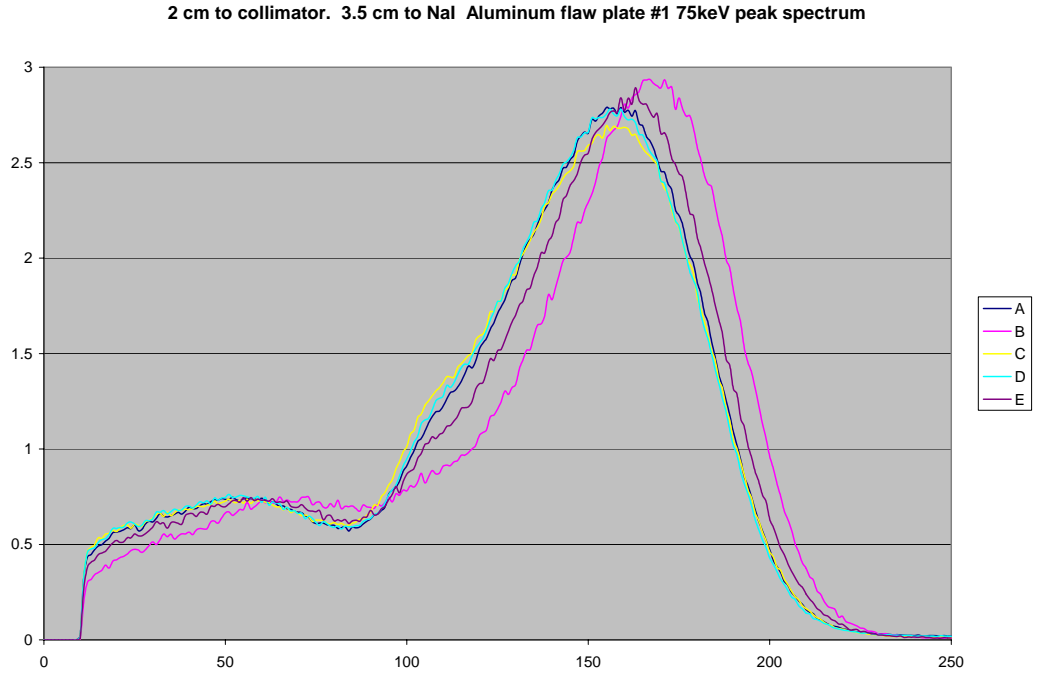
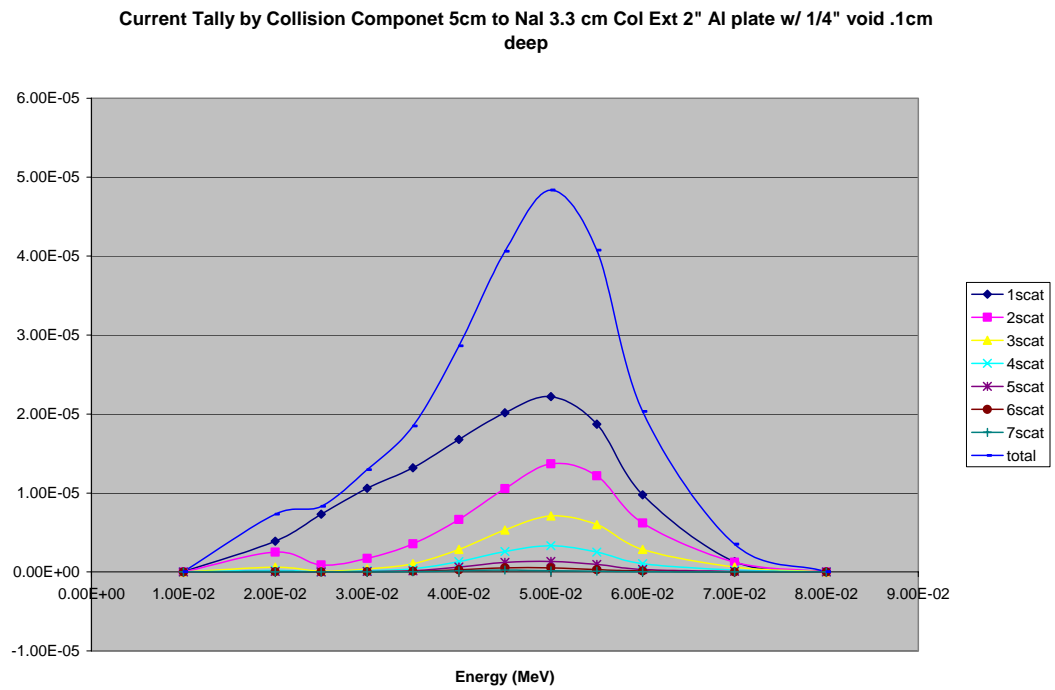


Figure E2 Trends for flaw depth. Flaws depth increases from A to E.



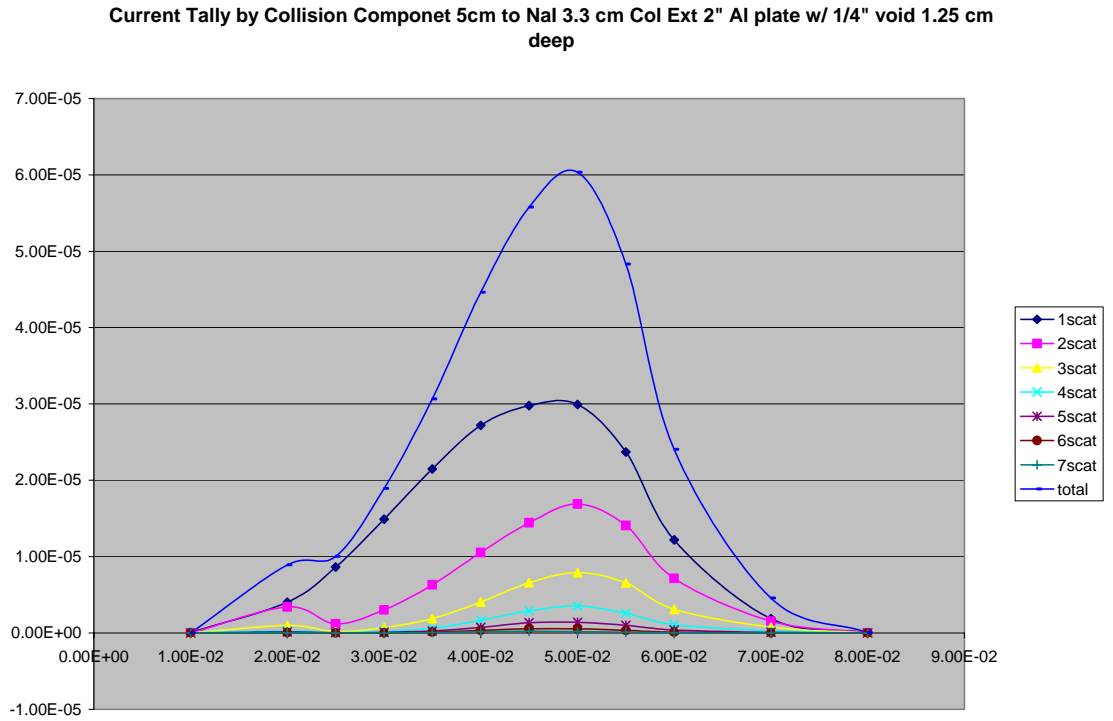


Figure E3 Scatter component break down for spectra.

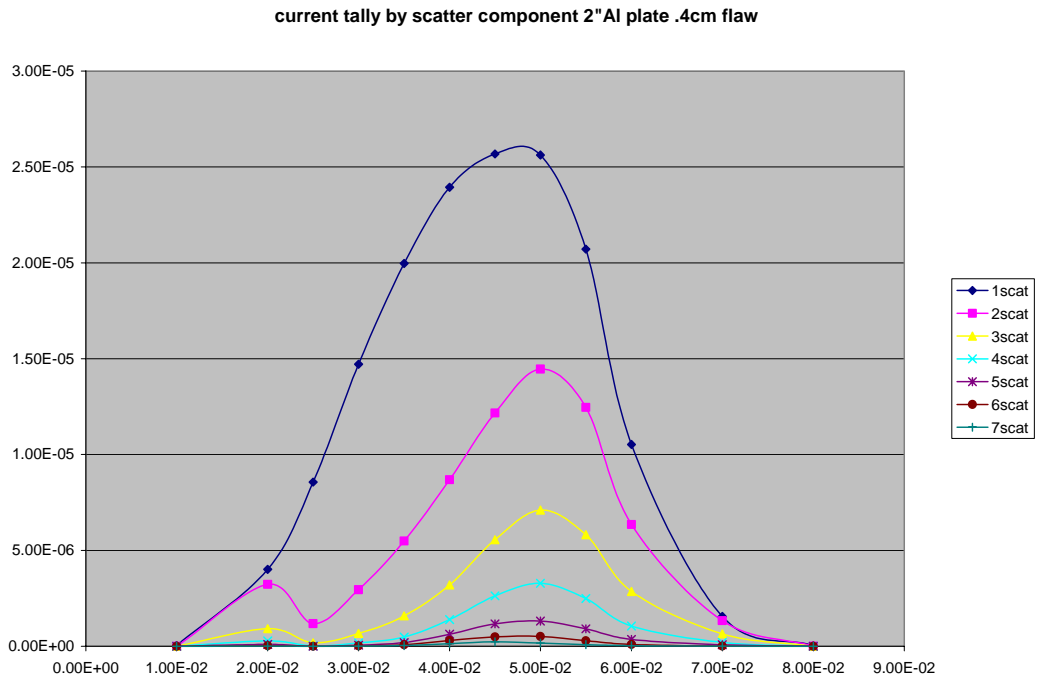


Figure E4. Spectral break down by scatter component.

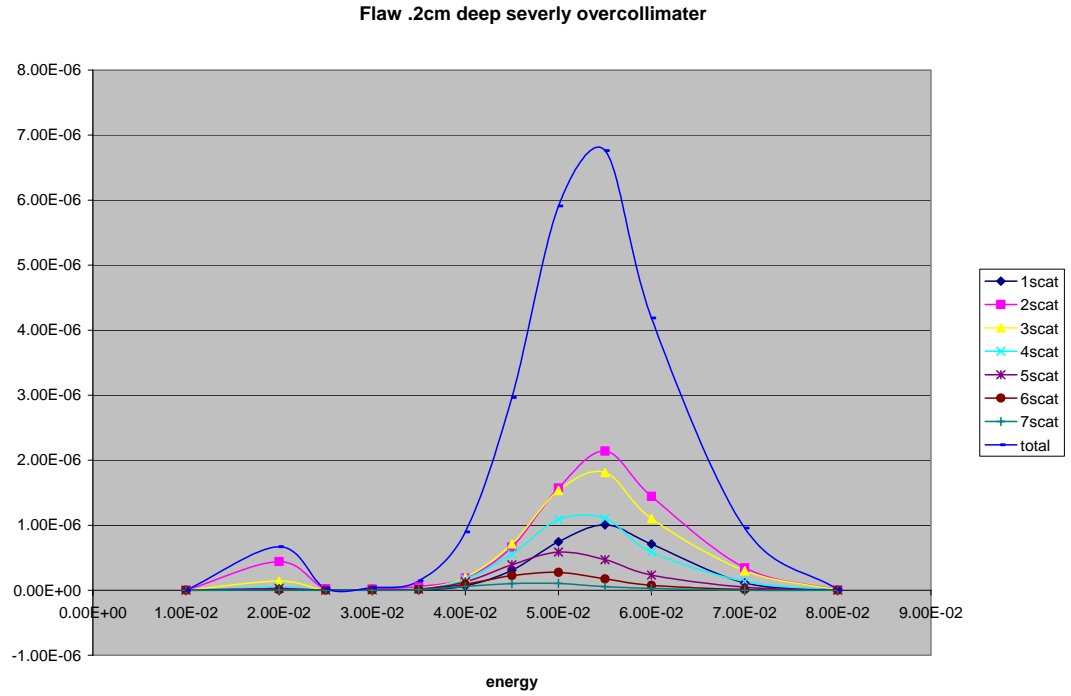


Figure E5. Spectral break down by scatter component. MCNP5 current tally.

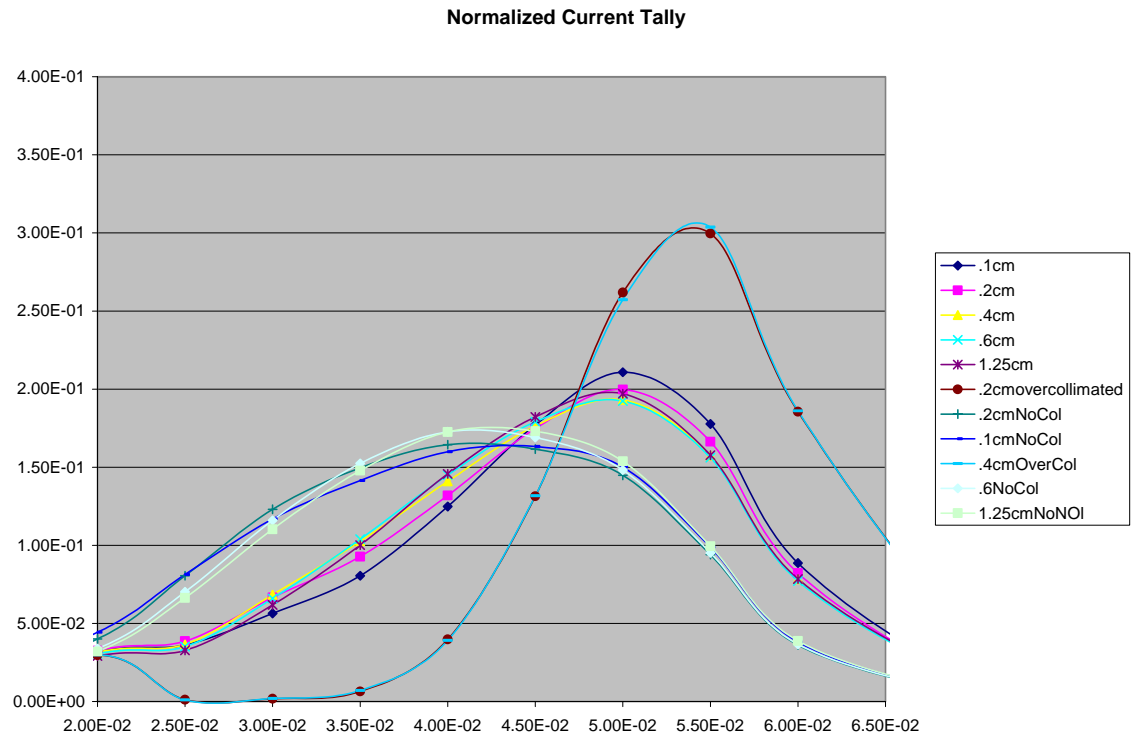


Figure E6. Current tally spectra for various flaw depths and collimation configurations.

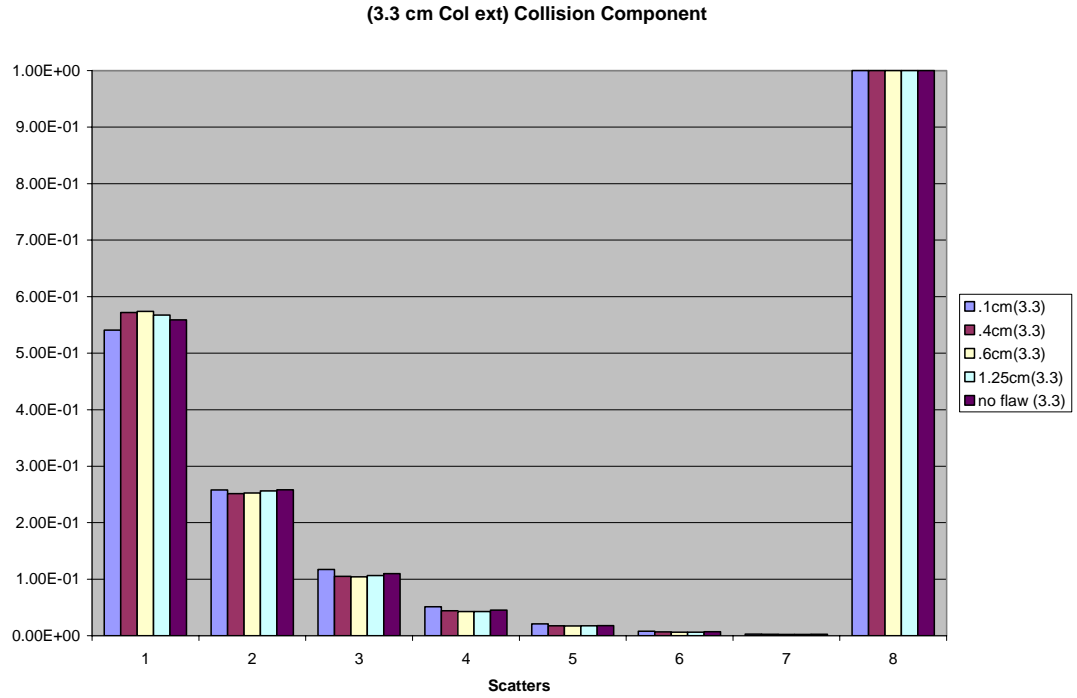


Figure E7 Collision component signal contribution for various flaw depths in aluminum.

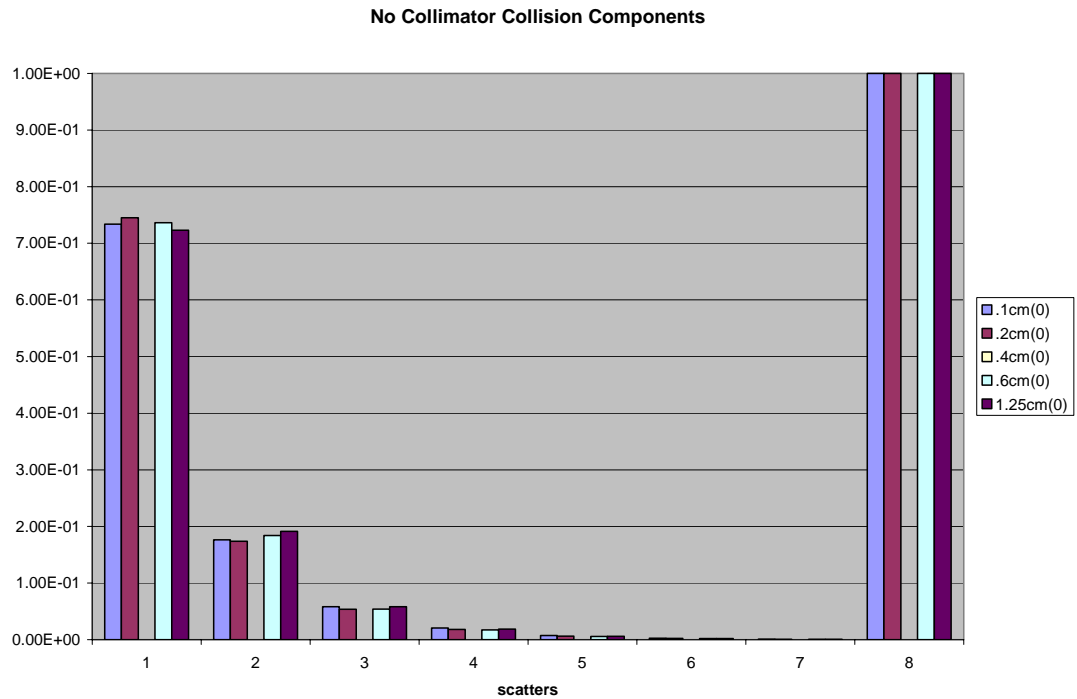


Figure E8 Collision component contributions for various flaw depths with uncollimated detector in aluminum.

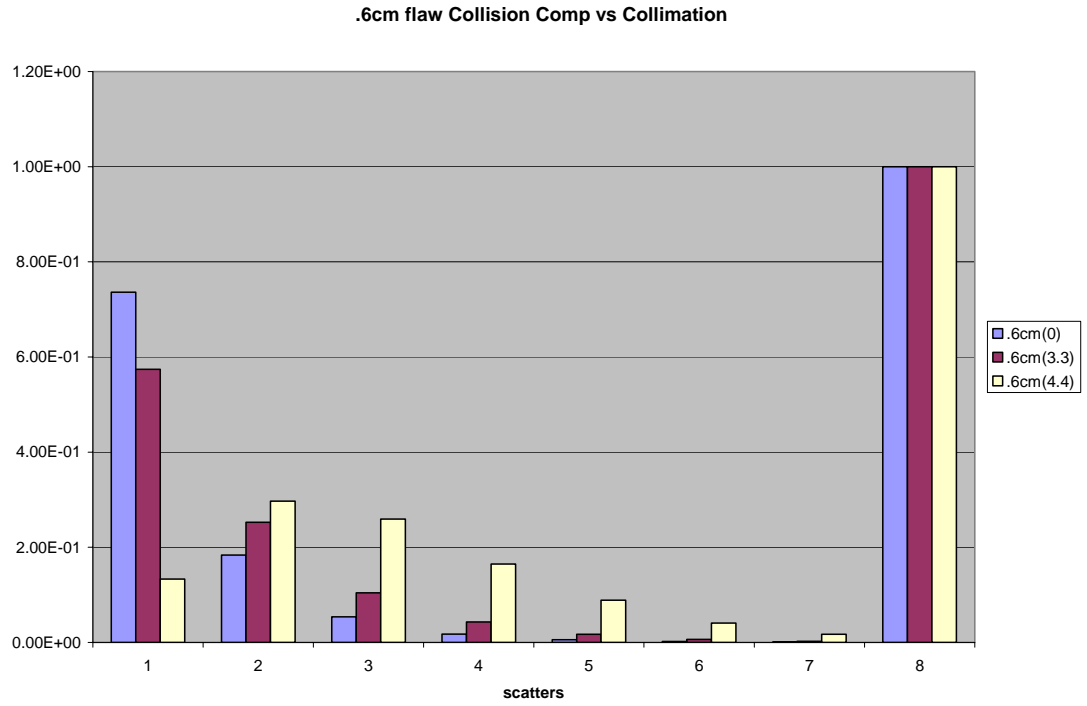


Figure E9 Collision component contributions to 0.6cm void flaw in aluminum with various collimations configurations.

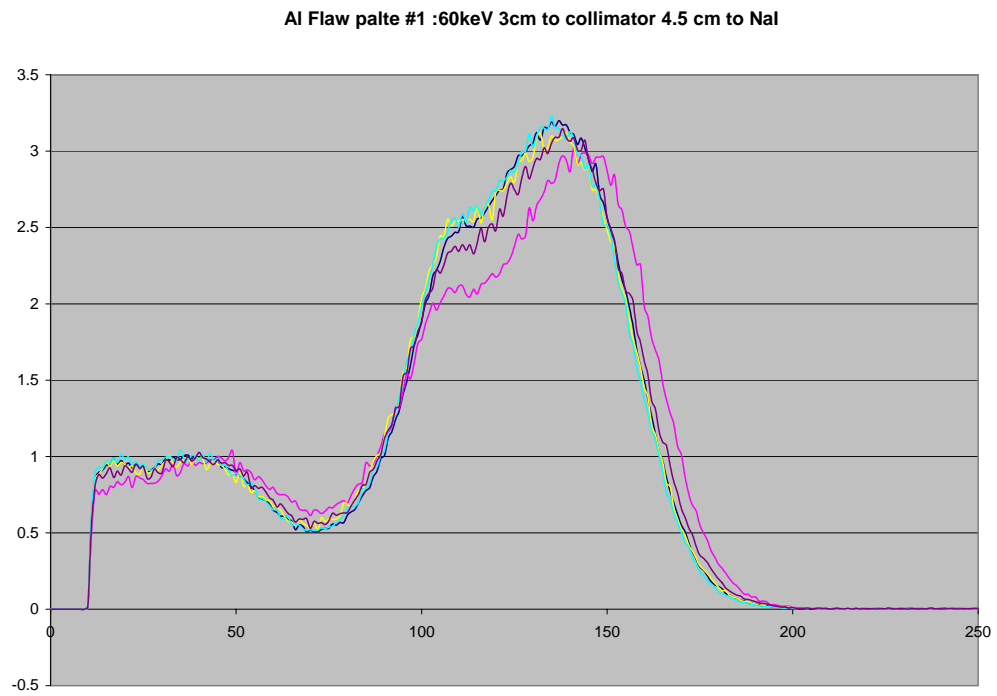


Figure E10 Spectroscopic trend with flaw depth. Flaw depth increases from A to E.

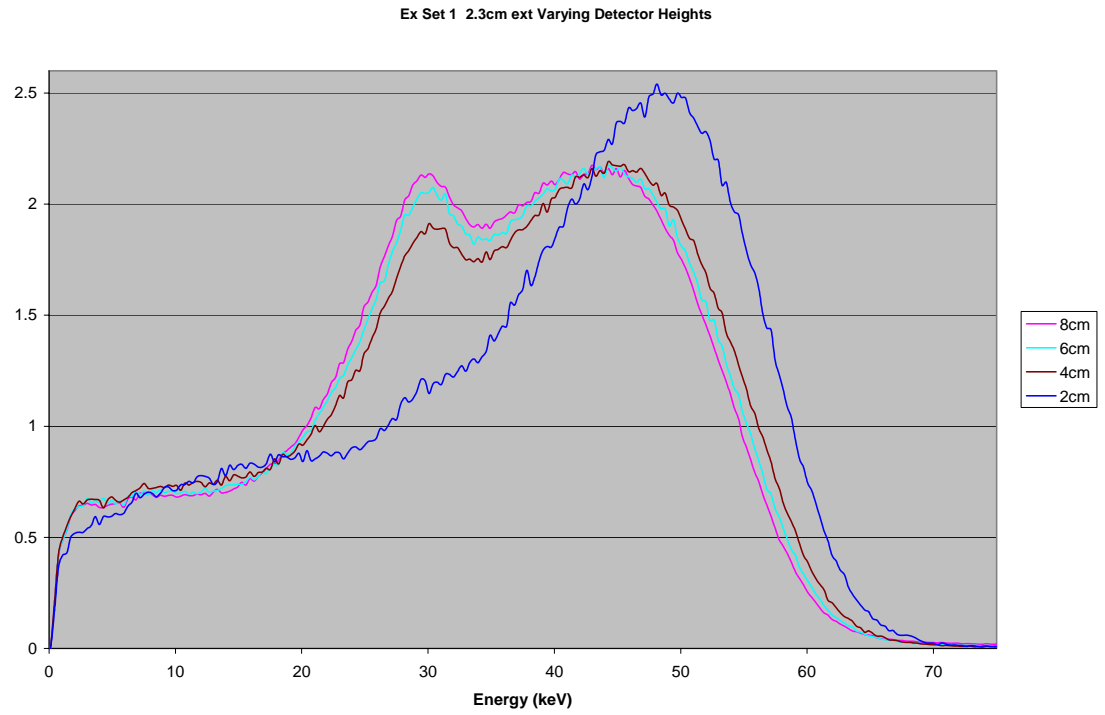


Figure E11. Experimental spectroscopic trend with detector height.

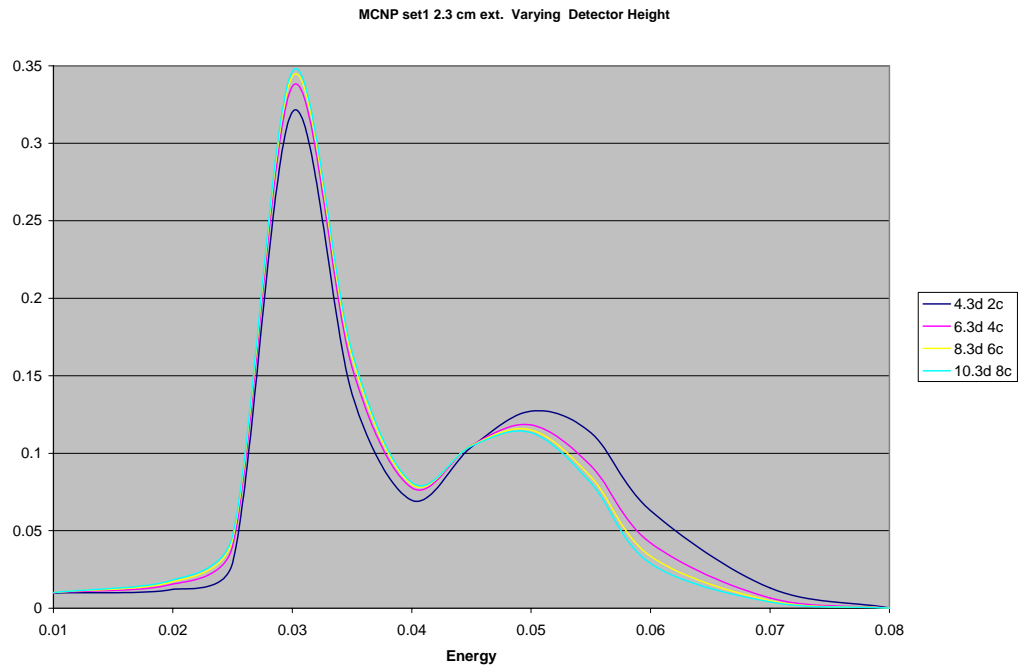


Figure E12 MCNP5 current tally spectroscopic trend with detector height.

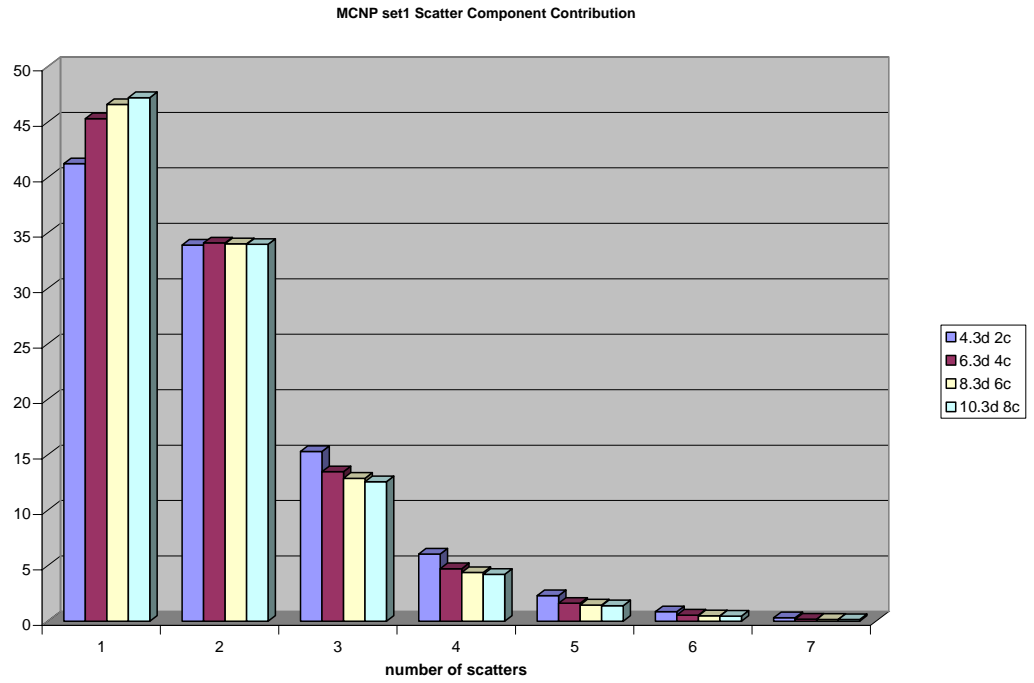


Figure E13 Scatter component contribution for various detector and collimator configurations.

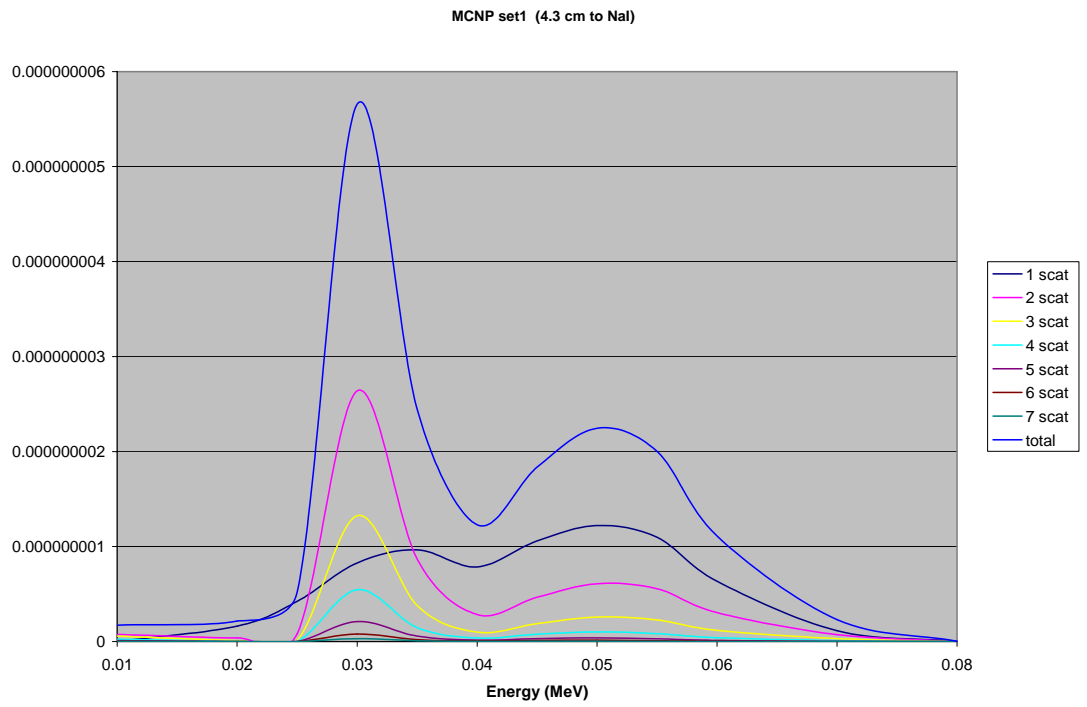


Figure E14 Spectral breakdown by collision component

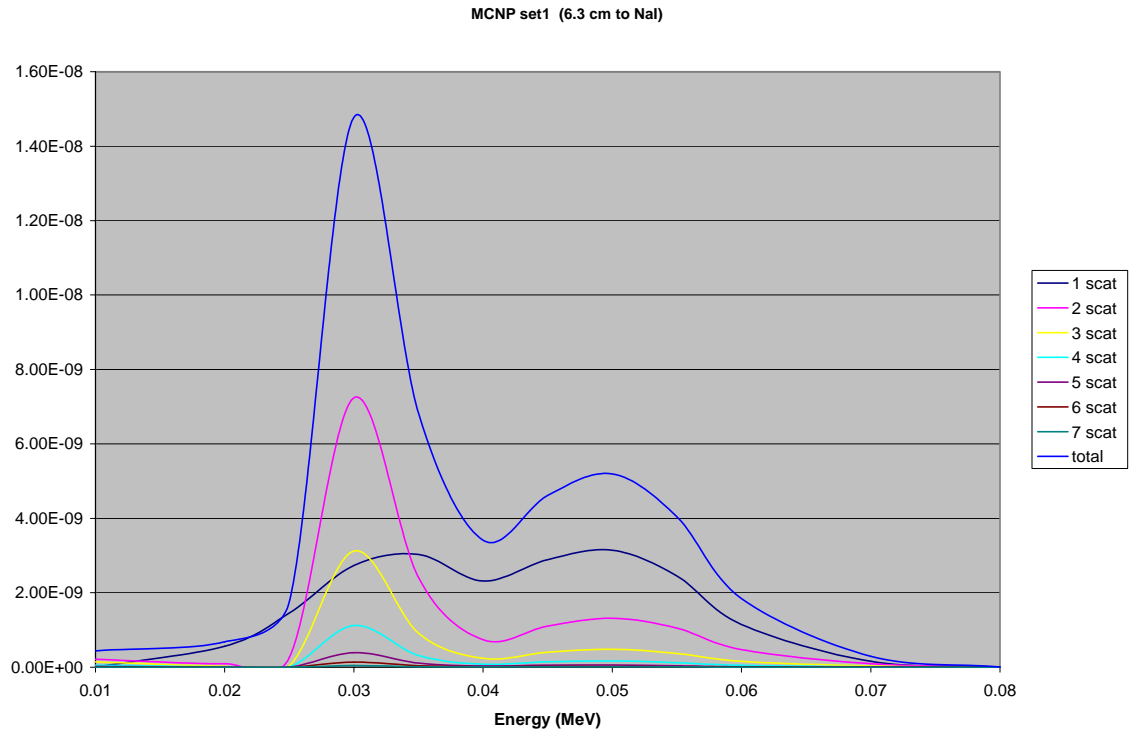


Figure E15 Spectral breakdown by scatter component

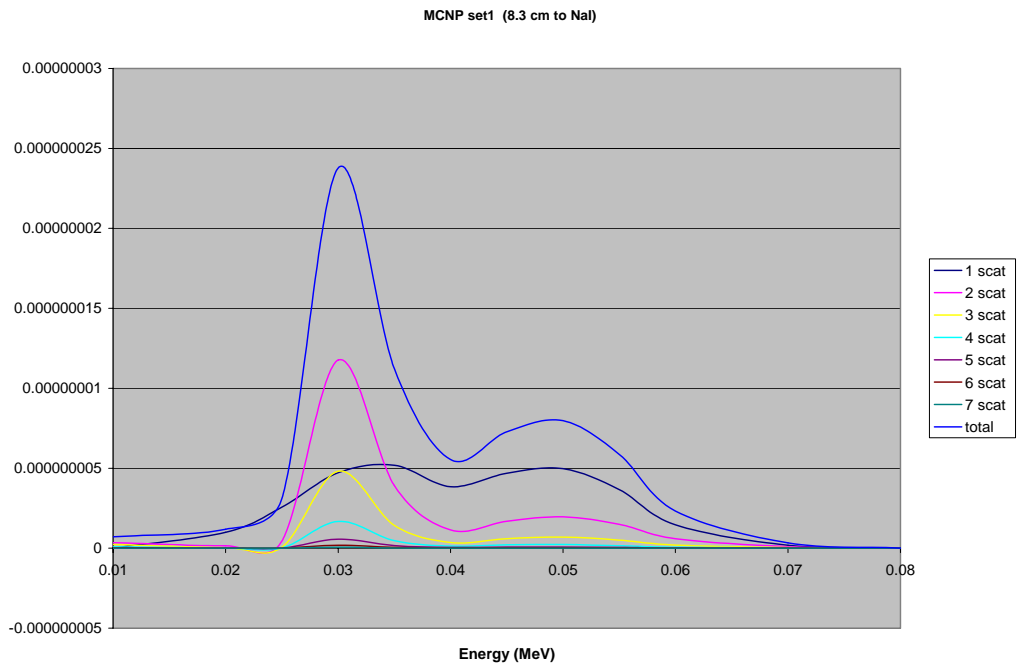


Figure E16 Spectral breakdown by scatter component

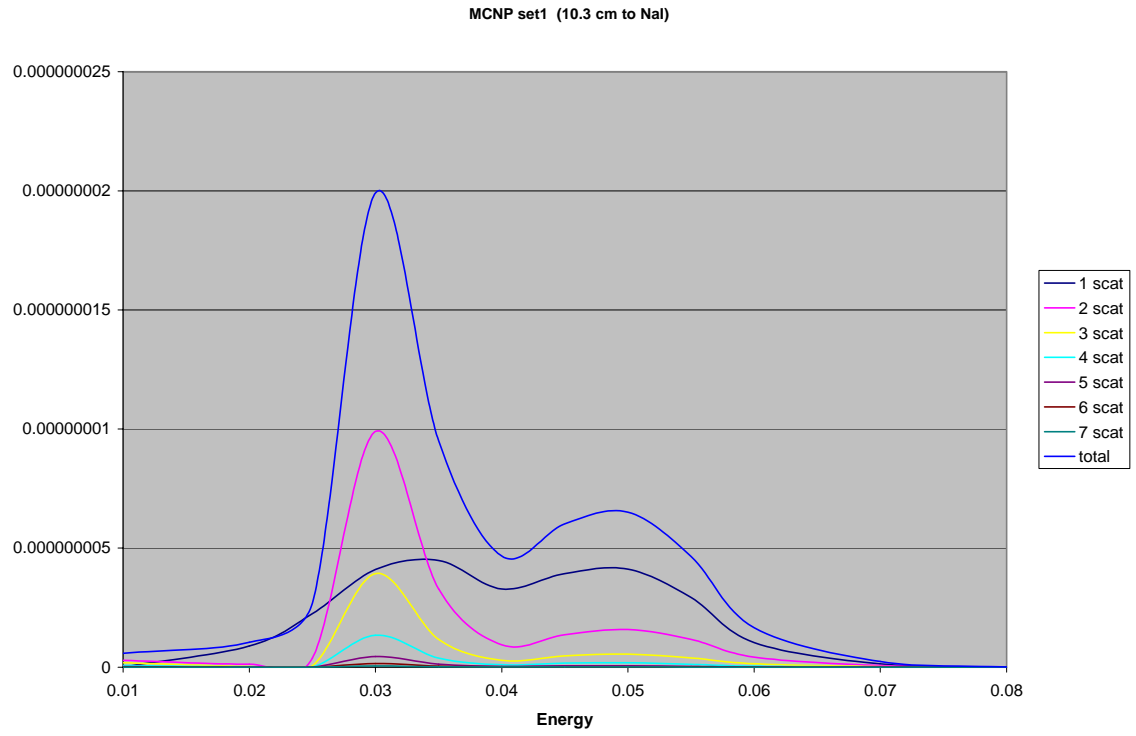


Figure E17 Spectral breakdown by scatter component

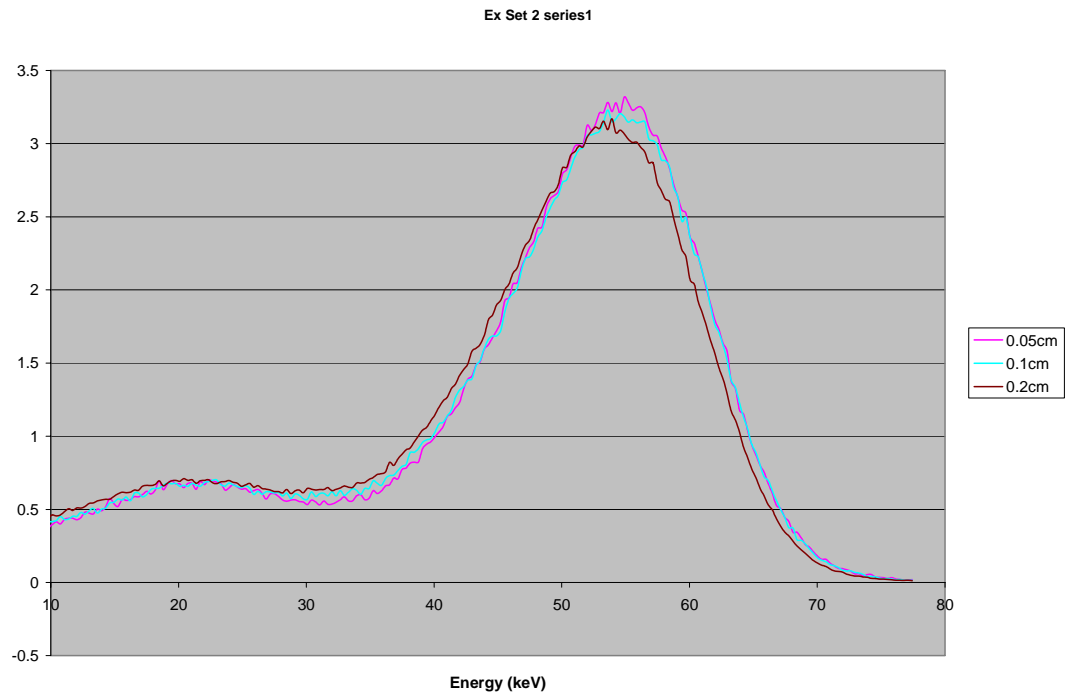


Figure E18 Experimental trend with flaw depth.

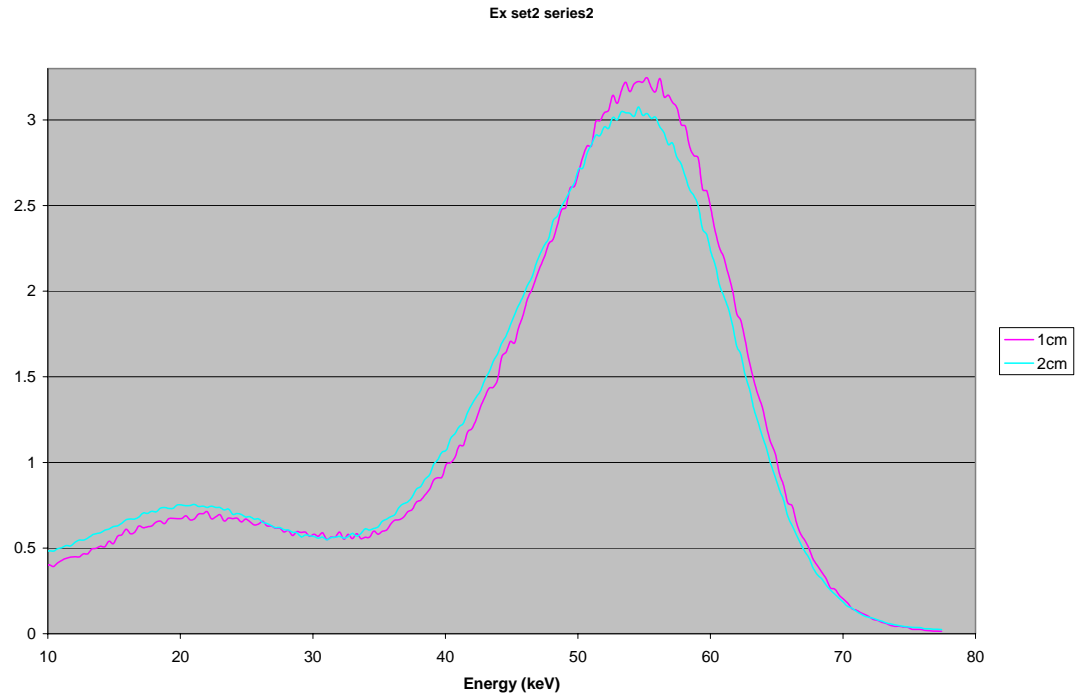


Figure E19 Experimental trend with flaw depth.

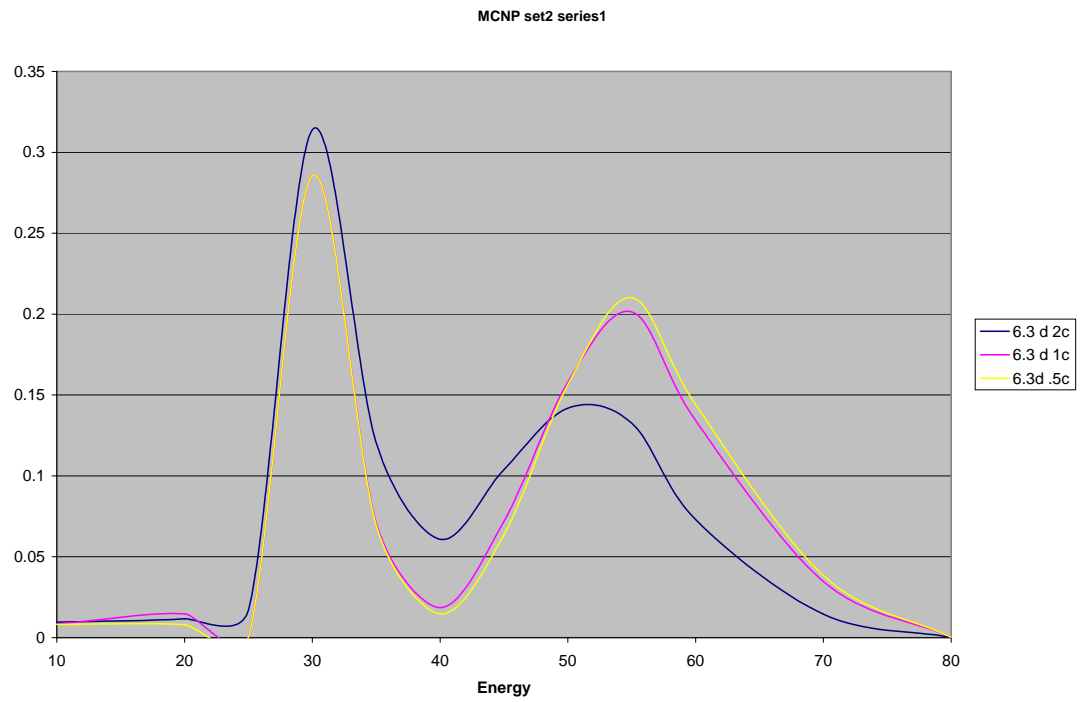


Figure E20 MCNP5 trend with collimation extension.

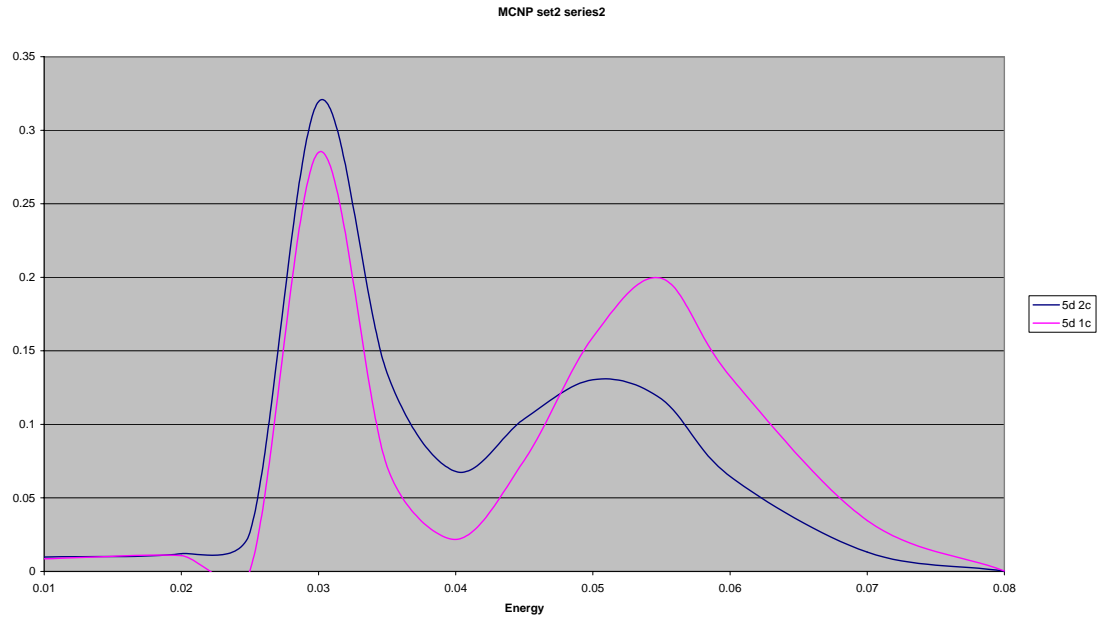


Figure E21 Experimental trend with collimation extension.

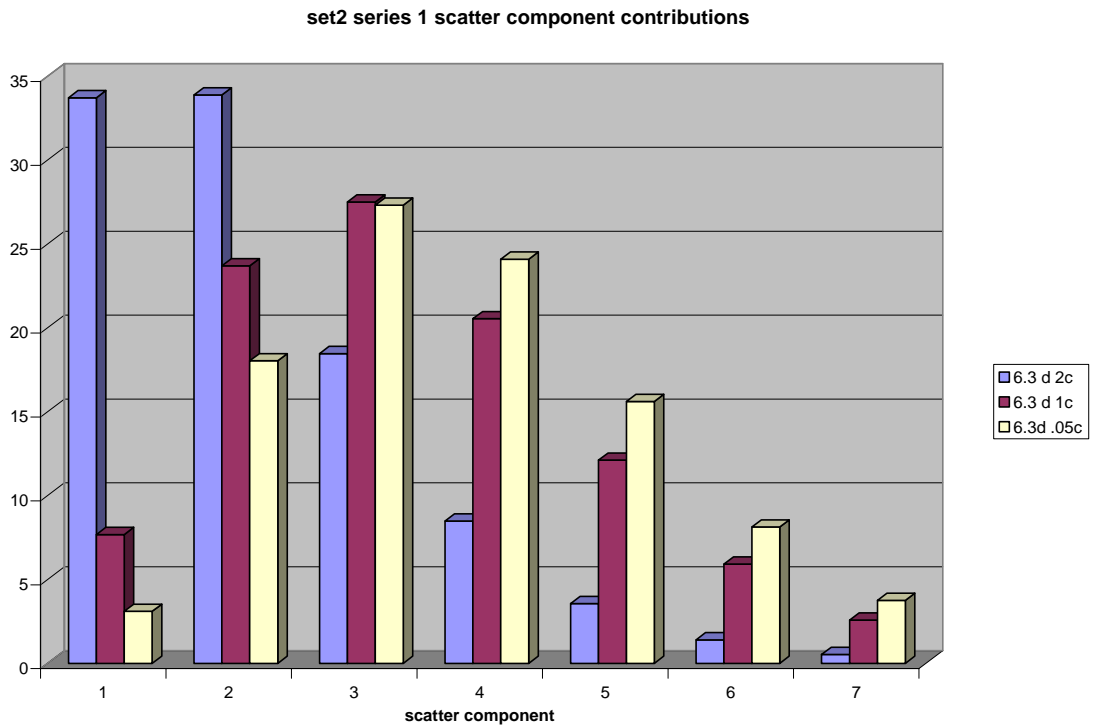


Figure E22 Scatter component contribution trends with varying collimation.

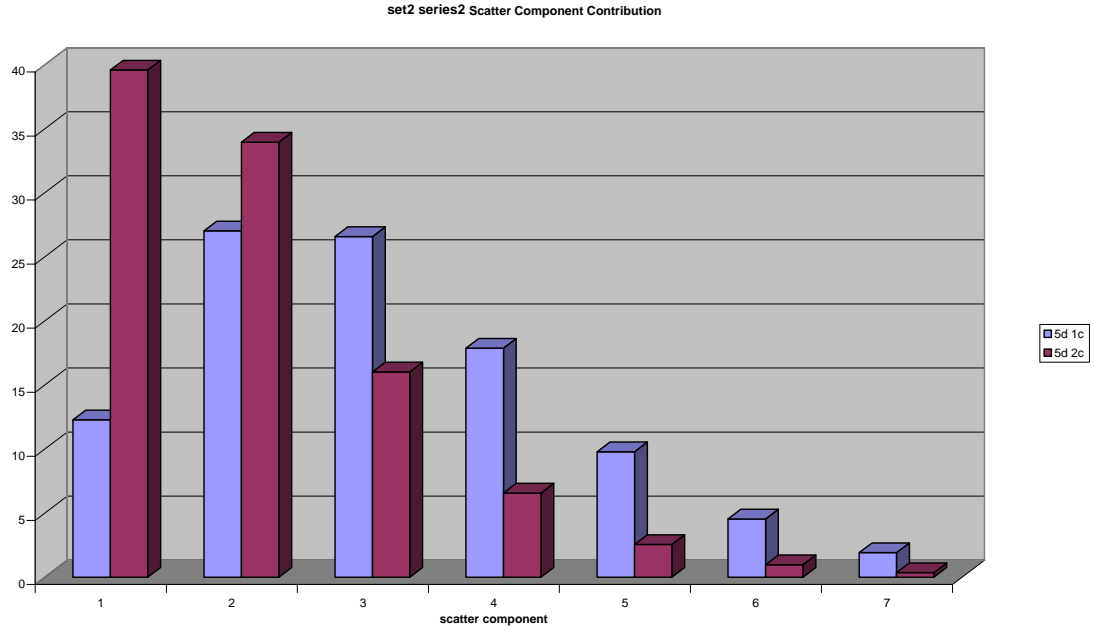


Figure E23 Scatter component contribution by collimation

**Flaws 10x10 Al plate. 75keV 2.5 cm to NaI 1 cm Ext  
Flaws A,B,E at 1/8, 3/16, 3/8 inch depths, respectively**

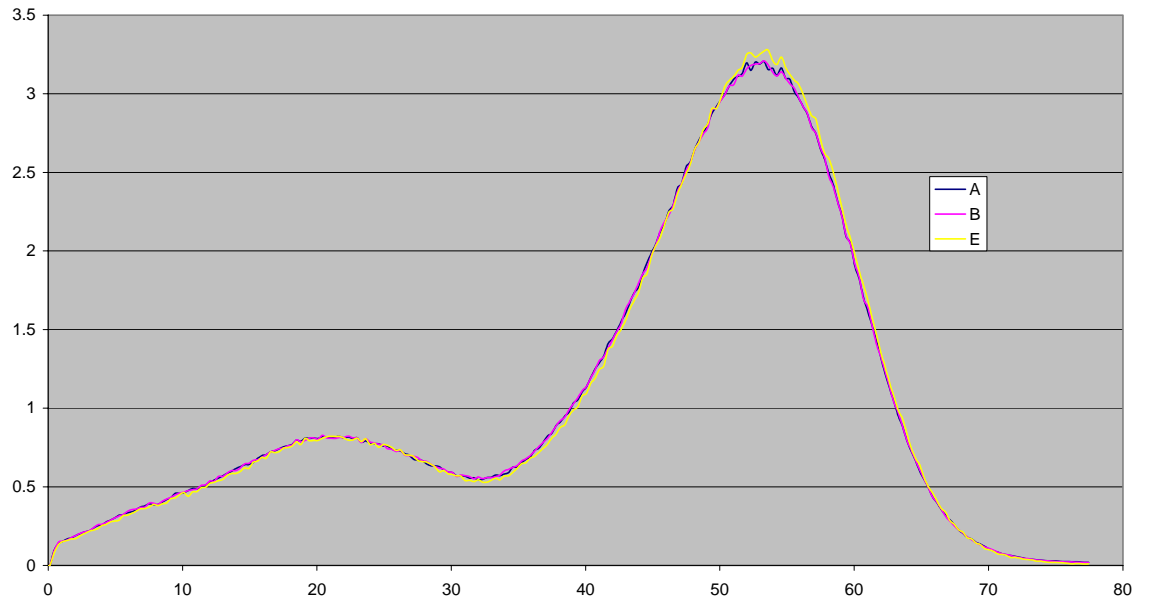


Figure E24 Experimental spectral trend with flaw depth.

**4.3 cm to NaI 3.3 cm Ext (MCNP5)  
Flaws at 0, .15 cm, .25cm Depths**

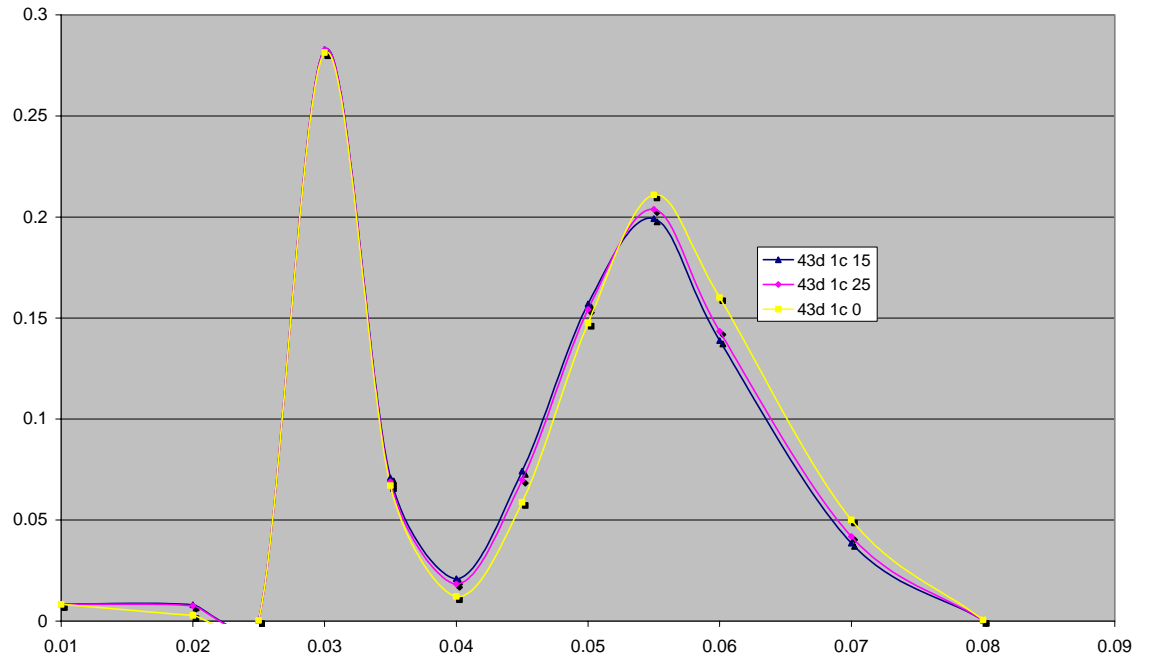
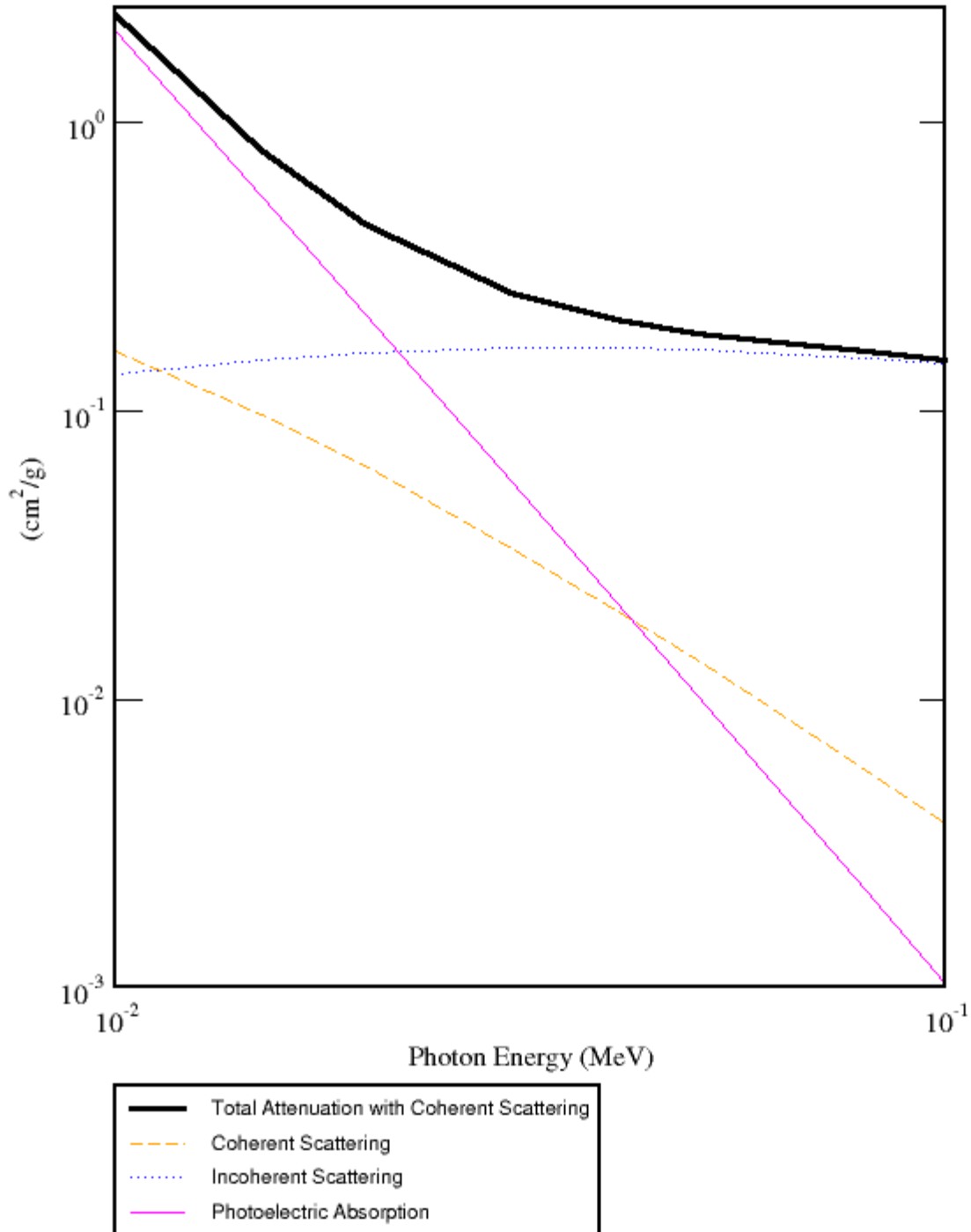


Figure E25 MCNP5 current tally spectral trend with flaw depth.

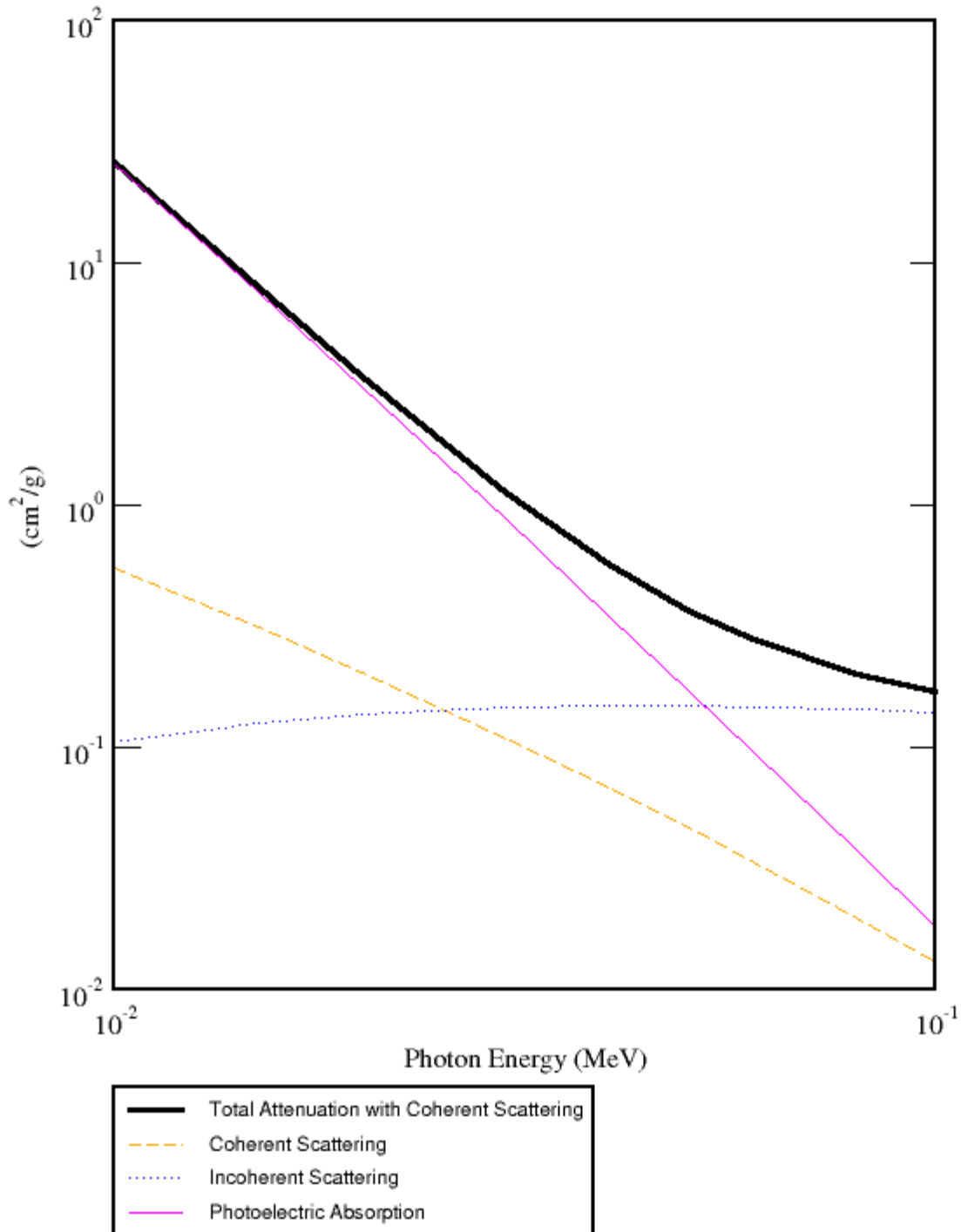
APPENDIX F  
PHOTON CROSS-SECTION DATA

All data from X-com<sup>32</sup>

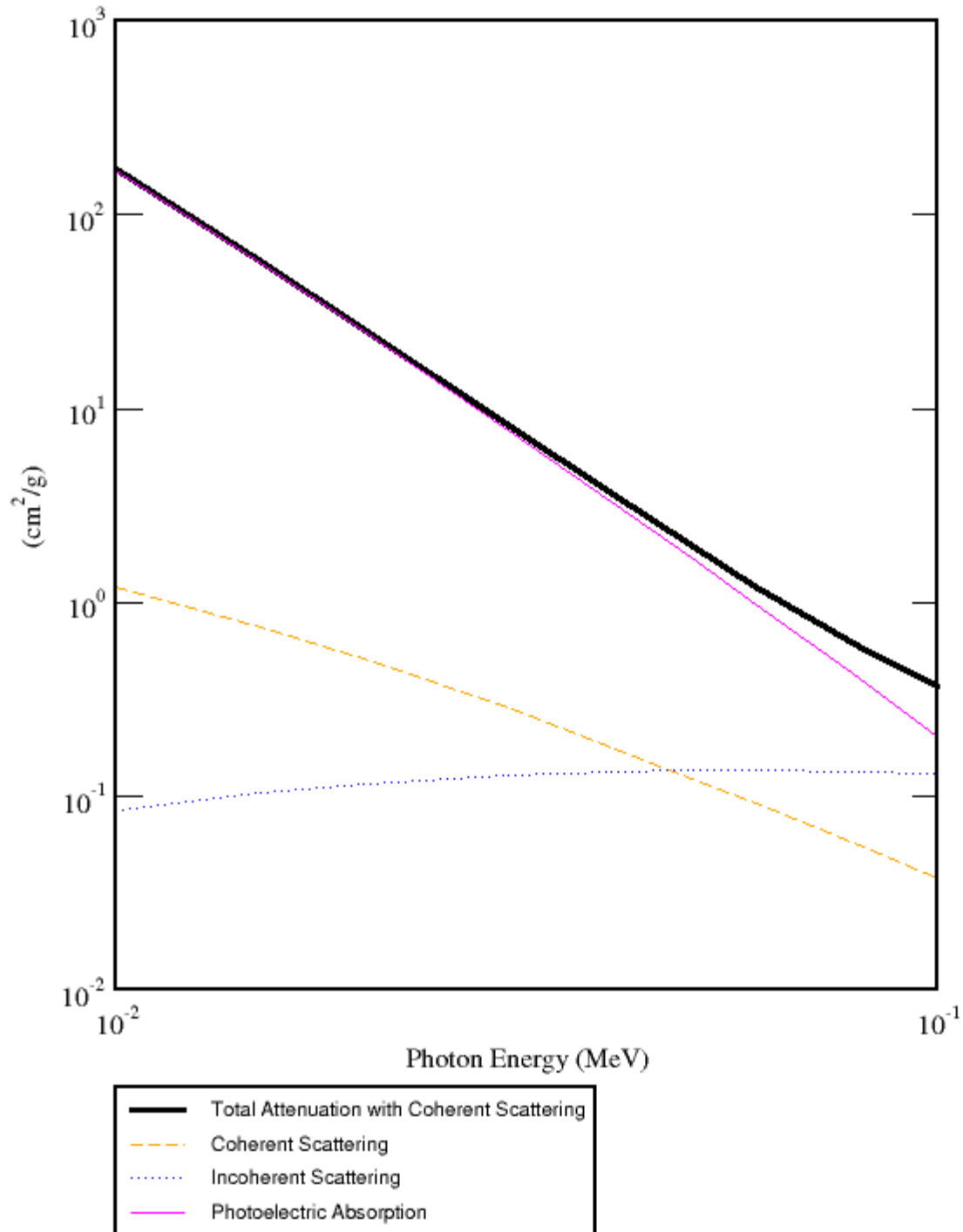
## Carbon



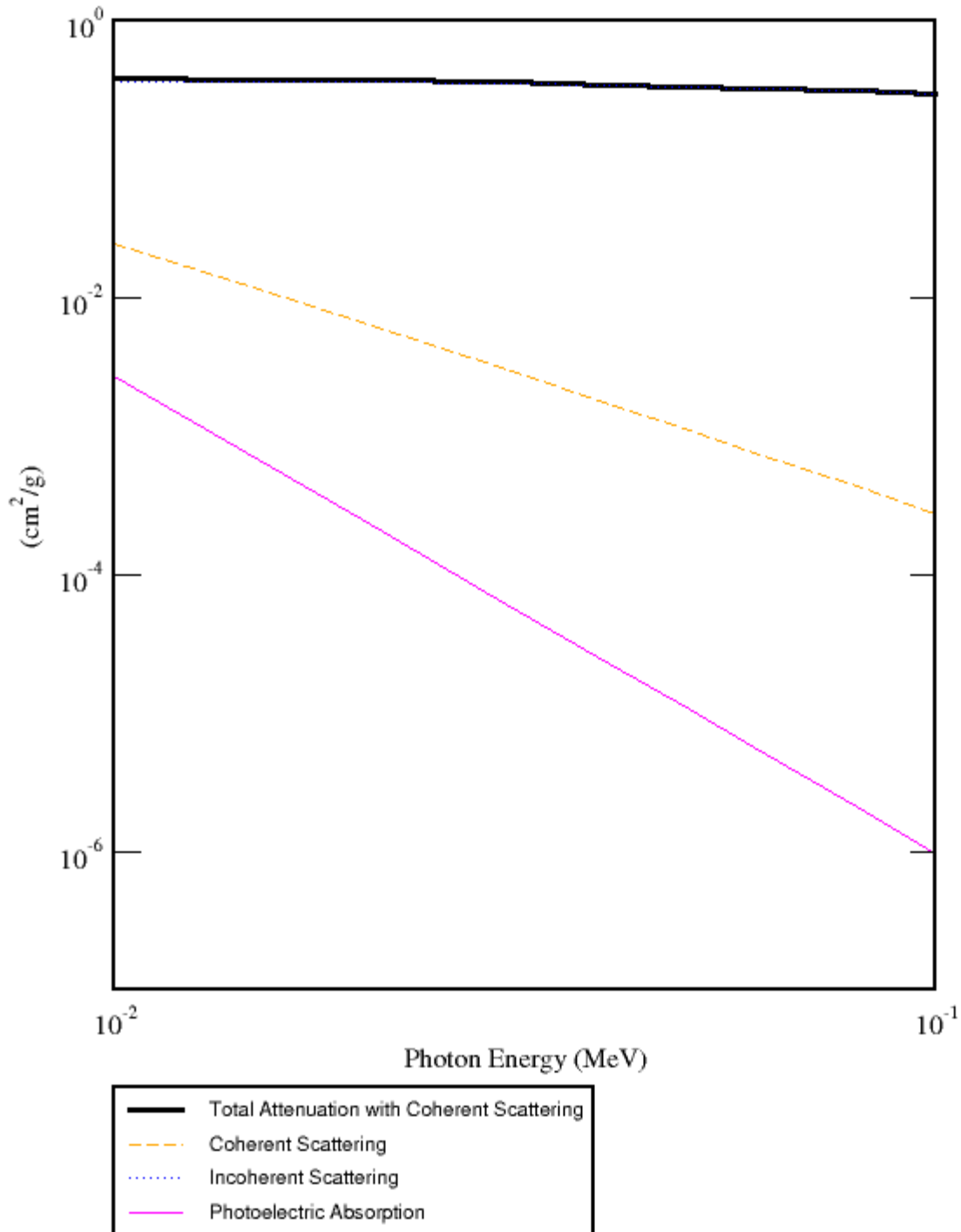
# Aluminum



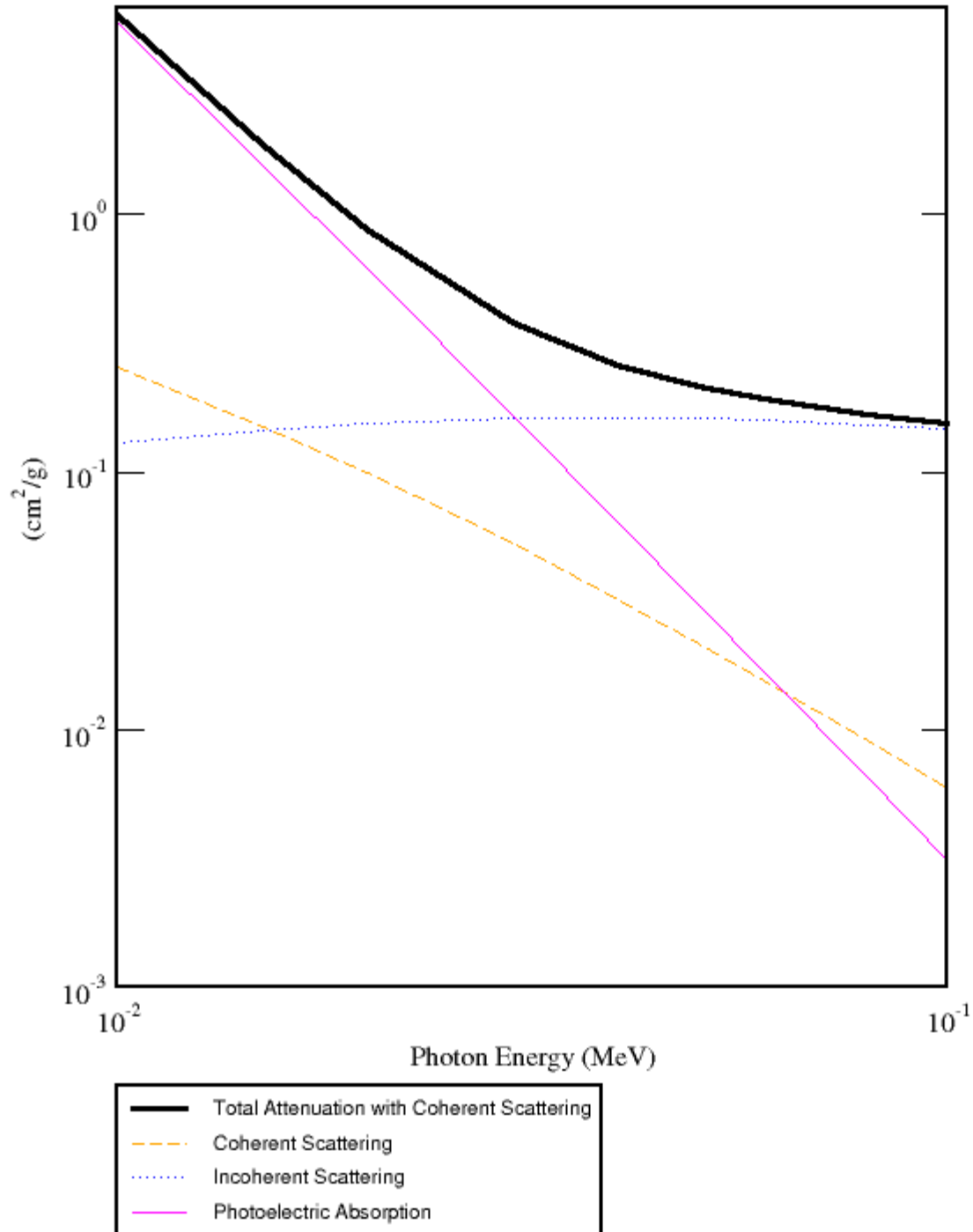
## Iron



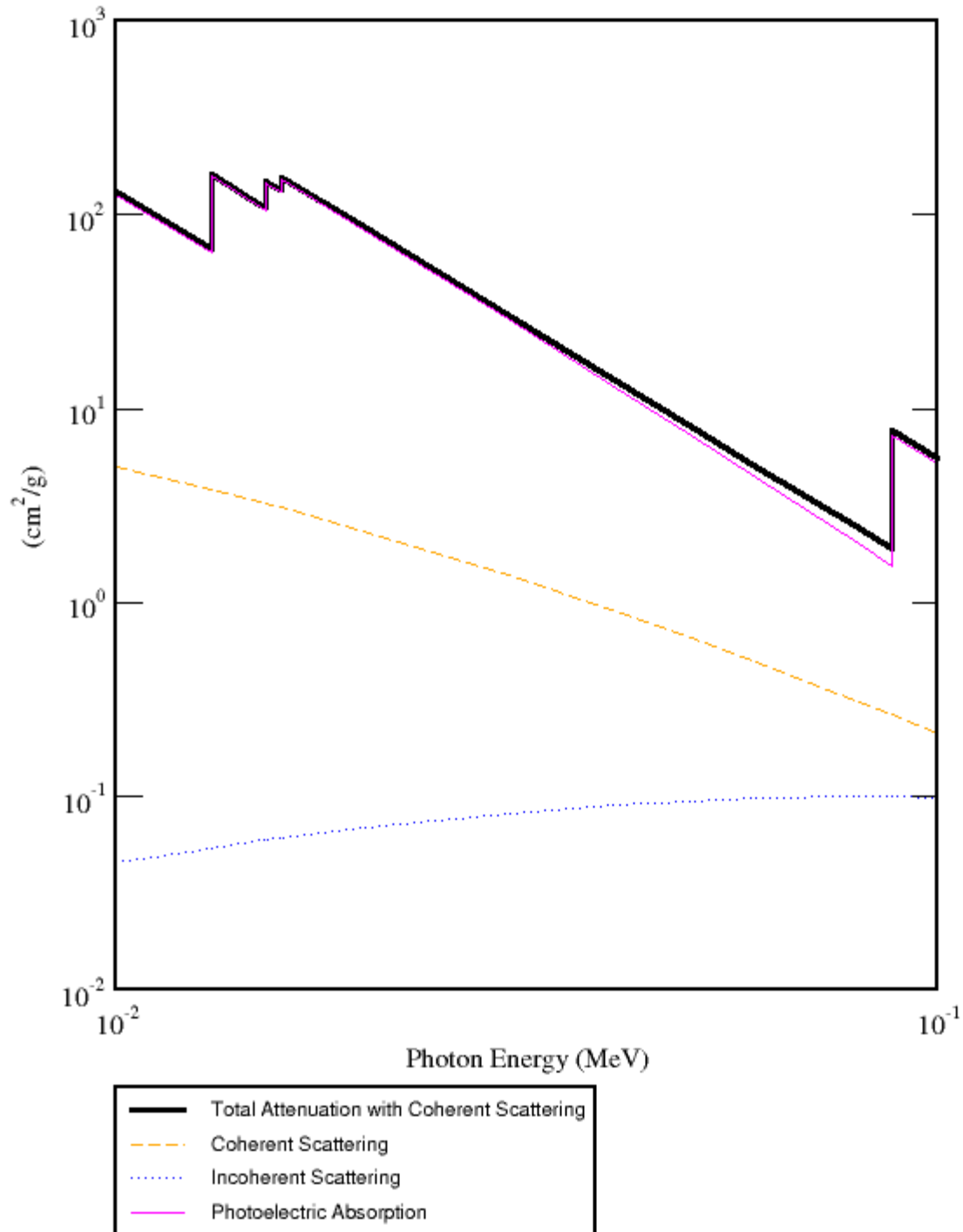
## Hydrogen



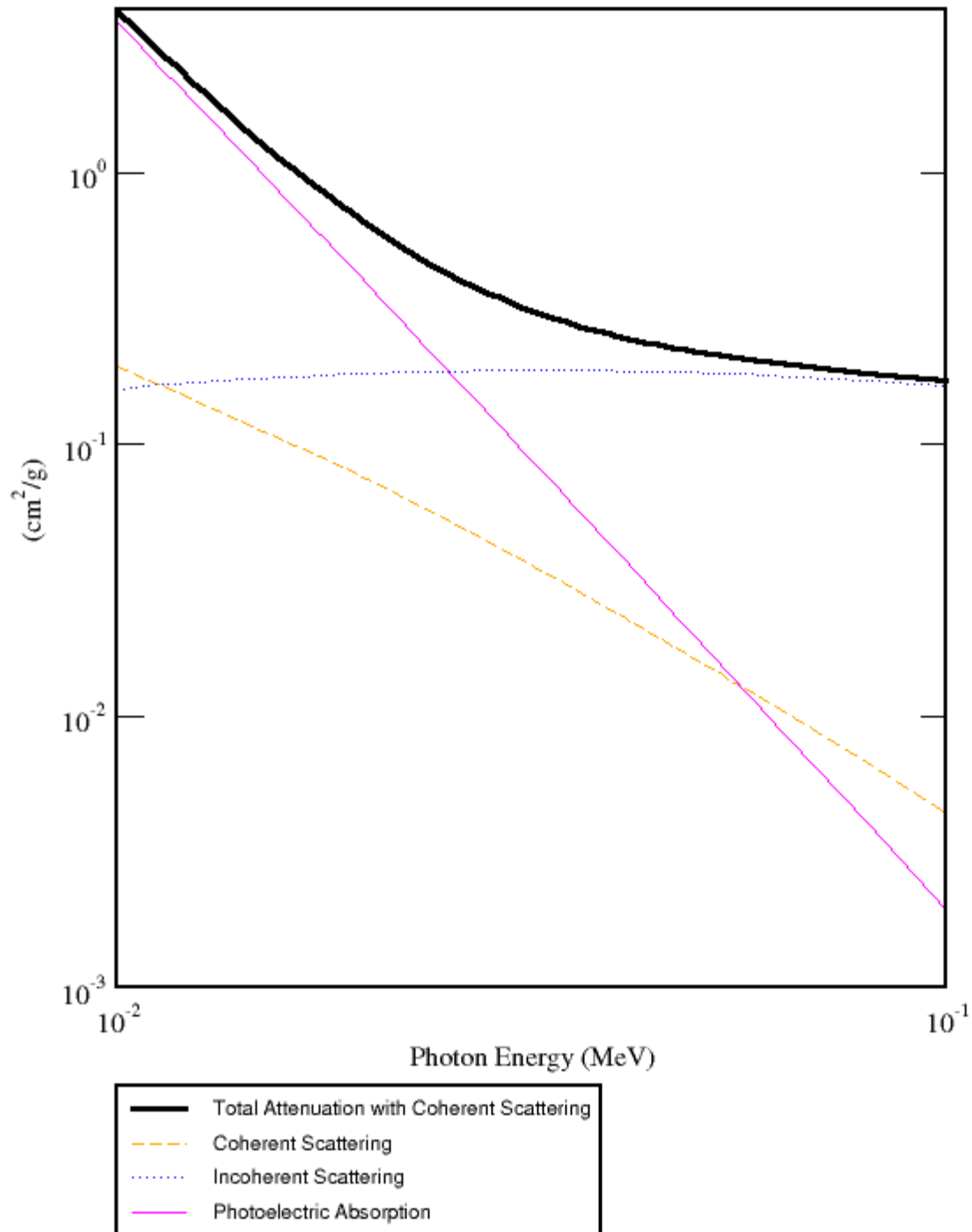
## Oxygen



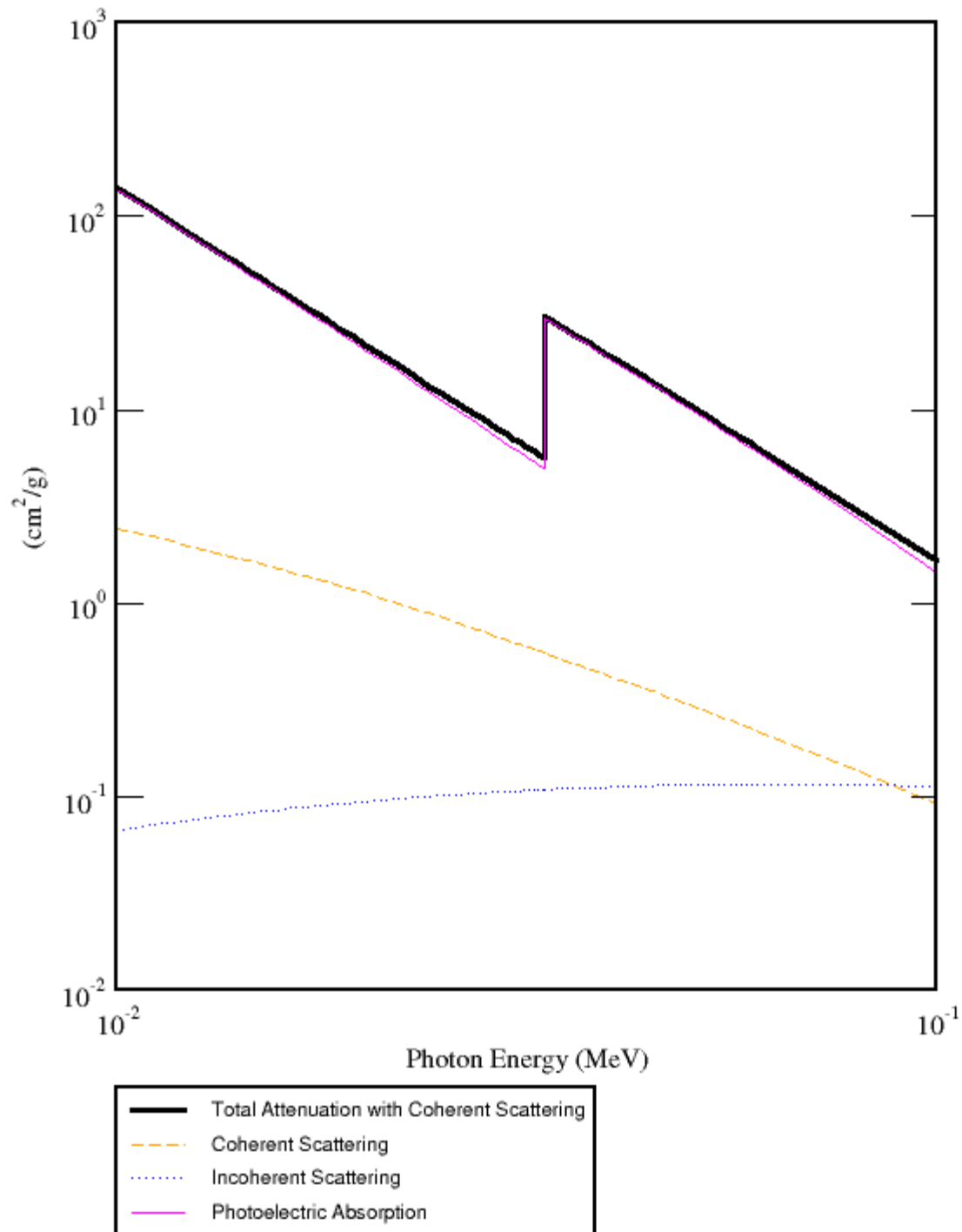
## Lead



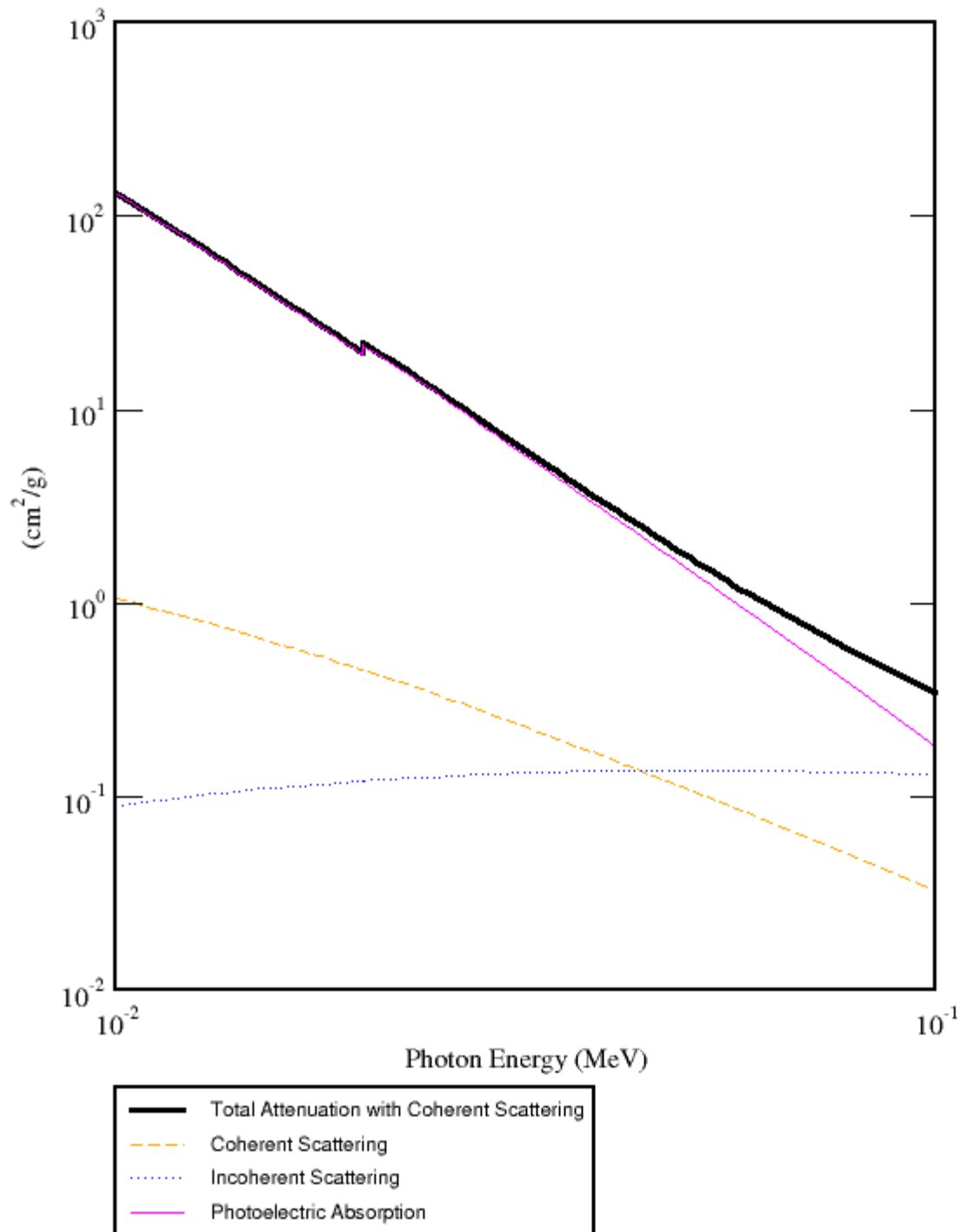
## Plastic



## NaI



## Steel



## LIST OF REFERENCES

1. Campbell, S., and Jacobs, A., 'Detection of Buried Land Mines by Compton Backscatter Imaging," *Nuclear Science and Engineering*, 110, 417-424 (1992).
2. Wehlburg, J., I "Development of a Lateral Migration Radiography Image Generation and Object Recognition System, " Ph. D. Dissertation, University of Florida, Gainesville, Florida, May, 1997.
3. Jacobs, J., "Examination of Backscattered Radiation from X Rays Directed into Sand and Cross-Talk Between Adjacent Detector Systems," Masters Research Project, University of Florida, Gainesville, Florida, December, 1997.
4. Dugan, E., Jacobs, A., Keshavmurthy, S., and Wehlburg, J., " Lateral Migration Radiography," *Research in Nondestructive Evaluation*, Vol 10, No. 2, pp 75-108, June, 1998.
5. Jacobs, A., Dugan, E., Howley, J., and Su, Z., "Landmine Detection/ Identification Using A New X-Ray Backscatter Imaging Technique," Third Symposium on Technology and the Mine Problem, Monterey, CA, April, 1998.
6. Su, Z, Howley, J., Jacobs, J., Dugan, E., and Jacobs, A., "The Discernibility of Landmines Using Lateral Migration Radiography," SPIE Proceedings on Detection and Remediation Technologies for Mines and Minelike Targets III, Vol 3392, pp 878-887, Orlando, FL, April, 1998.
7. Jacobs, A., Dugan, E., Moore, J., Su, Z., Wells, C., Ekdahl, D., and Brandy, J., "Imaging Subsurface Defects Using XRay Lateral Migration Radiography/A New Backscatter Technique," Proceedings of ASNT Conference on Real-Time Radioscopy and Digital Imaging, August, 1999.
8. Su, Z., Jacobs, A., Dugan E., Wells, C., Allard, A., Caniveau, G., "A Practical Land Mine Detection Confirmation System Based on X-ray Lateral Migration Radiography," Fifth Symposium on Technology and the Mine Problem4 Monterey, CA, April, 2000.
9. Edward T. Dugan, Alan M. Jacobs, Dan Shedlock and Dan Ekdahl "Edward T. Dugan\*, Alan M. Jacobs, Dan Shedlock and Dan Ekdahl" Paper for SPIE 49th Annual Meeting August, 2003 Denver, CO
10. <http://www.lockheedmartin.com/wms/findpage.do?dsp=fec&ci=11322&rsbci=13182&fti=0&ti=0&sc=400SOFI>. Lockheed Martin Space Corp. July 16, 2005.

11. NASA. "Return to Flight Focus Area: External Tank Thermal Protection System." Marshall Space Flight Center. Huntsville, AL
12. NASA. <http://www.ncfi.com/insulation.html>. April 2005.
13. MCNP5 – A General Monte Carlo N-Particle Transport Code. X-5 Monte Carlo team. Los Alamos National Laboratory, New Mexico. 2003
14. Jacobs, A., Dugan, E., Moore, J., Su, Z., Wells, C., Ekdahl, D., and Brandy, J., "Imaging Subsurface Defects Using XRay Lateral Migration Radiography/A New Backscatter Technique," Proceedings of ASNT Conference on Real-Time Radioscopy and Digital Imaging, August, 1999
15. Dugan, E. Jacobs, A. "Lateral Migration Radiography Image Signatures for the Detection of Buried Landmines. " Grant Extension Technical Report. ARO Grant Number DAAG-55-98-1-0400. Nuclear and Radiological Engineering Department. University of Florida. 2002
16. Jacqueline MacDonald, J.R. Lockwood, John McFee, Thomas Altshuler, Thomas Broach, Lawrence Carin, Russell Harmon, Carey Rappaport, Waymond Scott, Richard Weaver. Alternatives for Landmine Detection. RAND 2003
17. Lawrence Livermore National Laboratory. <http://www.llnl.gov/str/Azevedo.html>. November 1997
18. Garder, Paul D. "Landmine Detection with Ground Penetrating Radar Using hidden Markov Models." IEEE Transactions on Geoscience and Remote Sensing. Vol.39, No. 6, June 2001.
19. Jacobs, A., Dugan, E., Howley, J., Su, Z., and Wells, C., "Detection/Identification of Landmines by Lateral Migration Radiography," Proceedings of Second International Conference on The Detection of Abandoned Mines, Institution of Electrical Engineers Publication No. 458, pp 152-156, Edinburg, UK, October, 1998
20. Su, Z., "Concept and Application of a Vehicle-mounted Land Mine Detecton System Based on Lateral Migration Radiography," Masters Research Project, University of Florida, Gainesville, FL, August, 1998.
21. Howley, J., "Detailed Study of Lateral Migration Radiography Image, 5 Relevant to Landmine Detection," Master's Research Project, University of Florida, Gainesville, FL, August, 1998.
22. Keshavmurthy, Shyam Prasad "Development of Lateral Migration Backscatter Radiography and Associated Image Enhancement Algorithms" Master's Thesis. UF 1996

23. Salazar, SABRINA Katherine “Material Flaw Detection Characteristics of X-Ray Lateral Migration Radiography” Master’s Thesis. UF 2002.
24. Brygoo, Stephanie “X-ray Lateral Migration Radiography Non Destructive Flaw Detection Measurements and Simulations,” Master’s Thesis. UF 2002
25. Moore, Jeffery D. “Simulated Material Flaw Detection Using X-ray Lateral Migration Radiography UF 1999
26. Yxlon International Corporation. [http://www.yxlon.com/yxlon/yxlon\\_cms.nsf](http://www.yxlon.com/yxlon/yxlon_cms.nsf). April 2005.
27. Beiser Arthur. Concepts of Modern Physics 5<sup>th</sup> Edition. Mcgraw Hill. New York, NY 1995
28. Attix, Frank H Introduction to Radiological Physics and Radiation Dosimetry John Wiley & Sons, Inc New York, NY 1986
29. National Institute of Standards and Technology. <http://physics.nist.gov/PhysRefData/Xcom/Text/XCOM.html>. August 2005.
30. Uppsala Universitet: Biomedical Radiation Sciences. [http://www.anst.uu.se/hanslund/Med\\_Tekn/x-ray%20production.pdf](http://www.anst.uu.se/hanslund/Med_Tekn/x-ray%20production.pdf). May 2005
31. Knoll, Glen E. Radiation Detection and Measurement John Wiley & Sons New York, NY 2000
32. SABRINA 3.54: Three-Dimensional Geometry Visualization Code System. Radiation Transport Group, Los Alamos National Laboratory, Los Alamos, New Mexico.
33. LabVIEW. National Instruments. National Instruments Corporation. Austin, Tx.

## BIOGRAPHICAL SKETCH

Benjamin Addicott attended the University of Florida where he received both a B.S. and an M.E. in nuclear engineering.